



UNIVERSITÀ DEGLI STUDI DI ROMA
"TOR VERGATA"

XXIX-Cycle of Computer Science, Control And
Geoinformation Doctorate

Wireless and Battery-less Biointegrated Sensors for Bodycentric Internet of Things

Sara Amendola

ADVISOR:

Prof. Gaetano Marrocco

COORDINATOR:

Prof. Giovanni Schiavon

Summary

The advent of Internet of Things (IoT) – a paradigm emphasizing data interconnectedness through networked objects densely distributed in the environment – is deemed crucial to trigger innovations in healthcare. The traditional medical model is rapidly evolving towards a participatory personalized ubiquitous medicine. Indeed, empowering patients through wearable technologies, the augmented human bodies outfitted with imperceptible sensors might become the vehicle for a mine of pertinent health information. These data are straight accessible from anywhere at anytime, making the human beings an inherently integrated part of Smart Architectures (a facet of IoT often referred to as “Internet of the Body”).

According to a visionary perspective, 600 millions body-worn sensors are expected to be worldwide connected to the backbone of Internet by 2020 [1]. However, interfacing electronics with the body in a way that is comfortable and transparent for the users has to tackle the intrinsic challenge arising from the mechanical mismatch between the soft /curvilinear biological tissues and the rigid/planar nature of the conventional silicon-based devices. Over the last few years, there has been enormous progress in materials, designs, and manufacturing processes for flexible and stretchable systems that

resulted in the pioneering of a cutting-edge discipline known as *Epidermal* or *Skin Electronics*. This fertile research trend is stimulating the fast development of a new class of “tattoo-like” devices that seamlessly laminate onto the curve textured body surface and unobtrusively pick up a host of physio/pathological parameters over the epidermis. Besides academic flourishing, such *bio-integrated* technology is increasingly gaining the attention of forefront companies drawn by the huge potential growth markets in the biotech, pharmaceuticals, security, entertainment and consumer electronics.

However, most of the referenced skin-tight sensors - despite shaped in conformable and stretchy hi-tech configurations - still require bulky power sources and tangled wires or, at most, on near-contacting links for data transfer, thus hindering de facto the wearers’ comfort and their natural movements. Embedding ultra-low profile power sources, energy storage units and wireless modules in such minimally invasive forms is hence an essential prerequisite for the acceptance of bio-integrated devices in daily life.

In this scenario, the passive Radiofrequency Identification (RFID) technology appears mature enough to foster the overcoming of the above limitations. Indeed the communication through electromagnetic backscattering, typical of RFID architectures, requires just a small battery-less IC transponder, that entirely fulfill the vision of passive (energy autonomous) devices able to be wirelessly powered-up and remotely accessed by a processing unit. Thanks to the intrinsic sensing capabilities of RFID platforms, the simple interaction between the radiator, acting as an electromagnetic transducer, and the underlying tissues can be exploited to retrieve data about the state of the human body, without complex circuits. The UHF RFID standard (860- 960 MHz) is particular attractive over the HF frequency (13.56 MHz), due to the possibility of activation ranges up to one meter and even more. This potentiality paves the way to a broad range of pervasive application involving masses of uncooperative users that are unconsciously and continuously monitored by remote scanners spread into Smart Spaces.

RFID transponders for epidermal sensing have to play as both an antenna radiating/receiving outside the body and as a sensor capturing biophysical parameters over the skin; therefore - unlike wearable tags that are usually placed over clothes, armbands and chest

straps - they must intimately adhere to the body surface by means of very thin (sub-millimeter) insulating biocompatible materials, mostly acting as adhesive, eventually functionalized, interface between the conductor/electronics and the skin. However, the cohabitation of UHF radiator with the human skin, or with living matters in general, poses an intrinsic challenge due to the high losses of tissues which strongly degrade the radiation efficiency of the antenna and, accordingly, the length of the communication link of the radio system.

The virtuous synergy between Epidermal Electronics and the UHF RFID tech calls for a dedicated rigorous scientific activity on a rather novel topic which can be termed as *Epidermal Electromagnetics* and it is hence the subject of this Ph.D thesis.

The ambitious goal is to provide the emerging class of bio-integrated sensors with efficient communication means to remotely transmit the data collected over the body. The possibility of remotely interacting with epidermal transponders will turn such devices into a novel fundamental brick of IoT monitoring architectures, thus realizing a decisive step towards the implementation Smart Health practices.

My research efforts were driven by a multidisciplinary approach merging expertise from Applied Electromagnetics, Material Science, Signal Processing, Informatics as well as Medical Physio/Pathology. The comprehensive analysis covers multi-fold aspects, ranging from the basic principle of antennas radiating over lossy medium, technological research on low-cost biomaterials and manufacturing processes, up to the optimal design, calibration and experimentation of epidermal tag in real-life scenarios.

The expected potentiality of the research is to substantially boost the concrete usability of *stick-to-skin* devices, in the same way as the research on wearable antennas and bodycentric communication has concurred in recent past to the actual explosion of wearable devices for self-tracking.

Epidermal Antennas for UHF Radiofrequency Identification and Sensing

The first part of thesis concerns the electromagnetic investigation and technologic developments aimed at the remote wireless communication with the emerging family of epidermal devices interfacing with unconventional high permittivity/loss media like the human tissues.

Starting from the basic principle of antennas radiating over the lossy body, a systematic investigation is performed through numerical simulations and laboratory experiments to define fundamental limitations and possible upper bounds in the achievable performance depending on antenna layouts, conductors materials and substrates. Benchmark guidelines are accordingly derived for the optimal design of real RFID epidermal transponders. As the human variability strongly impacts on the response of low-profile skin antennas, a reference tag is extensively characterized for several body positions and subjects' builds and an on-body tuning mechanism is proposed and demonstrated to mitigate such effect. A focused activity is then dedicated to materials and manufacturing technologies suitable for epidermal RFID sensors. In particular the RF static and time-varying dielectric properties of sub-millimeter specialized membranes are characterized by using a combined ring-resonator measurement method and numerical data inversion. Advanced state-of-the art fabrication processes are explored to identify cost-effective and easily accessible methods for the rapid prototyping of preliminary samples in laboratory settings as well as the mass production of epidermal device over the large scale. All the previous findings are applied finally to the design of real epidermal RFID sensor for the wireless monitoring of the skin temperature.

From devices to IoT Pervasive Monitoring Systems

The second part of the thesis draws a landscape of RFID wireless sensor networks able to unobtrusively gather high-level information about the users' health state, the quality of the nearby environment and their mutual interactions. The study provides a comprehensive system vision which encompasses both hardware and software

topics. Starting from the physical issues of the sensor devices, the discussion will cover the processing of low-level analog and digital electromagnetic signals, up to the top application level.

RFID-based platforms with growing complexity are implemented by exploiting a unique interrogating infrastructure and one or a combination of different types of radio-transponders specifically conceived for various placements and sensing purposes:

- i) Ambient sensors* able to detect physical parameters (temperature, humidity, presence of toxic agents...) to assess the quality of the environment and its correlation with people's health;
- ii) Wearable tags*, in the form of "badge-like" antennas integrated within garments, for indoor people's identification and movements tracking;
- iii) Epidermal tags* stuck over the skin like a temporary tattoo to monitor specific bio-parameters, temperature as first, over the body surface.

The latter family of skin transponders, which is the primary kernel of this thesis, is now inserted the first in the perspective of (not so) futuristic IoT scenarios wherein it is expected to convey a real added value.

Three case studies are analyzed concerning the monitoring of 1) single physical parameters (skin temperature), 2) sleeping behavioral patterns and 3) advanced human/environment interactions.

Nomenclature

BAN	Body Area Network
COTS	Commercial off the shelf
DC	Direct Current
EIRP	Equivalent Isotropically Radiated Power
FAD	Finger Augmented Device
FDTD	Finite Difference Time Domain
IoT	Internet of Things
MOM	Method of Moment
NFC	Near Field Communication
PDMS	Polydimethylsiloxane
PET	Polyethylene terephthalate
PI	polyimide
PU	Polyurethane

RFID	Radio Frequency Identification
RSSI	Received Signal Strength Indicator
UHF	Ultra-High frequency
VNA	Vector Network Analyze

Contents

Summary	3
Nomenclature	9
I. Epidermal Antennas for UHF Radiofrequency Identification and Sensing	1
1. Beyond wearables: Bio-integrated Sensors for Health monitoring	5
1.1. Limitations of the current systems	7
1.2. The RFID approach	10
1.3. Challenges of UHF Epidermal antennas and Aim . .	13
1.4. Background: RFID Principles	16
1.4.1. RFID-based Sensing: Analog vs. Digital tag .	18
1.4.2. Reading Performance	20
2. Fundamental limitations and Optimal performance	25
2.1. Reference antennas, body model and method of analysis	27

2.2.	Efficiency and gain vs. antenna size	29
2.2.1.	Loop and Dipole	29
2.2.2.	Slotted Antennas	31
2.2.3.	Performance Comparison	32
2.3.	Gain vs. the trace width and conductivity	34
2.4.	Radiation performance vs. the spacing from the skin	35
2.5.	Performance on Anthropomorphic Layerings	38
2.6.	Design Guidelines	40
2.7.	Experimental validation	43
2.7.1.	Measurement method	43
2.7.2.	Prototypes	46
2.7.3.	Measurement results	46
2.8.	Summary and Conclusions	50
3.	Human Variability and On-skin Retuning	51
3.1.	Reference skin antenna: dual-loop tag	52
3.1.1.	Simulated performance vs. body regions . . .	54
3.1.2.	Simulated performance vs. body mass	56
3.2.	Prototype and on-skin performance	61
3.2.1.	Measured Performances vs. body placement .	63
3.2.2.	Measured performance vs. body mass	64
3.3.	On-skin retuning	65
3.4.	Examples	71
3.4.1.	Tuning at a given position	71
3.4.2.	Change of the UHF band	71
3.4.3.	Overall analysis	71
3.5.	Conclusions	74
4.	Biocompatible epidermal membranes	75
4.1.	RF Dielectric characterization: Measurement set-up and validation	77
4.2.	Hydrogels	82
4.3.	Moisture-retentive dressing	88
4.4.	Static membranes	89
4.5.	Conclusions	91

5. Self-Sintering Inkjet Printing and other Manufacturing Technologies	93
5.1. Inkjet Printing by Self-Sintering Ag Ink	95
5.1.1. Suitable printing substrates	96
5.1.2. The spontaneous-sintering effect	98
5.1.3. Resistivity v.s. sheet pre-treatment and drying conditions	99
5.2. Characterization in the UHF-RFID band	101
5.3. Application to a small-size epidermal tag	103
5.3.1. RF Performance versus the trace width . . .	106
5.3.2. Overprinting deposition	107
5.3.3. Resistance to bending	108
5.3.4. Immunity to body fluids	110
5.3.5. Tag coating	111
5.4. Comparison with other manufacturing techniques . .	112
5.4.1. Carved Adhesive Copper Sheet	113
5.4.2. Copper microwires	114
5.4.3. Microfabrication	114
5.4.4. On-skin performance comparison	115
5.5. Discussion and Conclusions	118
6. An Epidermal RFID Thermometer for remote skin temperature monitoring	121
6.1. Reusable and Sterile Epidermal thermometer	123
6.1.1. Prototypes	125
6.2. Thermal Characterization	130
6.2.1. Sensor Calibration	130
6.2.2. Time Response	132
6.3. Conclusions	135
II. From devices to IoT Pervasive Monitoring Systems	137
7. Real-Life Temperature Monitoring by Epidermal RFID sensors	147
7.1. Manual reading	148

7.2.	Automatic (unsupervised) monitoring	149
7.2.1.	Continuous overnight temperature monitoring	149
7.2.2.	On-flight temperature monitoring across gates	152
7.3.	Conclusions and open issues	157
8.	Remote Monitoring and Control of Overnight living environment	159
8.1.	Description of the System	160
8.2.	Electromagnetic Analysis	163
8.2.1.	Communication issues	165
8.2.2.	Safety Compliance Issues	166
8.3.	Detection of sleep events	168
8.3.1.	Classification of the sleeper's state	171
8.3.2.	Classification of the sleeper's activity	173
8.3.3.	Events Representation	174
8.4.	Validation of the System	175
8.5.	Example of Real-life Recordings	177
8.5.1.	Installation procedures	177
8.6.	Conclusions	182
9.	Advanced Human-Things Interactions and Multi-parameters monitoring	185
9.1.	The Radio-board	187
9.2.	Control & Coordination Software	188
9.3.	Application to the Physical Security in Electric Plants	192
9.3.1.	Events to be detected	192
9.3.2.	Network configuration	193
9.3.3.	Flooding and humidity	195
9.3.4.	Harness overloading	196
9.3.5.	Cabin Access and Manumission	197
9.4.	Conclusions	205
10.	Conclusions	207
Appendix A:	Legacy	211
11.	Finger-Augmented RFID System to Restore Peripheral Thermal Feeling	213
11.1.	Components of <i>RadioFingerTip</i> system	215

11.2. Prototypes and Measurements	216
11.3. Sensing the temperature of the objects	219
11.4. On-going research	220
Appendix B: Other Research	221
12. RFID-inspired microelectronic systems for Wireless Brain	
Machine Interfaces	223
12.1. Modeling of the Transcranial Wireless Link	224
12.2. Electro-Textile Transmit Antennas	226
12.2.1. Prototypes and Measurements	228
12.3. Millimeter size backscattering Neural Tags	233
12.3.1. Fabrication and Wireless Measurements	234
12.3.2. Conclusions	242
Bibliography	249
List of Publications and Awards	267

I

**Epidermal Antennas for UHF
Radiofrequency Identification and
Sensing**

The first part of thesis concerns epidermal RFID components. After introducing the background and motivation of the work (chapter 1), a systematic investigation on UHF antennas suitable for direct skin placement is presented. Both numerical and experimental analysis are discussed to define fundamental limitations of epidermal radiators and possible upper bounds in their achievable performance depending on layouts and materials (conductors and substrates).

Human tissues are challenging to be electromagnetically modeled, since different individuals, and even the same person, exhibit a broad range of parameters for a given body part and also over time. A reference dual-loop antenna is introduced in chapter 3 and extensively used to discuss the issues arising from the strong variability of the response of epidermal tag's with the positioning over different subjects and body regions. To master this effect a manual retuning mechanism is proposed and experimentally demonstrated to achieve optimum tag performance even after the mounting on a given individual.

Biomaterials to be used as substrates for epidermal tags play a crucial role as they represent the interface between the radiators and the skin. These materials are definitely unconventional substrates for RF devices and their dielectric properties in the UHF band mostly unknown. The chapter 4 focuses the RF characterization of both static and time-varying dielectric properties of suitable substrates by using combined ring-resonator measurement method and numerical data inversion. Different class of engineered membranes including functionalized hydrogels, moisture-retentive dressing and transpiring polymeric scaffolds were characterized for application to wireless measurement of the body temperature and wound care.

To comply with skin technologies, conductive traces must be patterned over biocompatible ultra-thin flexible membranes. Advanced fabrication processes are explored to identify cost-effective and easily accessible methods for the rapid prototyping of preliminary samples in laboratory settings as well as the mass production of epidermal device over the large scale. Among the viable manufacturing options, the potential application of recently developed Self-Sintering ink and low-cost printing equipment is especially investigated in chapter 5, starting from the characterization of the ink conductivity in the RF regime. Then a comparative analysis of

the achievable electromagnetic performance of epidermal antennas fabricated by different state of the art manufacturing technologies is performed to identify case by case the most appropriate manufacturing choice depending on costs, processing time, physical robustness and need of monolithic integration with other sensors.

The part ends with the design and the thermal calibration of a small-size RFID sensor able to wirelessly measure the skin temperature with acceptable clinical accuracy (chapter 6). The presented sensor is inherently prone to be integrated within RFID-based Smart Architectures for remote healthcare, as will be discussed in the second part of the thesis.

1

Beyond wearables: Bio-integrated Sensors for Health monitoring

In the last decade, the growing interest in advanced body-worn electronic systems for health monitoring has been widely evidenced both by the rapid proliferation of research articles and by the expanding collection of wearables devices available on the markets¹. While consumers currently use fashionable fitness trackers and smart watches to self-track their life style regimen and optimize their fitness profile, there is an emerging technological trend that expand beyond qualitative measurements (e.g., activity levels or “steps”) towards a more quantitative sensing with direct correlates to clinical gold standards and emphasis on continuous monitoring of all vital signs.

In this perspective, the next wave following the wearables is represented by the rise of *bio-integrated* technology, which aims at developing seamless sensory interfaces to the human body by moving electronics and sensors from clothes, wristband and straps directly to the skin.

The epidermis is indeed an exceptionally complex, time-evolving interface that provides a precious insight about people’s health and

¹The wearables database powered by Deloitte, <http://vandrico.com/wearables/>.

wellbeing. Its essential functions include physical protection from environmental agents, temperature regulation, water retention and vitamin production. The skin is able to reflect significant physiological changes earlier than central parameters, which are protected by homeostatic feedback. It is also the primary perceptual interface towards the surrounding environment and it is continuously “sampled” by the central nervous system in terms of tactile cues. In a social and psychological context, it even plays a role in establishing interpersonal bonds and in defining a sense of self.

Basically, the skin constantly conveys two-directional data flux, from the internal body to the external ambient and viceversa.

In line with this twofold role, the new-generation skin-mounted devices is envisaged to have the double functionalities of:

i) non-invasively collecting biophysical parameters over the epidermis;

ii) acting as invisible probes able to replace damaged sensory functions and even extend the sensing capabilities beyond the innate senses (e.g. tactile, thermal...).

The paradigm of *Epidermal* or *Skin Electronics* was originally introduced in 2011 [2] with the ambitious goal of bridging the gap between the flat and rigid wafer-based conventional electronics and the soft curvilinear surfaces of living organisms (skin, biological tissues, and organs). Pioneering research - mostly led by prof. J.A. Rogers and his worldwide scientists cohort - stimulated the fast development of a novel class of “tattoo-like” devices whose mechanical properties (thicknesses, moduli, physical and thermal mass, etc.) perfectly match with those of the skin, making them imperceptible to the wearers. The fertile scientific literature reports several examples of electronic systems that tightly adhere to the textured epidermis and unobtrusively collect physio/pathological indicators such as temperature [3], pH [4], bio-potentials [5] and strain [6]. Skin-mounted sensors has the potential to act as controlled actuators by locally modifying a clinical therapy, e.g. by triggering the transdermal drugs release, according to a feedback mechanism depending on the the measured parameters over the skin [7]. Another frontier of bio-integrated electronics concerns transient epidermal systems that are able to completely dissolve via resorption by the

body within a programmed period of time [8].

Being able to communicate with the body on such an intimate scale may enable a fan of applications that extend from medicine to entertainment and consumer electronics. Flexible circuits mimicking the sensory capabilities of skin are promising to replace painful skin grafts for amputees and burn victims as well as to restore the sense of touch in artificial limbs [9]. Human-computer interactions will benefit from skin technologies as biological inputs could dictate the behavior of machines or control communication devices, for example picking up on the muscular movements of speech to give voice to the mute. Skin-worn sensors could even enhance gaming experiences by enabling consoles to read biometric data and react in real time. Finally, the possibility to non-invasively measure different skin attributes (hydration, elasticity, renewal rate, UV exposure) is particularly appealing for the cosmetics industry aiming at developing personalized beauty routines.

1.1. Limitations of the current systems

The field of stretchable/flexible electronics is evolving rapidly, mainly driven by advances in materials, applied physics and assembly techniques. The valuable contributions published so far - mostly collected in [10] - clearly reveal that to date major scientific efforts have been devoted to:

- the mechanics design of stretchable serpentine layouts engineered to be deformation-tolerant;
- the high-tech fabrication methods that exploit established inorganic semiconductor materials in a unconventional way for patterning traces on soft, elastomeric, or flexible ultrathin substrates (micro-transfer printing, laser processing...);
- the development of a plethora of sensing elements having epidermal embodiments.

The referred examples of functional skin-tight sensors, although shaped as invisible tattoos, rests critically on bulky batteries and/or hard-wired connections for power supply and data transfer [11]. Early experiments have explored solutions including stretchable

super-capacitors and miniaturized platforms for harvesting solar, thermal or mechanical energy, while the first attempts to establish remote communication considers magnetic inductive coupling at low frequency of resonant LC circuits with an external reading coil [4, 6, 12], which makes the reading process cumbersome for the patient. The wireless powering and remote reading are still the current bottlenecks limiting the practical feasibility of the skin-mounted devices for the continuous monitoring of bioparameters outside of laboratory settings (see Fig. 1.1). Only recently pivotal works refer to farfield communication [13, 14, 15], but this topic is still in its infancy for the antenna community. Indeed, the related literature highlights a lack of deep understanding of the electromagnetics issues arising when moving radiating elements at direct contact with human skin. The influence of the lossy medium on both near and far field terms have to be understood and mastered at the purpose to perform an optimized design of skin-mounted antennas. A parallel pursuit is hence required to provide the emerging class of bio-integrated sensors with efficient communication means to transmit the collected data outside the body. This has to be considered as an essential step toward the integration of epidermal devices within connected IoT healthcare networks.

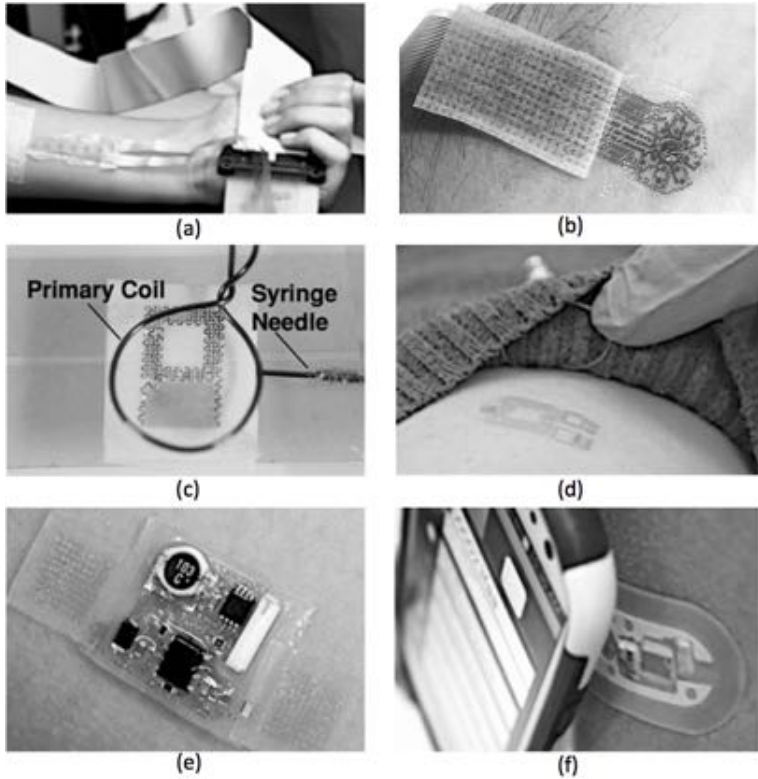


Figure 1.1.: Pioneering examples of epidermal electronics systems (EES) requiring wired interfaces (a,b), bulky batteries (e), or near-proximity to the reader device (coils (c,d) , (f) NFC smartphone).

1.2. The RFID approach

Recent advances in the domain of personal gadgets, sensing and monitoring technology for in-body and near-body use have come together under the rubric of *Body Area Networks* (BAN) [16]. Accordingly, considerable progresses have been made in characterizing wireless communications involving intra-body, on-body, and off-body channels in both the industrial, scientific, and medical (ISM) bands between 400 MHz and 2.45 GHz, and the ultrawideband (UWB). Among the existing standards for BANs, the Radiofrequency Identification technology (RFID) appears as the most promising technology to interact with epidermal devices. The communication scheme typical of RFID architectures requires just a small battery-less IC transponder (or tag), which is inherently suited for a integration within flexible, lightweight and ultrathin membranes, and offers jointed communication and sensing capabilities [17]. RFID tags have therefore a great potential to be properly reshaped in a completely novel form of epidermal-like plasters that are able to be wirelessly powered-up and accessed by a remote reader.

The few works exploring RFID solutions has favored the communication through near-field coupling at 13.56 MHz (HF-RFID, NFC) [18, 19, 20, 21, 22]. At this frequency the limited sensitivity to the presence of the underlying human tissues greatly simplifies the electromagnetic design of the antenna elements, which basically consist of multi-turns coils. Another undoubted advantage of NFC tag is the readability by mobile phone, which will likely remain a key element in the broader technology landscape. Nevertheless, as the magnetic field that is at the basis of the inductive coupling decays with the cube of distance, the reading device must be positioned very close (few centimeters) to the skin, thus strongly limiting the adoption of HF standards to supervised monitoring or self-assisted personal health tracking.

On the other hand, the telemetry in the UHF band (860-960 MHz), although strongly influenced by high dielectric targets like the human body, could provide in principle activation ranges up to one meter and more. This potentiality opens to a broad range of additional possible applications, where uncooperative users would be continuously monitored by remote scanners placed within IoT en-

vironments (smart home, hospitals, control gates..), without the active support from the users itself or from dedicated personnels. The UHF-RFID standard is particularly more attractive than the HF frequency for pervasive application to masses and it is hence the subject of this thesis.

The concept of an epidermal UHF RFID device is illustrated in Fig.1.2. The transponder comprises a miniaturized antenna for energy harvesting and communication with a remote interrogator, a microchip for data sampling modulation and several sensing elements connected to the IC or distributed over the radiator surface (e.g. sensitive coatings). The epidermal tag is deposited on a bio-compatible membrane which may dynamically interact with the skin interface by absorbing biofluids (sweat, exudates..) or releasing drugs. The resulting epidermal radio-sensor is able to perform a multivariate sensing of local skin features such as temperature, sweat loss and ph, thus realizing a real “Lab on skin”.

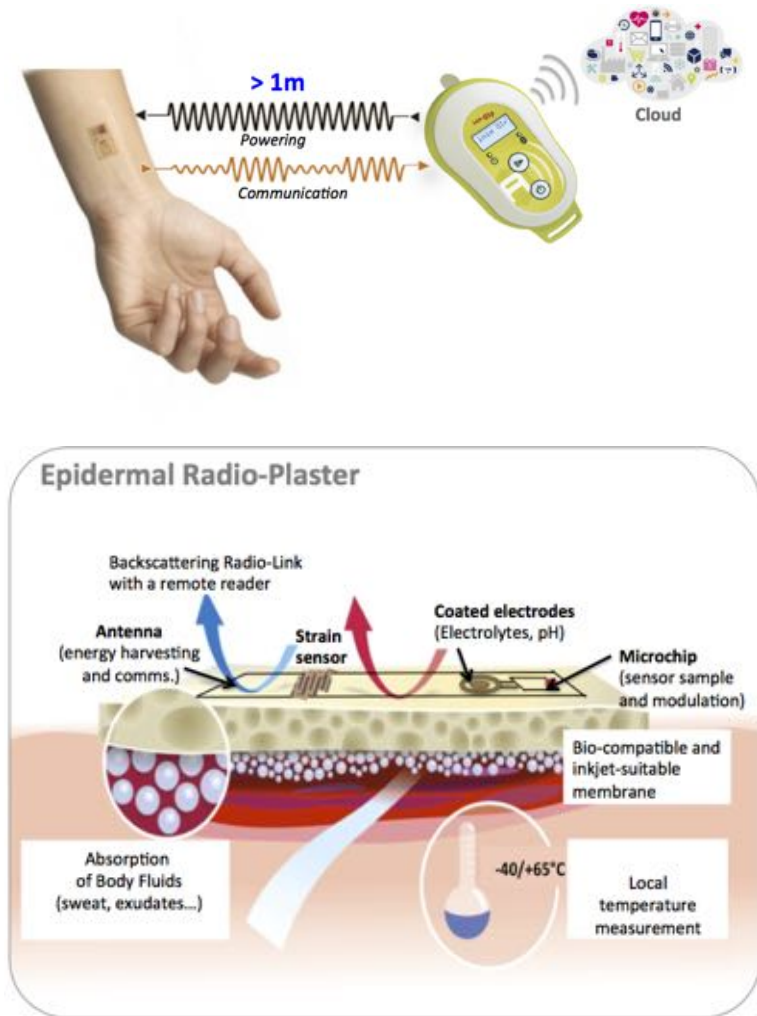


Figure 1.2.: Concept of the epidermal radio-sensor capable to monitor bioparameters over the skin (temperature, pH, the absorption of skin exudates..) and wirelessly interact with a remote reader.

1.3. Challenges of UHF Epidermal antennas and Aim

The presence of the human body imposes severe limitations to the upper bound radiation performance achievable by UHF radiators. This problem has been widely addressed in the past by the research on wearable antennas with the goal of decoupling the antenna from the body loss as much as possible by means of ground planes (patch-like antennas) [23] or multilayer spacers placed between the body and dipole, slot, or a loop antenna [24, 25, 26]. However, while wearable antennas are generally integrated within clothes/garments/wristbands without any severe constraint of micro-metric thickness, epidermal ones are conceived to be attached directly over the skin by using at most sub-millimeter thick flexible membranes.

As skin-mounted transponders must perform simultaneously as communicating and sensing devices, their presence must not interfere with local metabolism of the epidermis such to not alter the measurements of bioparameters over the skin surface. Accordingly, the epidermal substrates are required to be not only biocompatible, but also breathable to ensure the preservation of the natural transpiration and the temperature of the skin. Shielding planes, as in the case of patch antennas, must be avoided and the amount of the metal conductor minimized. As a consequence, the antennas are expected to be strongly affected by the inter-individual variability of human tissues as well as to the surface deformation due to the muscular contraction and body movements.

Epidermal antennas are definitely not an alternative technology aimed at replacing or outperform the functionalities of conventional wearable antennas, while instead they are the essential way to provide the emerging flexible/stretchable bioelectronics for medical devices and systems with communication capability.

This thesis paves the way to a novel discipline named as *Epidermal Electromagnetics* which refers to the study of the electromagnetic properties and technology developments aimed at the remote communication with skin-like devices interfacing with unconventional high-loss and dense substrates. Thanks to the multi-disciplinary

Table 1.1.: Comparison of the properties of conventional wearable antennas and epidermal antennas.

	Wearable Antennas	Epidermal Antennas
Placement	clothes, garments, watches, bands, wrists	skin
Thickness	Moderately thin (5-10mm)	sub-millimeter
Substrate	moderately flexible	flexible and elastic
Layout	shielded antennas multilayered structure (patch-like)	un-shielded antennas single-layer structure (dipoles, loops...)
Amount of Conductor	no constraints	Minimal to not alter skin ecosystem
Substrate materials	textiles, PCB	membranes
Conformability	low	high
Communication Performance	good	poor

synergy of different scientific background (Applied Electromagnetics, Material Science, and Signal Processing), the study will face the open challenges of:

- i)* theoretically investigating and optimizing the performance of UHF devices placed at micrometric distance from the human skin;
- ii)* selecting appropriate bio-compatible membranes and estimating their electromagnetic parameters;
- iii)* technological research on low-cost manufacturing processes;
- iv)* design, calibration and experimentation in real-life scenarios of an epidermal RFID tag suitable for skin temperature sensing

The research will generate an original knowledge base yielding to the design and demonstration of real epidermal transponders hav-

ing concrete applicability to be continuous and/or random monitoring of peoples health and wellness within domestic and clinical settings as well as the advanced identification of epidemic infection in dense regions (base hospitals, airports, train stations). The possibility to remotely access epidermal devices could permit to simultaneously interact with multiple skin devices in order to elaborate not only individual statistics but also cross-analysis patterns.

The expected outcome of the work is to boost the usability of the epidermal electronics in the same way as the research on wearable antennas and bodycentric communication has concurred in recent past to the actual explosion of wearable devices for self-tracking.

1.4. Background: RFID Principles

An RFID system [27] is composed of two main components: the remote transponder or *tag*, including an antenna and a microchip transmitter (IC), and the local querying system or *reader* which interrogates the tag, collects and eventually process the received data. Beside a unique identification code (ID), the data wirelessly transmitted back to the reader can include different sensing-related information that can be also stored inside the IC memory.

The tags could be *passive*, harvesting energy from the interrogating system, *semiactive* when a battery is included only to feed embedded sensors or to increase the sensitivity of the receiver inside the microchip, or fully *active* where a local source directly feeds a microcontroller and the transmitting radio. Battery-less tags have an almost unlimited life, are very low cost, lightweight, and need no maintenance. Because of the absence of a local power source, passive transponders provide the greatest flexibility in seamlessly integrating the RF devices with the human skin.

In *passive* and *semiactive* technology, at the beginning of the reader-to-tag communication protocol, the reader first activates the tag by sending a continuous wave that provides the required energy to perform actions. During this *listening mode*, the microchip exhibits an input impedance $Z_C = R_C + jX_C$, with X_C being capacitive reactance. The energy harvesting capability of the tag antenna with impedance $Z_A = R_A + jX_A$ is described by the *power transfer coefficient*:

$$\tau = \frac{4R_C R_A}{|Z_C + Z_A|^2} \leq 1 \quad (1.1)$$

which is maximum in case of conjugate impedance condition $Z_A = Z_C^*$, i.e. when the chip can use the entire power available at the tag antenna (a comprehensive review of the techniques for matching the antenna with the chip is provided in [28]).

During the next steps of the communication, the activated tag receives commands from the reader, and finally sends back the data stored in the IC memory through a *backscattered modulation* of the

continuous wave provided by the reader. In this case, the tag's IC acts as a programmable switching device between a low impedance and a high impedance states $\{Z_C^{ON}, Z_C^{OFF}\}$, thus modifying the reflectivity of the responding tag, and hence the strength of the reflected power [29].

Under the simplifying hypothesis of free-space interactions, the power budget of the UHF-RFID radio channel, that is, the power $P_{R \rightarrow T}$ transmitted by the reader and collected by the tag (direct link), and the power $P_{R \leftarrow T}$ backscattered by the tag toward the reader (backward link), is characterized through the *Friis* formula and the *radar* equation:

$$P_{R \rightarrow T} = \left(\frac{\lambda_0}{4\pi d} \right)^2 P_{in} \cdot G_R(\theta, \phi) \cdot G_\tau(\theta, \phi) \cdot \eta(\theta, \phi) \quad (1.2)$$

$$P_{R \leftarrow T} = \left(\frac{\lambda_0}{4\pi d} \right)^4 P_{in} \cdot G_R^2(\phi, \theta) \cdot G_T^2(\phi, \theta) \eta^2(\theta, \phi) \cdot \tau \frac{4R_A^2}{|Z_C + Z_A|^2} \quad (1.3)$$

where λ_0 is the free-space wavelength of the carrier tone emitted by the reader; ϕ and θ are the angles of a spherical coordinate system centered at the tag; P_{in} is the power entering the reader's antenna; $G_R(\phi, \theta)$ is the gain of the reader antenna; η is the polarization factor accounting for the mutual orientation reader-tag; $G_\tau(\phi, \theta) = G_T(\phi, \theta) \cdot \tau$ is the *realized gain* of the tag, i.e. the radiation gain $G_T(\phi, \theta)$ of the antenna corrected by the power transfer coefficient τ between tag's antenna and microchip.

At the reader side, various power-related parameters can be recorded besides the digital code of the tag. The first parameter obtainable from the forward link is the *turn-on power* P_{in}^{to} , that the minimum input power P_{in} through the reader's antenna required to activate the tag integrated circuit (P_{chip}). From turn-on measurement it is possible to extract the *realized gain* of the tag G_τ , as follows:

$$G_\tau(\theta, \phi) = \left(\frac{4\pi d}{\lambda_o} \right)^2 \frac{P_{chip}}{G_R(\theta, \phi) \cdot \eta(\theta, \phi) \cdot P_{in}^{to}(\theta, \phi)} \quad (1.4)$$

that is a useful metric to experimentally evaluate the combined radiation and matching properties of a tag antenna independently of the connected IC.

The backscattered power is also measurable by the reader in terms of the Received Signal Strength Indicator (RSSI) that is directly related to $P_{R\leftarrow T}$ through a reader-specific linear conversion formula.

1.4.1. RFID-based Sensing: Analog vs. Digital tag

The applicability of RFID technology to pervasive sensing is now a fact, as demonstrated by the countless worldwide scientific papers that refer to a myriad of engineered sensor-oriented transponders [30]. The two main sensing paradigms comprise:

1. *Analog tag* with standard chips where the antenna itself plays as electromagnetic transducer of some physical/chemical phenomenon under observation;
2. *Digital tag* with sensor-oriented chips that encode the sensed data at the chip level and transmit them in a digital form

The first approach positively exploits the intrinsic sensitivity of a bare tag to the time-variant boundary conditions. Indeed, the changing of the effective permittivity [31] and/or the presence of metallic and scatterings objects in the surroundings [32] sensibly impact on the tag impedance and the gain which, in turn, produce a variation of some measurable indicators (turn-on power, amplitude and phase of the backscattered signal). This sensing scheme can be enforced by loading the tag with lumped or distribute elements that are specifically sensitive to a target parameter, such as humidity, temperature or volatile compounds [33, 34]. Although simple and powerful, such operation mode has the intrinsic disadvantage that the impedance mismatch caused by the evolution of the sensing process is detrimental for the communication functionality. Moreover, as intelligence to retrieve the physical parameters from the measured signal is fully located at the reader side, the data readout is affected by the propagation noise, the specific arrangement of the measurement set up and the environment variability [35]. These uncertainties can be partly removed by a combined post-processing of power indicators derived from both the direct

and inverse links, e.g. through the Analog Identifier (AID) [36], which however narrows the dynamic range. Application-specific calibration procedures are nevertheless always required. Very recently introduced self-tuning chip [37, 38] are able to automatically modify their internal impedance within a discrete set of value at the purpose to compensate the mismatch due to an external stimuli, convert it into a digital information such to keep the readout performance stable. Their diffusion is however at a very embryonic stage. All these issues limit the real-life use of the analog tag to massive application involving low-cost (<1\$), eventually disposable, patches suitable only for a qualitative low-resolution [35] monitoring, which is based on the electromagnetic interaction between the the epidermal tag and some biological process occurring over or beneath the skin surface (wound healing, sweating, edema swelling...).

The real added value for epidermal sensing will be probably fostered by the new families of RFID ICs with augmented sensing capabilities [39, 40, 41]. They typically include an internal analog to digital converter (ADC), a high-speed non-volatile memory (EEPROM), an embedded temperature sensor, and a programmable analog front-end to connect general-purpose microcontrollers and sensor (thermoresistance, interdigital capacitors, strain gauge...). The physical information is sampled by the specific sensor, locally digitize and stored into the microchip's memory. The sensed data are then recovered by the reader straight away in a digital form, thus dropping out the source of errors due to the signal transmission.

These chips can be used in both passive and battery-assisted mode. In the latter case the tag can autonomously trigger measurements that are stored into the user memory and then retrieved asynchronously by the reader (log mode). The very-low power consumption of the IC circuitry (a few milliwatts) enable harvesting energy out of some cycles of the interrogation signal, as well as from piezo-electric, solar or thermal scavengers. These devices can be considered as a convergence point among fully passive tags and the autonomous sensor nodes with local computational capability that usually embed much more complex electronics. They could hence provide a possible tradeoff between superior sensing performance, immune to the environmental interactions and medium cost. The

price to pay for this very special capability is a higher cost of the chip (3 – 8 \$ versus a few cents for conventional RFID chips) and a rather poor IC sensitivity (more than 10 dB lower than conventional chips), which significantly limits the read distance when used in fully passive mode.

Augmented IC are definitively appealing for quantitative monitoring of biometrics by means of tattoo-like sensors as well as for the multi-parameter precise monitoring of environmental parameters in IoT healthcare scenarios, as will be shown in the following chapters.

1.4.2. Reading Performance

The maximum distance at which a tag can be detected by the reader is a practical indicator of overall tag communication performance. In the case of epidermal antennas, the close proximity with the lossy body induces a great dissipation of electromagnetic power, highly degrading the radiation gain ($G_T < -10dB$). Consequently, much shorter reading distances must be expected for skin-mounted RFID sensors with the respect of free-space tag, with activation ranges intermediate between wearable and implantable systems (Fig. 1.3).

Moreover, as sensing functionalities provided by the new RFID ICs are achieved at the expense of a reduced power sensitivity ($P_{chip} > -10$ dBm), the length of the communication link is further decreased. While extremely low-profile and cheap epidermal sensors are mandatory in most of the cases (e.g. fully passive disposable plasters), a slightly complex circuitry is acceptable as well when the improved reading performance and the reliable continuous monitoring are critical for the targeted application. Then, battery-assisted solutions may be also exploited, especially since flexible thin-film battery technologies [42, 43] still permit a certain degree of integration into soft skin-attachable patches.

Under simplified assumptions (impedance matching, polarization alignment) the reading range is derived for the direct link from eq.(1.2) by assuming $P_{R \rightarrow T} = P_{chip}$:

$$d_{forward} = \left(\frac{\lambda_0}{4\pi} \right) \sqrt{\frac{P_{in} G_R G_T}{P_{Chip}}} \quad (1.5)$$

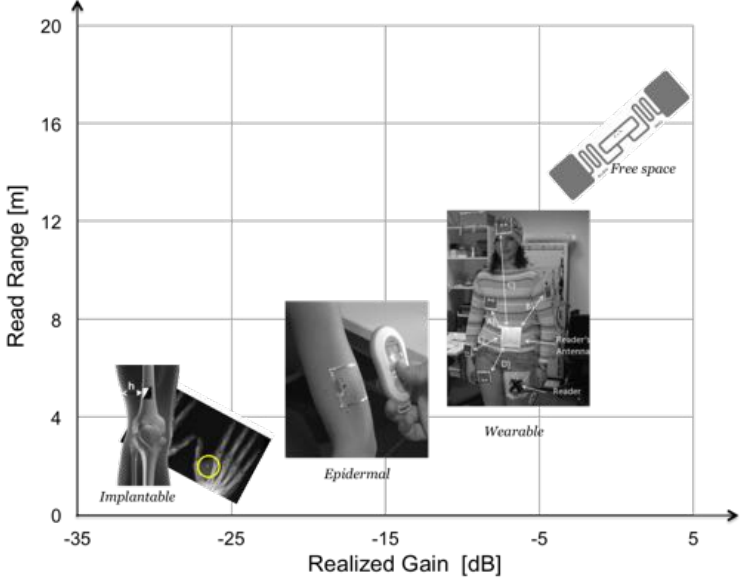


Figure 1.3.: RFID-Bodycentric Systems: Typical read distances of passive implantable, epidermal, wearable and free-space transponders assuming a microchip sensitivity of -22dBm

and for the reverse link from eq.(1.3) with $P_{T \rightarrow R} = P_{reader}$,

$$d_{reverse} = \left(\frac{\lambda_0}{4\pi} \right)^4 \sqrt[4]{\frac{P_{in} G_R^2 G_T^2 \rho}{P_{reader}}} \quad (1.6)$$

where P_{chip} is the IC sensitivity, P_{reader} the receive sensitivity of the reader and ρ the tag backscatter modulation loss [44]. The theoretical maximum reading distance is hence:

$$d_{max} = \min \{d_{forward}, d_{reverse}\} \quad (1.7)$$

The communication results forward-link limited when $d_{forward} <$

$d_{reverse}$, i.e. when the following condition is satisfied:

$$P_{reader} \leq \rho \frac{P_{chip}^2}{P_{in}} \quad (1.8)$$

while the bottleneck is the backward-link under the opposite inequality.

The nomogram in Fig. 1.4 shows the achievable reading range as a function of $\{P_{chip}, P_{reader}\}$ for the reader emitting 3.2 W EIRP, which is the maximum power allowed by the european regulation. The distances reported on the isolines are normalized by the square root of the tag's gain which equally impacts on the direct and return link, so the graph has general validity regardless of the radiator performance.

The read range of pure passive tag with sensing capability is strongly limited by the poor IC sensitivity (e.g. $d_{max} \sim 70$ cm for $G_T = -12dB$ and $P_{chip} = -4dBm$). By adding a battery the power needed to wake up the IC is significantly reduced (up to $P_{chip} = -31dBm$) with corresponding increase of d_{max} , which become backward-limited link (e.g. $d_{max} \sim 2$ m for $G_T = -12dB$ and $P_{chip} = -31dBm$). The current sensitivity of state-of-the art ICs for labeling ($P_{chip} \sim -22dBm$) places passive tag for identification purpose only in the middle between the above conditions.

For a given receiver sensitivity and tag layout, the maximum reading range is achievable by reducing P_{chip} down to the value computed from eq. 1.8. Just to give an example, lets consider a typical receiver sensitivity for long-range readers, i.e. $P_{reader} = -75$ dBm. The threshold sensitivity of the chip is around -22 dBm, regardless of the radiator's gain. Below this limits, the bottleneck of the communication is represented by the reverse link and the d_{max} remains constant independently of P_{chip} . Major efforts to further lengthen the link must be hence shifted to the reader side. The diagram in Fig. 1.4 gives practical indications for the optimal setting of ICs having programmable sensitivity, which must tune to get the maximum reading distance achievable with the available interrogating hardware (G_R, P_{in}, P_{reader}), while keeping the power consumption of the battery as low as possible (the lower the sensitivity, the higher the power consumption).

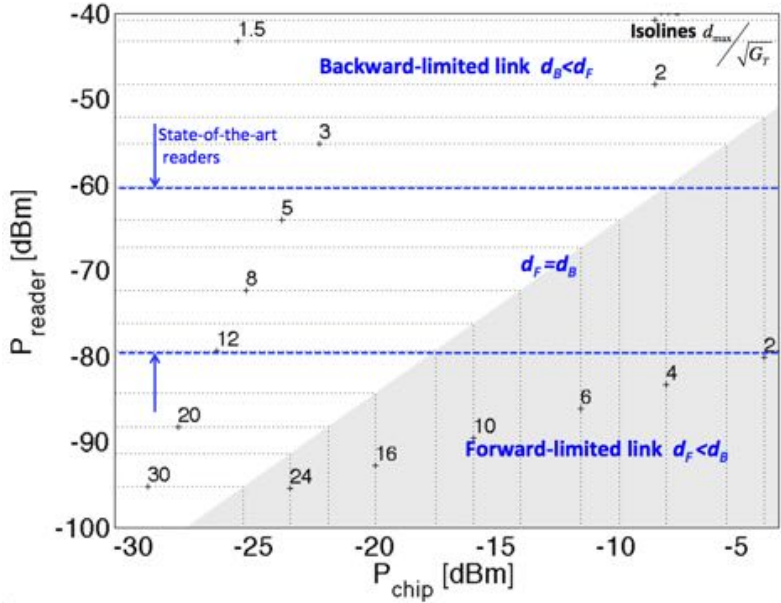


Figure 1.4.: Graphical representation of eq. 1.8 in dB for identification of the link bottleneck. Isolines of the maximum reading range are normalized by $\sqrt{G_{tag}}$. Without loss of generality it is assumed $P_{in}=1$ W, $G_R= 5$ dB, $\rho=0.04$.

Fundamental limitations and Optimal performance

This chapter provides a systematic investigation on the performance of canonical UHF low-profile antennas suitable to the direct application over the human skin. An extensive numerical and experimental analysis is presented to define the optimal size of the antennas depending on material and shape and derive possible upper bounds in the achievable radiation gain.

Epidermal devices demand for UHF-RFID antennas that are suitable to be fabricated with the same technology of the sensorized secondary skin without interfering with the natural metabolism of epidermis, i.e. with minimal impact on local sweating and heat exchanges. Such antennas are required to provide a low density of surface conductor, e.g. they should be preferably made of narrow traces and extremely thin substrates. Single-layer antennas are hence preferred over conventional multi-layer wearable layouts like patch configurations. The latter are indeed not suitable to monolithic integration with skin sensors because of their bulky structure and high filling factor of the conductive surface.

Overall, the few available papers on UHF antennas for direct on-skin placement refer to specific applications with an a-priori choice

of the shape and size of the antenna as well as of the kind and thickness of the attachment membrane. Accordingly, there is still a lack of understanding of how the several geometrical and electrical parameters of an epidermal antenna affect its read range and, hence, how they may be tuned to achieve optimal performance. For instance, it is well known that the radiating properties of an antenna are strictly correlated with its physical size [45]. Electrically large antennas have the potential to provide better gain than smaller ones do. As an example, the maximum gain of a straight dipole, radiating in free space, increases monotonically as a function of its electrical length (see Fig. 2.1). Similar curves can be obtained for other layouts too, such as loops and slots.

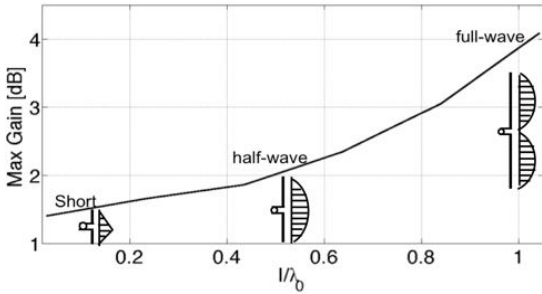


Figure 2.1.: Copper strip dipole in free space: Maximum radiation gain vs the electrical length.

However in the case of antennas radiating close to a lossy medium like the human body, the radiation efficiency degrades severely because of the high loss of the underlying tissues. Therefore, the gain-size relationship might not be trivial and not necessarily monotonic. In the past, antennas operating near the interface between air and lossy regions were the topic of extensive theoretical research in low-frequency radio-propagation, starting with the famous essay of Sommerfeld in 1909 [46]. Initially, the UHF antennas for epidermal transponders were tattoo-like nested-slot dipoles [47] or dual square

loops [48]. The loop shape is traditionally believed to outperform the dipole when placed over or inside a lossy body because of the dominant magnetic near-field, which should be less influenced by the presence of human tissues. However, since the electrical sizes of an epidermal loop for UHF communication can not be considered small, the distinction between the magnetic and electric fields is not so sharp. Finally, several techniques have been already experimented to manufacture tattoo-like devices involving sub-optimal conducting materials (silver nano-particles, biodegradable and even edible paintings [49]), but there is no knowledge about the lower-bound in the antenna conductivity that still allows copper-like performance.

This chapter is hence aimed at systematically investigating the response of UHF antennas suitable when attached over the skin by considering most of the possible design and manufacturing options such as the shape, the trace width and metal conductivity, the thickness and material of membrane as well as the positioning over different body parts. The final purpose is to identify optimal configurations and the upper-bound in the communication performance of skin-tight radiators. Following the above conjecture concerning the non-monotonic relationship between antenna size and gain, the overall goal is to derive the most convenient size and shape of the on-skin antenna that maximize the read distance in realistic fabrication and placement conditions. For the sake of generality, rather than focusing to any specific application, canonical layouts are considered. Both numerical and experimental analysis are performed and the obtained knowledge provide a starting tradeoff in the design of more complex configurations.

2.1. Reference antennas, body model and method of analysis

With the term *Epidermal Antenna* we hereafter refer to any kind of single-layer antenna directly attached over the skin at most by means of a sub-millimeter thick flexible membrane. Skin-attached antennas have intermediate behavior between the body-centric antennas, which are optimized to radiate outside the body through

shielded configurations, and the antennas for microwave heating, which are instead optimized to radiate inside the body. Indeed, epidermal antennas are conceived to work at a very small (micro-metrical) distance from the skin - to comfortably adapt to it and to capture and transduce some biophysical parameters - but they have to communicate with a reader outside the body. Shielded layouts like patch antennas [23] or thicker multi-layered dipole [50] and slot [25] structures, which could achieve better communication performance, prevent the required electromagnetic interaction with the body, and are hence not suitable for skin-mounted antennas. Accordingly, only single-layer radiators (dipole, loop and their complementary slotted counterparts, shown in Fig. 2.2), which are fully compatible with ultra-low profile “tattoo-like” devices, are considered in this study.

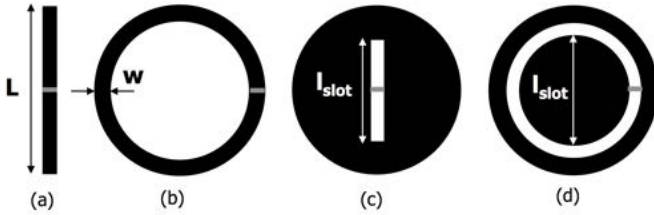


Figure 2.2.: Reference layouts for Epidermal Antennas: a) Planar Dipole b) Planar Loop c) Rectangular Slot d) Annular Slot. The grey pixel indicates the antenna port that interconnects with the RF microchip transponder. In all the configurations, L indicates the external radiator’s size and l_{slot} the dominant slot’s size.

Additional components for impedance matching [51], such as T-match and loop-match, which generally augment the main radiating body, are ignored here for the sake of generality and for minimizing the number of free geometrical parameters to be considered in the numerical analysis. The purpose of this investigation is broadly two-fold: (i) to analyze the correlation between the antenna performance (efficiency, gain) and the radiator size, and (ii) to identify the

geometry that suits best to epidermal transponders by comparing the performance of different layouts.

Antennas consist of planar traces laid over a simplified human phantom comprising a homogeneous parallelepiped box (size 30x30x20cm) having equivalent dielectric properties¹ ($\epsilon_{phantom}=43$ and $\sigma_{phantom}=0.9$ S/m) obtained by the volume average of the skin-fat-muscle layerings [53]. Simulations were performed using the Method of Moment (MOM) through the FEKO solver [54].

2.2. Efficiency and gain vs. antenna size

In the first set of simulations, the antennas were assumed to be made of lossy copper ($\sigma = 6 \cdot 10^7$ S/m) and placed directly over the body without any supporting substrate. The width of the traces of loops and of the dipoles, as well as the width of the slots in the complementary shapes (the parameter w in Fig. 2.2), was fixed at 1mm. The major size of the radiators (parameter L in Fig. 2.2) was, instead, progressively increased and the efficiency and gain were computed for each considered size.

2.2.1. Loop and Dipole

Fig. 2.3 shows that the radiation efficiency of dipoles and loops over lossy medium, unlike in free-space, exhibits a bell-shaped behavior. After an initial monotonic region with nearly linear relationship between maximum gain (and efficiency) and size, there are peak values ($\eta=0.3\%$, $G \approx -20$ dBi), which are rather similar for the two antennas of sizes $L=30$ mm and $L=50$ mm for the loop and the dipole, respectively. In both cases, the significant losses of the tissues resulted in extremely poor values for the radiation gain. Denoting the effective permittivity “sensed” by the antennas when placed on a thick slab [55] as $\epsilon_{eff} = \frac{\epsilon_{phantom}+1}{2} = 22$, the sizes (length and perimeter) of the optimal dipole and loop correspond

¹The dielectric properties of the human phantom are rather stable in the worldwide UHF RFID band (865-955 MHz), with percentage variations lower than 4% [52]; so, they are assumed to be constant in all numerical analyses.

to $L(\text{dipole})=5\text{ cm}=0.7\lambda_{eff}$ and $\pi L(\text{loop})=9.4\text{ cm}=1.3\lambda_{eff}$ where $\lambda_{eff} = \lambda_0/\sqrt{\epsilon_{eff}}$. Beyond the peak value, the maximum gain remained rather stable, while the radiation efficiency degraded significantly. The maximum value for the radiation pattern was obtained along the normal direction to the skin, which acted as both an absorber and a reflector.

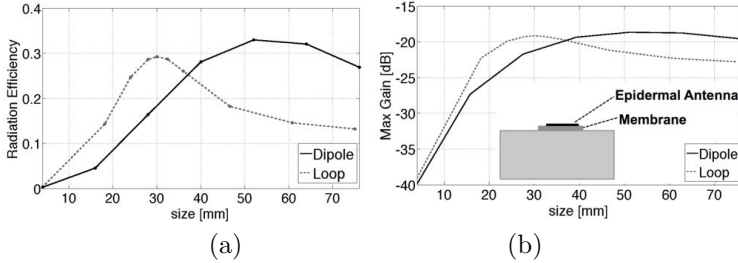


Figure 2.3.: Dipole and Loop Antennas over body-like medium. (a) radiation efficiency [%] and (b) maximum radiation gain at 870 MHz as a function of the antenna size. Inset: Reference geometry for numerical modeling ($30\times 30\times 20\text{ cm}^3$).

The non-monotonic relationship between the efficiency/gain and physical size of antennas can be explained by considering the presence of two counteracting phenomena. The initial increase in the efficiency (see Fig. 2.3) is mostly due to the increase in the radiation resistance, which is proportional to the overall length of the antenna. Further enlargements of the antenna produce more intense dissipation of power into the conductors and the surrounding tissues, because of the high conductivity of the hosting medium, which dominates radiation. Fig. 2.4 illustrates the surface current plot of dipoles of different lengths. The presence of the body below the antenna causes progressive dampening of the amplitude of the currents flowing through the conductor, which resulted in inefficient use of the available conductive area. Thus, enlarging the

antenna beyond its optimal size is not only undesirable for epidermal applications, which require small and unobtrusive devices, it even produces a negative impact on radiation properties.

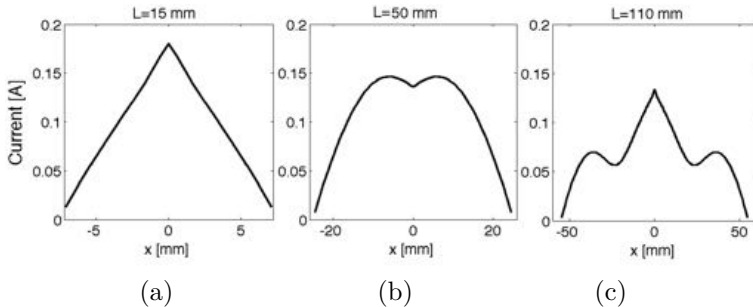


Figure 2.4.: Current distribution at 870 MHz for strip dipoles with different lengths over a body-like uniform substrate. Diagrams normalized by 1W input power.

Fig. 2.5 shows the diagrams of the input impedance of the antennas with optimal size versus the frequency. Unlike the dipole, the impedance of the loop is nearly broadband within the frequency range 800-1000 MHz, thus rendering the matching of impedance easy, as will be shown later.

2.2.2. Slotted Antennas

Complementary configurations of dipoles and loops were obtained from a copper disk of variable diameter $20 \text{ mm} < L < 100 \text{ mm}$. For each ground diameter, the size of the slots (length and diameter of rectangular and annular slots, respectively) was gradually increased within the range $2 \text{ mm} < l_{slot} < L-4 \text{ mm}$. Since the induced current spreads over the disk and hence interacts with the human body, the diameter of the disk impacted the definition of the optimal size of this family of epidermal antennas. The radiation performance

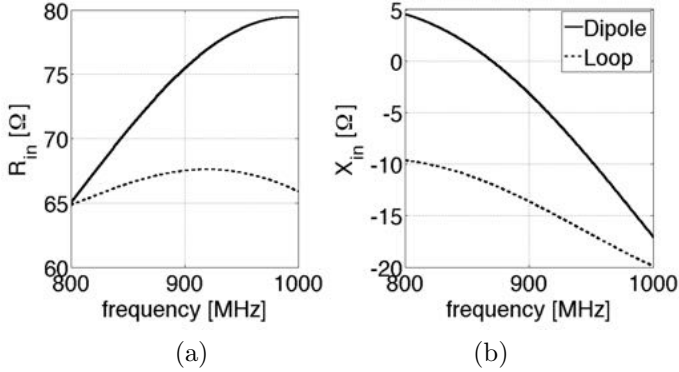


Figure 2.5.: Input impedance at 870 MHz of dipole and loop antennas placed over a body-like medium as a function of frequency.

(Fig. 2.6) is related to the combined effect of the size of the disk and that of the slot, since the increase of the slot leads to reduction in the area occupied by the surface current. Accordingly, the optimal size of the slot is in turn strongly dependent on the diameter of the disk (Fig. 2.6). On the whole, the rectangular slot works better than does the annular slot, in terms of size and gain.

2.2.3. Performance Comparison

The summary of the results, presented in Tab. 2.1, shows that efficiency and maximum gain are almost the same for all the considered configurations (the gain of dipole is less than 1 dB - higher than that of other radiators) and the optimal performance decreases slightly with increase in the area of the conductor (and hence in the surface current). Contrary to the general belief, the loop has thus no tangible advantage over the dipole as epidermal tag, at least in terms of gain and efficiency. Nevertheless, the loop has an overall smaller optimal size and a highly stable input impedance.

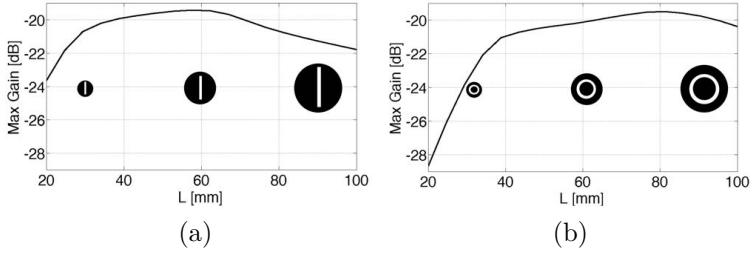


Figure 2.6.: Optimal peak Gain at 870 MHz (with the length l_{slot} of the slots) v.s. the disk size L for (a) rectangular and (b) annular slotted antennas.

Table 2.1.: Electromagnetic performance and geometrical parameters at 870 MHz of the reference epidermal antennas

Antenna	η [%]	G [dB]	L_{opt} [cm]	A_{metal} [cm ²]
	0.3	-18.7	5	0.5
	0.3	-19.1	3	0.9
	0.3	-19.4	6	27.6
	0.2	-19.5	8	46.7

Finally, since the complementary structures did not prove to be particularly advantageous, except where a ground plane is required for additional electronics, further numerical and experimental analysis are restricted only to dipoles and loops.

2.3. Gain vs. the trace width and conductivity

Fig. 2.7 shows the maximum gain, as obtained by simulations, when the copper trace is increased from $w=1$ mm (as in the previous case) up to $w=20$ mm. The radiation parameters turned out to be roughly independent of the conductor width, except for a negligible decrease in the loop's parameters. Therefore, wider layouts yield the same radiation performance as that of the narrow ones at the expense of a greater amount of conductor and a major invasiveness for the skin. The analysis of the input impedance (Fig. 2.7b) finally provided an unexpected result: except in the case of thin traces ($w=1$ mm), there was no appreciable difference between the impedances dipole and loop, which are, therefore, inferred to have been governed mostly by the hosting medium. Moreover, the width parameter can be used to tune, at least, the input resistance of the antenna in the typical range ($R < 50$ ohm) of RFID microchips.

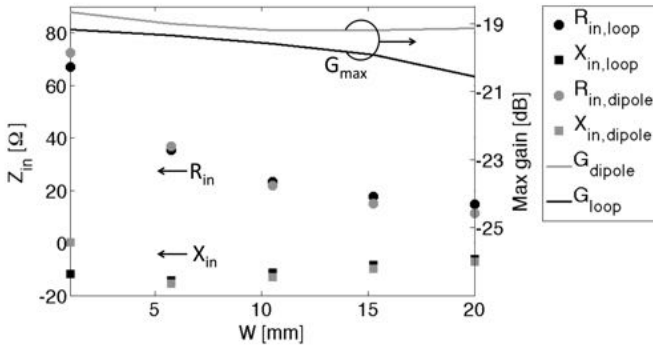


Figure 2.7.: Computed radiation gain and input impedance at 870 MHz of optimal size dipoles ($L=50$ mm) and loops ($L=30$ mm) over body-like medium versus the width w of the traces.

Epidermal devices demand that conductor traces be deposited on

thin membranes and suitable technologies are inkjet printing or stencil-based techniques (screen printing) that utilize conducting paints and nanoparticle inks [49, 10]. These materials are more flexible and robust against the cracks than is bulk copper, but at the price of a reduction in the conductivity of one order of magnitude or even more. Fig. 2.8 shows the efficiency and gain of the optimum-sized dipole and loop placed in direct contact with the body, when the conductivity of the metal trace was decreased from $\sigma = 10^8$ S/m (good conductor) down to $\sigma = 10^2$ S/m (poor conductor). No visible variation was noticed in the radiation performance, provided that $\sigma > 10^4$ S/m. Furthermore, even by reducing the conductivity down to $\sigma = 1000$ S/m, the gain dropped by less than 2 dB. This result is not trivial and is a consequence of the power losses of the hosting human body.

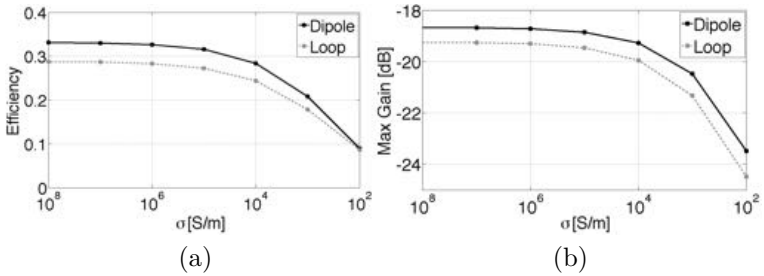


Figure 2.8.: (a) Efficiency and (b) Maximum Gain of a 50×1 mm dipole and a 30×1 mm loop at 870 MHz versus the finite conductivity of the trace.

2.4. Radiation performance vs. the spacing from the skin

Epidermal antennas were stuck onto the skin by ultra-thin materials (fraction of a millimeter). The thickness of the membrane is

expected to have a remarkable influence on the radiation performance of the antenna, since, in the case of thick membranes, the electric near-field remains partially confined to the low-loss region of the substrate, thus reducing the power loss. By initially assuming the separating membrane as a numerically simulated air gap, it is shown in Fig. 2.9 the maximum achievable gain and the optimal size for dipole and loop antennas when the skin-antenna gap is increased from $d=0$ (direct contact) to $d=600\ \mu\text{m}$. Mesh refinement was enforced into the numerical electromagnetic solver (cell side $25\ \mu\text{m}$) for the purpose of properly modeling the field discontinuities among different dielectrics. As the antenna is moved far from the skin (e.g. the thickness of the membrane increases) the power loss into the body reduces, the optimal size of the antennas is larger and, accordingly, the antenna gain and efficiency sensibly improve. In particular, the gain is linearly correlated to the logarithmic change in the antenna/body distance. More than 9 dB gain improvement was achieved by both the dipole and the loop by moving them from direct placement over the skin (smart tattoo) to a separating membrane of 0.6 mm. The difference in size between the dipole and the loop is more evident with increasing distances to the extent that the loop layout becomes even more compact. A separating distance $d>50\ \mu\text{m}$ (thin plaster) results in a radiating gain peak of more than -15dBi, which is compatible with a read distance of up to 1 m, according to the technological limitations of current RF microchips and readers.

Finally, the case of a more realistic membrane is discussed using the data presented in Tab. 2.2 (refer to chapter 4 for a detailed description and characterization of the biomaterials). Among the possible substrates we selected a bio-compatible silicone with low permittivity and low losses and PVA/XA-based hydrogels [56], whose dielectric properties vary depending on to the amount of body fluids (e.g. sweat, wound exudates) absorbed/released by the membranes. The case of air gap is also reported alongside for reference, as it can be considered representative of the family of materials with highly porous and fibrous architecture (PCL [48], EPDM foam [57]). When using very thin substrates ($d=25\ \mu\text{m}$), the loop exhibited similar optimal sizes for all the considered membranes,

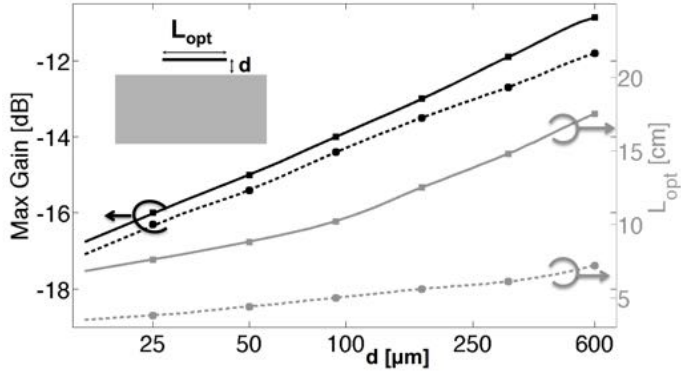


Figure 2.9.: Optimal sizes and corresponding peak radiation gains at 870 MHz for dipoles (continuous line) and circular loops (dotted line) as a function of antenna/skin separation. In all the cases, the trace width was fixed at $w=1\text{mm}$.

while the corresponding peak gain decreased by 1 dB for each order of magnitude increase in membrane conductivity. As expected, thicker substrates generally provided higher gain at the expense of a bigger radiator size, except for the wet hydrogel whose gain/size properties are rather constant with the respect to the membrane thickness because of its high dielectric properties that are comparable with those of human tissues.

Table 2.2.: Optimal size and peak gain at 870 MHz for loop antennas placed on body-like medium by means of different membranes of thickness d .

Membrane	$d=25\mu m$	$d=100\mu m$	$d=500\mu m$
Air	3.8 cm -16.3 dBi	5.1 cm -14.2 dBi	6.8 cm -12 dBi
Bio-silicone $\varepsilon = 2.5$ $\sigma = 0.005 \text{ S/m}$	3.4 cm -17.7 dBi	4.4 cm -15.4 dBi	5.8 cm -13.4 dBi
Dry Hydrogel $\varepsilon = 3$ $\sigma = 0.03 \text{ S/m}$	3.4 cm -18.2 dBi	4.4 cm -16 dBi	5.4 cm -14.8 dBi
Wet Hydrogel $\varepsilon = 32$ $\sigma = 0.4 \text{ S/m}$	3 cm -19.3 dBi	3 cm -18.9 dBi	3.2 cm -18.3 dBi

2.5. Performance on Anthropomorphic Layerings

For the final parametric analysis, the same loops and dipoles, as those mentioned above, were considered, but they were now placed over a non-homogeneous medium of planar layers (skin, fat, muscle and bone) whose permittivity profiles are similar to those of some regions of the human body, such as the forehead (F), the abdomen (A) and the limb (L) over which the sensors can be applied. The thickness of the layers were defined as in Tab. 3.2. The substrates were a subset of those shown in Tab. 2.2, namely the bio-silicone (Substrate 1), representing the cases of low-permittivity and low-loss, and the wet hydrogel (Substrate 2), representing the extreme case of high-permittivity and high-loss. The insulator thickness was $d = \{25, 500\}\mu m$. For each of the twelve combinations of the dipole and of the loop, the optimal sizes and the corresponding gains were computed by assuming an infinite layering so that the Green function for planar structures can be applied with sensible speed-up of the computation. The aggregated results,

presented in Fig. 2.10, show that the smallest optimal size always corresponds to loop-shaped devices, in so far as the homogenous and finite cases are concerned. But, the most remarkable outcome is that the optimal size is rather independent of the stratification for a fixed insulating substrate (permittivity and thickness), while the corresponding optimal gain depends on the position of the antenna on the body, as better investigated in the next chapter. Since the two materials considered here represent the extreme cases of possible choices of substrates, the optimal size of other configurations can be therefore assumed to roughly fall within the range of $30\text{mm} < L_{opt}[\text{loop}] < 60\text{mm}$ for loops and $60\text{mm} < L_{opt}[\text{dipole}] < 150\text{mm}$ for dipoles. The same analysis at the upper part of the UHF RFID band ($f=950$ MHz) showed a similar trend but the optimal size of the antenna was slightly smaller (few millimeters) than what was found at 870 MHz. Therefore Fig. 2.10 provides the upper bounds for the expected performance of epidermal antennas in the UHF band and can be used as a starting point for the design of epidermal antennas, as discussed in the next section.

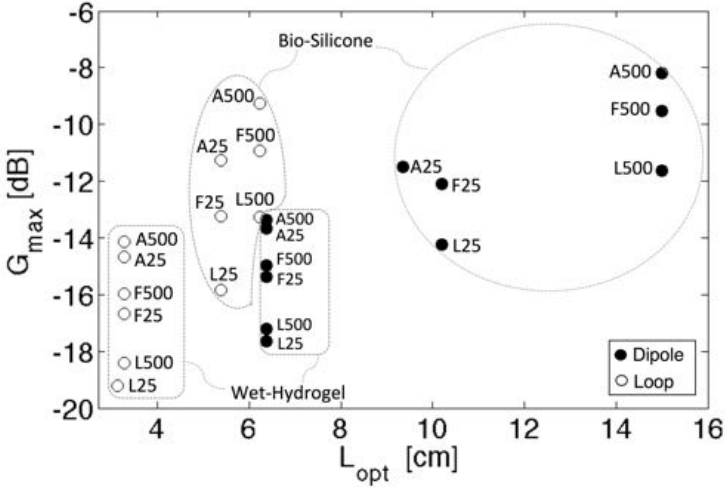


Figure 2.10.: Optimal size and corresponding radiation gain at 870 MHz of loops (white circles) and dipoles (black circles) placed over stratified planar media, simulating abdomen (A), a limb (L) and the forehead (F) for two different substrates {bio-silicon, wet Hydrogel} and for different two thicknesses $d = \{25, 500\} \mu\text{m}$.

2.6. Design Guidelines

The foregoing numerical findings can be summed-up to constitute practical guidelines for optimal epidermal antennas with conjugate matching to complex microchip impedances.

The position over the body and the substrate material for the epidermal tag are assumed a-priori for the target application. Then, the tag design can be performed according to the following steps.

1. Selection of the antenna layout. Even though the previous research demonstrates that loop antenna provides the best compromise between gain and size, there are some ICs whose pads can not be shortened by closed path radiators. In such cases, open structures, such as dipoles, have to be considered.

2. Selection of the antenna size from the diagram in Fig. 2.10. When optimal dimensions can not be met due to eventual size constraints, sub-optimal configuration can be considered. Fig. 2.11 illustrates the relationship between degradation of read-distance and the reduction of antenna size, with respect to the optimal value. The curves were obtained by averaging the results in Fig. 2.10. Dipole and loop antennas, reduced in size by 30%, provide respectively 90% and 80% of maximum read-distance
3. Impedance matching in two steps. First, the antenna input resistance is tuned by varying the width trace of the radiator (see Sec. sec. 2.3): as a general rule, the wider the trace, the lower the resistance. Then, the residual reactance X_A of the antenna is adjusted to that of the microchip by connecting a tuning inductor of value $L_t = -(X_A(f_0) + X_{chip})/2\pi f_0$ in series to the chip. Alternative T-match or loop-match impedance transformers may be however applied, as in the case of standard tag [51].

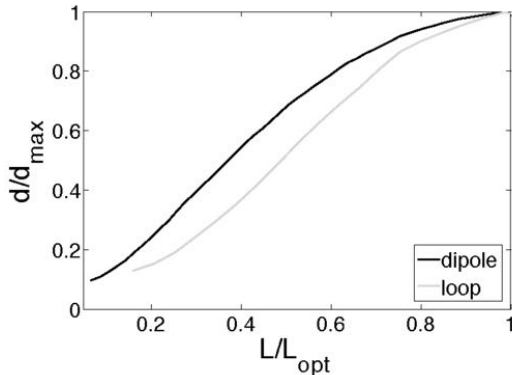


Figure 2.11.: Degradation of reading distance, for dipole and loop, as a function of suboptimal size.

By way of example, the above procedure was applied to the design of the following two epidermal tags, both tuned at 870 MHz: 1) a dipole on a 25 μm wet hydrogel; 2) a loop on a 25 μm biosilicone.

The microchip impedances, assumed as references for the dipole and loop examples, differ for the reactances e.g. $Z_{chip1} = 31-j 320 \Omega$ (dipole) and $Z_{chip2} = 23-j 145 \Omega$ (loop). The external sizes of the antennas, as deduced from Fig. 2.10, were are $L(\text{dipole})=63 \text{ mm}$ and $L(\text{loop})= 50 \text{ mm}$. The widths of the conductor traces producing the required antenna resistances were $w(\text{dipole})= 13 \text{ mm}$ and $w(\text{loop})=20 \text{ mm}$, with residual reactances $X_A(\text{dipole})= -8 \text{ ohm}$ and $X_A(\text{loop})=-6 \text{ ohm}$, so that the inductances of the required tuning inductors were $L_t(\text{dipole})=56 \text{ nH}$ and $L_t(\text{loop})=27 \text{ nH}$. The power transfer coefficient (τ) of the resulting tags are shown in Fig. 2.12 and once again the loop tag exhibits a more stable response.

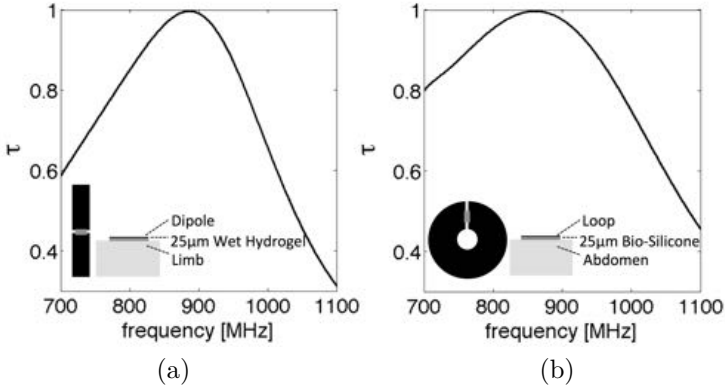


Figure 2.12.: Power transmission coefficient τ vs frequency for optimized UHF epidermal tag. a) dipole ($L=63\text{mm}$, $w=13 \text{ mm}$) on a $25 \mu\text{m}$ wet hydrogel connected to an IC-inductor series ($Z_{Chip1} = 31-j 320 \Omega$, $L_t=56 \nu H$) placed over the limb b) Loop ($L=50\text{mm}$, $w=20 \text{ mm}$) placed on a $25 \mu\text{m}$ biosilicone connected to a IC-inductor series ($Z_{Chip2} = 23-j 145 \Omega$, $L_t=27 \nu H$) placed over the abdomen.

2.7. Experimental validation

The above numerical analysis is validated by laboratory experiments, aimed at verifying the optimal size and the upper bound of the antenna gain in the case of placement over a body-like lossy media. Two configurations of linear dipoles and square loops made of adhesive bulk copper and inkjet-printed silver nanoparticles are considered. Then, a second set of experiments concerns the sensitivity of the epidermal monopole to the width of its trace and to the type and the thickness of the attaching membrane.

2.7.1. Measurement method

The measuring technique involved two separate transmitting and receiving antennas, connected to a calibrated 2-port vector network analyzer, by means of coaxial cables. The reference lossy biological region was a cooked box-shaped pork shoulder, whose dielectric parameters ($\epsilon_r = 55$, $\sigma = 1.8$ S/m) were estimated by means of the setup described in chapter 4. The parameters of the experimental phantom differed from those of the previous numerical model and, in particular, the losses were much higher due to the presence of salt. Finally, the box was enveloped by a thin layer of PET (thickness $150 \mu\text{m}$, $\epsilon = 2.26$, $\tan\delta = 3 \cdot 10^{-4}$).

To simplify the antenna-probe interconnection, an image-plane configuration was used (Fig. 2.13). Half the antenna was placed vertically over a copper plane and connected to a coaxial connector on the rear side of the copper plane. The transmitting antennas consisted of a quarter-wave planar monopole, whose input impedance was matched to 50Ω at 870 MHz. The prototype was fabricated with adhesive copper sheet (size 78×55 mm, thickness $35 \mu\text{m}$), stuck over a 3 mm-thick foam substrate ($\epsilon_r = 1.55$, $\tan\delta = 2 \cdot 10^{-4}$ S/m).

The close interaction between the epidermal antenna over the phantom and the dipole probe is described by the formalism of the two-ports network as in [58], so that the performance of the antenna can be conveniently evaluated in terms of the scattering matrix of

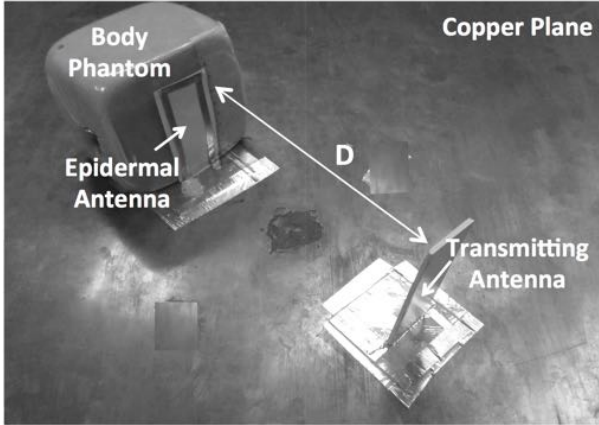


Figure 2.13.: Experimental setup for characterization of the epidermal antennas, comprising a reference monopole antenna placed at distance $D=17$ cm from a cooked-pork box (size $10\text{ cm} \times 10\text{ cm} \times 7\text{ cm}$) hosting the monopoles and half loops under test. The antenna ports were connected to a VNA for measurement of scattering matrix.

the system, which accounts for channel path loss, reflection, diffraction and power absorption by the hosting medium [59]. An easily measurable performance parameter of the epidermal antenna is the following *system gain* (non directly comparable with the radiation gain):

$$g = \frac{P_{out,av}}{P_{in}} \quad (2.1)$$

where P_{in} is the net power entering the transmitting dipole and $P_{out,av}$ the maximum available power the network may deliver to the load of the epidermal antenna (in case of a proper impedance matching).

Assuming that the cables and the network analyzer are perfectly

matched, the input power is related to the *available input power* [60], e.g. the maximum power the generator may deliver to the network (in case of Hermite matching) by the equation:

$$P_{in} = P_{in,av}(1 - |S_{11}|^2) \quad (2.2)$$

The power P_L delivered to the real load of the epidermal antenna is

$$P_L = P_{out,av}(1 - |S_{22}|^2) \quad (2.3)$$

and hence

$$g = \frac{P_L}{P_{in,av}} \frac{1}{(1 - |S_{11}|^2)(1 - |S_{22}|^2)} \quad (2.4)$$

The quantity $P_L/P_{in,av}$ is by definition [60] the transducer power gain $G_T = |S_{21}|^2$ under the above hypothesis and finally

$$g = \frac{|S_{21}|^2}{(1 - |S_{11}|^2)(1 - |S_{22}|^2)} \quad (2.5)$$

This performance parameter is independent of the specific impedance matching of the two antennas and it hence characterizes the radiation properties of the epidermal antennas over the lossy medium. At the frequency where the probe monopole is matched to the cable impedance (e.g. around 870 MHz), the quantity $(1 - |S_{11}|^2) \rightarrow 1$, and hence the system g , coincides with the *available power gain* $G_a = P_{out,av}/P_{in,av}$ [60].

2.7.2. Prototypes

Two planar layouts (monopole and a half rectangular loop) were selected to facilitate easy manufacturing. The rectangular loop was preferred to the circular one, because its shape can be varied during experiments by sweeping only the length parameter without disconnecting the antenna from the feeding source and the image plane.

Radiators made of bulk copper were carved out of an adhesive copper film by means of a digitally-controlled cutter and then directly stuck on the planar side of the phantom.

The same monopoles and half loops were also fabricated by means of inkjet-printing, using the silver ink from Mitsubishi Paper Mill [61] and a low-cost desktop printer, as described in chapter 5. The volume resistivity provided by the manufacturer is $10 \mu\Omega\text{cm}$, which corresponds to a conductivity that is two orders of magnitude lesser ($\sigma \simeq 10^5 \text{ S/m}$) than that of bulk copper. A silver-based paint was used for connecting the printed antennas to the coaxial pin, and, in the case of half loop, to the ground plane.

2.7.3. Measurement results

The first experiments considered monopole and half-loop layouts having fixed trace width (5mm) and sizes progressively reduced from $L=6 \text{ cm}$, by steps of 5mm, for an overall set of forty-five antennas. The S-parameters were measured by the VNA in the 600-1100 MHz range and the corresponding system gain were computed according to (2.4). Overall results (Fig. 2.14) clearly reveal the presence of different optimal sizes of the epidermal antennas for which both monopole and half-loop configurations achieve similar values of peak system gain ($g_{\text{mono}} \simeq g_{\text{loop}} = -30 \text{ dB}$). The performances of copper and the inkjet-printed antennas are comparable, despite of the significantly poorer conductivity of the silver nanoparticle ink. The smaller optimal layout is the half loop ($L_{h,\text{loop}} \simeq 3 \text{ cm}$, $L_{\text{monop.}} \simeq 4 \text{ cm}$), as expected from the numerical analysis². It is

²The corresponding sizes of the full dipole and loop are larger than those reported in Table. I, because the geometrical and electromagnetic parameters of the phantom differ from those of the computer model.

worth mentioning that, even though Fig. 2.14 refers to 870 MHz, the same behavior was observed in the whole range 600-1100 MHz with negligible change in the optimal length of the antenna whose peak gain becomes sharper as the frequency increases because of higher losses of tissues.

In a second experiment we considered a copper monopole with optimal length and variable trace width $5 \leq w \leq 25\text{mm}$ by 5 mm steps. Fig. 2.15(a) shows the variation of the system gain and of the input impedance at 870 MHz with respect to the reference size $w_0 = 5\text{mm}$. As already predicted in Fig. 2.7, there is a 35 ohm range useful for tuning the resistance without impacting on the antenna gain.

Finally, the 5 mm-width copper monopole was stuck over the phantom by means of bio-silicone membranes having different thickness $\{50\mu\text{m}, 1\text{mm}, 2\text{mm}\}$. The system gain vs frequency (Fig. 2.15.b) exhibits up to 4 dB degradation within the UHF RFID band in the case of ultra-thin ($<100 \mu\text{m}$) films, as expected by the numerical analysis (Fig. 2.10).

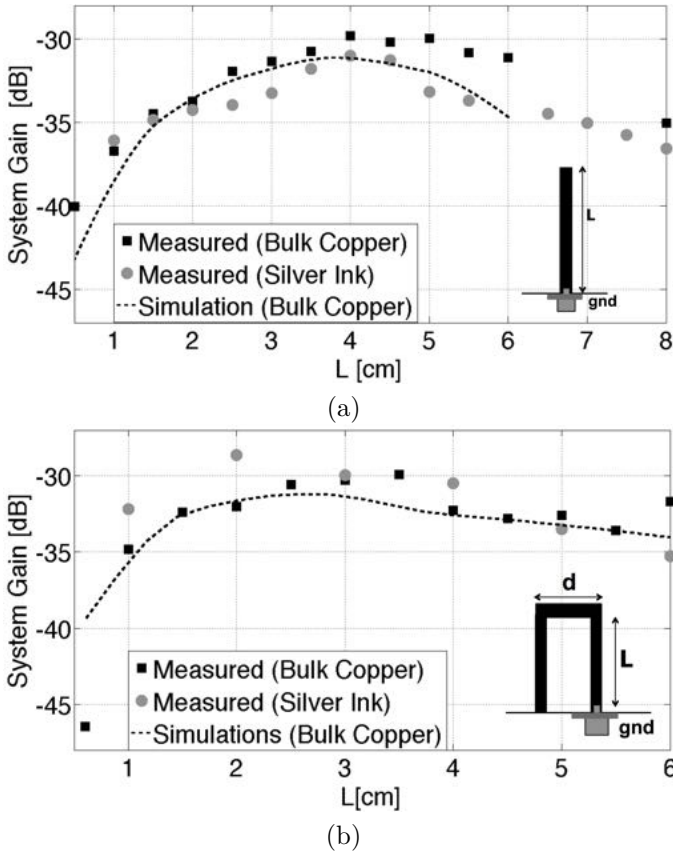


Figure 2.14.: Measured and simulated *system gains* g , defined as in eq.2.1, at 870 MHz for the prototyped (a) monopoles and (b) half loops over a cooked-pork phantom versus their vertical size. Antennas were made of adhesive bulk copper and silver nano-ink through inkjet printing on functionalized PET.

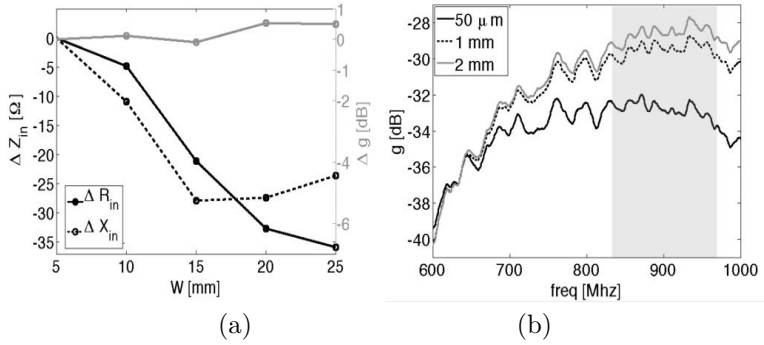


Figure 2.15.: (a) Measured variation of system gain and input impedance at 870 MHz of the copper monopole ($L_{opt} = 4cm$) versus the width trace and with respect to the reference size $w_0 = 5mm$ ($R_0 = 54\Omega$, $X_0 = 29 \Omega$, $g_0 = -30.7$ dB). (b) System gain of the copper monopole ($L_{opt} = 4cm$, $w = 5mm$) stuck over the phantom through bio-silicone membranes with different thickness. The grey area highlight the UHF RFID frequency band.

2.8. Summary and Conclusions

The close interaction of epidermal antennas with the lossy human body and the consequent strong power loss clearly delimit electromagnetic performance of epidermal antennas and strongly polarize their impedance and gain. The following are the most significant findings of this study: *i*) the existence of a roughly fixed upper-bound in the achievable maximum gain and efficiency, independent of the shape of the antenna. The epidermal antenna response is instead fully governed by the permittivity and losses of the hosting media; *ii*) As a consequence, there is an optimal size of the antenna, the smallest in the case of loops ($30\text{mm} < L_{\text{opt,loop}} < 60\text{mm}$, depending on the substrate) and nearly double for dipoles; *iii*) Dipoles and loops require lesser space than their counterparts, having a same gain; *iv*) The quality of the antenna conductor plays a minor role in radiation performance. Conductors with $\sigma > 10^4$ S/m conductivity provide the same results as those of bulk copper so that low-cost inkjet printing devices may be used for mass production to avoid cumbersome transfer procedure for metal trace placement over the membrane; *v*) The width of the conductor strip does not affect the gain, but can be adjusted to control the antenna input resistance; *vi*) The radiation performance is significantly modified by the thickness and dielectric characteristics of the underlying membrane.

3

Human Variability and On-skin Retuning

This chapter investigates the performance of a reference UHF RFID epidermal transponder in the form of a dual-loop tag depending on the specific placement over different parts of the human body and for a variety of volunteers. An on-body tuning mechanism is also introduced and demonstrated in real applications at the purpose to improve the tag response for several placement loci and operating bands.

Unlike wearable antennas, the strong and unshielded proximity between an epidermal antenna and the human body produces a significant sensitivity of the radiation performance of the tag versus the placement modalities. Although an early evidence of the body-dependent behavior of the epidermal antennas in UHF RFID bands was already highlighted in [47] and then in [48], the effectiveness of such interaction is still mostly unexplored and no mitigation method has been proposed so far.

This chapter addresses in full details the characterization and optimization of the communication performance of the epidermal tag for placement over several regions of the human body with the following goals:

i) to evaluate the possible variability of the tag's realized gain de-

pending on the position over the body, but also on the users' body mass and gender;

ii) to introduce and to fully characterize by simulations and measurements a retuning mechanism tailored for loop layouts and consisting in removing pre-cut portions of the impedance transformer of the antenna;

iii) to demonstrate throughout real experimentations how a same tag can be retuned directly on-body to achieve the best performance for the specific placement and for the specific frequency in the worldwide RFID band.

A reference dual-square loop layout is introduced and the expected performance are investigated by the help of numerical simulations over simplified canonical models of the human body. The real communication performances of a fabricated prototype attached over different regions of body are experimentally quantified. In order to get rid of the variability of the tag responses with different placement configurations, an on-skin tuning mechanism is introduced and experimented by using a phantom. Finally some realistic examples of the tuning method are provided.

3.1. Reference skin antenna: dual-loop tag

A possible antenna layout that is compatible with the strict requirements of epidermal antennas (unshielded layout, minimum amount of conductor, ultrathin insulating materials...) could be the planar dual-loop configuration (Fig. 3.1). The geometry, which was originally proposed in [26] for wearable applications with a thick spacer, consists of an external resonating loop connected to the RFID microchip through a loop-match impedance transformer [62]. The chip was the NXP-G2X-TSSOP-8 having nominal RF input impedance and power threshold $Z_{chip} = 16 - j148\Omega$, and $P_{chip} = -15dBm$, respectively. The external sizes of the loop are 5cm x 5cm so that the physical area of the tag can be compatible with that of a medical plaster. The size of the internal loop was instead designed by numerical simulations (Moment Method throughout FEKO solver [54]) for optimal impedance tuning at 950 MHz which is the upper bound of the worldwide UHF-RFID

band. It is worth anticipating that an ad-hoc retuning methodology permits to easily shift the tag response toward lower frequencies as desired (see sec. 3.3).

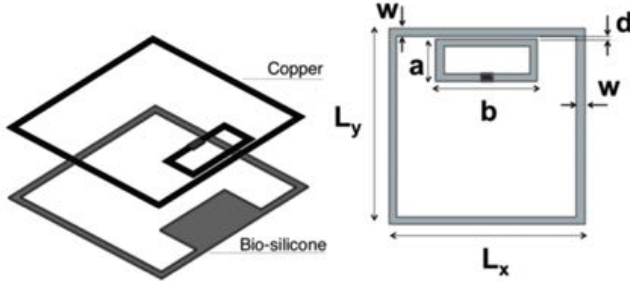


Figure 3.1.: Layout of the epidermal tag. Size [mm]: $L_1 = L_2 = 50$, $w = 2$, $d = 0.5$, $a = 26$, $b = 10$.

For the sake of the simulation speed, the tag was initially placed onto a reference model of the human body [53] which consists of infinite planar tissue layers (thickness as in Tab. 3.1 and frequency-dependent permittivity and conductivity as in [52]). The antenna was separated from the body only through a thin layer of biosilicone ($\epsilon_{sil} = 2.5$, $\sigma_{sil} = 0.005$ S/m, thickness $600\mu\text{m}$, see chapter 4) profiled as the radiator. Simulation results are shown in Fig. 3.2. The maximum value of the realized gain along the broadside (frontal) direction is -12.7 dBi around 940 MHz.

Table 3.1.: Physical and geometrical parameters of the layered anatomical model at 870 MHz.

Layer	ϵ_r	σ [S/m]	Thickness [cm]
Skin+fat	14	0.25	2.6
Muscle	55.1	0.93	3.7
Bone	20.8	0.33	2.1
Internal Organs	52.1	0.91	8.4

The performance of the tag when it is placed over different regions

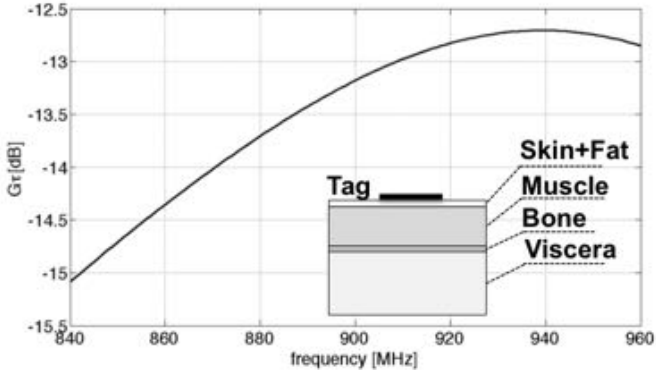


Figure 3.2.: Simulated frequency-dependent realized gain of the epidermal tag over the reference planar model as in Table Tab. 3.1.

of the body and for some body masses are now discussed by the help of some parametric simulations wherein simplified planar and cylindrical models of body parts are considered.

3.1.1. Simulated performance vs. body regions

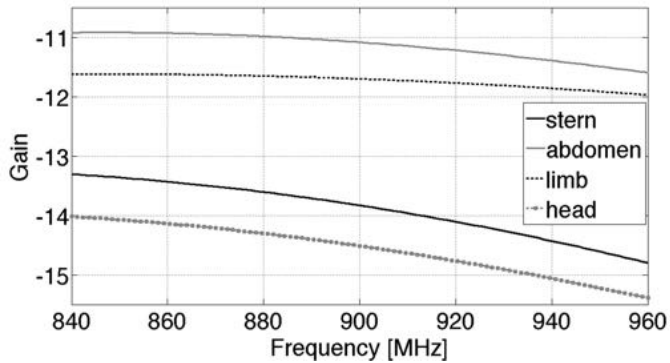
The first set of simulations focused on the sensitivity of the epidermal tag to the specific body parts where it could be placed in real applications. Four reference planar layerings were considered as in Tab. 3.2. They are representative of two regions with high water content, like limbs and abdomen, and of other two regions with a significant presence of bone, e.g. thorax and forehead.

Fig. 3.3 shows the simulated gain of the epidermal tag in the four considered conditions. A difference up to 3-4 dB is visible between the two classes of layerings with better values in case of abdomen and limbs. Accordingly, the read distance, that is proportional to the square root of the the tag gain, could be reduced by more than one third when moving the tag from one region to another. The input impedance of the tag (Fig. 3.4) is less sensitive to the change of the geometry. The resulting effect on the performance param-

Table 3.2.: Reference tissue Layer Thickness (in mm) of some body regions

Tissue	Limb	Abdomen	Thorax	ForeHead
Skin	2.5	2.5	2	2
Fat	8	10	-	2
Muscle	25	20	3	
Bone	-	-	10	7
Dura	-	-	-	1
CSF	-	-	-	2
Viscera (termination)	Bone	Intestines	Lung	Brain

eters is however appreciable as a frequency shift and degradation of the power transfer coefficient (τ). The overall sensitivity of the realized gain versus the tag placement is hence a combination of an amplitude scaling and a frequency shift.

**Figure 3.3.:** Simulated gain of the epidermal tag when it is placed onto four different planar layered models emulating typical body districts.

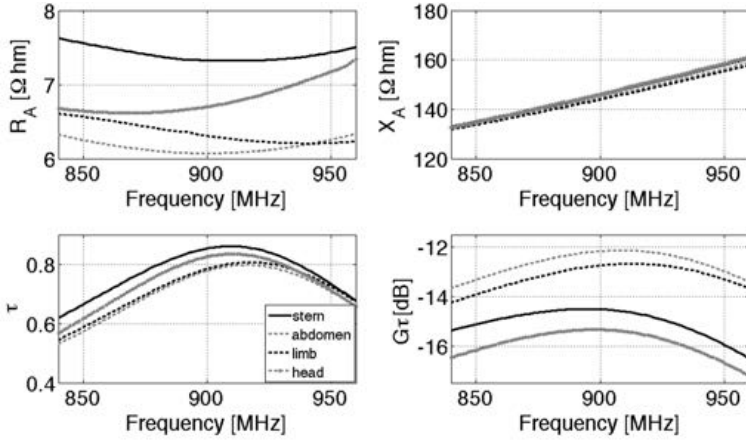


Figure 3.4.: Simulated input impedance $Z_A = R_A + jX_A$, power transfer coefficient τ and maximum realized gain ($G\tau$) of the epidermal tag when placed onto four different planar layered models emulating typical body districts described in Tab. 3.2.

3.1.2. Simulated performance vs. body mass

The epidermal tag was then simulated over a finite-size layered cylinder at the purpose to investigate the effects of the bending of the epidermal loop around a curved surface and the dependence of the tag's performance on the physical size of the underlying body segment. A human arm was modeled by four concentric tissues layers (skin, fat, muscle and cortical bone, Fig. 3.5). Three geometries were considered in order to resemble different form-factors of the arms (see Tab. 3.3). The thickness of the skin and fat layers were kept constant in the models while only the muscular mass was changed.

Fig. 3.5 shows the simulated radiation pattern at 930 MHz in the horizontal plane ($\theta = 90^\circ$). The peak radiation occurs along the direction perpendicular to the tag and in all the cases there is a slight directionality effect. The radiation performance are resumed in the Tab. 3.4 wherein the maximum gain, the radiation efficiency and the front/back (FB) ratio are reported.

Table 3.3.: Radius (in mm) of the three cylindrical numerical phantoms

model	R_{skin}	R_{fat}	R_{muscle}	R_{bone}
A	38	35	27	15
B	48	45	37	15
C	64	61	53	15

Table 3.4.: Radiation performances of the tag over the three cylindrical models.

model	G_{max} [dBi]	η_R [%]	FB [dB]
A	-8.2	6.6	5
B	-10.5	5.8	4
C	-9.6	4.5	8

Differences are visible for both the peak gain and the efficiency and even more concerning the uniformity of the pattern. In particular the most affordable configuration to establish the RFID link is the smallest cylinder, while the largest one produces the least uniform pattern and a lower efficiency so that the interrogation of the tag may be more challenging. In all the cases, the Half Power Beamwidth is of the order of $130^\circ - 175^\circ$. Therefore the expected read distance does not degrade below the 70% of the maximum value, which occurs in the optimum alignment, provided that the reader is placed reasonably in front of the tag. Even considering a few electromagnetic shadowing by the human body, the exact alignment between the epidermal tag and the reader's antenna is not expected to be a critical issue.

It is worth analyzing the near electric field pattern inside the cylinder close to the tag, which was simulated considering the tag antenna in radiating mode (Fig. 3.6). Two phenomena are clearly visible: a resonant-like behavior, especially in the smallest and medium cylinders and a back-reflecting effect in the large cylinder which forces the radiation pattern to be more directive. The efficiency loss and the different front/back ratios are hence the result of the two concurrent phenomena of strong energy dissipation

inside the muscle and its reflector-like effect.

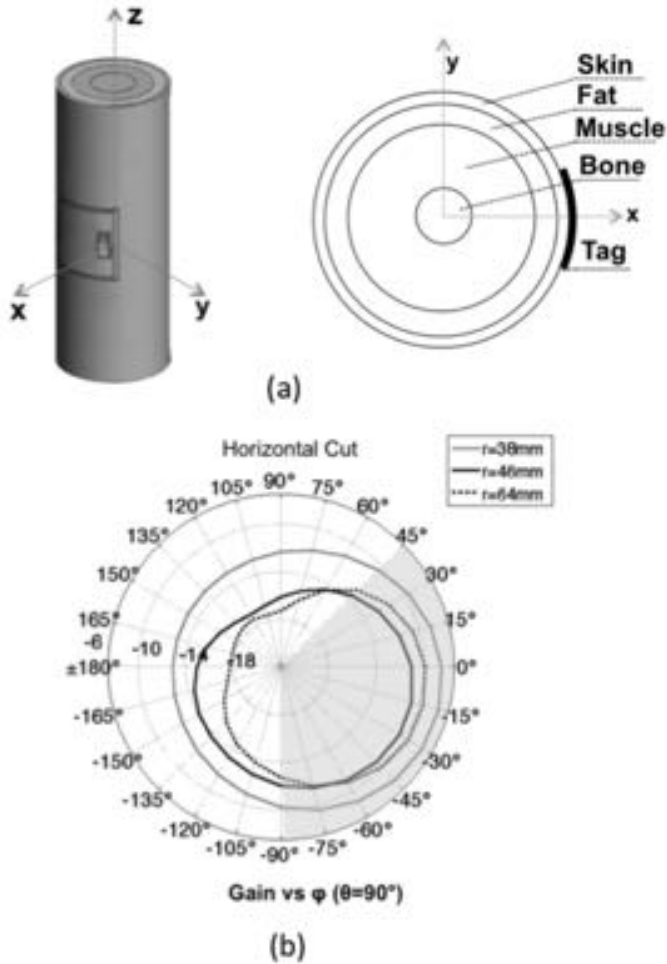


Figure 3.5.: (a) Epidermal loop bent around the 4-layers cylindrical limb model of a human arm. (b) Radiation pattern of the conformal tag at 930 MHz for three different arm sizes. The grey area in the radiation pattern indicates the Half Power Beamwidth.

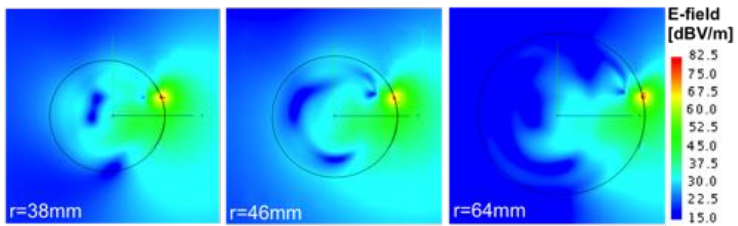


Figure 3.6.: Electric near-field distribution (cross section, $z=0$) inside and outside the layered limb model at 930 MHz when the tag antenna was assumed as sourced by 1W.

3.2. Prototype and on-skin performance

A prototype of the epidermal tag (Fig. 3.7) was fabricated by adhesive copper (thickness $35\mu\text{m}$) which was carved by a two-axis digital-controlled cutter. The profiled tag was applied on a $600\mu\text{m}$ -thick bio-compatible silicone by means of an adhesive transfer tape. The biosilicone layer was shaped just around the conductors and the material in excess was removed in order to improve transpiration. A commercial transparent and breathable adhesive film (TegadermTM) was applied on top of gummy loop. The obtained plaster was hence still adhesive, with the copper placed between the two membranes, and suitable for a comfortable and nearly invisible placement over the skin. As the coating dressing is breathable, the tag can be worn by the user for many days without any discomfort. The ratio between the total area of the conductor and the size of the resulting tag is less than 10 %, with great benefit to skin transpiration. The residual internal surface of the skin could be moreover used to host other devices such as chemical sensors and even drug delivery mechanisms.

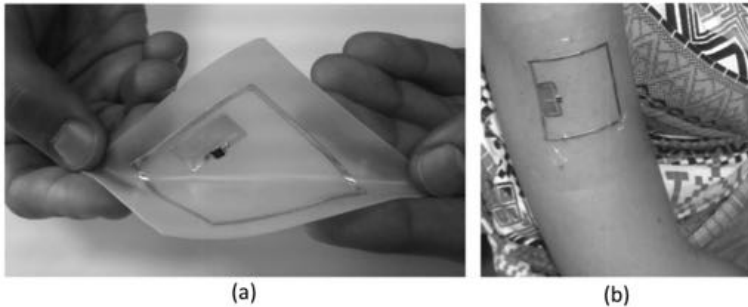


Figure 3.7.: (a) Prototype of the epidermal RFID tag sensor over biocompatible silicone shape and Tegaderm fixing. (b) Epidermal RFID tag transferred over an arm.

The communication performances of the prototype were univocally characterized through the measurement of the realized gain of the tag attached onto a liquid phantom resembling the human body

($\epsilon_{phantom}=43$, $\sigma_{phantom}=0.33$ S/m). The liquid was contained within a $13\text{cm}\times 13\text{cm}\times 20\text{cm}$ parallelepiped box of PET ($\epsilon_{PET}=2$, $\tan\delta_{PET}=0.005$ S/m) having 1mm thickness.

The measurement set-up comprised a ThingMagic M5 long-range reader, connected to a 4 dBi broad-band PIFA antenna. The system was controlled by a custom software implementing the turn-on measurement procedure [29] for the estimation of the realized gain. The distance between the reader and the tag was kept fixed at 40cm in all the experiments. The antenna of the reader and the epidermal tag (attached over the body or over the phantom) were mutually aligned in order to obtain the best polarization match.

Results for the case of reader-tag alignment are shown in Fig. 3.8 together with simulated data. For comparison, the antenna was simulated over a parallelepiped box mimicking the measurements phantom. Measurement results follow the same profile as simulations with realized gain's peak around 940 MHz as expected.

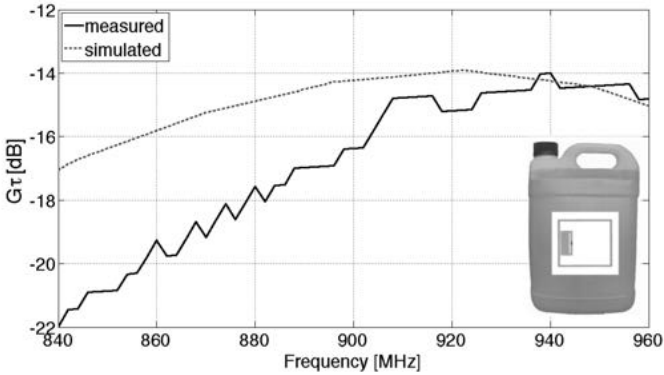


Figure 3.8.: Measured realized gain along frontal (broadside) direction of the fabricated epidermal RFID sensor when applied onto a plastic box filled with a body-equivalent liquid phantom.

The performance of the epidermal tag in real conditions are now discussed by the help of measurements over four volunteers: a “*normal*” male, a “*muscular*” male a “*tiny*” female and “*robust*” female,

whose height and weight are reported in Tab.3.5. They were informed of the experimental procedures and of the goals of the research before the participation to the measurements.

The experiments aimed at investigating the sensitivity of the epidermal tag to the specific locus of placement over the human body and on the user's body-mass, thus corroborating the results from previous numerical simulations.

Table 3.5.: Data of the four volunteers for epidermal tag measurements

Volunteer	height [cm]	weight [Kg]	Body mass Index
tiny female	155	45	18.7
robust female	178	75	23.7
normal male	174	64	21.4
muscular male	184	85	25.1

3.2.1. Measured Performances vs. body placement

In the first experiment, the tag was attached onto different body parts of the tiny female volunteer such as arm, forearm abdomen, stern, hand, neck, and forehead. Fig.3.9 shows the measured realized gain for all the cases. As expected from simulations, the profiles are mutually scaled (due to change in the power absorption) and partially shifted by the effect of impedance detuning. The placement over the leg provides the highest realized gain, even better than what was predicted by simulations for the reference layered model (similar to the case of the former abdomen). In particular, the realized gain was higher than -10 dBi at 950 MHz and higher than -13dBi in the whole UHF RFID band. The worst case was instead the stern position with a degradation of about 10dB in the realized gain, which is even worse than the value predicted by simulations. In most of the cases, a successful communication link was correctly established at the distance of 40cm by just 17-20 dBmW of power from reader that is much lower than the maximum available level.

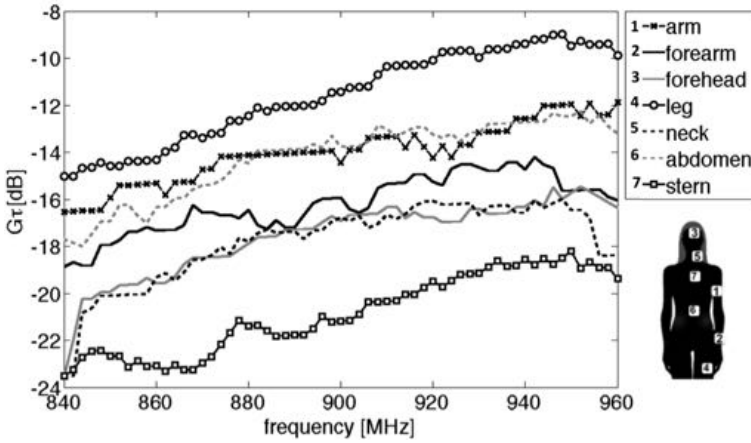


Figure 3.9.: Variability of the measured realized gain of the epidermal tag when attached onto different body regions of a thin female volunteer.

3.2.2. Measured performance vs. body mass

The measurements were repeated for the four volunteers when the epidermal tag was attached onto arms, legs and abdomen. The resulting realized gains (Fig. 3.10) are sensibly different in scale and peak position, when varying both the placement of the tags as well as the body size of the user, as previously obtained in simulations. The tag placed onto the female and normal male volunteers exhibits, on average, better performance in comparison with the muscular man. The tag placed onto the two female volunteers provides comparable results in all the three configurations. Differences among male and female volunteers are particularly visible for arm and leg placement, in agreement with simulations. In case of abdomen there is instead no apparent difference since water-rich tissues dominate in both men and women. The placement over the leg provides instead the highest gain which approaches -9 dBi in the case of the tiny woman because of the larger content of fat tissues.

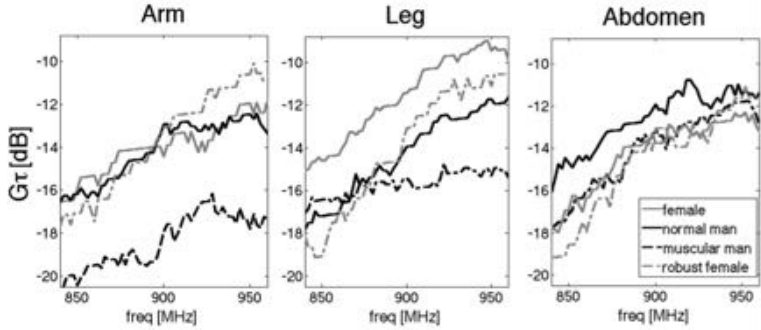


Figure 3.10.: Variability of the measured realized gain of the epidermal tag when it is attached onto corresponding body regions of the four volunteers.

The maximum read distances, estimated in free space from the measured realized gains in Fig.3.10 are summarized in Tab.3.6. We assumed the reader emitting 3.2 W EIRP, which is the maximum power allowed by the European regulation, and a polarization mismatch of 0.5. In all the cases the read distance is close to 1m and more, so that the UHF-RFID epidermal technology is suitable for comfortable and robust interrogation procedures.

Table 3.6.: Estimated maximum read distances (in meters) when the reader emits to 3.2 W EIRP

	arm	leg	abdomen
tiny female	1.6	2.2	1.4
robust female	1.9	1.8	1.4
normal man	1.5	1.6	1.7
robust man	0.9	1.1	1.6

3.3. On-skin retuning

Previous simulations and experiments suggest the need to provide the antenna with some retuning capability in order to obtain a

true communication-reliable epidermal device whose response is independent on the working frequency, on the specific position over the body and also on the user's mass.

A new family [37] of self-tuning UHF microchips is becoming available on the market. They have the capability to automatically adjust the chip impedance in order to partially compensate for possible antenna mismatch. This emerging technology looks promising for epidermal devices. Anyway, epidermal tags are mostly envisaged for sensing applications besides the mere identification and the few RFID chips capable to handle sensors are not currently equipped with self-tuning. Therefore a more general-purpose tuning procedure needs to be developed. A post-fabrication and, possibly, post-placement retuning should be activated case by case, without removing the tag from the body. The considered tag consists of two loops and therefore the antenna impedance can not be simply adjusted by trimming portion of the conductor length, as typically done with dipoles, since the galvanic continuity of the loop has to be preserved. Starting from the observation (Fig. 3.11) that the simulated surface currents flowing over the inner loop are more intense in the inner perimeter, a perturbation of such a profile is expected to change the equivalent self-impedance of the loop and of the mutual inductance between the two coupled loops (recall the equivalent circuit model in [26]). The input impedance of the epidermal tag will be modified accordingly. A practical way to implement this idea in a controllable manner is partitioning the segment of the inner coil, which is closely coupled with the external loop, into some equal-size pre-cut strips (Fig. 3.11). They could be easily removed, even after placement over the body, without affecting the tag integrity.

Fig. 3.12 shows the simulated changes of the power transfer coefficient for the epidermal tag when the strongly coupled subregion of the inner loop ($a=24\text{mm}$, $b=12\text{mm}$) was enlarged and partitioned into six strips of size $20\text{ mm} \times 1.9\text{ mm}$ and one strip was removed at time. The tag was again assumed as placed onto the layered geometry as in Table I. The peak of the power transfer coefficient τ shifts toward the lower frequencies with even some improvement in the maximum value. As a result, the operating region of the tag may be freely modified within the whole UHF RFID band without changing the most part of the antenna and hence providing a viable

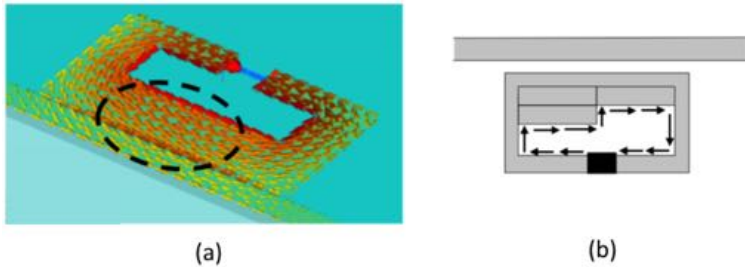


Figure 3.11.: (a) Zoomed view of the simulated current of the feeding loop. (b) The black arrows show how the path of the excitation currents can be modified by removing/adding equal sized strips made of conductor.

mean to achieve an inter-operable device. A detail of the prototype of the tunable tag is shown in Fig. 3.13.

The pre-cutting of the inner loop is expected to produce a perturbation in the path of the surface currents since the galvanic integrity has been partially altered by discontinuities which are induced within the copper foil. Indeed, the tag performance, evaluated for application over the liquid body phantom as above, was different with respect to the continuous loop, as clearly visible in Fig. 3.14. In particular, the cuts produced a down-shift of the frequency response of the antenna, due to the increased current path around the strips, as in meandered antennas [?, 63]. This behavior can be however easily numerically modeled by including a $100\mu\text{m}$ air gap among the strips and the results compare reasonably well with measurements (see again Fig. 3.14).

By removing the strips, the realized gain translates toward lower frequencies (Fig. 3.15) as expected from simulation in Fig. 3.12. Experiments started with the six-strips tag configuration, which theoretically peaks outside the frequency window of the measurement allowed by the considered reader. The realized gain is then gradually tuned to the Japanese band (952-956 MHz) by removing two strips, to the US band (902-928 MHz) by removing three strips and finally to the EU band (865.6 - 867.6 MHz) by removing four strips.

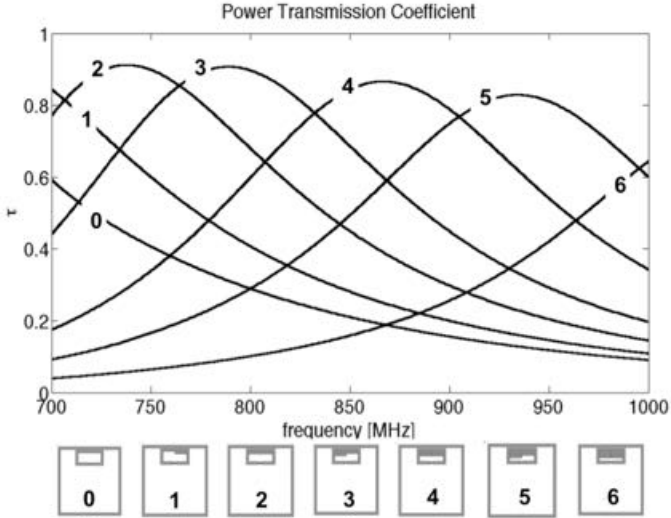


Figure 3.12.: Parametric exploration of simulated power transmission coefficient of the epidermal tag (placed over the reference layered medium of Table I) that is tuned by modifying the size of the feeding inner loop through removal of pre-carved strips of conductors.

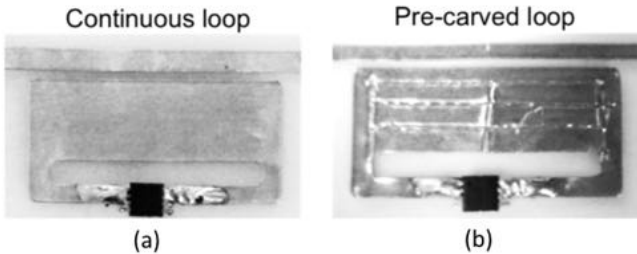


Figure 3.13.: (a) Detail of the inner loop of the epidermal tag that has been pre-cut into six strips of size $20\text{mm} \times 1.8\text{mm}$ and (b) its continuous version, used for comparison.

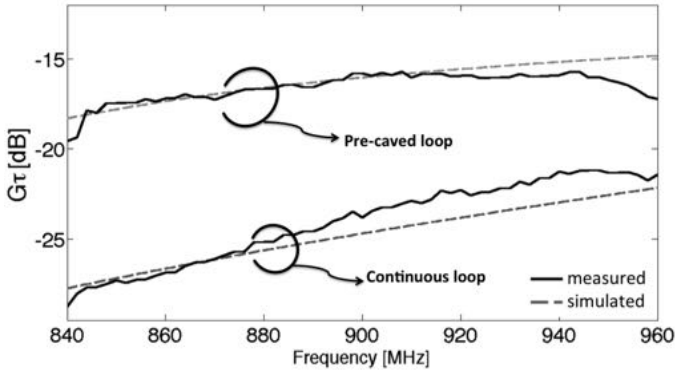


Figure 3.14.: Measured realized gain of a double-loop epidermal tag with pre-cut inner loop in comparison with its continuous version. Tags were placed over the liquid phantom box as previously described, and three measurements were performed for each prototypes.

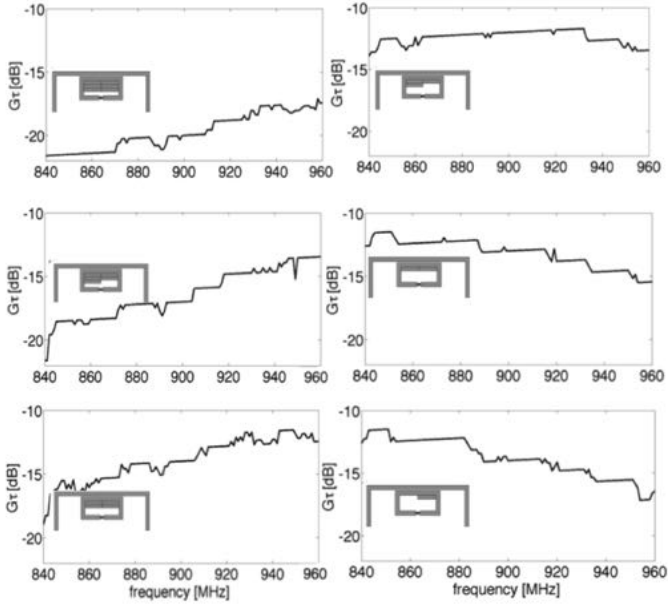


Figure 3.15.: Experimentation of the tuning method: measured realized gain of the epidermal tag placed over liquid phantom mimicking human tissues. From the top to the bottom and from the left to the right side the pre-carved strips are subsequently removed and, accordingly, the peak value of the $G \cdot \tau$ shifts downwards.

3.4. Examples

Some examples of frequency retuning are finally given for application of the epidermal tag onto the volunteers. Experiments considered the improvement of performance when

- i*) the realized gain of the tag placed at a given position is initially rather poor;
- ii*) the same tag needs to be used in different RFID band (USA or EU).

3.4.1. Tuning at a given position

The unperturbed tag (e.g. with all the six strips) was stuck onto the hip of the female volunteer. The peak of the realized gain occurred at 950 MHz, with a poor maximum value close to -20 dBi (a worse case than those experimented before). An improvement of more than 4 dB was achieved by removing only a single strip and the read distance is consequently increased of about 1.5 times.

3.4.2. Change of the UHF band

A new tag in its initial full configuration was then attached onto the arm of the same volunteer and looks well matched in the US band (realized gain of -13 dBi). Three strips were removed in order to have the tag tuned in the EU band (realized gain at 870MHz equal to -13 dBi).

Finally the tag was applied onto the leg of the *normal* male volunteer. Antenna tuning in the Japan and US bands (realized gain close to -12 dBi) was achieved by four strips and two strips configurations, respectively.

3.4.3. Overall analysis

The results of previous experiments can be summarized as in Tab. 3.7 to better highlight the effectiveness of the on-body retuning. The application of a same tag on different users and on different regions

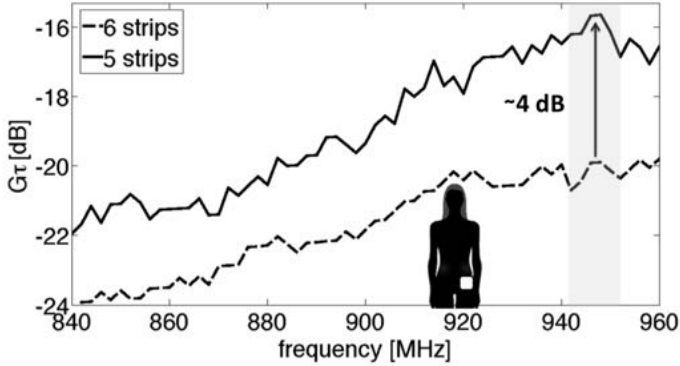


Figure 3.16.: Example of on-skin retuning at 950 MHz when the epidermal tag in Fig. Fig. 3.13 was applied over the hip of the “woman” volunteer.

of the body (hip, arm, leg) really benefits at 950 MHz of the retuning (5, 6, 4 strips, respectively) with an overall nearly stable realized gain. The tag with 4 strips is suitable to multiple applications over hip and arm of the tiny female volunteer at 870 MHz and at 900 MHz as well as to the leg of the normal man but at 950MHz. In all cases the read range performance will be reasonably similar.

Table 3.7.: Summary of the strip numbers and (measured realized gain) for some placements and frequencies

Placement	870 MHz	900 MHz	950 MHz
tiny female, hip	4 (-17 dBi)	4, (-16dBi)	5, (-16dBi)
tiny female, arm	3 (-13 dBi)	4, (-14dBi)	6, (-14dBi)
norm. man, leg	2 (-15 dBi)	2, (-14dBi)	4, (-15dBi)

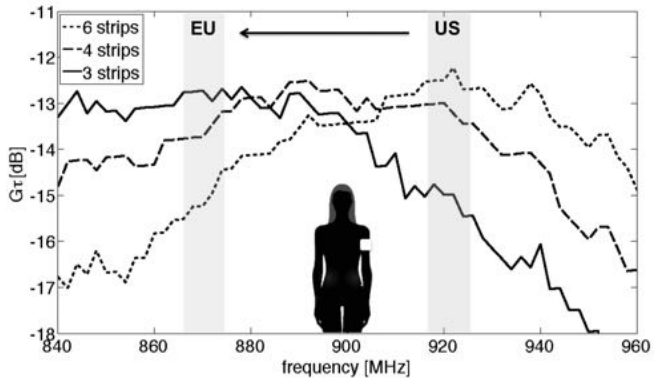


Figure 3.17.: Example of on-skin retuning from US to EU band of the epidermal tag placed onto the arm of the woman volunteer.

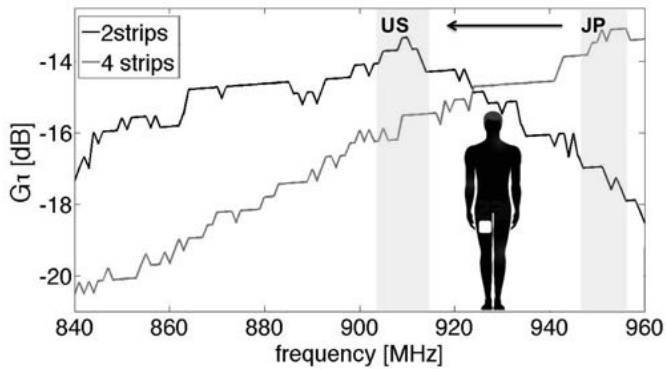


Figure 3.18.: Example of on-skin retuning from 950 MHz to the US band when the epidermal tag in Fig. Fig. 3.13 is applied over the “normal” man’s leg

3.5. Conclusions

Unlike shielded wearable tags, epidermal antennas revealed as significantly sensitive to the placement conditions. Simulations and experiments demonstrated that loop-like epidermal tags, insulated from the human skin by just a thin membrane, provide a realized gain ranging between -17 dBi and -9 dBi depending on the body region where it is placed and on the body mass of the user.

Limbs and arms are the most suitable targets for what concerns communication properties and the epidermal tag may be used for general purpose applications involving just identification or even for the wound monitoring or controlled transdermal drug-delivery. Placement over stern, forearm and forehead, which could be relevant for instance at the purpose of temperature measurement, are more critic concerning the RFID link and may hence greatly benefit of on-body retuning. In real applications we may envisage an epidermal tag tuned by default at high frequencies (for example around 960 MHz). After the placement of the tag over a given body region the user will have a few degrees of freedom in sequentially removing some strips until the tag is read. This tool will adapt a unique epidermal tag to different kinds of placements and frequency bands thus making its mass production more affordable.

4

Biocompatible epidermal membranes

This chapter addresses the electromagnetic characterization in the UHF band of a set of skin-like membranes suitable to host RFID tag for epidermal sensing applications. By using a multilayer ring resonator the dielectric properties are estimated in both static and time-variant condition during the absorption of biofluids (sweat, exudates...).

Epidermal devices must intimately integrate with the human skin to enable the transparent *on-skin* sampling of bio-parameters. Membranes to be used as substrate for epidermal tag play a crucial role as they represent the interface between the radiators and the human skin. Their mechanical and thermal properties must closely match to the skin itself, such to permit an effective adhesion to the skin surface without altering its natural metabolism (sweating, perspiration...). From an electromagnetic point side, the presence of thin separating layer helps mitigating the loss of body tissue by concentrating the near field in the low loss region between the antenna and the epidermis, as discussed in chapter 2. These materials can be a simple physical means supporting the antenna element and the co-integrated electronics or even work as sensing transducers in case some of their dielectric and/or geometrical parameters undergo sig-

nificant variations along with the physio/pathological process under monitoring. By exploiting such interaction with the skin and properly conditioning the sensoristic elements, conventional bandages may be turned into intelligent dressings which act as a fluidic collectors for a quantitative analysis of bio-fluids (sweat, inflammatory exudates, blood..) containing electrolytes, metabolites and inflammatory biomarkers that are useful to detect dangerous dehydration state, screen for systemic disease (screening of Cystic Fibrosis) and optimize the wound-care procedures [64].

The study in [56] has recently demonstrated the feasibility of integrating the dual-loop tag described in the previous chapter with medical hydrogels for wound-care applications. Indeed, the uptake of biological fluids by the membrane sensibly impacts on the matching and radiation of the overlying antenna, which could be hence exploited as a sensor-less transducer to monitor the wound healing process (see Fig. 4.1).

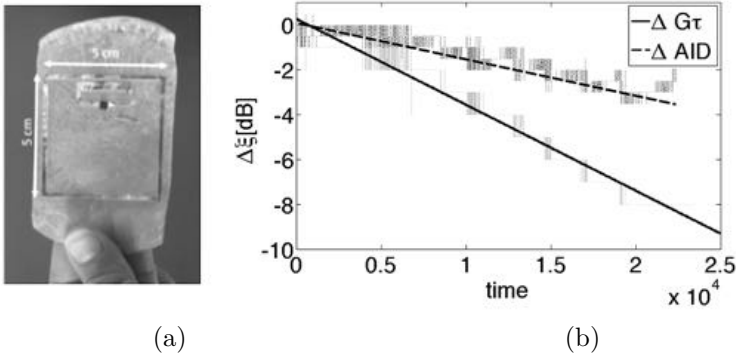


Figure 4.1.: Proof of concept of the *Smart Plaster*: (a) prototype of the dual-loop tag (Chap. chapter 3) over a hydrogel membrane. (b) Measured variation (raw and filtered data) of the realized gain and of the Analog Identifier at 868MHz during the progressive absorption of fluids. Adapted from [56].

The proper selection of substrates for skin-worn RFID tags is hence a crucial step of antenna design, conditioning the overall performance of the epidermal device. However, the materials referred in

literature as possible epidermal substrates are definitely non conventional materials for RF devices. Their dielectric parameters in the UHF band are mostly unknown, thus hindering the engineered EM modeling of the epidermal transponder. This issue is even more tricky in the case of sensitive materials whose properties change along with the time according to a target biological process. It is hence necessary to characterize the RF properties of the substrates in both static and dynamic conditions in order to fully master the sensing mechanism, i.e maximize the tag sensitivity, and simultaneously ensure good communication performances.

This chapter addresses the electromagnetic characterization in the UHF band of epidermal membranes by using a low-cost non destructive microstrip-based resonant setup. Different classes of unconventional material were selected and experimentally characterized:

- i)* membranes capable of reversible absorbing/releasing of body fluids and drugs like hydrogels;
- ii)* moisture-retentive dressings undergoing to irreversible transformation after exposure to fluids;
- iii)* non-reactive polymeric membranes.

4.1. RF Dielectric characterization: Measurement set-up and validation

The measurement set-up for the electromagnetic characterization of the membranes is based on a microstrip ring resonator (Fig. 4.2). The ring and the ground plane/feed network are located in separate planes [65] at the purpose to enable the easy placement of an arbitrary sample between the two layers. Compared to conventional single-layer resonators, the multilayer structure enables a stronger interaction between the sample and the ring fields, forcing the latter to physically cross the sample before coupling with the ground plane. This feature is particularly important for thin film characterization. The measurement method provides good flexibility in term of shape and size of the sample, it is not disruptive and it does not require any preliminary calibrations with reference materials.

Although the device was originally proposed only for the characterization of foams, i.e. materials with permittivity close to one [65], it was found by numerical simulations and experimentations that it can be also applied to denser materials provided that a direct contact between the ring and the sample is enforced. In this way, the ring resonator can be applied even to solids up to biological liquid phantoms.

Finally, in order to perform dynamic characterizations, e.g. the measurement of the permittivity during the exposure of the membranes to different external agents such as liquid, gases and other mechanical solicitations, the suspended ring structure was modified by carving in the upper substrate a circular slot ($r=17.5$ mm) concentric to the ring at the purpose of provide a direct access to the underlying sample.

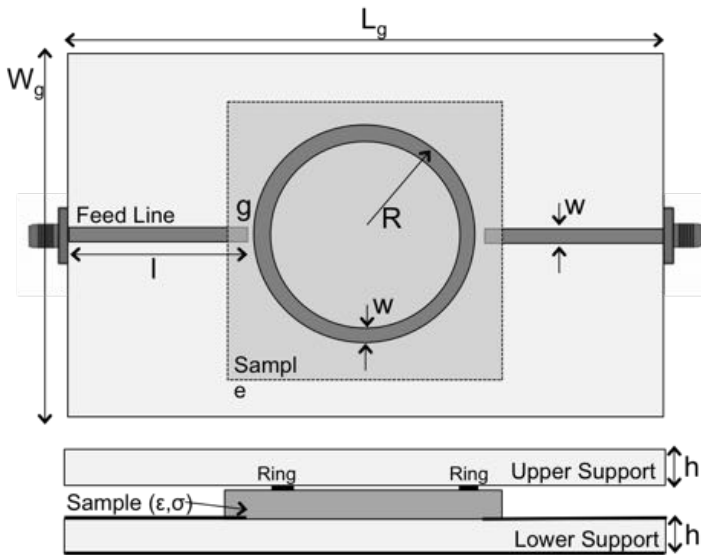


Figure 4.2.: Suspended ring resonator. Traces are etched over two FR4 PCBs ($\epsilon = 4.25$, $\tan\delta = 0.016$). Size in [mm]: $L_g = 136$, $W_g = 90$, $g = 0.25$, $R = 25.9$, $w = 2.2$, $l = 40.75$, $h = 1.575$.

The characterization of the membranes relies on a hybrid experimental/numerical procedure. The two ports of the ring resonator were connected to a VNA which measured the S_{12} scattering parameter versus frequency. The peak frequency and quality factor $\left\{ f_r, Q = \frac{f_r}{|f_{max} - f_{min}|_{-3dB}} \right\}$ of the measured S_{12} are extracted during post-processing. These two features intrinsically bring information about the unknown permittivity and conductivity of the sample, as visible in Fig.4.3 showing an example of measured S_{12} for two different membranes having high permittivity and low losses (gray line) and, viceversa, low permittivity and high losses (dark line).

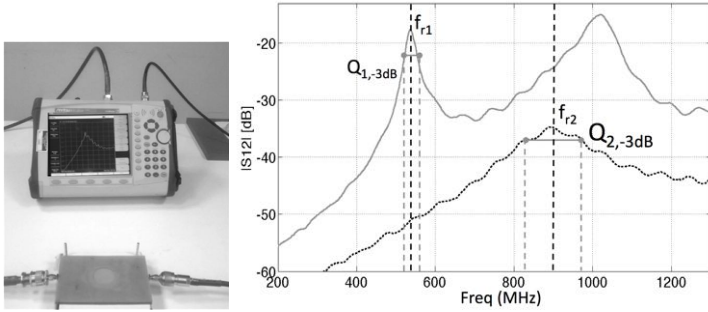


Figure 4.3.: (a) Measurement Setup of the Suspended ring resonator connected to VNA (b) Example of raw S_{12} measurements for two different samples with 1mm thickness.

The identification procedure is performed by using a numerical model of the ring resonator including the sample with variable dielectric properties. The optimal identification of the electromagnetic parameters (ϵ_r, σ) of the membrane is performed by minimizing the following penalty function:

$$s = w_1 |f_{0,meas} - f_{0,sim}(\epsilon_r, \sigma)| + w_2 |Q_{f_{0,meas}} - Q_{f_{0,sim}}(\epsilon_r, \sigma)| \quad (4.1)$$

where $w_1 = w_2 = 0.5$ are weighing coefficients. Minimization was achieved by using the *Trust Region Framework* optimization

method which was applied to a Finite Element Method model of ring (in the FEKO implementation, [54]).

The nomogram in Fig. 4.4 shows typical iso-lines $f_{r,sim}(\epsilon_r, \sigma)$, $Q_{sim}(\epsilon_r, \sigma)$ versus the trial parameters (ϵ_r, σ) for a given membrane thickness. It is worth appreciating that the two families of iso-curves are mostly orthogonal with great benefit to the identification accuracy.

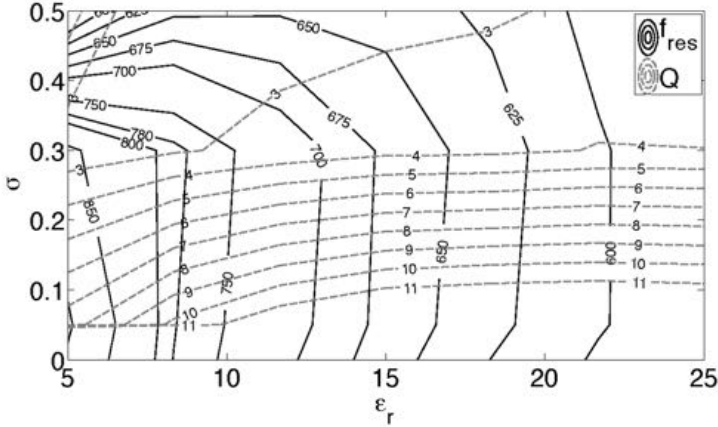


Figure 4.4.: Example of data inversion charts, here $f_{r,sim}(\epsilon_r, \sigma)$, $Q_{sim}(\epsilon_r, \sigma)$ are the peak frequency and the quality factor of the simulated S_{12} response of the ring resonator on varying the electromagnetic parameters of the sample.

Formally, the method provides the estimation of the permittivity and conductivity of the sample at the frequency of S_{12} peak. It is hereafter assumed that such permittivity may be approximated as constant in the UHF-RFID band of interest, as in the case of human tissues [52].

The device has been preliminarily validated over a large set of solid and liquid ¹ materials having different thickness and known dielec-

¹Liquid materials were placed into a 1mm-thick plastic container with known dielectric properties (PET $\epsilon_r = 2$, $\tan\delta = 2$, @1 GHz), which was included in the simulation model.

4.1 RF Dielectric characterization: Measurement set-up and validation

tric parameters in the broad range $1.1 < \epsilon < 79$, $10^{-5} < \sigma < 0.9$ S/m. In the scatters plots of actual vs predicted properties in Fig. 4.5 all the materials lie close to the diagonal, thus confirming the goodness of the identification procedure.

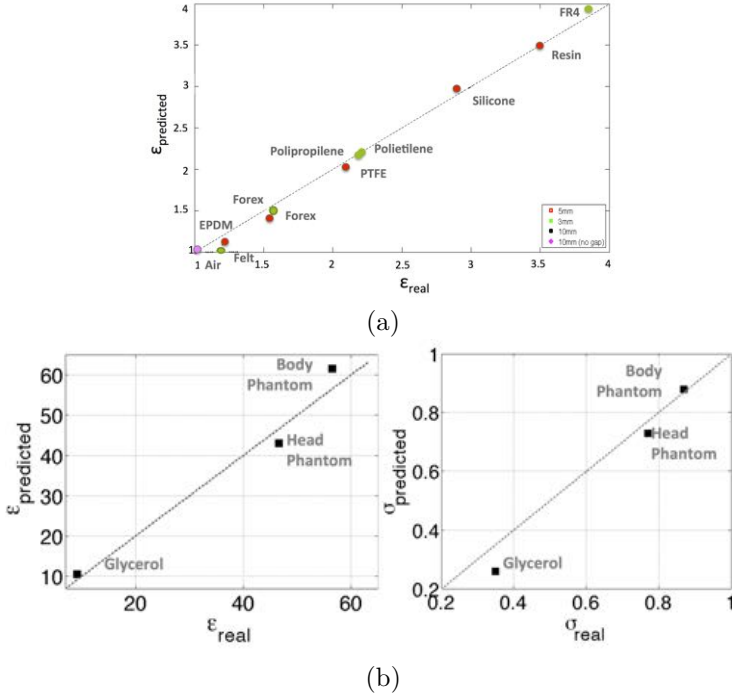


Figure 4.5.: Validation of the measurement setup: actual vs. predicted dielectric properties for (a) low-losses ($\sigma < 5e4$) solid materials and (b) lossy dense liquid samples.

In the next paragraphs the proposed method is specifically applied to the RF characterization of different types of epidermal substrates.

4.2. Hydrogels

Hydrogel dressings are being extensively investigated for wound treatment as they are able to absorb secretions from exuding wounds, cool the infected areas and recover the dehydrated tissues thus creating and maintaining the ideal environment for the wound healing process [66]. These materials can be moreover functionalized by adding doping components for selectively detecting biochemical compounds or activating programmable drugs release (e.g. antibacterial agents, growth factors). These features, combined with good mechanical properties (flexibility and stretchability) and excellent tissue compatibility makes hydrogels very promising substrates to fabricate RFID-based smart plasters.

This work considers PVA/XG-based hydrogels made in collaboration with the Department of Chemical Engineering of the University of Palermo (Italy). The polyvinyl alcohol (PVA) is a water-soluble biocompatible synthetic polymer while Xyloglucan (XG) is a hemicellulose which occurs in the primary cell wall of all vascular plants. PVA/XG hydrogel membranes were prepared starting from the aqueous solutions of the two polymers. These polymeric solutions were then mixed in different ratios and the resulting mixtures were poured into molds. Proprietary plasticizers were added to provide the required flexibility to the membranes. The mixtures were finally air-dried until a constant weight was attained. After the further drying in a vacuum oven at 60°C for 4h, the residual water content was about 1%. Six films of different sizes and shapes that are listed in Tab. 4.1 were produced (Fig. 4.6). It is worth noticing that the membranes show some visible irregularities in term of thickness s , shape (radius r , sides length A and B) and weight due to the not completely optimized fabrication procedure, which could lead to some uncertainties in the dielectric characterization.

The permittivity of the hydrogel membrane in the UHF band is expected to be intermediate between that of the PVA powder $\epsilon_r = 1.6$, $\sigma = 4.8 \cdot 10^{-3}$ S/m [67] and the much higher permittivity of the absorbed solution.

RF Static Characterization The hydrogels in Tab. 4.1 were characterized in the initial dry condition. A commercial hydrogel based

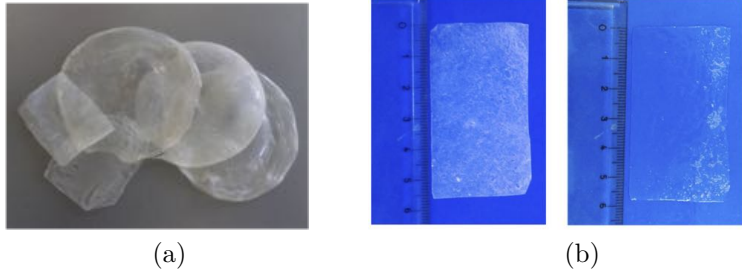


Figure 4.6.: (a) PVA/XG hydrogel membranes under test having different compositions as shown in Tab. 4.1. (b) Example of dry (right) and swollen (left) hydrogel.

Table 4.1.: PVA/XG film compositions and size

	PVA	XG	s [mm]	r [cm]	AxB [cm ²]	weight (g)
M1	1	1	0.7-1	-	6x5	2.2
M3	1	1	0.7-0.9	-	5.5x8	2.8
M6	1	1	0.3-0.6	9	-	2.4
M2	4	1	0.4	-	4.5x5.5	1.8
M4	4	1	0.8-0.9	9.5	-	2.2
M5	1	2	0.6-0.9	10	-	4.5

plaster MySkin [68] was also considered as reference to enrich the analysis. As shown in Fig. 4.7, all the membranes exhibit a quite smooth S_{21} profile which indicates a not negligible conductivity which is mainly related to some amount of water/fluid at room condition (as absorbed from the environment or residual from the fabrication). This effect seems particularly evident in the case of the commercial membrane, which contains, as explicitly declared by the producer, a well defined amount of water to create a wet environment around the wound. The retrieved data are listed in Tab. 4.2. The permittivity is rather low and it is typical of polymeric films. As expected, membranes with the same composition exhibit extremely similar values of $\{\epsilon_r, \sigma\}$ (see the diagram in Tab. 4.2), thus corroborating the possibility to have a quite reproducible measure-

ments in spite of the irregularities of the samples.

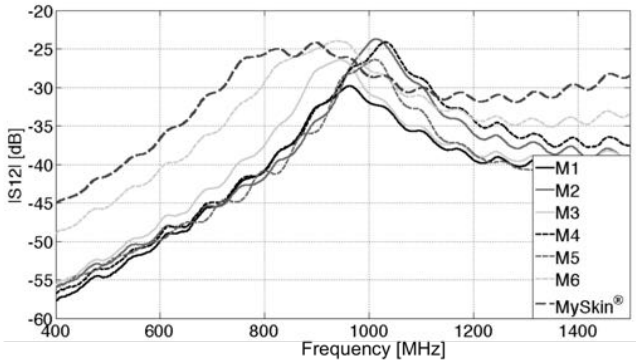


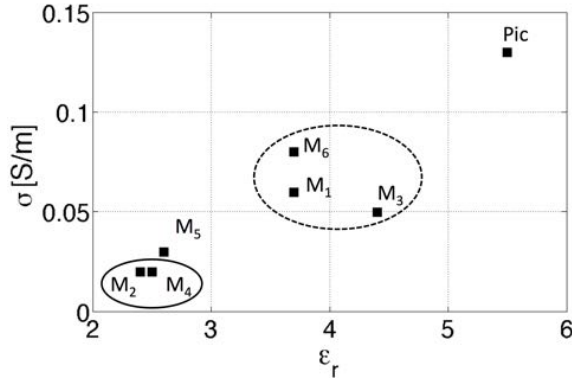
Figure 4.7.: Measured S_{21} for the dry membranes.

RF Dynamic Characterization One of the tested membrane (M5) was characterized during progressive swelling. The release of body fluids from the skin and the consequent absorption by the hydrogel film were emulated by dispersing a saline solution (NaCl 0.5 gr/l) directly over the membrane through the circular slot by means of a spray nozzle. 0.2 g fluid were approximately released for each application, up to a total amount of 2.5 g. A digital scale was used to further monitor the fluid dispersion by continuously weighing the entire measurement setup (inset of Fig. 4.8). This exposure set-up could emulate both physiological and pathological conditions, such as sweating or large skin lesions (large burns, ulcers, bedsores..) underneath the plaster. Steady measurements were performed after each spray once the diffusion of the solution within the hydrogel was extinguished.

The RF response of the membrane significantly changes along with the amount of fluid absorbed by the bulk hydrogel. In particular, the absorption of the fluid produces (Fig. 4.8) a progressive shift

Table 4.2.: Retrieved dielectric properties of the dry hydrogel membranes.

	M1	M3	M6	M2	M4	M5	MySkin [®]
ϵ_r	3.75	4.4	3.7	2.4	2.6	2.5	5.5
$\sigma[S/m]$	0.06	0.05	0.08	0.02	0.03	0.021	0.13



of the S_{12} peak towards lower frequencies (increase of permittivity) and a reduction of the quality factor (increase of conductivity), corresponding to a monotonic variation of the permittivity and the conductivity up to intermediate values between those of the dry membrane and of the saline solution (Fig. 4.9). By performing a weighted average between the dielectric properties of the PVA powder ($\epsilon_r = 1.6$, $\sigma = 4.8e - 3$ S/m) and of those of the saline solution ($\epsilon_r = 79$, $\sigma = 0.26$ S/m) at the central and the final exposure conditions (1 g and 2.5 g of water respectively, approximately corresponding to the 20% and 40% of the total weight), the expected dielectric parameters are $\{\epsilon_{r,20\%} = 17$, $\sigma_{20\%} = 0.05$ S/m $\}$ and $\{\epsilon_{r,40\%} = 32$, $\sigma_{40\%} = 0.1$ S/m $\}$, which reasonably agree with the retrieved parameters. Slight discrepancies, especially regarding the conductivity, should be ascribed to the specific properties of the membrane as a whole and to the plasticizer added during their synthesis.

It is worth noticing that the tested membrane slightly dissolved after fluid absorption (bioresorbable film). By reacting the PVA-

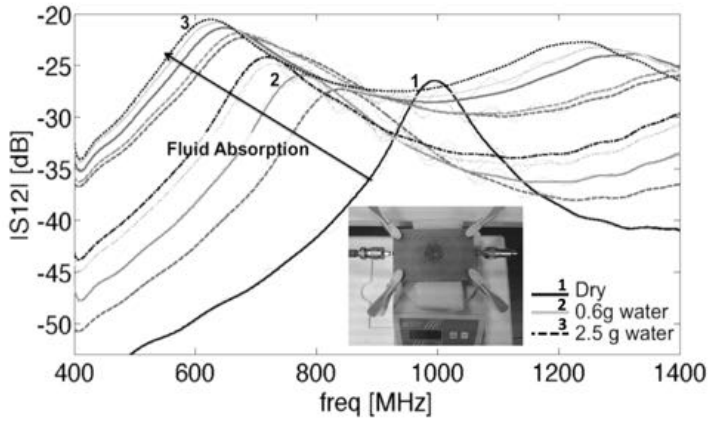


Figure 4.8.: S_{12} measurements during the progressive absorption of fluid.

XG solution with a certain amount of GA (25 wt.%) a cross-linked film capable of reversible swelling and recovery can be obtained, whose properties are currently under investigation.

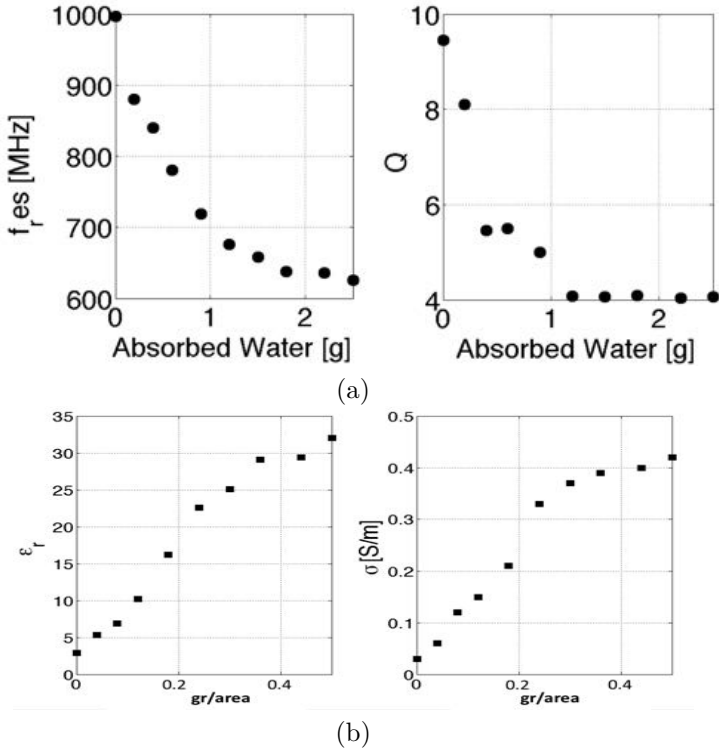


Figure 4.9.: (a) Features (f_r, Q) extracted from S_{12} measurements in Fig. 4.8 and (b) the corresponding estimated dielectric properties of the hydrogel membrane related to the amount of absorbed water per unit area. .

4.3. Moisture-retentive dressing

The second class consists of highly absorptive commercial dressings commonly used in clinical practice for the treatments of severe wounds with moderate to heavy levels of exudate. These membranes absorb the exudate vertically and locks the fluid away within their structure, by holding bacteria and microbes in retained fluid, thereby reducing the risk of periwound maceration compared with films that absorb lateral. Two materials are here considered:

- *Aquaceℓ® Hydrofiber* (by ConvaTec, Princeton, NJ, USA) made of non-woven sodium carboxymethylcellulose (CMC) fibers which forms a cohesive gel on contact with fluid (gelification)
- *Biatain®* (by Coloplast Pty Ltd, Mount Waverley, VIC, Australia) soft and conformable polyurethane foam dressing whose thickness increase with swelling.

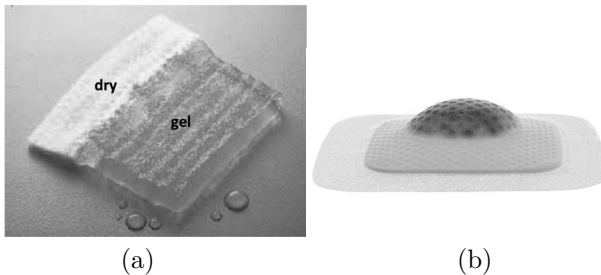


Figure 4.10.: (a) Fiber-based gelling membrane (*Aquacel*) (b) Absorbent polyurethane foam (*Biatain*)

To characterize the dynamic electromagnetic behavior of the membranes the fluid absorption was inducted by repetitively placing the samples over a synthetic sponge soaked with the saline solution. After two minutes the samples were weighted and placed between the two layers of the ring to measure S_{12} . This procedure was repeated four times up to the full immersion of the membrane. In the dry state both the dressings exhibit permittivity close to that of the air and due to the fibrous matrix of the substrates and relatively low losses ($\epsilon_{r,AQUACEL} \sim 1$, $\sigma_{AQUACEL} = 7.4e - 4$ S/m,

$\varepsilon_{r,BIATAIN} \sim 1.4$, $\sigma_{BIATAIN} = 2.5e - 3$ S/m). When the *Aquacel* is exposed to the fluid it gradually changes into a cohesive gel along the vertical direction and the dielectric parameters increase up to very high values, which practically correspond to the parameters of the saline solution. During fluid absorption the *Biatain* swelled with remarkable variation of the thickness (3.5mm-8mm) that was included in the model for the parameter identification. The retrieved parameters have a stepwise trend but a rather modest dynamic range compared to the hydrofiber dressing. Results are in Fig. 4.11 as a function of the absorbed saline solution per unit area. Both the membrane irreversibly changed their texture with fluid absorption even after complete drying therefore they are not usable for cyclic exposure.

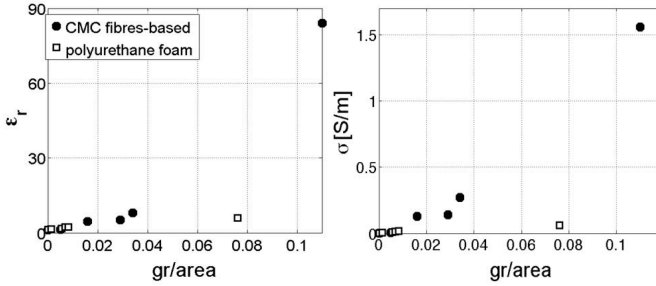


Figure 4.11.: Estimated dielectric properties of the moisture-retentive dressing as a function of absorbed fluid per unit area.

4.4. Static membranes

The last set consists of polymeric membranes that are conceive for holding the epidermal transponder without interacting with the skin interface

- Medical-grade silicone rubber sheet;
- Transparent PET film (by Mitsubishi Paper Mills [69]) with PVA-based surface treatment suitable for ink-jet printing;

- Breathable dressing (by Fixomull®) made of transversely stretchable non-woven polyester backed by hypoallergenic polyacrylate adhesive;
- Poli(ϵ -caprolactone) (PCL) bioresorbable and transpiring scaffolds-like membrane,

The dielectric properties summarized in Tab. 4.3 were accordingly derived only for the static reference condition. The biosilicone and coated PET exhibits values typical of solid polymers, while fibrous dressing have intermediate parameters between the polymeric components and air. The losses were rather low in all the cases ($\sim 10^{-3}$), apart from the coated PET whose conducted resulted one order of magnitude higher.

Table 4.3.: Estimated UHF dielectric properties of bio-compatible static membranes

	ϵ_r	σ (S/m)	Thickness [mm]
Biosilicone	2.5	0.005	0.600
PVA-coated PET	1.9	0.015	0.135
Fixomull	1	0.004	0.220
Poli(ϵ -caprolactone) (PCL)	1.1	0.008	0.450

The latter is a synthetic membrane [70], composed by semicrystalline bioresorbable poly α -hydroxyester with slow degrading rate due to its hydrophobic nature and the high crystallinity degree. This membrane was produced at the Chemistry Department of the University of Rome Tor Vergata by electrospinning PLC granules solved in CHCl_3 and THF:DMF (1:1) solutions. Electrostatic fiber-spinning [71], shortly denoted as electrospinning, is a straightforward, cost-effective methodology to fabricate non-woven micro and/or nano-fibrous fabrics for several biomedical applications, e.g. scaffolds for tissue engineering or wound dressings. The resulting PCL membrane is free of toxic residues, flexible and stretchable and preserves the natural transpiration of the skin thanks to its fibrous structure. Fig. 4.13 shows an example of the dual-loop tag deposited over the electrospun PLC membrane for an early exper-

iment of skin temperature monitoring [48].

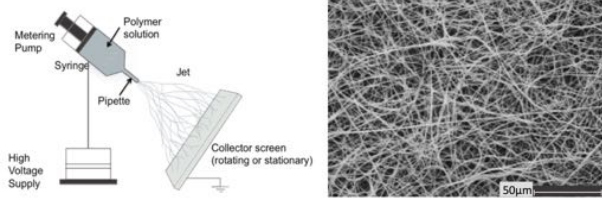


Figure 4.12.: (a) Fabrication scheme by electrospinning. (b) SEM image of the membrane.



Figure 4.13.: Prototype of the stretched epidermal RFID temperature sensor over PCL membrane

4.5. Conclusions

The presented work focused on the electromagnetic characterization in the UHF of a set of different dressings by means of low-cost and non disruptive resonant method, with particular focus on responsive bio-materials acting as exudate/ sweat sensitive elements. When exposed to biological fluids, PVA-XG hydrogels swelled uniformly with a remarkable variation of their RF dielectric properties, which may increase by 10 times with the respect to the dry state. Moisture-retentive dressings allowed vertical wicking and prevented lateral movement of fluid within the dressing. This localized distribution of bio-fluid within the membrane that accordingly change its

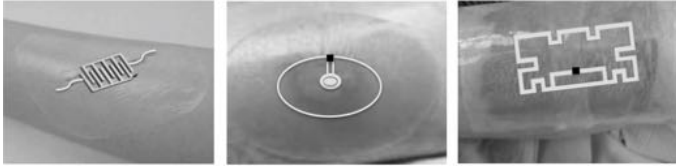


Figure 4.14.: Concept of RF transducer engineered for specific skin lesions: (a) finger capacitor for surgical incision, linear cut; (b) disk capacitor for rounded ulcer and punctures; (c) loop antenna for large burns, pressure sores.

dielectric properties (up to the values of the solution) in a limited region can be modeled as a variable loading impedance of the overlying antenna [72]. Combined dielectric/geometrical transducing mechanism can be exploited in the design of antenna and capacitive sensors embedded within superabsorbent dressing like *Biatain*. Low-cost commercial dressings commonly used in clinics were also characterized to be used as substrate for epidermal RFID transponder.

These early results open interesting scenarios for smart bandage technology in the management of acute and chronic wound, where the possibility to monitor the time-variant distribution of moisture within the applied dressings without the need of removal is critical for an effective healing process. Future work must be devoted to the engineering of the RF transducers by tailoring their response to the specific the shape of the skin lesion (linear cut, rounded, large), the type of applied dressing and the nature of the absorbed exudate (serous, purulent...), as sketched in Fig. 4.14.

5

Self-Sintering Inkjet Printing and other Manufacturing Technologies

This chapter investigates the feasible usage of a recently developed inkjet printing technology by ambient-sintering ink and presents a comparative analysis of suitable state-of-the-art manufacturing technologies (carved adhesive copper, copper micro-wire and photolithography).

Reshaping RFID transponders, conventionally used in logistics of bulk objects, into a form suitable for skin mounting demands for efficient techniques to deposit conductive traces over biocompatible ultra-thin flexible membranes. Cost-effective and easily accessible methods are hence required for both the rapid prototyping of laboratory samples as well as for the mass production over the large scale [73].

Printed technology on flexible and even stretchable substrates [74, 75, 76] is increasingly adopted by the electronics industry for the fabrication of RF circuits and wireless devices [?] by using electrically engineered inks. The first referred prototypes of *tattoo*-like UHF tags were fabricated by profiling conductive silver painting or a nickel-based screening spray by means of stencil techniques

[47]. Then, inkjet printing and low temperature sintering of silver nano-particle inks was experimented onto transfer tattoo paper [49]. Most of the published works refers to highly specialized and expensive printing equipments, like the FUJIFILM Dimatix DMP-2800, with nanoparticle silver-based inks (e.g. from Xerox, Sigma Aldrich). This technology requires thermal or laser post-deposition sintering treatments of the trace to provoke the coalescence of discrete nanoparticles enclosed in a polymeric shell - designed to forbid agglomeration prior to the deposition - and hence to earn the optimal electrical conductivity.

Very recent progresses in Materials Science originated a new class of conducting inks [61, 77] which dry at room temperature and form an instantly conductive layer, without the need of time-consuming thermal sintering [78]. These sintering-free inks are hence suitable to be cheaply and easily deposited on a flexible substrate by using consumer-grade, low-cost, inkjet printers. The feasibility of the fabrication of a variety of functional electronic prototypes, including touch and proximity-sensitive surfaces and capacitive liquid-level sensors, have been already demonstrated in [79, 80]. The same authors proposed in [81] some procedures to make interconnections between double sided patterns at the purpose of fabricating multilayered instant-printed circuits. However, to the best of the author's knowledge, most of applications concern DC or low-frequency circuitries. Even if a very early example of a true planar antenna can be found in [82], the trace's surface resistance was still characterized in DC and a thermal sintering was nevertheless used.

The application of the considered manufacturing technique to epidermal antennas working in the UHF-RFID band (860-960 MHz) requires a more in-depth analysis to take care of a number of additional parameters which are specific to the co-habitation of an antenna with the human skin, such as the presence of the sweat, the possible bending over body curvatures and the need of a biocompatible coating. Moreover, antennas placed at micrometrical distance from the skin are affected by high losses and hence information on the ink conductivity at the frequency of RFID systems is required to optimize the communication performance. This chapter describes a broad characterization of the Self-Sintering ink-jet technology for the specific fabrication of epidermal antennas with

the overall goal of identifying the most appropriate modalities to achieve read-range performance as close as possible to the bulk copper, and to test the sensitivity of the ink-jet printed antennas in variable boundary conditions typical of body-centric systems. The basics of the sintering-free conductive ink are first reviewed regarding the ink conductivity in the DC regime and the identification of suitable printing substrates. Then the ink conductivity is estimated in the UHF-RFID band by means of a combined experimental/simulated identification procedure. The achievable performance of realistic epidermal antennas depending on the number of printing layers, the resistance to bending and to body fluids is discussed and some possible bio-compatible coatings are experimented.

Finally, the self-sintering printing technology is demonstrated for the real application over the skin and systematically compared with other conventional manufacturing options (carved adhesive copper, copper micro-wire and microfabrication) in terms of achievable maximum gain, usability of bio-compatible conformable substrates, time and costs for large-scale production.

5.1. Inkjet Printing by Self-Sintering Ag Ink

The silver nano ink from Mitsubishi Paper Mill [61] consists of an aqueous solution containing silver nanoparticles of approximately 20 nm diameter uniformly dispersed in a solvent consisting of polymer latex and a halide emulsion. The conductivity of this ink spontaneously emerges at ambient temperature as soon as the solution is dried thanks to the formation of interconnections among the silver nanoparticles which is triggered by the halide [83]. The printer selected for the ink deposition was the Brother MFC-J5910DW whose specific nozzles eject higher volumes of ink than other printers, meaning that a greater amounts of conductive ink can be deposited in a short time. The standard cartridges were refilled by the Ag-ink using a syringe through disposable filters. When all cartridges available for the CMY colors are loaded, four layers of ink are deposited at once. The print quality is 6000x1200 dpi with a measured minimum line spacing of 300 μm .

5.1.1. Suitable printing substrates

Different substrates widely reported as materials suitable for hosting epidermal devices were selected as possible supports for ink deposition: ink-jet tattoo-paper, polyurethane-based dressing, cellulose membrane, adhesive non-woven fabrics. Tattoo transfer paper, in particular, has been already experimented for printing silver ink dispersed in organic solvent and then sintered at 135 °C [49]. Two additional media suggested by the ink manufacturer were also considered: a resin-coated paper and a Polyethylene terephthalate (PET) film (white or transparent) having a PVA-based ink receptive layer on top [69].

The tested materials with the corresponding optical micrographs of a 2x10 mm² printed trace are listed in Tab.5.1. None of the skin-like membranes revealed adequate for self-sintering ink which penetrated within the fibrous matrix (4, 5), spread over hydrophobic surface (2) or formed evident cracks (1), thus preventing the activation of chemical sintering and the creation of a continuous conductive path (the resistance between the two extremities was higher than 1 MΩ). A low resistance was achieved only with the commercial printing sheets (6, 7) thanks to their specific surface treatment based on a porous coating layer that facilitates the ink adhesion and the solvent absorption at the nano-scale and prevents smearing. Although rather flexible thin and bio-compatible, the texture of these sheets is not suited to adhere closely to the skin but they have been anyway used in the study for the ink characterization of epidermal-oriented applications.

Table 5.1.: Flexible substrates tested for the deposition of self-sintering ink by desktop printer.

Substrate	Optical micrograph (60x)
1. Ink-jet tattoo-paper Crafty computer paper 20 μm	
2. Polyurethane-based dressing Rollflex Master-Aid 22 μm	
3. Cellulose Membrane Visking Dialysis Medicell International ltd 30 μm	
4. Adhesive non-woven fabric Fixomull® Stretch 120 μm	
5. Adhesive non-woven fabric Amuchina 70 μm	
6. Resin coated paper Mitsubishi Paper Mills 177 μm	
7. PVA coated PET Mitsubishi Paper Mills 135 μm	

5.1.2. The spontaneous-sintering effect

Fig. 5.1.a shows an example of the sheet resistance of a single-printed (four ink layers) rectangular patterns over PET substrate with size ratio Width/Length=100, according to the standard in [84]. The spontaneous chemical sintering of the ink activates right after the printing and it continues for the next 30 minutes with a progressive reduction (up to 17%) of the sheet resistance (R_S) down to its asymptotic value that is hereafter considered as the ink resistivity.

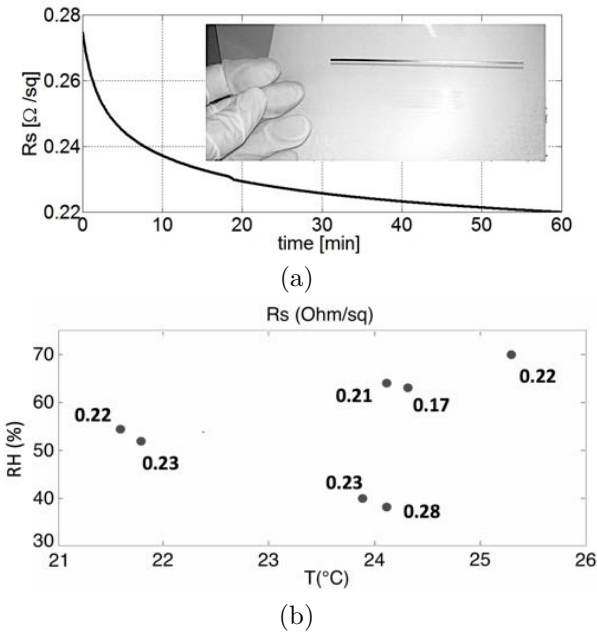


Figure 5.1.: a) Time-variant DC sheet resistance of a printed $W/L=100$ trace on PET transparent film as measured at ambient conditions ($T = 24.1^{\circ}\text{C}$ and relative humidity $RH = 64\%$). Time $t=0$ marks the end of the print procedure. b) Sheet resistance of several printed traces on PET for variable ambient conditions during the printing process.

The resulting value of R_S is rather unaffected by the temperature of the printing environment while tends to slightly reduce in case of high humidity conditions (Fig. 5.1b). The thickness of the profiles of printed traces, as measured by Dektak 3ST surface profilometer, is rather non-uniform with an average value $t = 300$ nm due to ink agglomeration and substrate porosity (Fig. 5.2).

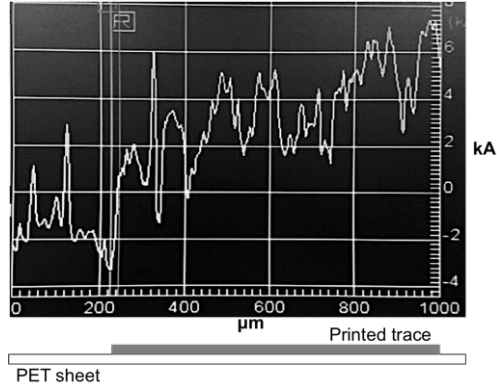


Figure 5.2.: Measured profile of the inkjet printed trace on PVA-coated PET film.

5.1.3. Resistivity v.s. sheet pre-treatment and drying conditions

Although the resistance achieved directly after printing is already acceptable, some methods to further reduce the resistivity were explored. Measurements of the sheet resistance as above were repeated in three different conditions concerning the environmental conditions (humidity level and temperature) during drying and the humidity of the printing substrate.

Drying in saturated air condition To create a humid environment without using an expensive humidity chamber a plastic container properly insulated was connected to a kettle through a heat-resistance tube (Fig. 5.3). When the vapor is blown into the box,

the humidity becomes higher than 90% after few minutes (which is the full-scale of the digital hygrometer).

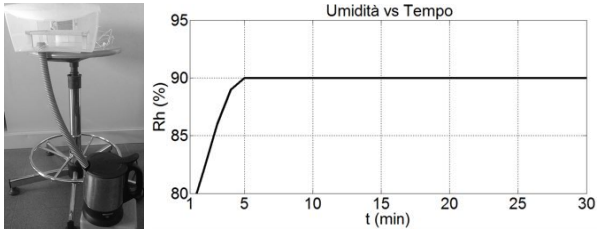


Figure 5.3.: Experimental setup for drying the printed layouts in saturated humid air

To assess the effect of drying in high humidity conditions, five traces were simultaneously printed on a PET sheet at room conditions ($T_{est,i} = 21.8^{\circ}C$ and $RH_{est,i} = 52\%$) and then inserted into a plastic box ($T_{int,i} = 23.9^{\circ}C$ and $Rh_{int,i} = 90\%$) through a small slot immediately after the printing.

Printing/Drying in high-temperature condition This test addressed the increase of the local temperature in the surrounding of the paper output tray by means of a heat gun so that both the printing and the drying procedures happened at an average temperature of $65^{\circ}C$.

Printing on a wet substrate The last experiment concerned the possibility of using a pre-treated substrate exposed to a humid environment prior to printing. The objective was to verify if the greater amount of water inside the substrate could be beneficial for enhancing the chemical sintering, which is a referenced technique for accelerating the process [83]. The PET transparent film which is a material permeable to water was left in the plastic box at saturated humid air (Fig. 5.3) for 4 hours and changed color from transparent to opaque due to water absorption.

Tab. 5.2 summarizes the results from the above experiments. The measured sheet resistances exhibit a rather modest change (wors-

ening) only when the sheet was humid and when printing/drying happened in high temperature conditions. In overall there is no apparent convenience of deviating from the simplest printing/drying procedure.

Table 5.2.: DC ink resistivity in various printing and drying conditions.

	R_S (Ω/\square)
Ambient Conditions	0.220 ± 0.001
Drying in saturated humid air	0.230 ± 0.001
Vapor Pretreatment	0.270 ± 0.002
Drying at high temperature	0.300 ± 0.002

Finally, the average sheet resistance derived from multiple measurements at normal ambient condition is $R_S = 0.22 \Omega/sq$ and the corresponding conductivity in DC can be hence estimated as:

$$\sigma_{DC} = \frac{1}{R_{St}} = 1.5 \cdot 10^7 S/m \quad (5.1)$$

which is just a quarter of that of bulk copper.

As it will be shown in the next Section, the conductivity in the UHF band is expected to be rather different due to the frequency dependance of the response of the non-metallic matters inside the composite ink.

5.2. Characterization in the UHF-RFID band

The RF conductivity of the Ag-ink in the UHF band was experimentally evaluated by means of a parameter-identification technique involving numerical simulations and measurements over an

ink-jet printed resonant antenna. The S_{11} parameter was measured over frequency and a numerical model of the same layout was optimized with respect to the unknown conductivity of the traces in order to match some features of the measured S_{11} . In the considered experiments the test antenna was a meander-line monopole (MLA, inset of Fig. 5.4) since the presence of the transmission line current mode in the meanders generated by the multiple foldings [63, 85] induces a huge sensitivity of the antenna response to the conductivity of the traces. The monopole was designed to be matched to 50Ω around 870 MHz, by initially assuming copper traces. Accordingly, the antenna responses exhibit two sharp nulls of the S_{11} around 870 MHz and 2500 MHz. Two samples of the monopole were then printed over the PET substrate and placed over a copper ground and hence connected to a Vector Network Analyzer via a glued SMA connector so that the reflection coefficient S_{11} was measured in the frequency band 300-3000 MHz. Finally, the following penalty function was minimized to identify the unknown

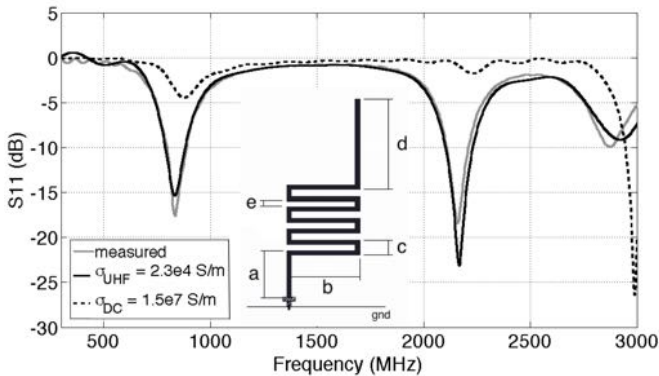


Figure 5.4.: Meandered monopole used as reference antenna. Size [mm]: $a=11$, $b=16$, $c=3.4$ $d=21$, $e=1.4$. Comparison between the measured S_{11} of the printed MLA and the simulated response of the corresponding FDTD model including the identified conductivity in the UHF band and also the response obtained with the DC conductivity.

trace effective conductivity:

$$s = \sum_{n=1}^2 \begin{aligned} &w_1 |f_{n,meas} - f_{n,sim}(\sigma)| + \\ &+ w_2 |B_{meas}(f_n) - B_{n,sim}(f_n, \sigma)| + \\ &+ w_3 |S_{11,meas}(f_n) - S_{11,sim}(f_n, \sigma) - 5| \end{aligned} \quad (5.2)$$

where $\{f_1, f_2\}$ are the first two resonant frequencies of the MLA around the UHF band, $S_{11}(f_n)$ the reflection coefficient at such resonances (expressed in dB), $B(f_n)$ the bandwidth referred to $S_{11} = -10$ dB around the resonances and $w_1 = w_2 = 0.2$, $w_3 = 0.1$ the weighing coefficients. Minimization was achieved by using the *Trust Region Framework* optimization method which was applied to a Finite-Difference Time-Domain (FDTD) model of antennas with variable conductivity. The identified effective conductivity for a single-print trace was $\sigma_{UHF} = 2.3 \cdot 10^4$ S/m and hence sensibly worse than the corresponding DC one. The estimated value permits to satisfactorily match (Fig. 5.4) the numerical model with the measured data, while the use of the DC conductivity would have returned incorrect results.

5.3. Application to a small-size epidermal tag

The applicability of the considered sintering-free inkjet printing to wireless skin technology is now discussed by prototyping an epidermal RFID tag.

A first example of an epidermal-like loop tag was introduced in chapter 3 and extensively investigated with respect to the body position and the user's body mass. Nevertheless, the size of the described antenna was still too large for a comfortable application over any body curvatures without user's discomfort. As the external rectangular loop radiates like a two "C" dipoles (Fig. 3.1), a smaller tag was derived from the original layout after 2:1 miniaturization achieved by folding the "un-useful" segments of the loop where the currents are in phase opposition (these currents dissipate power but do not contribute to the radiation).

Then, additional meanders were introduced in the vertical segment of the loop to provide the epidermal antenna with flexibility along the two direction. The internal matching loop was replaced by a T-match impedance transformer [28] since it avoids the criticality of alignment allowing a more robust manufacturing. The considered chip was the EM4325 IC with input impedance $Z_{in} = 23.3-j145\Omega$. The final layout (Fig. 5.5) is halved in the size (2.5cm x 5cm) but it provides the same radiation Gain (-12 dB) along the broadside direction as the previous one (in the case of the copper conductor).

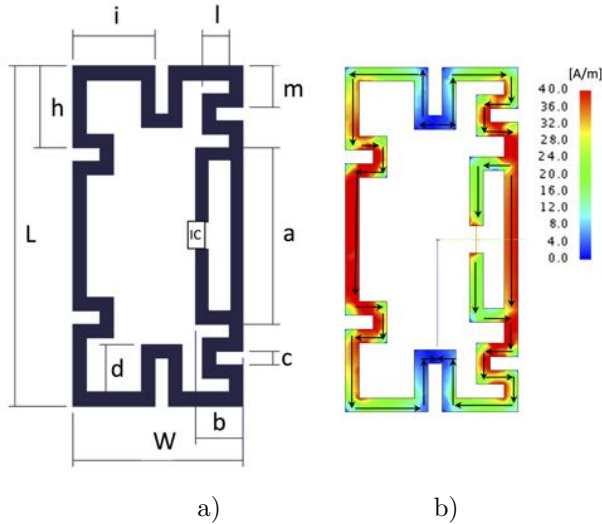
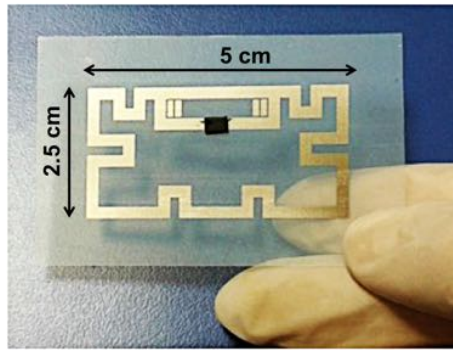


Figure 5.5.: a) Layout of the small-size epidermal RFID sensor with tuning mechanism. Size [mm]: $L=50$, $W=25$, $a=26$ $b=7$, $c=2$, $d=7$, $i=12$, $m=6$, $l=4$, $h=12$. b) Simulated current distribution of the tag placed over a body-like homogeneous planar model. Arrows indicate the current-flow over the antenna.

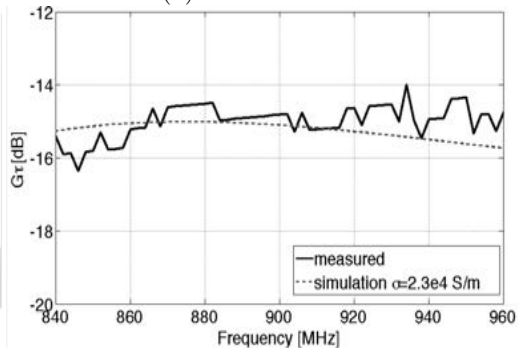
The geometrical parameters of the antenna were then optimized by means of numerical simulations accounting for the estimated conductivity of inkjet-printed traces for the application over a plastic box (PET $\epsilon_r = 2$, $\tan\delta = 0.005$ @1GHz) filled with a liquid mixture mimicking the electromagnetic properties of human tissues

(HSL900V2 by Speag[®], $\epsilon_r = 41.2$, $\sigma=0.95$ S/m).

The printed antenna was connected to the IC by silver-based conductive glue. The performance parameter of the so obtained RFID tag is the realized gain which is directly related to the read range of the sensor. The comparison in Fig. 5.6 between simulated and measured realized gain shows a good agreement in the world-wide RFID band with a local error of less than ± 1 dB, thus confirming the correctness of the estimated conductivity in the UHF band.



(a)



(b)

Figure 5.6.: a) Inkjet-printed meandered-loop epidermal antenna over PET substrate. b) Simulated and measured realized gain (broadside direction) when the tag is attached onto a liquid phantom simulating the human body.

5.3.1. RF Performance versus the trace width

The first experiments involved the manufacturing of the above antenna with traces of reducing width $w = \{1, 0.5, 0.25\}mm$ at the purpose to derive the best compromise between radiation performance (realized gain) and cost (i.e. the amount of used ink). Case by case, the T-match section was slightly readapted to account for impedance changes, mostly the imaginary part, versus the width trace. Despite similar performance (± 1 dB variations) should be expected from simulations regardless of the width of the antenna's traces, the measurements exhibited instead a rather different behavior.

The comparison in Fig. 5.7.a shows that the peak of realized gain slightly decreases (1 dB) when the trace is halved down to 1 mm but it is reduced by 5 dB in the case of 0.5 mm width. For thinner 0.25 mm traces the communication performance is further degraded down to the point where the tag was not readable at all for distance larger than 10 cm. Similar results were found in [86] concerning the sheet resistance measured in DC. As visible in the magnified detail of the 0.25 mm trace (Fig. 5.7.b) several pinholes appears within the traces. As a consequence, when the width is less than 1 mm,

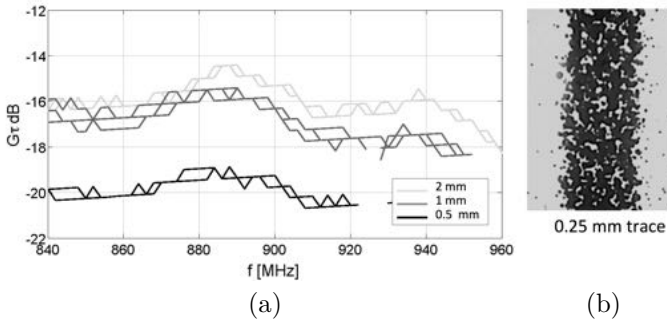


Figure 5.7.: (a) Measured realized gains of the epidermal antennas with different trace width $w = \{2, 1, 0.5, 0.25\}mm$. Performance of two different prototypes for each width, (b) Magnified details (60x) of the 0.25 mm printed trace with pinholes.

there are not enough connected conductive clusters for electric current to flow. The degradation of the radiation performance of the narrower trace tags and the discrepancy with simulation is due to the fact that the estimated conductivity is an “effective” value that accounts for the non-uniform distribution of the silver nanoparticles in the trace, and hence of the presence of discontinuous (low density) zones (holes). When the trace become narrower, the absolute reduction of the contiguous (interconnected) conductive path will strongly degrade the overall effective conductivity of the ink, while the simulation always uses a same constant value. Accordingly, for the considered printing procedure and materials, a 1 mm trace width could be considered as a practical and conservative lower bound.

5.3.2. Overprinting deposition

The conductivity of ink-jet printed conductors improves by increasing the number of the printed layers. Since the desktop printer does not permit to freely control the amount of deposition, the only way to test this effect is to re-load several times the same sheet for a new printing task at the purpose to increase the ink density. Accordingly, the microstructure of the pattern evolves as illustrated in Fig. 5.8. Single-printed layouts are highly porous, then, as additional ink is deposited, the patterned structures densify as the excess silver nanoparticles fill in the underlying pores in a given area. It is worth noticing that the tray-based paper loading mechanisms, which is typical of the low-cost desktop inkjet printers, unavoidably produces misalignments of up to 0.2-0.5 mm when the substrate is re-inserted into the printer distributor (Fig. 5.8). In overall, misalignments produce a widening and blurring of the trace and a local reduction of the effective conductivity close to the edge of the trace. Thus, to profitably apply this procedure, the printed antenna does not have traces smaller than 1 mm, which is coherent with the lower bound defined above. The resulting measured realized gains obtained for $n=\{1,2,3\}$ printing steps are summarized in Tab. 5.3 along with the corresponding conductivity estimated by the same parameter-identification technique similar to that described in sec. 5.2 The peak value of the realized gain

increases by about 1 dB per overprint so that nearly bulk copper conductivity ($\approx 10^7$ S/m) is achieved with just three-fold printing (corresponding to 12 layers of inks). Since the reading range is related to the square root of the tag realized gain, the expected benefit of the threefold printing process is a 25% increase in the range of the antenna.

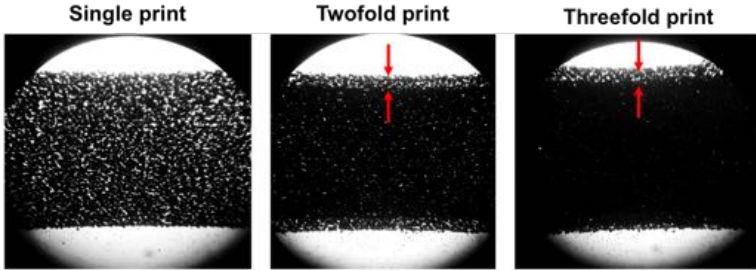


Figure 5.8.: Optical micrographs (60x) of the silver microstructure as a function of the overprinting. Arrows indicate the misalignments caused by manual paper loading during multiple printings.

Table 5.3.: Performance of epidermal Tag vs. number of printings.

	$G\tau_{max}(dB)$
single print (4 layers)	-15
twofold print (8 layers)	-14
threefold print (12 layers)	-13

5.3.3. Resistance to bending

Depending on the attachment region of the body, epidermal tags could be subjected to two different mechanical stresses: *i*) bend around a pin with fixed radius of curvature (movements of elbow,

knee, ankle, and finger joints) and *ii*) flexure around circles with different radii of curvature (movements of spine, shoulder, abdomen, chest and neck), which can potentially damage the inkjet layer by the physical act of compressing and tensioning the conducting surface.

A threefold printed tag was hence subjected to a bending fatigue test by using the set-up described in [87], which consists of a stepper motor driving the central pin of a hinge with 12 mm radius (worst case, small curvature like a finger) (Fig. 5.9). The bending angle was swept from 0° to 180° for up to 2000 cycles at the speed of 12 cycles per minutes. Visual inspection by optical microscope did not reveal any substantial change (micro-cracks/wrinkles/ or permanent folds) in the trace morphology before and after the fatigue test and even the measured realized gain was invariant (See Fig. 5.10).

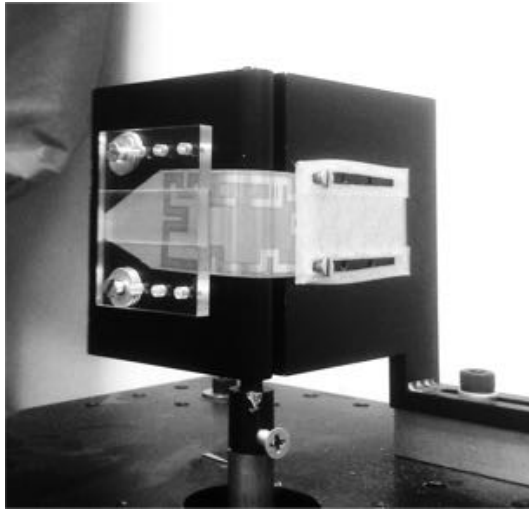


Figure 5.9.: Ink-jet printed antenna mounted over hinge set-up for the bending fatigue test.

5.3.4. Immunity to body fluids

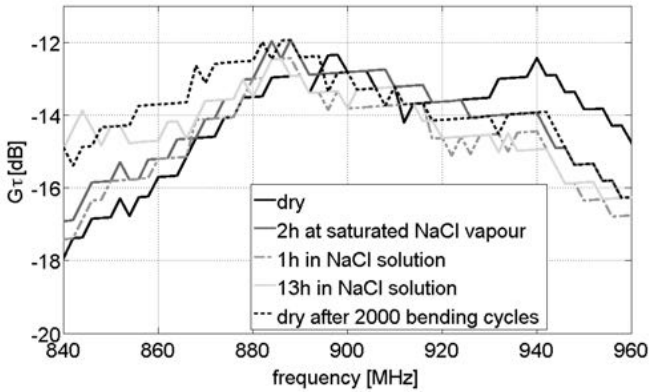


Figure 5.10.: Measured realized gains of a threefold printed epidermal antenna before and after exposure to 100% RH, after immersion in saline solution and after 2000 of bending cycles.

Ink-jet printed layouts conceived for epidermal sensing applications can be exposed to moisture, including perspiration and sweat, especially in the case of printed resistive electrodes which can not be insulated. It is hence crucial to assess the conductance of the considered ink against different levels of exposure to body fluids. A sample of the threefold printed epidermal tag having only the IC connections protected by waterproof film was initially placed inside a plastic chamber partially filled with physiological solution (NaCl 9 gr/l). After closing the box, the water gradually evaporates so that humidity increases from ambient level to saturation (100%) in about 1h. The tag was then left at saturated vapor for two hours and finally characterized in terms of realized gain. In a second test the same tag was fully immersed in the saline solution for 1 and 13 hours. In all the cases, measurements performed after quick drying of the tag revealed that its radiating performance (Fig. 5.10) remained practically unchanged.

5.3.5. Tag coating

The conductivity of silver ink-jet printed layouts tends to degrade along with time in ambient air due to oxidation. A bio-compatible coating layer is hence required for the encapsulation of the antenna. Two possible encapsulations were considered involving a silicon-based organic polymeric paint and a thin commercial polyurethane adhesive film. In both the cases the internal area of the PET substrate was carved out to permit skin transpiration.

Polydimethylsiloxane (PDMS) PDMS is a silicon-based organic polymer, belonging to a group of siloxanes, which has become a very popular substrate for skin electronics since it is highly flexible, stretchable and biocompatible material with very-low dielectric losses and dielectric permittivity approximately equal to 2.7–3.2 at UHF frequencies. The polymer substrate (Sylgard 184 by Dow Corning) was prepared by mixing the two liquid components of the kit provided by the manufacturer - a base pre-polymer and a curing (cross-linking) agent - in a 10:1 mass ratio. Then, degassing was performed for 15-20 min to remove the excessive air bubbles formed during the mixing. Ink-jet printed traces were covered by manually brushing the viscous liquid polymer and then cured at 60°C for 20 mins.

Polyurethane (PU) film dressing The second coating is a medical grade dressing (Rollflex from Master-AID) consisting of an ultra-thin ($25\mu\text{m}$) polyurethane backing with hypoallergenic acrylic adhesive for gently adhesion to the skin. This transparent and extremely flexible membrane acts as semi-permeable breathable film that is occlusive to liquids, bacteria, and viruses while preserving the natural skin transpiration. The membrane can be directly and quickly applied over the tag and does not require any thermal curing. The drawback is the non perfect adherence to surface discontinuities like the chip interconnections.

The response along with time of bare and coated tags is compared in Fig. 5.11. All the prototypes were printed simultaneously, i.e. at the same ambient conditions. The peak gain of the uncoated

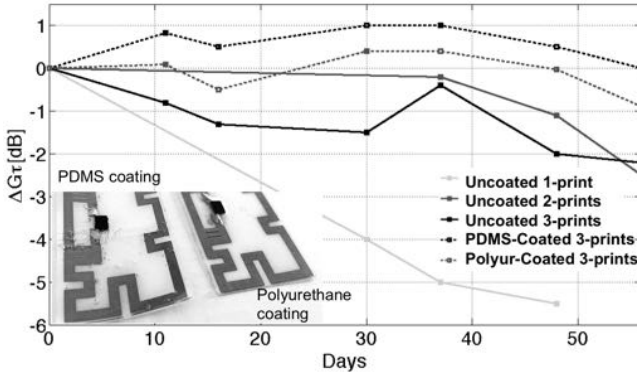


Figure 5.11.: Variation of the maximum realized gain v.s. time of bare tags (single and overprinted) and coated tags with the respect of the initial value (printing time, $t=0$).

single-printed trace severely decreased (-4 dB) after one month, until becoming unreadable two weeks later. Overprinting slows down the degradation ($\Delta G\tau = -2$ dB after two months) as the oxidation process initially involves the most superficial ink layers. Both the polymeric coatings revealed instead adequate to protect the ink ensuring reasonably unaltered tags' gain over the time.

5.4. Comparison with other manufacturing techniques

The performance of the instant inkjet-printed epidermal tags are now evaluated for real on-skin placement and compared with the response of the same layout fabricated with more conventional and assessed manufacturing technologies. *Additive* (microwires) and *subtractive* (digital cutting, photolithography) methods involving different conductors - copper, Ag, Gold - and substrates - biosilicone, PET, polyimide - are considered for the prototyping of the RFID skin-like sensor. Pictures of the corresponding prototypes are shown in Fig. 5.12.

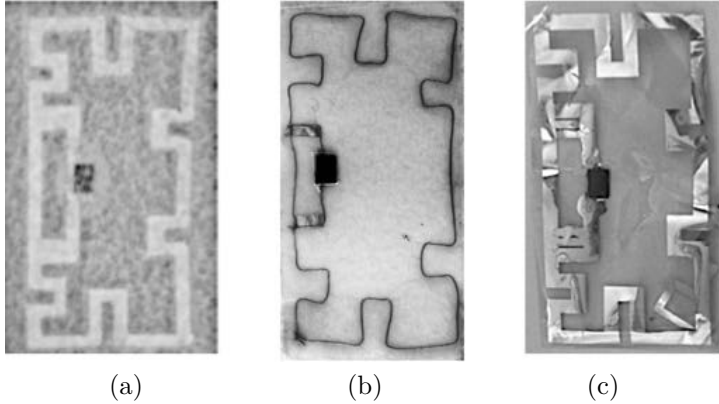


Figure 5.12.: Prototypes of the small-sized epidermal RFID antennas manufactured by (a) carved adhesive copper (b) copper microwire (c) Photolithography process

5.4.1. Carved Adhesive Copper Sheet

A flexible adhesive-backed copper foil (thickness $35\ \mu\text{m}$) was carved by a two-axis digital-controlled cutting plotter. An adhesive tape was temporarily applied on top of the copper sheet to prevent the breaking of the copper traces during the cutting of meanderings. After manually removing the extra copper, the RFID IC was soldered onto the terminals of the matching shorter dipole. The IC-equipped loop was removed from the release liner of the adhesive copper and placed over a $600\ \mu\text{m}$ -thick biosilicone membrane ($\epsilon_r = 2.2$, $\sigma = 5 \cdot 10^{-3}\ \text{S/m}$) by using an adhesive transfer paper-tape which preserved the shape of the cutout metallization during the transfer. The so formed strong copper-silicone bonding made the top transfer layer easy to peel off. Finally a commercial medical adhesive tape (*Soft fix* by PIC Solution[®]) was stuck over the gummy loop to comfortably attach the tag onto the epidermis.

5.4.2. Copper microwires

The epidermal antenna was prototyped by using a 120 μm -radius copper wire. To manually outline the radiator a set of nails were driven in a styrofoam holder in correspondence of each corner of the layout. At first, the wire was turned around the nails to reproduce the shape of the meandered external loop, by taking care that during the profiling the wire get attached to the double-sided adhesive tape stuck on the top surface of the styrofoam (Fig. Fig. 5.13.a). The two extremities of the wire were soldered at one corner. Then, two additional wires were soldered to the chip pads and the IC-equipped T-match transformer was connected to the main radiator (Fig. 5.13.b). After removing the nails, the profiled wire was transferred from the adhesive tape to the biosilicone and covered by a protecting layer (*Soft fix* by PIC Solution®).

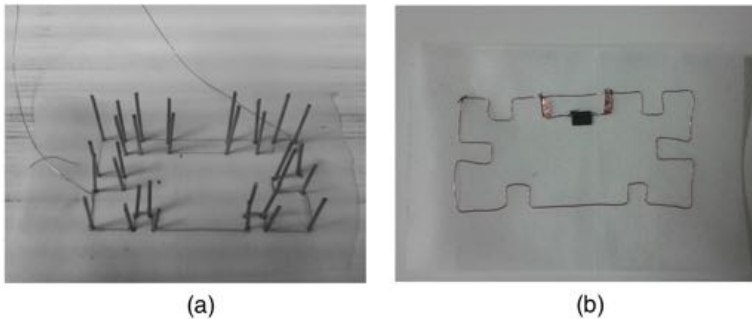


Figure 5.13.: Deposition of copper wires over flexible substrate: a) nails driven in a styrofoam holder at the layout corners; b) outlining of the copper wire around the nails; c) IC- equipped copper wire antenna.

5.4.3. Microfabrication

Microelectronics fabrication represents the current standard for the manufacture of Epidermal Electronics Systems (EES). A prototype of the epidermal radiosensors made of gold on a ultra-thin Poly-

imide (PI) substrate was hence fabricated by cleanroom techniques at the ESIEE Paris. The antenna was processed on a 4" rigid silicon carrier wafer. Aluminum was deposited by Sputtering (cathodic pulverization) as sacrificial layer to permit peeling off the upper PI structure at the end of the process. PI (5-7 μm thickness) was spin-coated over aluminum and dried in oven under N_2 atmosphere at 350 °c during 30 minutes.

Two layers of Ti/W (120 nm) and Au (500 nm) were sequentially deposited by DC magnetron sputtering on the PI-covered silicon wafer. Ti/W acted as transition adhesion layer while the gold, which is a well-know biocompatible and inert material, was used as the functional metallization layer. The metallic layers were then patterned by photolithography (spin-casting of PFR 7790 photoresist for 30s at 3000 tr/min with acceleration 1500 tr/min to achieve 1 μm thickness ; soft baking at 110 °C for 3 min; UV irradiance for 300 mJ/cm² for 7/ sec, PR development for ~45s with pure pure PRD 238t, hard baking at 110 °C for 3 min). The unprotected metallic region were wet etched (ACL2 etchant for gold and H_2O_2 peroxyde water with ultrasound around 1 min for Ti/W). After PR removal with acetone, the Au-patterned polyimide was peeled off from the rigid silicon through the anodic metal dissolution process of aluminum in a concentrated 10 wt% sodium chloride solution and PI released film rinsed in deionized water to remove traces of salt. The RFID IC was finally glued on the resulting antenna by using pick&place equipment and encapsulated by a drop of PDMS polymer to ensure the endurance of the connection. Fig. 5.14 schematically illustrates the main steps of microfabrication.

5.4.4. On-skin performance comparison

The epidermal antennas manufactured as above were placed onto the arm of a volunteer (Fig. 5.15.b), at different times, by means of a 600 μm thick bio-silicone substrate and then fixed with an extremely thin (25 μm) double-sided medical tape (3M™ 1509). The corresponding measured realized gains are shown in Fig. 5.15.c . All the prototypes exhibit similar performance, with the peak value of the realized gain comprised between -15 dB and -11.5 dB and a rather broadband behavior. As expected from the previous

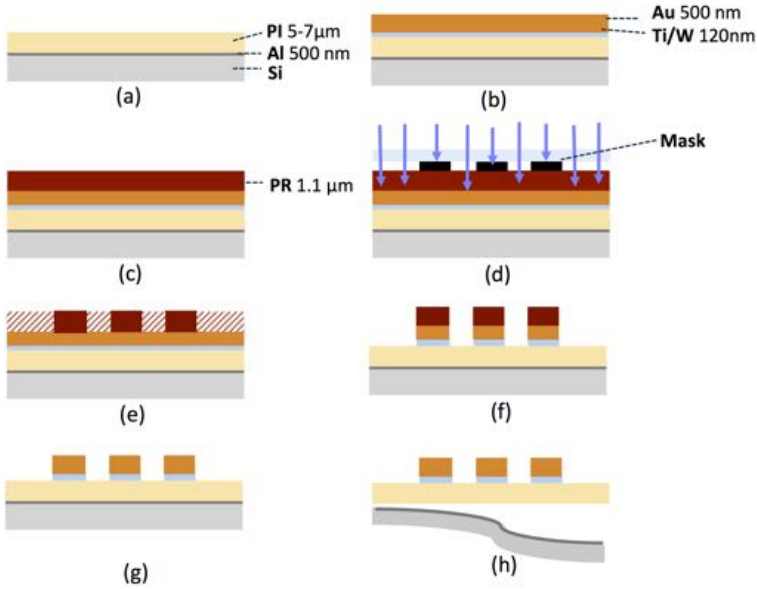


Figure 5.14.: A cross-sectional sketch of the microfabrication process of the RFID epidermal tag: (a) Preparation of silicon-base carrier wafer with Polyimide (PI) coating (b) Deposition of Ti/W and Gold layers by DC Sputtering (c) Spin-Coating of the photoresist (d) UV exposure (e) PR development (f) Wet Etching of the metals in excess (g) PR removing (h) Peeling of the epidermal sensor from the rigid substrate.

investigations over phantoms, the mono-printed antenna returned a gain degradation of about 2-3 dB with respect to the bulk conductor prototypes while instead nearly identical performance was achieved by the threefold printed tag. Accordingly, the maximum achievable reading distance varies with the manufacturing process from 50 cm to 70 cm, when considering very low chip sensitivity for temperature sensing ($P_{chip}=-4.5$ dBm), up to 2 m when considering *state-of-the-art* chip for labeling ($P_{chip}=-22$ dBm).

To identify the most convenient prototyping methods for RFID epi-

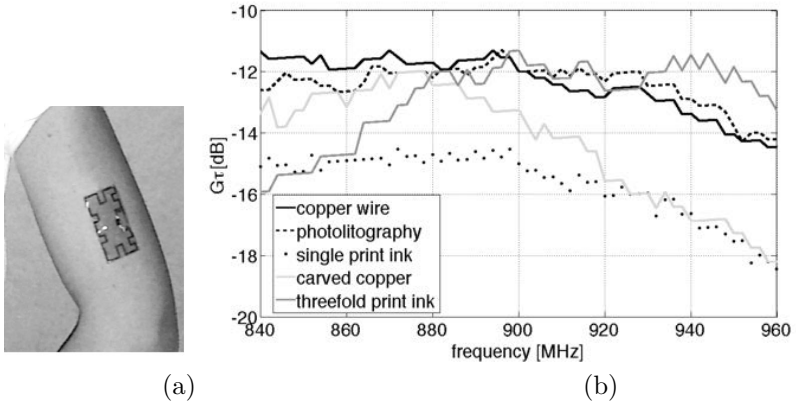


Figure 5.15.: a) Reference antennas made by bulk-conductor fabrication technologies; b) Example of a printed epidermal tag placed onto a volunteer arm. c) Realized gain (broadside direction) vs. frequency.

dermal sensors, the analysis should be completed by elements other than the electromagnetic performance such as processing time, cost, achievable resolution and physical robustness. In general, technologies supporting ‘additive’ approach to production (copper microwire, ink-jet printing) are preferable over ‘subtractive’ cutting and photolithography processes which imply waste of conductors.

Cutting adhesive-backed copper foil is a relatively cheap and versatile method due to the high conductivity of copper and the physical flexibility of the adhesive foil which can be stuck over a wide range of bio-substrates (biosilicone [88], fibrous electrospun polymer [48], hydrogels [56]). However, the achievable resolution for the carved layout is limited by the cutting plotter resolution (which is around 0.5 mm for professional machines) and by the fragility of the copper. Indeed, once the antenna shape has been incised, the elimination of the extra copper becomes a crucial and time-consuming operation as thin traces can break when the material around them is removed, especially in the case of meandered layouts for which lines larger than 1 mm should be preferred.

The deposition of microwires made of electrically conductive material over flexible substrates, which is an already assessed technique for the production of standard low-cost electromagnetic labels, represents a very appealing alternative for the realization of skin sensors. Conductors wires with circular section revealed to outperform planar strips made of the same materials. This inlay-less process is very eco-friendly (no polluting chemicals are used) and offers great versatility in terms of shapes and substates materials. The fabrication procedure can be automatized by adopting patented apparatus for making wire antennas suitable for a large-scale production [89]. These machineries provide limited resolution for meanderings (smoothed corners) which should not represent a prominent issue for epidermal radiators, but has to be nevertheless included in the electromagnetic model of the antenna.

Finally, microfabrication has been also proved effective for the realization of epidermal antennas. The high cost associated with cleanroom facilities, photo masks, photolithography chemicals, and manpower may prevents epidermal sensor from being inexpensive and disposable. The standard microfabrication remains the benchmark approach for high-resolution layouts, for handling the deposition of ultra-thin ($<20 \mu m$) biocompatible substrates and, above all, for the monolithically integrated fabrication of both the radiator and additional flexible electronics components (e.g. piezoelectric sensors [90]) within the same process.

5.5. Discussion and Conclusions

The presented experimentations demonstrated that self-sintering conductive inkjet manufacturing by low-cost printers is a feasible technology for the fabrication of planar antennas suitable to epidermal radiofrequency identification and sensing. The attractive feature of this manufacturing process is the possibility to use low-cost printers without any high-temperature curing. The conductivity of ink in the UHF-RFID band is estimated to be three orders of magnitude lower than that of the bulk copper ($\sigma_{UHF} = 2.2 e4 \text{ S/m}$).

In spite of the few degrees of freedom in controlling the manufac-

turing process, self-sintering ink-jet printing can be easily tuned to achieve epidermal antennas with the same radiation performance of the bulk copper, provided that two over-printings is performed. Nevertheless, suboptimal printing could be still attractive for the quick (few second) and cheap (< 0.10 €) prototyping of intermediate samples, whose characterization represents the feedback for potential re-optimizations and for tests where a modest reduction of the read distance could be acceptable. The printed traces resulted resistant against repeated cycles of bending and to the possible exposure to body fluids, making the antenna compliant with the natural deformation and sweating of the human body. Moreover, the electromagnetic response reveals stable over the time when the printed layouts are coated with biocompatible membranes

The printing resolution is mostly imposed by the quality of the printer nozzle. By accounting also for the effective conductivity of mono-print layouts and for misplacements occurring during the overprinting, the minimum practical size of a trace should be roughly 1 mm. This looks enough for conventional UHF meandered dipole and loop antennas and for the interconnection to strap and TSSOP chip packages. This lower bound could be however inadequate for the fabrication of fine detailed patterns like multi-turn coils and the interconnecting lines of a QFN chip package, as also discussed in [91]. In this last case the chip could be mounted on a peel and stick small flexible PCB made by a process suitable to sub-millimeter details (such as etching or photolithography) and then coupled to the antenna.

Concerning the printing substrate, despite the PET film is an excellent biocompatible medium, additional research is needed to identify other pliable membranes that are intrinsically ink-compatible or to develop ad-hoc surface treatments to make printable any bio-film which can be more comfortably adhere to the human body like a real second skin.

The comparative analysis of viable fabrication options for RFID epidermal antennas revealed that similar electromagnetic performance can be achieved with the described technologies. Case by case, cost, processing time, physical robustness and need of monolithic integration with other sensors suggest the most appropriate manufacturing choice.

6

An Epidermal RFID Thermometer for remote skin temperature monitoring

This chapter describes a real epidermal RFID thermometer consisting of a flexible small-size antenna and sensing microchip. The transponder can work in passive mode as well as in battery-assisted configuration for improved read ranges. Electromagnetic and thermal performance are experimentally characterized to get clinically relevant measurements of the skin temperature.

The previous chapters investigated the electromagnetic performance of epidermal antennas from the basics, analyzing the optimal size/shape of radiators closed to lossy skin, the effect of human variability and then experimenting suitable bio-membranes and manufacturing technologies. Having treasured the presented findings, the first part of the thesis ends up with the description of a real epidermal RFID transponder suitable for the skin temperature measurement.

The knowledge of the surface temperature of the human body is indeed a powerful tool to detect and even foresee diseases or altered health conditions. Increased local skin temperature is a classic sign of wound infection, repetitive trauma, and deep inflammation which can be used as early predictor of chronicity before apparent changes of the injured tissues are observed [92, 93]. The

occurrence of sleepiness/wakefulness cycles are closely related to the circadian variations of skin temperature which show anomalous trends in subjects affected by sleeping disorders (insomnia, narcolepsy) [94]. Skin-surface temperature measurements are usually performed throughout perioperative procedures to assess the thermoregulatory effects of anesthetic drugs and prevent hypothermia during surgery. Possible fields of applications of cutaneous temperature monitoring extend to sport medicine, concerning the evaluation of athletes' performance [95], and to occupational medicine for the assessment of stressful conditions of workers in harsh environments. Furthermore, the dermal temperature collected on "central" sites (forehead, axilla, abdomen, chest) and under controlled ambient conditions provides a non-invasive approximate estimate of core temperature.

Conventional techniques for the measurement of surface body temperature generally involve *i*) manual procedures by either contacting devices (tympanic and glass thermometers) or non-contacting devices (infrared or radiometric receivers) or instead *ii*) automatic detection protocols generally based onto wired sensors (thermocouples and thermo-resistances) attached over the skin and connected to a fixed acquisition system [96, 97]. Manual procedures permit only sporadic measurements which cause constant disturbance to the patients and increase the nursing workload. Automatic systems are instead capable of providing a continuous real-time monitoring at the price of reduced user's mobility due to the tangled wired interconnections. Contact-less instruments like thermal camera scanners, although suitable to remotely scan at once a large number of subjects, have some serious limitations concerning the un-adequate accuracy (around 2°C), the mandatory Line Of Sight to the target body and the strong sensitivity to the variable environmental parameters and to the skin conditions (sweat, cosmetics, topical treatments) that alter the radiant characteristics (emissivity) of the body.

Recent developments in wireless thermometry offer viable alternatives that are based on battery-equipped small sensors with data-logging features (i-button [98]) or even capable of real-time data sampling and remote transmission through wireless interfaces [99, 100, 101]. Autonomy, size and costs are main issues limiting a true

diffusion of these kinds of body-centric devices. Innovative solutions may hence originate from the epidermal RFID devices.

In a recent paper [48] the author introduced and qualitatively demonstrated a possible application of the epidermal tag (chapter 3) to the on-skin measurement during cycle exercise. So far, research efforts have been devoted to model and master the electromagnetic response of the device as an antenna, with care to retune its response to the remote interrogation depending on the specific placements over the body and on the operating RFID band. Many issues are still open to turn the proposed epidermal device into a reliable temperature sensors providing continuous temperature measurements with clinical meaning since no information is currently available about the sensor accuracy and reliability in real physio/pathologic conditions.

This chapter presents an evolution of the concept of epidermal wireless temperature sensor with the goal of qualifying the achievable thermal performance in realistic operative conditions. The small-size epidermal RFID layout described in sec. 5.3 is slightly adapted to include tuning mechanism and possibly embed a small battery for improved performance. The fabrication processes was improved to permit the reuse of part of the sensor for multiple applications, thus reducing fabrications costs and pollution. The experimental characterization of the accuracy and the time response of the thermal IC sensor is then addressed in sec. 6.2.

6.1. Reusable and Sterile Epidermal thermometer

Fig. 6.1 shows the proposed sensors-tag in the form of a $2.5 \times 5 \text{ cm}^2$ rectangular meandered loop radiating like two C-dipoles. The tag was connected to the EM4325 IC which includes a standard RFID transponder and provides temperature measurement in the range -40°C to $+64^\circ\text{C}$ with a resolution of $\pm 0.25^\circ\text{C}$. The chip can be used in both battery-less mode (input impedance $Z_{in} = 23.3 - j145\Omega$ and power sensitivity $P_C = -4.5 \text{ dBmW}$) as well as in battery-assisted mode ($Z_{in} = -18.1 - j169\Omega$, P_C programmable down to -31 dBmW)

to significantly improve the read range. The inclusion of the battery requires two insulation inductors ($L_i=120nH$) to prevent the RF currents induced onto the battery-traces from entering the DC pin of the chip with consequent changes in the IC impedance and sensitivity and, more in general, an overall failure of the device.

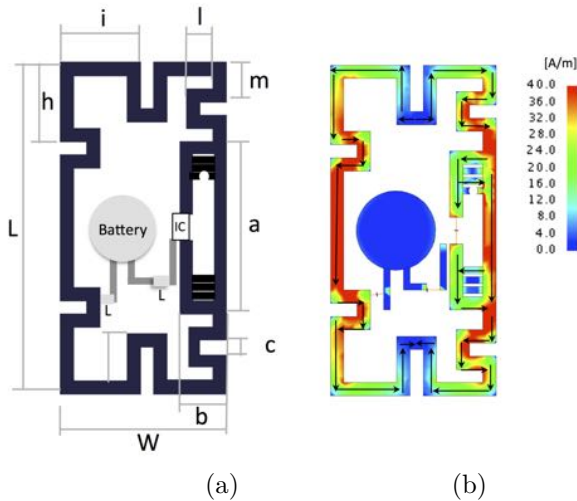


Figure 6.1.: a) Layout of the miniaturized epidermal RFID sensor with tuning mechanism. The gray components are included in the Battery-assisted configuration. The IC and chock inductances ($L_i=120nH$) are simulated as discrete lumped elements and the battery as a metallic cylinder (radius 6mm, thickness 2mm) b) Simulated current distribution of the tag placed over a body-like homogeneous planar model. Arrows indicate the current-flow over the antenna. Size [mm]: $L=50$, $W=25$, $a=26$, $b=7$, $c=2$, $d=7$, $i=12$, $m=6$, $l=4$, $h=12$.

The antenna is provided with a post-fabrication tuning mechanism to optimally adapt its response to the specific placements over the body and to freely shift the working frequency in the European (866-869 MHz) or US (902-928 MHz) RFID bands, similarly to what described in chapter 3. At this purpose, the T-match sec-

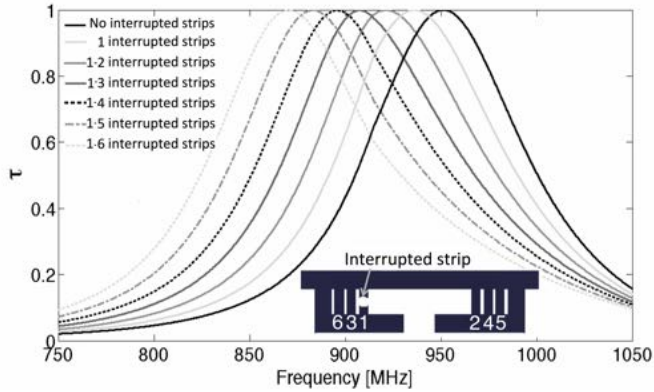


Figure 6.2.: Simulated power transmission coefficient of the epidermal tag in passive mode which is tuned by modifying the size of the inner perimeter of the T match through interruption of the strips inside the T-match (magnified detail in the inset).

tion includes thin strips that can be progressively interrupted, for instance by a simple hole-puncher, in order to modify the current paths over the T-match and, accordingly, the impedance transformation ratio. As a consequence, the power transfer coefficient (τ) of the antenna can be shifted with a resolution of 12 MHz/strip for the chip in passive mode (Fig. 6.2). The same layout can be easily matched at 868 MHz to the IC impedance in BAP mode by adopting the configuration with four interrupted strips.

6.1.1. Prototypes

The fabrication process of the epidermal thermometer was optimized to account for some practical issues:

i) the use of low-cost biocompatible materials commonly used in clinical practice; *ii)* hygiene concerns as the device is placed at direct contact with the skin; *iii)* the possibility to retrieve and reuse the sensor at the end of the monitoring session; *iv)* ensuring the direct contact of the sensing element, the IC, to the skin surface to not alter the temperature measurement.

The sensors were prototyped by attaching a flexible adhesive-backed copper foil on PET sheet ($135\mu\text{m}$ thickness) and carving the meandered loop out of the layered sheet (Cu-Pet) through a digital plotter. Then the IC was soldered onto the terminals of the matching shorter dipole. In the case of the BAP tag, the battery (3.2 V Lithium with solder pins) and the choke inductors were also connected at this stage. The loop was enclosed between two layers of a medical-grade adhesive dressings (Fixomull® stretch, $220\mu\text{m}$ thickness) to comfortably attach the tag over the epidermis.

An intermediate medical gauze was preliminary placed between the antenna (Whitetex Merilin®, $200\mu\text{m}$ thickness) and the upper dressing to prevent the adhesion of the copper traces to adhesive film. A hole was carved out of the dressing underneath the IC to ensure the direct contact between the temperature sensors and the skin, so that the thermal resistance of the substrate doesn't affect the local sampling of the temperature. The IC was then insulated by a small patch of ultra-thin biocompatible film (Rollflex film from Master-AID®, $22\mu\text{m}$ thickness) for hygiene reasons. This layer was proved not to delay the thermal time response of the tag (see sec. 6.2.2).

The layered structure of the epidermal thermometer is schematized in Fig. 6.3. The resulting modular device (total thickness $< 800\mu\text{m}$) is sterile and features two detachable components (Fig. 6.4): a reusable inner part that carries electronics elements (the antenna, the IC and the optional battery) and disposable dressings that encapsulate the sensor and fix it to the skin surface. It is worth noticing that the reusable core sensor can be fabricated by adopting any of the manufacturing processes described in chapter 6. A prototype of the battery-assisted sensor is shown in Fig. 6.5.

The communication performances of the prototypes were characterized through the measurement of the realized gain of the tags over a liquid body phantom (HSL900V2 from Speag®). The maximum realized gain (Fig. 6.6) is of the order of -13dB . The measurement outcomes¹ are compared for corroboration with numerical MOM-based simulations (FEKO solver [54]), which considered the epi-

¹The measurement of the gain for the BAP sensor was restricted to the only European RFID frequency band due to the reader limitations to interact with a chip set in active mode.

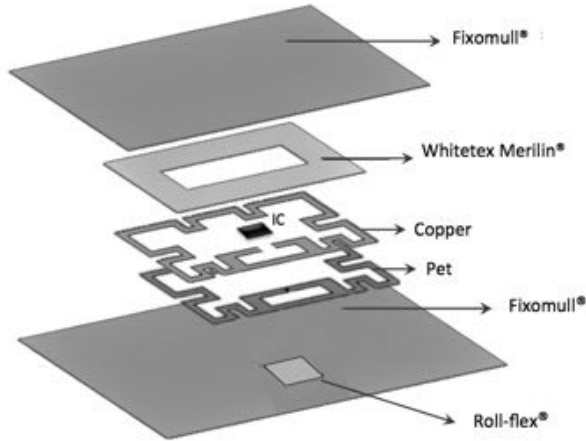


Figure 6.3.: Sketch of the various layers of the reusable epidermal RFID thermometer.

dermal antenna as planar. As the smallest dimension of the sensor is quite reduced (25mm), the performance of the antenna is not expected to be altered by the natural curvature of body surfaces. Typical bend radii of limbs are indeed in the range 30-80 mm, while other region such as torso, abdomen, forehead can be conveniently assumed as flat. A good agreement was achieved, especially within the european RFID band centered at 868 MHz, where the antennas are optimally tuned. Some discrepancies are observed in the case of the battery-assisted version because of uncertainties due to the manual soldering of the coin battery and the inductors on the antenna that were not accounted by the numerical simulation. The measured antenna response is quite broadband (3dB bandwidth of 60 MHz) because of high loss of the human tissues. Possible detuning effects induced by the specific placement over the body (chapter 3) can be easily compensated by means of the tuning mechanism described before.

By assuming a free-space like interaction between the sensors and

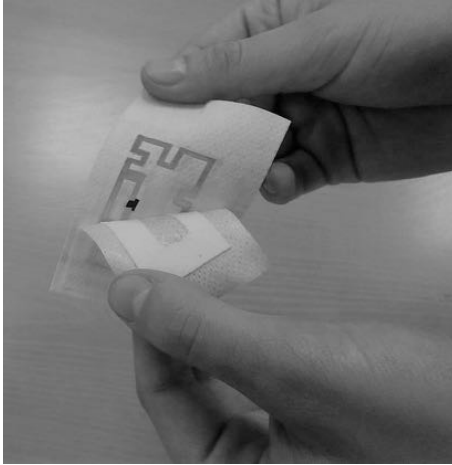


Figure 6.4.: Sterile and reusable battery-less epidermal thermometer made of disposable dressings and a reusable inner transponder.

a reader with $P_R=-75\text{dBmW}$ sensitivity and emitting 3.2 W EIRP (the maximum allowed according to the EU regulations), the battery-less prototype will be readable up to 0.70 m (forward-link limited), while the battery-assisted model will be reachable up to 2.3 m (backward link limited).

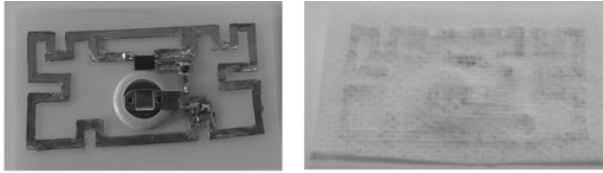


Figure 6.5.: Bare and Covered prototypes of the battery-assisted epidermal thermometer.

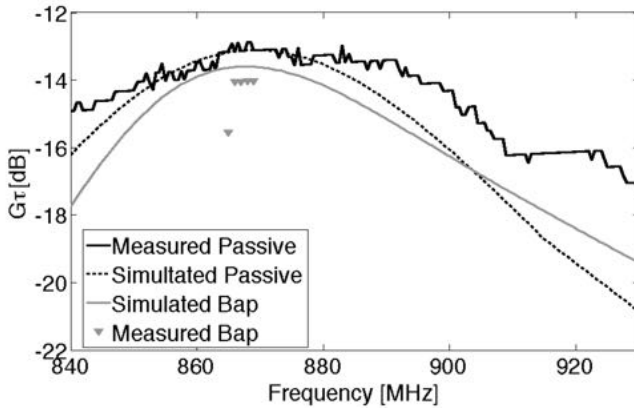


Figure 6.6.: Measured and simulated realized gain of the passive and battery-assisted epidermal sensors placed over a liquid phantom..

6.2. Thermal Characterization

The EM4325 sensor chip comes by default with a single-point on-wafer calibration at $+5.0^{\circ}\text{C}$. The manufacturer declares a mean accuracy of $\pm 1.0^{\circ}\text{C}$ (max $\pm 2.0^{\circ}\text{C}$) over the whole temperature range and $\pm 0.6^{\circ}\text{C}$ (max $\pm 1.5^{\circ}\text{C}$) over the typical range for cold chain $-1^{\circ}\text{C} < T < 12^{\circ}\text{C}$. The sensor accuracy for the skin temperature monitoring can be nevertheless improved by re-calibrating the chip when it is embedded into the epidermal antenna, within the temperature range of interest for biomedical applications, e.g. from $+5^{\circ}\text{C}$ (post-mortem temperature) up to 45°C (severe feverish state). The accuracy of the RFID epidermal thermometer was determined by using a water bath and a reference thermometer. A calibration function is accordingly derived to correct the sensor outcomes. An impulsive method was then applied to extract the time response of the epidermal thermometer.

6.2.1. Sensor Calibration

The accuracy of the EM4325 IC integrated into the epidermal antenna was estimated by stationary measurements within a calibration bath providing a very stable and uniform temperature environment. Stability refers to a temperature remaining constant over time, while uniformity refers to the spatial distribution (vertically and horizontally) of the temperature throughout the calibration bath. The experimental setup (Fig. 6.7) comprised: *i*) a closed-circuit liquid bath where the epidermal thermometer was immersed together with a reference temperature probe (calibrated certified Platinum Thermo-resistance, PTR25); *ii*) a thermostat (JULABO, MW-F33) for the control and the regulation of the temperature of the liquid consisting of a mixture of 33% of distilled water and 66% of ethylene glycol; *iii*) high-resolution DAS, (data acquisition system, Keithley 2700) connected to the PRT25 terminals (4-wires measurements); *iv*) compact RFID reader (R1270 - Quark Up from CAENRFID) for the wireless reading of the temperature data from the epidermal sensor with a data-rate of 5 samples/sec.

The epidermal sensor was glued over the sensitive part of the PTR and then inserted at the bottom of the concentric cylindrical glass

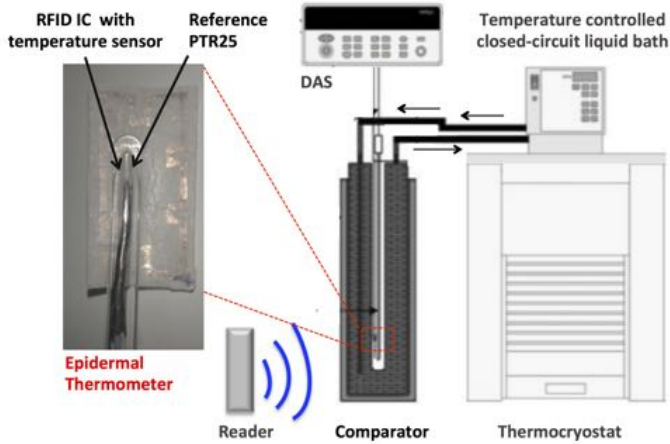


Figure 6.7.: Experimental set up for the stationary measurements of the accuracy of the epidermal RFID thermometer inside a calibration water bath.

comparator by means of a glass rod properly insulated by wadding to minimize convective heat flux due to the vertical temperature gradient. The entire comparator was then covered by an insulating layer of fiberglass to further minimize thermal dispersion. The reader interrogated the sensor from a distance of 10 cm outside the chamber.

The temperature of the water bath was gradually increased from -5°C to 60°C by 5°C steps. For each temperature level, after the thermal equilibrium between the circulating fluid and the thermal sensors was established, stable (plateau) measurements were collected by both sensors for 15 minutes at the purpose to gather enough data for statistical analysis and to verify the absence of thermal drifts. Four epidermal sensors were tested in independent measurement sessions.

The mean error between the temperature of the ICs and that of the reference PTR (ΔT in Fig. 6.8) resulted dependent on the specific chip and spans in the range $0.35^{\circ}\text{C} < \Delta T < 0.85^{\circ}\text{C}$. Such random differences in the mean error are likely due to the fact the

ICs are coarsely calibrated during the mass production of low-cost sensors. The standard deviation is instead rather small for all the chips ($\sigma < 0.13$ °C) and it is lower than the resolution (± 0.25 °C). Each epidermal thermometer should be therefore individually recalibrated, but a few-points (at least two-points) calibration is sufficient. After uniform recalibration, the total uncertainty of the sensors evaluated following the ISO-GUM [102] is 0.18°C, which is hence much lower than that declared by the manufacturer and fully comparable with *state-of-the art* skin temperature sensors [103]. The calibration offset can be written into the microchip memory for an easy use by the interrogating reader.

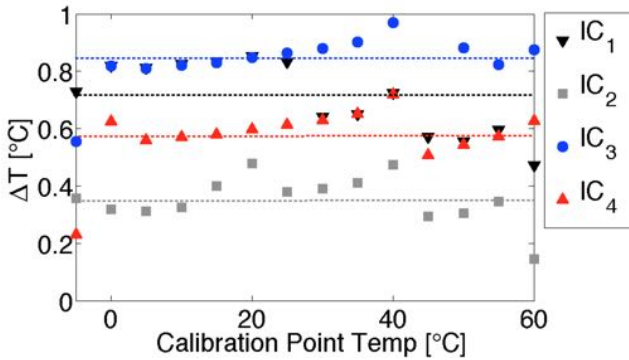


Figure 6.8.: Multi-Point Calibration: mean error between the IC and the reference PTR at the thermal equilibrium.

6.2.2. Time Response

The time response of the epidermal sensor depends on the heat capacity and the conductivity of the human body and on the hosting substrate (thickness and thermal resistance) inter-placed between the IC and the skin. The time constant (τ) of the sensor was estimated from its response to a power pulse emitted by a 1.5 kW flash which produced an impulsive-like heating of the IC [104]. Then, the τ value was retrieved by the non-linear least square regression of the cooling response following the pulse ($T \simeq a_1 + a_2 \cdot e^{-t/\tau}$). Three

different configurations (in air, over a plastic box filled with a liquid phantom and over the human arm) were considered. The time constants, averaged over 15 flashes, and the corresponding standard deviations are reported in Fig. 6.9 together with an example of the processed signals and the corresponding fitted curves. In all the experiments the IC was insulated by ultra-thin biocompatible film (22 μm Rollflex film from Master-AID[®]). When the sensor is applied over the human arm, the shortest response is achieved ($\tau \simeq 4$ s) as the thermal conductivity of the human body is one order of magnitude higher than that of the air [105, 106]. By assuming a conservative reference value the time constant of the liquid phantom ($\tau = 6$ s) and by considering that the time required to damp the thermal transient is $5 \cdot \tau$, the proposed sensor will provide a stable temperature data after less than 30 seconds from the placement onto the body. For the sake of a comparison, the iButton [98] would need 95 s to give a stable temperature. The low value of the time constant is finally compatible with the physio/pathological time variations of skin temperature even in the case of fever rush or rapid hypothermia and rewarming during cardiac surgery.

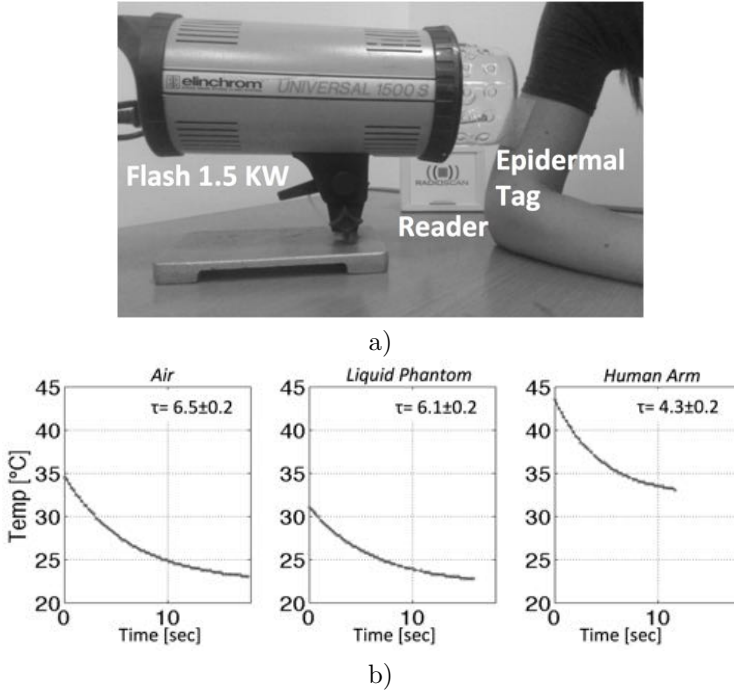


Figure 6.9.: (a) Set-up for the *flash-method*. (b) Example of thermal Response of epidermal sensor to the power pulse (measured signals and fitted curves) when it is placed in air, attached over a liquid simulating the body phantom and over the human arm. Mean values and standard deviation of time constants as computed over 15 flashes are also reported in the insets.

6.3. Conclusions

A small-size epidermal RFID thermometer suitable for the direct placement over the skin has been described. After uniform recalibration, the accuracy of the IC sensor satisfies the target value for standard thermometers (ear 0.2°C, underarm 0.5°C). The proposed epidermal sensor gives stable temperature readings as long as it is properly attached to the skin and it is given sufficient time to warm up ($\simeq 20$ seconds), provided that the surroundings of the sensor are not subjected to any localized heat or cold. In battery-mode, the epidermal sensor may last up to three years that is comparable with the lifespan of a digital thermometer for personal use. When compared with thermo-cameras, the epidermal wireless thermometer provide substantial advantages in terms of accuracy, robust reading also in Non-Line-Of-Sight conditions (through clothes and moderate obstacle), expected lower cost of the overall system and the capability of univocally identifying the users while scanning.

The capability of wirelessly reading the sensor up to distance of 0.7 m (battery-less mode) and 2.3 m (battery-assisted mode), and its potential low-cost (a single electronic component is required in the simplest configuration) appear very promising for the forthcoming integration of such skin-mounted transponders in the context of IoT-based architectures. The feasibility of using the epidermal thermometer in a wide range of both supervised and un-supervised applications for healthcare and security will be extensively discussed though experimental tests in the second part of the Thesis (chapter 7).

II

From devices to IoT Pervasive Monitoring Systems

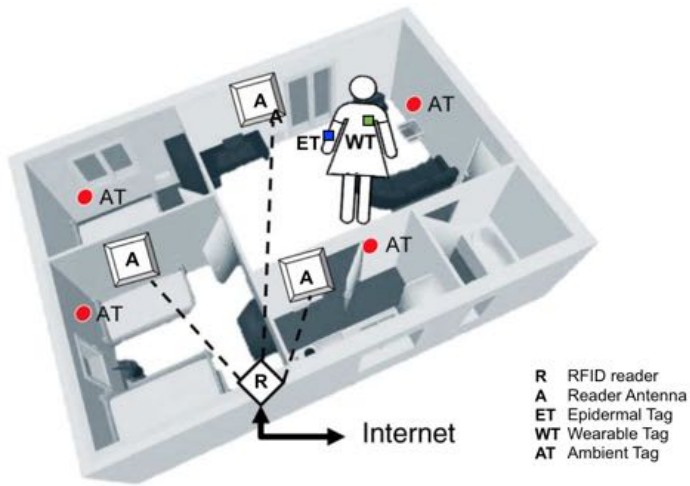
Moving from the research on epidermal hardware, the thesis shifts now the focus to the architectural level, getting into the system aspects of a real wireless sensor network. The second part is devoted to the development of a multi-level RFID platform for care delivery and remote assistance in various health-related settings - including acute (in-hospital), long-term (nursing homes, hospices) or and community-based (in-home, schools, airports...).

Indeed, innovative healthcare programs call for decentralized, pervasive and patient-centric methodologies [107] to fulfill the compelling needs of the modern societies of delivering affordable medical assistance to anybody, everywhere and at anytime. The rise in life expectancy and the consequent progressive aging of the population, with a prevalence of chronic diseases, triggers a careful thought about novel means of providing care to people aimed at ensuring a decent quality of life, without imposing traumatic changes of habits and living environment, while saving the global sanitary costs. In this context, ambient Intelligence architectures [108], where people are empowered through a digital environment that is aware of their presence and responsive to their activities, have the great potential to put in place personal health systems [109, 110, 111] hosting new interconnections between the natural habitat of the persons, their body and the Internet.

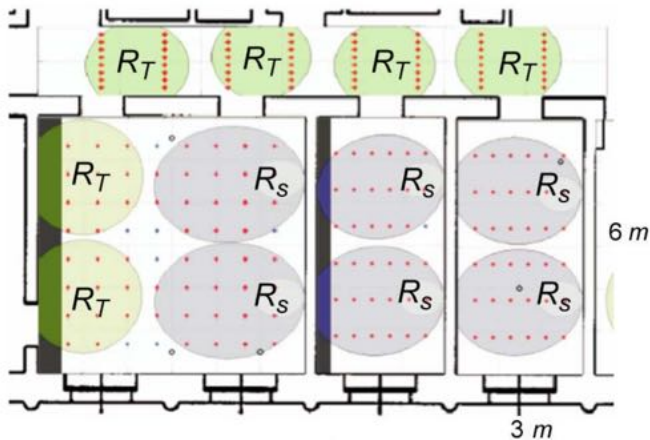
Throughout the following study, the reference scenario will be a RFID-powered environment (Fig. 6.10) that is invested with the responsibility of discretely sampling the health state of its inhabitants in order to compile statistics for preventive diagnostics, identify precursors of altered conditions and, accordingly, activate alarms for prompt assistive procedures.

The space to be monitored - here a *Smart House* - is equipped with a network of readers and interrogating antennas distributed in the most relevant areas that interact with a multiplicity of heterogeneous tags according to a single-to-multipoint link. The readers communicate via WIFI, Bluetooth or ethernet links with a centralized gateway that handles the continuous streaming of the data towards external servers performing on-line analysis.

Within the EM field radiated by a such a infrastructure, the presence of a subject interacting with the surrounding habitat brings



(a)



(b)

Figure 6.10.: a) Sketch of an RFID-powered habitat with Ambient tags (AT) attached over the walls and objects, Wearable tags (WT) and Epidermal tags (ET) placed over the garments or the human skin, one or more reader antenna (A) scanning the rooms and a wireless Concentrator (R) capable to pack the collected data for in-house processing and/or for internet streaming. b) Example of RFID coverage [112] of a home-portion by a multiplicity of readers' antennas placed at the walls' side (R_S) and over the top ceiling (R_T).

precious information about behavioral and physical parameters related to the personal health. Indeed, the response of ambient tags dispersed over the walls and the furnitures is strongly disturbed by the scattering and the shadowing effects caused by the human body when it moves in the close proximity [113]. To give an example, Fig. 6.11 shows the power backscattered by passive tags aligned on a corridor wall and received by an opposite reader when a man walks forward and backward at different speeds. By processing the envelope of the signal nulls, it is possible not only to infer the presence of the person in the corridor but also analyze its walk capabilities (the velocity, the direction, passages rate...) that can be linked to the course of several cardiovascular and neural pathologies.

Even more complex information can be gathered by collecting also signals from on-body tag (wearable and epidermal), such to simultaneously identify and track multiple subjects and detected specific activities. Indeed, typical backscattered traces from body-worn tag are subjected to a movement-dependent modulation Fig. 6.12 to be processed by algorithms leveraged from the Machine Learning background [114] for classifying body gestures and motion patterns [115].

On the whole, all the *analog signals* from ambient and wearable transponders define an electromagnetic fingerprint of the environment, whose measurable perturbation with the respect to a reference condition can be detected and analyzed from the system to retrieve high-level macroscopic behavioral data and discrete events.

The number of the collected radio-channels can be further increased by including *digital signal* from the programmable electronic-packed digital tags [40, 39] able to sample multiple physical parameters (temperature, light, humidity, strain...).

The novel class of epidermal device, which is the kernel of this thesis, is now framed within the IoT architectures in combination with more assessed wearable and ambient tags. The read ranges achievable nowadays by bio-integrated sensors are nevertheless only partly compatible with a true remote monitoring, due to low radiation efficiency of the skin antennas and the high-power demand of ICs with sensing capabilities. Epidermal tags that monitor target bio-parameters like the skin temperature are suitable for interro-

gation by fixed scanner at moderate distances, e.g. a gate, or by manual hand-held device. In the near future, the expected progress in the microchip transponder technology (3 dB reduction in the chip sensitivity each 1–2 years) will permit to implement body-centric communications entirely based on seamless devices. For the time being, conventional patch-like wearable tag are still used for the reliable indoor people’s identification and tracking because of the superior communication performance (5-10m).

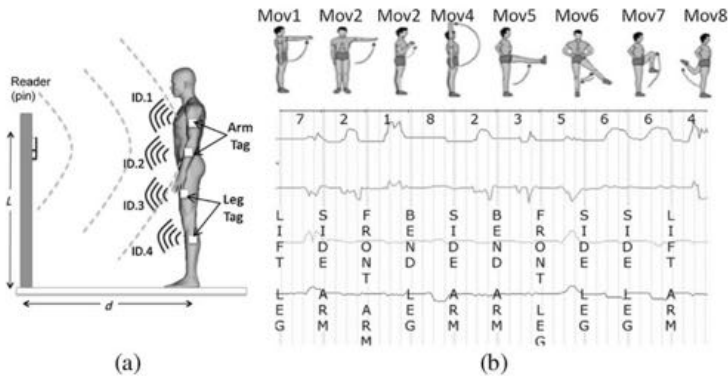


Figure 6.12.: . (a) Set-up as in [115] for the classification of limbs’ gestures by passive RFID (b) Examples of RFID backscattered patterns to be classified by the Support Vector Machine (SVM) algorithm performing data mining.

The simplicity and the poor computational capabilities of battery-free transponders are key points for the capillary distribution of wireless probes within the environment, but pose intrinsic limitations to the level of intelligence each sensor node is provided with. High-level knowledge about people’s actions as well as the occurrence of dangerous situations can be hence inferred only through the combined processing of multi-channel signals gathered from a multitude of transponders, which, not singularly, but collectively convey precious information. As a consequence, most of the reasoning functions are delegated to the reader side where a middle-

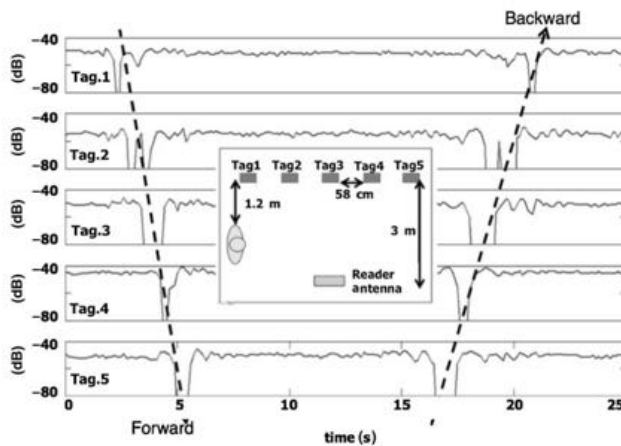


Figure 6.11.: Backscattered power variation from a linear cluster of tags attached on the wall during the walk of a subject along the corridor. The sequence of the nulls carries information about the direction of motion (delays among nulls) and velocity (slope of the enveloping line through the nulls).

ware implementing data-mining and event detection algorithms is required to convert raw signals into meaningful data.

A RFID Sensing Network (RFID-SN) like the one sketched in Fig. 6.10 can be described through the following formalism. The entire system is organized as a multi-level hierarchical structure suitable to achieve spatial selectivity and sensing selectivity (Fig. 6.13). From a logical side, the *space* under observation is partitioned into M *zones*. Each zone includes N_m *things* of interest (persons or objects) and the nm -th thing has K_{nm} *attributes*, i.e. some physical parameters to be monitored along with the time. The proper processing of singular or combined K_{nm} attributes led to the definition of an *event*, e.g any occurrence that is relevant for the monitoring infrastructure. This scheme is physically implemented by considering a multi-channel interrogation module, the RFID reader, connected via coaxial cables to transmitting/receiving antennas (A_m), which interrogates the different RFID sensors tags (T_{nm}) properly dispersed into the environment. The electromagnetic coverage of each antenna, which depends on the antenna gain, the radiated power and the interaction of the electromagnetic field with the nearby environment [112][116], defines the extension of a *zone*. The RFID sensor tags, either analog or digital, identify the *things* to be monitored and integrate one or more sensing mechanisms generating the K_{nm} attributes of the thing itself. The number of the independent channels C (each channel being a sensor signal coming from a tag) produced by this architecture, e.g. the number of signals $\{S_{knm}\}$ collected by the reader node, is hence

$$C = \sum_{m=1}^M \sum_{n=1}^{N_m} K_{nm} \quad (6.1)$$

The reader unit interacts with the sensors in time-division according to a dynamic strategy allowing a periodic activation of all the beams to control the whole space volume, or, alternatively, trigger a reduced set of reader antennas at the purpose to control a subregion of the environment with a higher data-rate. A remote handling of the power is moreover possible, e.g. the power emitted from the reader and even from the single interrogating antenna can

be modified at runtime to properly shape the extension of the zones and focus the available resources on the most critical areas where abnormal events have been detected. The reader node is fully managed by a Control & Command software living into the reader unit itself or into a remote system. Readers of different zones may be connected through Ethernet/WiFi links to an higher-level network, whose description is however out of the scope of this thesis.

This architecture offers a great freedom in the onsite physical reconfigurability (addition, repositioning and dismantling of sensors) and, accordingly, in the space granularity of the surveillance. An important issue concerns how the system complexity scales with respect to the size of the space under observation. The number of interrogating antennas, and hence of the cables, increases only linearly with the volume of the space to monitor, while it is independent of the number of things in each zone. Most of off-the-shelf RFID readers are provided with multiple antenna ports (up to four) and an even larger number of antennas could be addressed by using an electronic-controlled switch so that large infrastructures (nursing home, hospital yard...) can be monitored by a reduced number of centralized nodes.

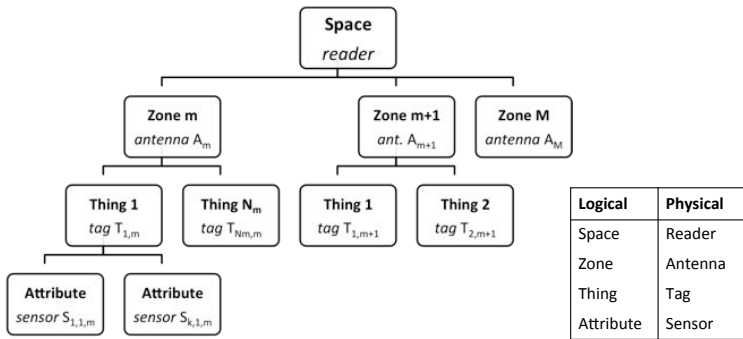


Figure 6.13.: Schematic multi-level architecture of the RFID Sensor Network.

The following chapters introduce growing complexity RFID platforms that exploit the human interactions with the nearby environment at different levels. Multi-fold issues are addressed in details:

1. the deployment of sensor network integrating different types of radio-transponders specifically conceived for various placements and sensing purposes;
2. the quantitative analysis of the reliability of the radio-link;
3. the development of control software framework for the remote and dynamic handling the network topology and the data acquisition;
4. the processing of low-level analog and digital electromagnetic signals for data-mining.

The presented applications are referred to a unitary modular and scalable ecosystem (Fig. 6.13) offering multiple and diversified health-care services, such as the remote assistance to pediatric, elderly and impaired patients, the supervision of chronic diseases, the management of private health and wellbeing and, not last, the people's security in critical infrastructure.

The first example concerns the monitoring of a single physiological parameter by means of epidermal sensors. The epidermal RFID thermometer resulting from the scientific and technological research conducted in the previous part (chapter 6), is experimented in real-life conditions involving supervised and automatic screening procedures (chapter 7).

The case-study in chapter 8 focuses on a multi-parameter body-centric system aimed at the unobtrusive monitoring and diagnostic of the sleeping behaviors.

Finally, a multi-level reconfigurable network capable of capturing advanced human-things interactions is implemented for the control of critical settings (e.g. operating theater, intensive care...) where it is essential to ensure controlled ambient conditions and detect and even prevent unauthorized access and possible cyber/physical tampering of crucial equipments (chapter 9).

All the volunteers engaged in the experiments were properly informed about the purpose of the study and signed an informed consent before participation.

Real-Life Temperature Monitoring by Epidermal RFID sensors

This chapter describes the application of skin-mounted RFID devices suitable for surface body temperature measurements in realistic settings (home, hospital, airport...).

The clinical relevance of the knowledge of the body surface temperature has been highlighted in chapter 6. The potentials of the developed epidermal RFID thermometer are now demonstrated in real-life conditions by the help of two classes of experiments involving *i*) a manual (supervised) reading of the temperature and *ii*) an automatic (un-supervised) reading with no human effort in both *continuous* and *on the flight* data collection modalities.

The selected experiments are exemplifying of potential use cases of epidermal sensors in IoT scenarios, such as the fever control in the case of infective disease, common seasonal influenza and epidemics as well as the early detection of viremic travelers during mass-screening at Country Borders [117].

In all the considered cases, the reliability of the interrogation link and of the thermal response are experimentally quantified and discussed.

7.1. Manual reading

The body temperature of a 25 years old female volunteer's (height 1.75m, weight 50 kg) down with the flu was monitored along with the three hours following the administration of an antipyretic drug that produced a 1°C temperature drop. Two epidermal thermometers were placed over two central sites - the right hypochondrium of the abdomen and the forehead - whose temperature is less sensitive to the external ambient conditions than peripheral regions [118].

Temperatures samples were periodically recorded by an handheld micro short-range reader (CAENRFID qIDmini) manually put near (few centimeters) the sensor. As reference, the core temperature was sporadically measured by a standard digital thermometer (Tecnic*Eco*) placed underarm. Measurements results are shown in Fig. 7.1 together with the subject's actions noted during the monitoring period.

The profile of the abdominal temperature does not correlate with that of the core one since, due to the motion of the user, the measurements were strongly affected by the time-variant ambient conditions surrounding the epidermal sensor. When the subject rested in supine position under blankets, the skin temperature increased

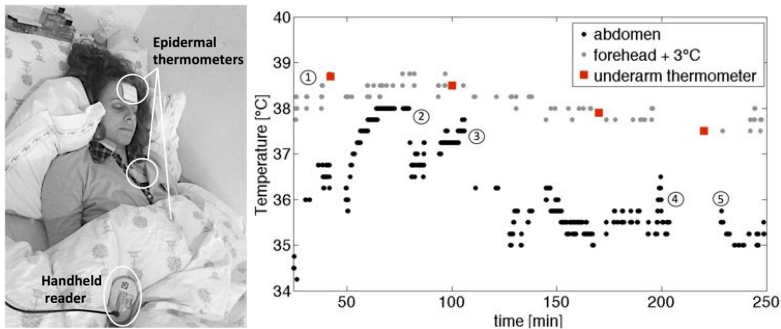


Figure 7.1.: Fever monitoring by epidermal thermometers during the measurement session when 1) taking antipyretic and covering the body under blanket; 2,3) uncovering the abdomen; 4) leaving the bed; 5) returning back to bed.

up to 38°C due to the microclimate established under the beddings, which prevented the dissipation of the augmented heat produced by the body. As soon as the subject uncovered the abdomen, the temperature quickly dropped by 1.5 °C due to the combined effect of the colder air and to the consequent cooling of the abdominal surface. A different behavior was instead recorded for the sensor placed onto the forehead skin. Although such temperature is sensibly cooler than the core, its profile greatly correlates with the reference measurement. After an offset compensation of 3 °C, the non-invasively measured data over the forehead provide indeed an acceptable estimate of the core temperature. It is worth noticing that this compensation could be avoided in all the situations where thermal variations of body temperature along with the time are clinically significant rather than the absolute values. Furthermore, there exist lots of clinical applications where it is necessary to monitor exactly the surface temperature over a certain region (wound healing, vascular diseases, sleep research...) and this compensation is not required.

7.2. Automatic (unsupervised) monitoring

The establishment of a robust communication link is a critical issue for both the reading modalities considered below (continuous and on flight), where the user stays for just a short period within the reader's range (gate) or, although permanently in the read region, he rotates his body producing possible shadowing effects (overnight monitoring).

7.2.1. Continuous overnight temperature monitoring

The continuous real-time monitoring of the body temperature is relevant in both domestic and hospital settings. Historical temperature recordings permit to classify fever patterns (intermittent, remittent, periodic) and support the diagnosis of infections, malignancies and inflammatory diseases while the instantaneous detection of fever spikes avoid the serious consequences of epileptic convulsions in children. In clinical practice, a prompt collection

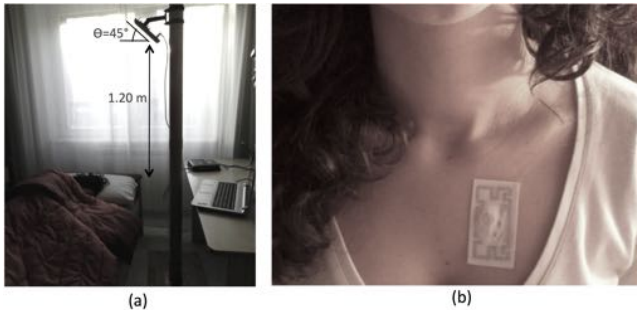
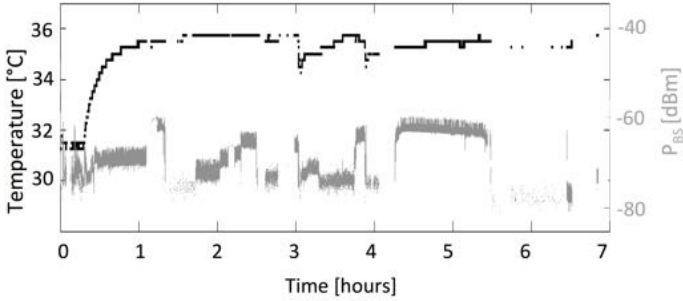


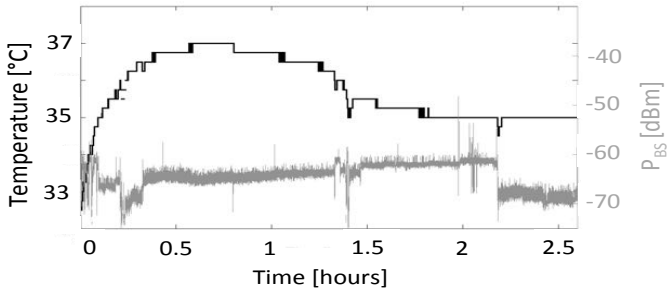
Figure 7.2.: Overnight temperature monitoring: (a) RFID monitoring system installed in a domestic bedroom. (b) Semi-passive epidermal thermometer placed over the volunteer's thorax.

of the specimen for blood cultures during temperature elevations maximizes the likelihood of finding the pathogenic microorganism [119] to prepare the specific antibiotics.

The feasible application of the epidermal RFID thermometer to the continuous monitoring was demonstrated in real-life conditions by measuring the skin temperature of a young volunteer (26 years old) for four consecutive nights. The reading system, comprising a long-range IF2 Intermec reader and a 7 dBic gain circularly-polarized antenna, was installed within a domestic bedroom and the epidermal thermometer was stuck over the volunteer's thorax (Fig. 7.2). The position of the reader antenna (height from the floor, distance from the bed, inclination) was experimentally determined by minimizing the turn-on power of the sensor in the supine and lateral sleep position of the subject, while preserving the compliance of the electromagnetic exposure with the Italian regulation (Electric field less than 6V/m in the region of the user)[120]. Since the distance between the reader antenna and the subject was higher than 1m, a battery-assisted sensor version of the thermometer was used. Fig. 7.3 shows two examples of the overnight recording of the skin temperature along with the power backscattered from the tag. After proper processing (refers to chapter 8) this latter parameter provides additional useful information about the user's activity



(a)



(b)

Figure 7.3.: Examples of skin temperature and backscattered power traces recorded during two nights for an epidermal sensor placed onto the thorax of a volunteer. (a) Normal temperature and (b) temperature elevation induced by a hot water bag.

(sleeping positions, limbs movements...) that can be correlated with the temperature changes at the twofold purpose of removing measurement artifacts and interpreting temperature variations related to subject's motion.

In the first plot (Fig. 7.3a), the temperature exhibits an initial rise which corresponds to the creation of the nocturnal microclimate under beddings of about 34-36 °C [121], then it remains rather stable for the rest of the night, except when the user changed position (as suggested by the abrupt variation of the backscattered power). In those cases, the user probably moved the bedding, thus letting

colder air entering inside. In the second experiment (Fig. 7.3b), the onset of a febrile state was emulated by placing an hot water bag close to the subjects under the beddings which produce a 2 °C elevation in the temperature over the thorax.

The reliability of the wireless link can be quantitatively evaluated through the percentage of the night-time when the temperature reading was missed for a time longer than {5, 10, 15, 20, 30} min. Tab. 7.1 shows that in all the four measurement nights, the interruptions longer than 10min occurred for less than the 15% of the total observation time and the measurement system may be accordingly considered rather reliable for that specific user. In most of the cases, the data loss occurred when the subject slept in a prone position thus completely shadowing the tag over the chest by his body. A couple of epidermal sensors placed over the front and the rear part of the trunk could ensure more robust communication link regardless of the sleeper's position.

Table 7.1.: Percentage of the night-time when the temperature was lost for a time longer than the indicated interval.

	5min	10min	15min	20min	30 min
1 st night	12%	8%	6%	5%	2%
2 nd night	10%	8%	4%	1%	0%
3 rd night	20%	15%	14%	12%	9%
4 th night	20%	14%	8%	4%	0%

7.2.2. On-flight temperature monitoring across gates

Augmented human body temperature is often an indicator of acute infections. Since the outbreak of serious flu strains such as H1N1, the spread of severe acute respiratory syndrome (SARS) and the more recent epidemic of Ebola and Zika viruses, public health authorities have been looking for a fast, easy, non-invasive, and reliable method to early detect and isolate suspected cases of infection. The proposed wireless epidermal thermometer has the potential to be a useful tool in the detection of feverish state in high-risk groups

such as travelers entering a country via mass transportation (airports) or medical personnel and patients within hospitals handling with epidemic emergencies.

The reference setup for the instantaneous screening of people in transit is an access gate equipped with one or more antennas connected to a long-range reader. When a person equipped with the RFID skin-sensor on his body passes through the gate, the system automatically registers its passage, store his identity (through ID cards or medical records stored into the IC memory) and instantaneously collect the value of his body temperature, which can be eventually stored into the IC itself to be used for comparison during the next control stage (Fig. 7.4, see [122] for a demo video). Such RFID-based scanning system could be particularly prone to false negative readings when an epidermal tag within the read range of the reader antenna is not detected and/or the temperature measurements fails. Many factors impact the read reliability, including the position of the tag over the body, the mutual orientation between the RFID sensor and the reader antenna and the walking speed of the subject.

An access gate was installed in a laboratory environment. The set-up comprised a long-range IF2 Intermec reader emitting 0.8 W power and a 5 dBi Gain linearly polarized antenna mounted at one the side of the portal (see Fig. 7.5.a). The experiment involved two volunteers having different physical size (27 years old female - height 1.55 m, weight 42 Kg, a 34 years old male - height 1.82 m, weight 74 Kg). Battery-less epidermal sensors were attached over the lateral abdomen in order to be aligned with the reader antenna (same height and polarization match). The two subjects were asked to cyclically cross the gate with a controlled gait cadence (expressed as the number of steps per minute) prompted by means of a metronome. An example of the raw signals of skin temperature and backscattered power collected for multiple gate crossings is reported in Fig. 7.5(b). It is worth noticing that the temperature was collected only within a sub-set of the time interval when the system correctly detected the crossing user. In particular the system failed the temperature sampling at the borders of the identification interval, e.g. when the user was at the edges of the read-region of the gate. In those conditions, the power collected by the chip was

enough to activate it (power threshold $P_{chip,labeling}=-8.3$ dBm) but not sufficient to enable the temperature reading (power threshold $P_{chip,sensing}=-4.5$ dBm).

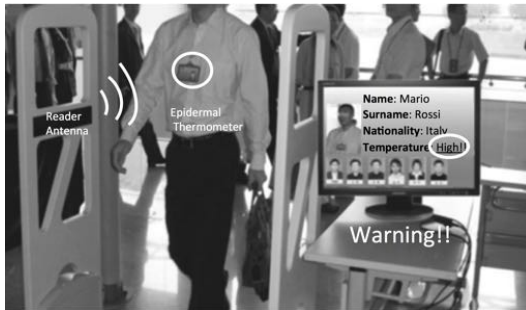


Figure 7.4.: On-flight fever screening across gates. A demo video can be found at [122].

Fig. 7.6 shows the mean number of IDs and of temperature readings (averaged on 14 consecutive gate crossings) as function of the walking pace, which was progressively increased from 60 steps/minute (slow gait) up to 140 steps/minute (fast gait). This data provides an indirect figure of merit for the on-flight monitoring reliability: the larger is the number of collected samples, the more stable the estimation of the temperature is expected to be, thus avoiding outliers. Up to 4-5 temperature samples were correctly received for a moderate crossing speed (up to 80 steps/minute) that is typical of a security check in an airport. If the user instead crossed the gate at his natural gait of 100-120 steps/minute (one gait cycle per second), as in the case of normal walking inside a house or hospital, the system was able to collect 2-3 samples that are still enough to perform some elementary processing. Beyond the normal cadence, as in case of rushed motion, only one temperature sample was collected and false negative may occurs. To improve reliability, multiple antennas could be installed in the gate to increase the extension of the read region.

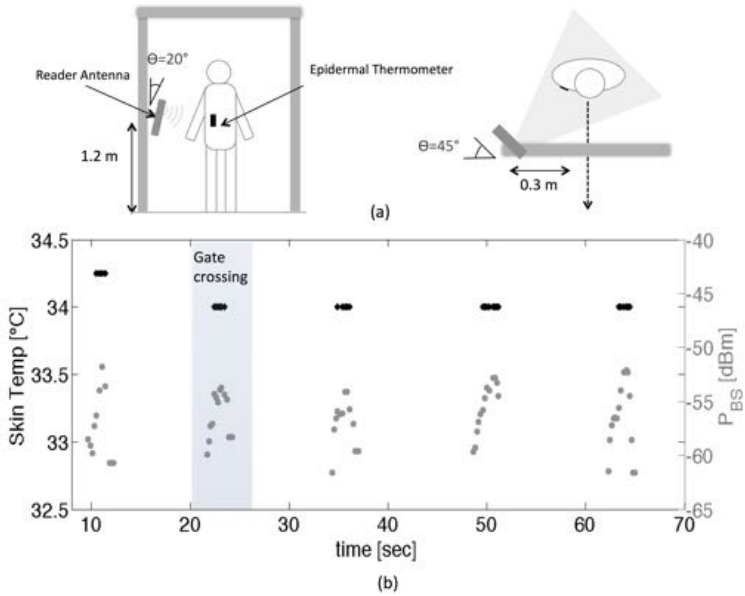


Figure 7.5.: (a) RFID portal for the automatic temperature screening of crossing people. (b) Skin temperature and backscattered power collected from the epidermal sensor for sequential crossings of the RFID gate.

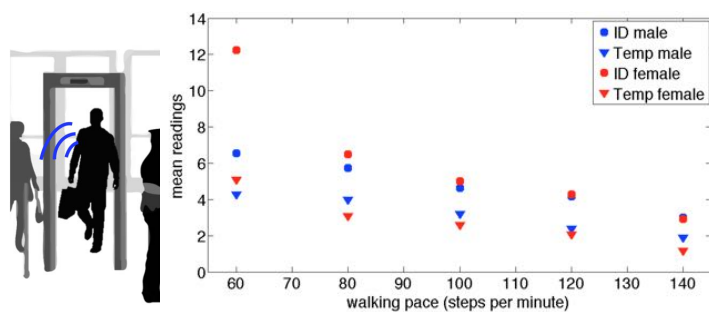


Figure 7.6.: Mean number of ID and temperature readings (averaged on 14 consecutive gate crossings) versus the walking pace for two users (tiny female and normal male) crossing the RFID gate sketched in Fig. 7.5 (a).

7.3. Conclusions and open issues

The reliability of the wireless radio-link of an epidermal thermometer placed over different body regions was experimentally quantified. The communication resulted robust for health and security monitoring applications in clinical and domestic settings and even for the automatic detection of anomalous temperature peaks of people walking within airports and at country border crossing.

Further analysis must be devoted to the refinement of this device:

i) The application of a significant skin-to-core temperature translation requires a statistical analysis of the variability and of the correction offsets with different subjects and body positions. The Ethics Committee of the Tor Vergata University Hospital has recently (August 2016) given the formal approval to set up a clinical study involving a large number of patients (see early experimentations at [123], Fig. 7.7). Experimentations is currently running.

ii) The reliability of the temperature measurement is strictly dependent on the adherence of the sensor to the body (at least of the thermal sensitive area, i.e. the IC), as in the case of any other convectional contact-thermometers (thermistor, thermocouple. . .). The fixing method can influence the skin blood perfusion or locally alter the heat exchange mechanisms through skin, its surrounding, and body core, thus imposing local artifacts on the sensed data. The choice of the adhesive substrate is hence crucial since thermal, electromagnetic and biocompatibility requirements must be simultaneously satisfied. The chip-to-skin adhesion could be enforced by using a ultra-thin transpiring and breathable adhesive dressing, for instance the *Rollflex*[®] or *Tegaderm*[®]. Being impermeable to water, the same film could be moreover used as a top protection of the sensor traces to insulate the IC from humidity and moisture. Other medical grade adhesive usually applied to adhere the electrodes to the scalp for long-term EEG (e.g. collodion) may be considered as well, but the effect on the thermal response of the IC and on the electromagnetic response of the antenna must be investigated.

iii) Temperature measurements can be influenced by the environmental factors surrounding the sensor. Empiric correction formulas specific for the operative conditions (temperature, air velocity. . .)

could be implemented as in [?]. However this approach would be rather unpractical as the ambient conditions in real non-controlled environment are mostly unknown and rapidly varying. Rapid temperature variations produced by external high air-flows could be nevertheless mitigated by proving the IC with an insulating top coating, which acts as a thermal low-pass filter.



Figure 7.7.: Early experimentations at the Tor Vergata Polyclinic: a) A doctor while positioning the plaster with the wireless thermometer over the patient’s chest. Examples of reading modalities: continuous automatic monitoring by fixed reader (b) and manual measurements by key-fob reader with real time feedback on custom apps developed for tablets (c) and smartphone (d)

Remote Monitoring and Control of Overnight living environment

The chapter describes an Ambient Intelligence system able to monitor the parameters of sleep quality, identify anomalous events and prompt for remote or local assistance. The system analyzes the interactions of the person with the surrounding environment (bed, carpets...) by using wearable and ambient tags and versatile signal processing real-time engine.

Among the clinically-relevant physical and behavioral parameters to be monitored, *sleep* is definitively important since sleep disorders could sensibly affect the quality of life, leading to daytime sleepiness, spread weariness and even moodiness. Furthermore, especially for weak subjects such as elderly, children and neurologic patients, the night could be a source of several dangerous events (falls, disorientation, nighttime wandering) demanding for early detection and prompt actions. These requirements are even more pressing in case of alone-living subjects or inside hospitals and nursing houses, where many patients need to be contemporarily monitored all along the night with the consequence of high personnel costs.

Previous applications of RFID technology to the sleep monitoring involved wearable or environmental tags loaded by active or pas-

sive accelerometers to detect pathological limbs movements[124], mitigate the risk of nocturnal falls [125], infer postures and global movements [126] or finally to automatically detect movements related to bed exit [127]. Such systems mostly relies on high power-consuming active nodes and machine learning based classifiers that required ad-personam training [128]. Therefore they appear quite complex and not straightforwardly suited to be applied in clinical applications, especially when many subjects need to be contemporarily monitored during the night.

This chapter describes an implementation of the RFID-SN in Fig. 6.13, hereafter denoted as *NIGHTcare*, for monitoring people during the night. The goal is detecting the presence or the absence of the user in the bed, his jerky movements and his motion patterns, accidental falls, persisting absence from the bed and prolonged periods of inactivity as well as his instantaneous sleeping posture. The proposed system is preliminary investigated by a three-dimensional electromagnetic computer model to plan the most convenient placement of reader and tags and the compliance with the electromagnetic exposure limits. The accuracy and the potentiality of the system are then demonstrated throughout extensive laboratory and real-life experimentation involving young and aged volunteers.

8.1. Description of the System

Fig. 8.1 shows a pictorial representation of the RFID data acquisition set-up for the *NIGHTcare* system. The patient, lying on the bed, wears four RFID tags (wearable tags - WT) sewn into his night-suit at the level of abdomen, back, left and right hip. A conventional dipole tag (Ambient tags - AT) is placed underneath the mattress so that it will be completely shadowed by the body when the subject lies on the bed, regardless the position assumed by the user. One or two additional ATs are finally placed at each side of the bed, eventually hidden by carpets such to mitigate their visual impact. The radio scanner device is placed in correspondence of the headboard, properly tilted and lifted in order to uniformly illuminate the entire bed and the surrounding floor. The response of the tags to the reader's query is subjected to an ambient modulation,



Figure 8.1.: NIGHTcare: Ambient intelligence system aimed to monitor and take care of the night sleep involving RFID tags placed over the body (WT: wearable tags) and in the surrounding environment (AT: ambient tags). A long-range UHF-RFID reader, properly placed in proximity of the bed headboard, scans the environment interrogating the tags.

in the sense that the strength of the backscattered field is modified by the proximity of the human body with the tags themselves. Moreover, in case of specific body-environment configurations, a tag may be fully shadowed by the sleeper so that it will not be able to reply the reader's interrogation. For example, if the subject lies on the bed, the tag under the mattress will be totally shielded and it will be prevented from responding while the others on the floor will be free to communicate. Vice-versa if the subject falls. The activity of the sleeper during the night may be therefore recognized by processing the signals received from the tags. More in details, the IDs of the responding tags can be used to recognize the *status* of the sleeper (whether he is in the bed, he is fallen down or instead he is outside), while the processing of the strength of the electromagnetic fields reflected by the responding tags can be used to extract information about motion and about specific *postures* during the sleep.

The selected components for the NIGHTcare setup are described below.

The wearable RFID tag is a miniaturized UHF-RFID layout, already proposed by the author's group in [57]. The lightweight and the small sizes ($35\text{mm} \times 45\text{mm} \times 2\text{mm}$) make this tag suitable to be integrated into plasters, wristbands or various clothes. The maximum measured realized gain of the tag when placed onto the human body is -7dB (at the European frequency 868MHz). Accordingly, when considering a linearly polarized reader antenna and an IC's power sensitivity $P_{chip} = -18\text{dBm}$, the estimated free-space maximum read range is about 5m (Fig. 8.2).

The Ambient tag is a commercial AD-843 inlay (Fig. 8.2) with external size of $94\text{mm} \times 38\text{mm}$ [129] suitable to be placed on the bed and on the ground thanks to its proven good performances in a wide range of applications. The measured realized gain for the tag placed on the ground, with an IC's power sensitivity $P_{chip} = -15\text{dBm}$, is -4dB (at 868MHz), leading to a maximum read range longer than 5m . Even better performance are expected when the tag is placed under the mattress.

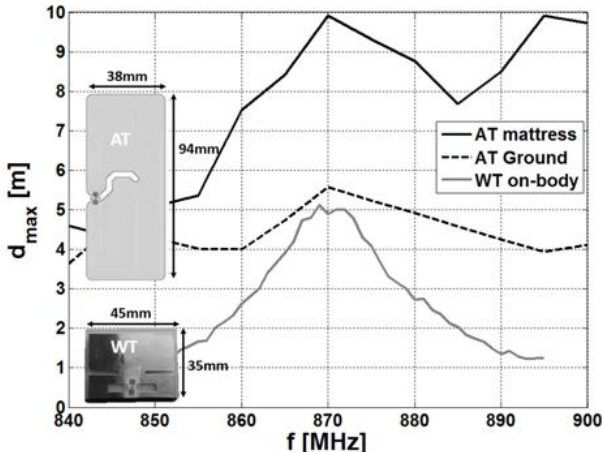


Figure 8.2.: Estimated maximum read ranges along the broadside direction of the ambient tag (AT) placed on the mattress and ground and of the miniaturized wearable tag (WT) placed on-body.

Finally, the reader is the CAEN ION [130] equipped with a broadband linear-polarized Stacked Planar Inverted-F Antenna (SPIFA) over Teflon substrate, having $130\text{mm} \times 200\text{mm} \times 12\text{mm}$ external size and 5.8dB maximum simulated gain evaluated at 868MHz along the broadside direction (Fig. 8.3). The half-power beamwidth of the antenna (85° and 108° for the H-plane and the E-plane, respectively) enables a uniform illumination of the environment. The height and the angular tilt of the antenna are design parameters of the system to be optimized as shown later on in the next paragraph.

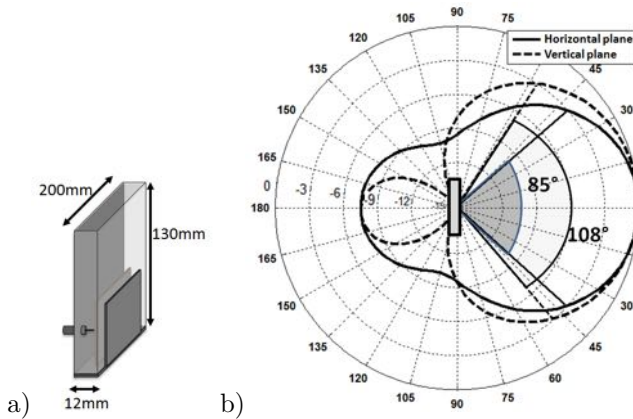


Figure 8.3.: a) Layout of the Stacked Planar Inverted-F Antenna (SPIFA) used for the interrogation; b) Normalized radiation patterns of the reader antenna for horizontal and vertical planes.

8.2. Electromagnetic Analysis

In order to optimize some geometrical parameters of the monitoring system, and to take into account the electromagnetic emission and exposure issues, the *NIGHTcare* platform was preliminary analyzed by a three-dimensional computer model implementing the Method of Moment [54]. The model (Fig. 8.4) comprises the reader antenna, that is accounted by means of its radiation pattern simulated in standalone configuration, the floor (represented by the

Green function), the bed (with a conductive structure and a dielectric mattress) and the user, here emulated by considering an anthropomorphic homogeneous phantom (electromagnetic parameter at 868MHz $\epsilon_r = 41.5$ $\sigma = 0.94\text{S/m}$, $\rho = 1000\text{Kg/m}^3$).

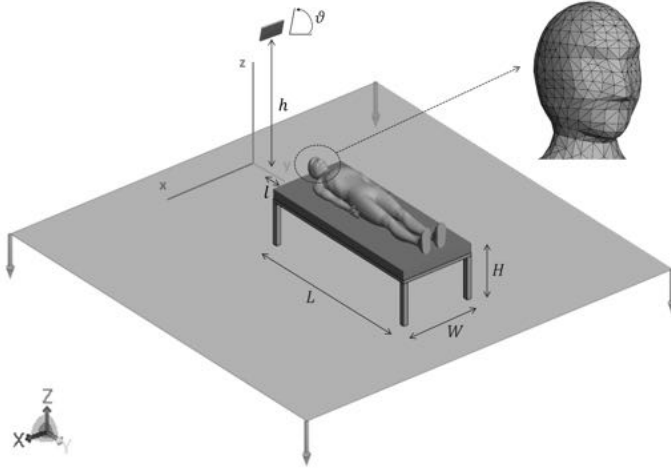


Figure 8.4.: Numerical Model of the *NIGHTcare* platform comprising the reader antenna, the bed and the human phantom. Geometrical parameters: $L=190\text{cm}$, $W=80\text{cm}$, $H=52\text{cm}$, $h=180\text{cm}$, $l=40\text{cm}$, $\vartheta=45^\circ$.

Fig. 8.5 shows the computed electric field map for a realistic arrangement of the reader, placed at $h=180\text{ cm}$ height from the floor, at $l=40\text{ cm}$ distance from the bed and tilted by $\theta_0 = 45^\circ$ with respect to the horizontal plane. The reader was assumed to emit 3.2W EIRP, that is the maximum allowed value in Europe. The shadowing and diffraction from the bed and the body, as well as the reflections from the floor, produce a non uniform field distribution, with visible nulls on the floor, close to the bed, wherein ambient tag should be placed.

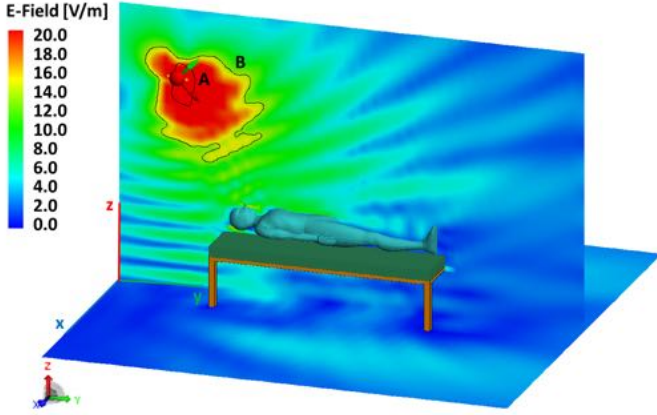


Figure 8.5.: Electromagnetic field on vertical and horizontal planes (the last one corresponding to the floor level) radiated by the reader antenna emitting 3.2 W EIRP. The highlighted iso-lines A and B correspond to the r.m.s. field $E(r)_{r.m.s.} = 20V/m$ and $E(r)_{r.m.s.} = 6V/m$, respectively, when the communication duty cycle is $d = 0.2$ (one interrogation per second).

8.2.1. Communication issues

The position and orientation of the antenna need to be selected so that all the tags could receive enough power to be activated in operative conditions. At this purpose, a parametric analysis over $1.5m < h < 2.5m$ and $45^\circ < \theta_0 < 80^\circ$ allows evaluating the most appropriate system configuration. The minimum power P_{chip} that is required to activate the tags is related to the local field radiated by the reader and impinging on the tags

$$E_{min} = \sqrt{\frac{P_{chip}}{\eta_p \hat{G}_T} \frac{4\pi z_0}{\lambda^2}} \quad (8.1)$$

with z_0 the characteristic impedance of the medium, η_p the polarization mismatch between the reader and the tag and \hat{G}_T the

realized gain of the tag. With reference to the setup in Fig. 8.4, the tags on the floor are assumed to be placed at each side of the bed, at $y = 170\text{cm}$ from the reader antenna and $x = 30\text{cm}$ from the sides of the bed, such to intercept the strongest field (see Fig. 8.5) and to be fully overlaid by the user in case of falling. The wearable tags are placed on abdomen, back, left and right hip. By introducing into eq. (8.1) the tag realized gains indicated in sec. 8.1 decreased by a 3dB safe margin, the estimated minimum fields required to activate the environmental and the wearable tags were found to be 3.5V/m and 3.7V/m , respectively.

The bottleneck of the communication mostly concerns the tags placed on the floor since they are positioned at the longest distance from the reader antenna, therefore the optimization will be referred only to the ground tags. Fig. 8.6 shows the electric field isolines at the ground level versus $\{h, \theta_0\}$ parameters. In the shadowed area the field impinging the ground tags is lower than the minimum activation level E_{min} , and hence the antenna tilt must be kept between 45° and 68° , while the height is much more effecting and must be kept between 1.5 and 1.75 m.

8.2.2. Safety Compliance Issues

Constraints over electromagnetic field exposure and power absorbed by the human tissues are imposed by local Recommendations. In particular, the European rules [120] enforces requirements on the the r.m.s. emitted field averaged over a prescribed time interval T_{av} .

The reader interrogates the environment according to a given repetition period T_0 . Denoted with T_{com} the time duration of a typical reader-tag communication, the duty-cycle is accordingly $d = T_{com}/T_0$. The averaged r.m.s electric field is hence

$$\langle E(r)_{r.m.s.} \rangle_{T_{av}} = \sqrt{d} E(r)_{r.m.s.} \quad (8.2)$$

that is required to be less than $E_0 = 1.375\sqrt{f} = 41.3\text{V/m}$. Even more restrictive constraints may be found in some Countries, as in

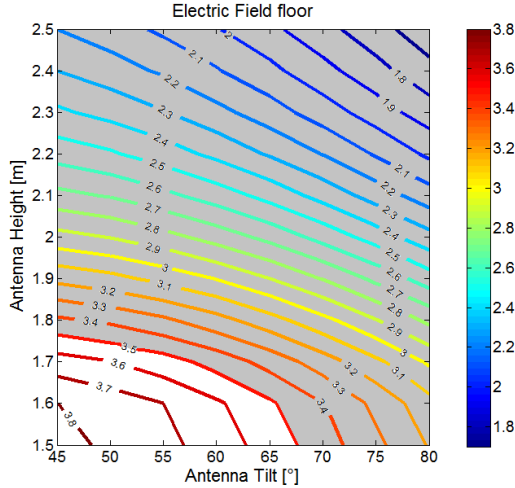


Figure 8.6.: Optimization of the reader antenna placement. Electric field isolines on the ground versus the height and the tilt of the reader’s antenna.

the case of Italy where $E_0 = 6V/m$. Some iso-lines of the simulated averaged r.m.s electric field are traced within Fig. 8.6 where it is clearly visible how the user is placed in a fully compliant radiating region ($\langle E(r)_{r.m.s.} \rangle < 4V/m$) if a duty cycle $d=0.2$, corresponding to an interrogation per second, is considered.

The Specific Absorption Rate (SAR):

$$SAR(r) = \frac{\sigma(r) \cdot d \cdot |E(r)|_{rms}^2}{\rho(r)} \quad (8.3)$$

averaged on the entire body needs to be less than $SAR_{body,max} = 0.08W/Kg$ and the SAR averaged over 10 g of tissue less than $SAR_{10g,max} = 2W/Kg$. Fig. 8.7 shows the estimated SAR profiles inside the body. Also in this case, the averaged values $SAR_{body} = 0.6mW/Kg$ and $SAR_{10g} = 4mW/Kg$ (expected to arise in correspondence of the upper portion of the body) are greatly below the exposure limits.

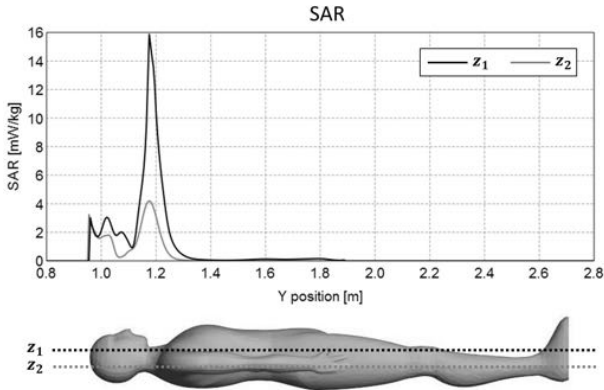


Figure 8.7.: Simulated values of SAR along the sagittal plane of the body exposed to the reader’s radiation as in Fig. 8.5

8.3. Detection of sleep events

The detection of sleep events is performed by applying a threshold-based algorithm. The procedure used to identify the different events occurring during the nightly sleep comprises two parallel branches, aiming at the detection of the user’s state (presence/absence from the bed or accidental falls) and at the discrimination between activity and quite sleep condition. In the latter case, the classification of the sleeping posture is performed, too. The considered events, and their logical relationship, are summarized by the classification tree of Fig. 8.8, to be walked from left to right.

The detection of the user’s state relies on the processing of the signals coming from the three ambient tags (bed, left/right floor), forming a three-elements time-variant vector:

$$\underline{\mathbf{S}}_{\mathbf{A}}(t) = [s_{A1}(t), s_{A2}(t), s_{A3}(t)] \quad (8.4)$$

while the estimation of activity rate and sleeper’s posture requires

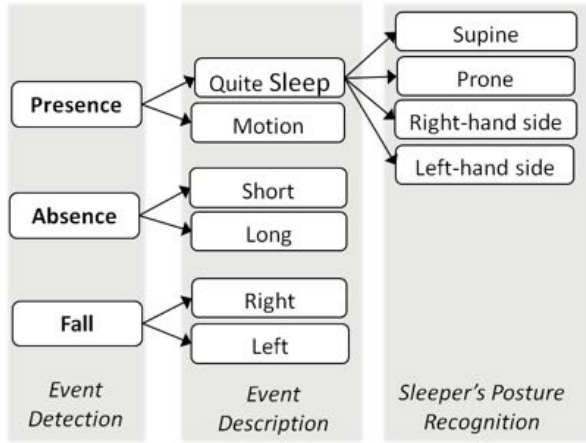


Figure 8.8.: Classification tree implemented into the NIGHTcare platform. The relevant sleep events are recognized starting from left to right.

the signals from the four wearable tags:

$$\underline{\mathbf{S}}_{\mathbf{W}}(t) = [s_{W1}(t), s_{W2}(t), s_{W3}(t), s_{W4}(t)] \quad (8.5)$$

Such data stream is provided by the reader in term of RSSI. As shown in Fig. 8.9, RFID backscattered signal is characterized by low values ($\sim -60\text{dBm}$) and high fluctuations, mainly due to the receiver internal noise, the limited stability of its components and above all the non-stationary communication channel. To overcome these drawbacks and ensure the reliability of the sleep monitoring system, the raw data are pre-processed before feeding the event-detection algorithm by low-pass filtering which is performed through rolling average with fixed temporal windows. In doing so, the information about the user's state is inferred by analyzing a temporal record taking into account the past story of signals rather than the instantaneous noisy measurement. Furthermore, since the interrogation protocol could randomly fail because of environmental interferences

and collisions, missed readings are dropped out the useful time series, in order to prevent false positive events detection, as in the case of on the floor tags, whose response to the reader query is strongly related to the user's fall detection. Moreover, the proposed algorithm exploits a cross-validation between signals coming from multiple channels and it relies on on/off digital data, which are more robust to environmental interferences, for the detection of most dangerous events (e.g. fall or long absence). A high-level description of the monitoring procedure is summarized in the flow chart in Fig. 8.10 and described in detail in the next sub-sections.

It is worth noticing that the proposed algorithm does not imply any preliminary ad-personam training as required for classification techniques [115], thus reducing the complexity and the uptime of the system which is ready to monitor any subjects.

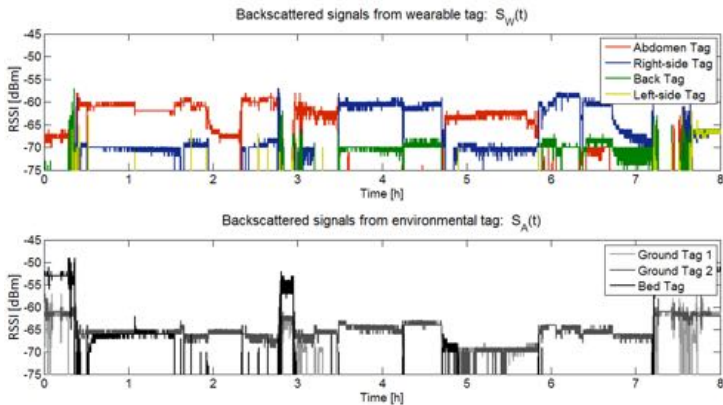


Figure 8.9.: Example of raw RSSI signals $\mathbf{S}_W(t)$ and $\mathbf{S}_A(T)$ collected by the reader from wearable and ambient tags during sleep events.

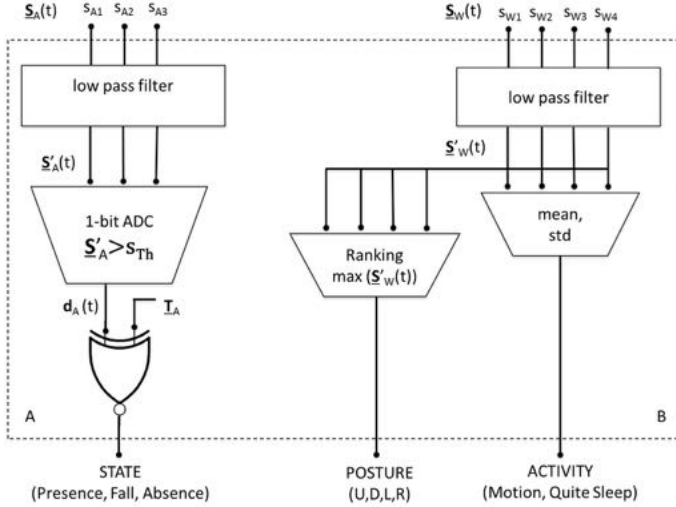


Figure 8.10.: Flow chart of the classification procedure for the discrimination of the sleeper state (left) and of his activity/posture (right).

8.3.1. Classification of the sleeper's state

After a low-pass (LP) filtering to remove noise, the resulting ambient signals $\underline{s}'_A(t) = LP\{\underline{s}_A(t)\}$ undergo a 1-bit A/D conversion yielding the 3-bit data stream $\underline{d}_A(t)$, so that

$$d_{A,n}(t_m) = \begin{cases} 1 & \text{if } s'_{A,n}(t_m) \geq s_{Th,n} \\ 0 & \text{otherwise} \end{cases} \quad n = 1..3 \quad (8.6)$$

where $\mathbf{s}_{Th} = [s_{Th1}, s_{Th2}, s_{Th3}]$ are predefined threshold values whose values can be a priori defined depending on the absolute range of RSSI values provided by the specific reader (for example if RSSI values for a detected tag range from 80 to 130, a RSSI value greater than 90 would ensure a reliable reading and consequently convert into digital signal as 1).

Let $\mathbf{T}_A [3 \times 4]$ denote a binary representation, the *coding table*, of the four meaningful states of the user, labelled as STATE=[*Presence, Absence, Left-fall, Right-fall*], with respect to the set of responding ambient tags (Fig. 8.11.a). A XNOR-like gate is applied to $\mathbf{d}_A(t)$ and to $\mathbf{T}_A [3 \times 4]$ thus enabling the following binary output matrix at the time t_m :

$$\mathbf{out}_A(t_m) [3 \times 4] = XNOR(d_A(t_m), \mathbf{T}_A) \quad (8.7)$$

That column of $\mathbf{out}_A(t_m)$ having the maximum norm, will yield the estimated user's state. An example of application of this last step is reported in Fig. 8.11.b.

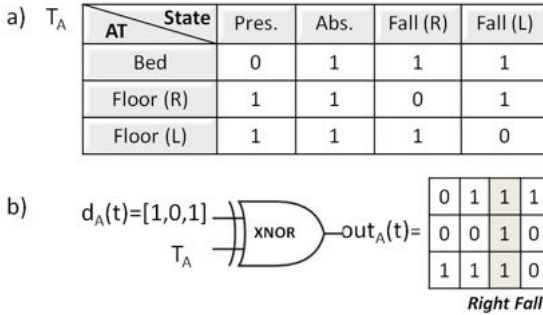


Figure 8.11.: a) Coding binary table T_A relating the set of responding ambient tags to the four considered states of the sleeper. b) An example of identification of the actual sleeper's state by means of the XNOR gate: the third (shaded) column of \mathbf{out}_A exhibits the maximum norm and hence the retrieved sleeper's state is the third label of the STATE vector, e.g. "right fall".

Finally, an additional state, the *Long-Absence*, is recognized when the *Absence* condition lasts for a period longer than a given threshold time accounting for physiological absence of the user (for instance for going to the toilet). These temporal windows are set during the calibration phase (see sec.8.5.1) and may be possibly adapted accordingly to the patient's own habits.

8.3.2. Classification of the sleeper's activity

The detection of the activity/posture relies instead on the simultaneous processing of the analog signals coming from the wearable tags that are subjected to low-pass filter as before: $\underline{S}'_{\mathbf{w}}(t) = LP\{\underline{S}_{\mathbf{w}}(t)\}$. The discrimination between motion and quite sleep is performed through the standard deviation of the signals. If the standard deviation exceeds a given threshold, then the sleeper is assumed to be moving. The threshold value, corresponding to the intrinsic signal fluctuation due to internal noise and environmental interferences, was empirically deduced by collecting a large amount of data during experimental sessions performed by the help of volunteers having different ages and physiques and by computing the rolling standard deviation both in the quite and the motion condition. This value turn out to be globally valid for each subject if only the binary classification of the quiet/motion state is required, thus avoiding ad-personam training. Even more complex information such as the classification of movements according their intensity or the distinguish between physiological and pathological patterns could be inferred by defining thresholds on individual basis (motions strength strongly depends on the sleeper's age) with the help of clinician.

When the subject is instead in the rest condition, his posture is retrieved by applying a maximum-value rule that is based on the assumption that the tag related to the maximum RSSI is the closest to the reader's antenna. Since the user wears a tag on each side of the body, it is hence possible to introduce a classification table (Fig. 8.12) univocally relating the tag having the highest backscattering power value to one of the four possible sleeper's postures.

tag position	posture
abdomen	S: supine
right hip	R: right side
left hip	L: left side
back	P: prone

Figure 8.12.: Classification table for the sleep's posture depending of the position of the tag that produces the maximum RSSI

Hence, at time t_m the elements of $\underline{\mathbf{S}}'_W(t_m)$ are ranked according to their RSSI at the purpose to recognize the tag producing the highest signal. The sleep posture is finally estimated from the above classification table.

8.3.3. Events Representation

Fig. 8.13.a shows a typical trace of the night sleep when the user alternated periods of quite sleep (grey area), short absence (yellow area), physiological movements (green bars) and fall events (red bars). Each condition is classified according to its duration: a short absence from the bed could be considered as physiological, while a prolonged one (second yellow frame) could foresee a problem (for example illness in the bathroom) and thus an automatic alarm has to be generated, as well as in the case of a fall detection. The occurrence of events can be finally counted to produce statistics about the user's sleep quality and behavior (Fig. Fig. 8.13.b,c), e.g. how many time he left the bed in the night, the number of movements and the time percentage spent in each position, as shown in the next experimental session.

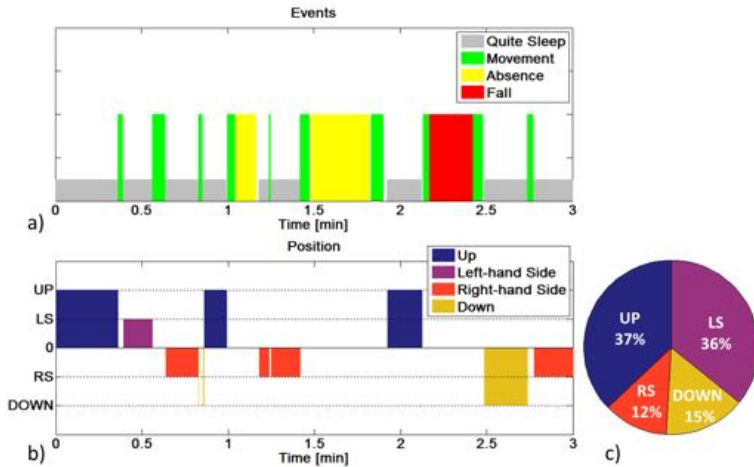


Figure 8.13.: a) Example of a recorded sleep activity trace. b) Classification of body postures for each quite sleep slots. c) Example of aggregated statistics.

8.4. Validation of the System

The accuracy of the algorithm for the detection of the sleeper’s posture and state was evaluated by involving 20 volunteers (5 men and 15 women, whose ages span from 24 to 45 years {24, 26(x2), 27(x2), 28(x5), 29(x6), 30, 31, 32, 45}). Subjects were asked to take the four sleeping positions and the four states (presence, absence, left and right fall) separately, according to the indications randomly given by an acoustic pre-recorded “go-signal” phrase prompting for timing (e.g. “Prone Position”, et similar). Each position was kept for about 20s (corresponding to the time interval between two consecutive audio commands) and it was repeated 8 times. The dataset hence consists of 32 positions to be recognized during 10 minutes and 40 seconds of recording session. Instruction labels were collected and synchronously stored together with the backscattered signal coming from wearable tags to keep track of the desired (asked) outputs as well as of the predicted ones. The

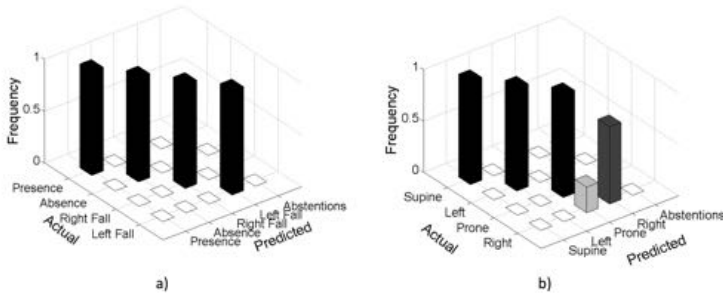


Figure 8.14.: Example of confusion matrices for the sleeper state (a) and the bed positions classification (b).

statistic model was calculated every 20 seconds of acquisition, and the predicted position was then compared with the real one. Accuracy and error-rate were then estimated by means of the confusion matrix (Fig. 8.14) that provides a graphical representation of classification accuracy. More in detail, denoting with $N=4$ the number of considered sleep positions and states, a confusion matrix (CM) is a $N \times N$ table whose columns correspond to the postures predicted by the algorithm, while each row represents the true ones. The fifth extra-column of the matrix in Fig. 8.14 refers to the “abstention condition”, namely the case in which the algorithm is not able to classify the posture in any of the four predetermined cases so that the “unclassified position” is assigned. The diagonal elements of the matrix give the number of correctly classified positions and state while the off-diagonal elements correspond to misclassified ones. The classification accuracy is finally the ratio between the sum of the diagonal elements and the sum of all the matrix elements. In the specific, the estimated average accuracy of posture detection achieved in the performed experiments was 97%, with right-hand side position showing the highest value of misclassification. The accuracy of state detection was instead 100% for all the subjects confirming the robustness of the on/off-based algorithm. It worth noticing that the abstention condition never appears.

8.5. Example of Real-life Recordings

The NIGHTcare system was finally experimented into two real scenarios without any supervision of technicians during the night. In both cases, the RFID data were corroborated by videocamera information or by notes about the activity directly provided by the volunteers the morning after.

8.5.1. Installation procedures

The installation procedure of the system is performed as follows: 1) The first step is to place the ambient tags on the carpets and mattress, making sure they are readable all the time, unless they are fully covered by the patient. Ambient tags on the floor are placed on both sides of the bed in the areas where the electric field is maximum (Fig. 8.4) and the reader's antenna is slightly moved up or down and tilted according to Fig. 8.5 up to obtain a stable and reliable value of RSSI of all the uncovered tags during the interrogations. 2) At this point, the patient wears the four wearable tags as in Fig. 8.1. Interrogations of all the tags with the patient in the bed are then performed to register some profiles of the received signals. 3) From previous measurements, amplitude and time thresholds are set, based on the typical behavior of the subject and on the levels and fluctuations of the received signals. Less than twenty minutes are requested to complete the procedure and calibrate the system.

Experiment 1: Young Subject in Domestic Environment

The first experiment was performed by applying the NIGHTcare system to a young volunteer (27 years old) during three consecutive nights. The set-up was installed into a domestic room (Fig. 8.15a). A video recording system was positioned onto a support at 70cm from the floor and at a distance of 30cm from the bed so that all movements of the monitored subject were clearly visible. Fig. 8.16 shows the NIGHTcare response of one of the three nights. The user went to bed around 23:30 and slept approximately until 7:00 in the



Figure 8.15.: NIGHTCare setup installed a) into a domestic room and b) into a nursing home for aged guests.

morning, with two short absences between 4:00 and 5:00, for going to the toilet. The sleep was peaceful, with only 7 small movements detected during the whole night, mainly related to the change of the sleep posture. Fig. 8.16.b shows some snapshot taken by the videocamera that fully agree with the NIGHTCare output. Aggregated statistics about the body posture, sleep duration, absence and movements are shown in Fig. 8.17. The user mainly sleeps on the sides, while the prone position is never detected.

Experiment 2: Elder Subject in Nursing Home

The second experimental campaign involved an elder subject (age 95) in good mental and physical conditions resident of a nursing home (“Residenza Maria Clarà, Monte Porzio Catone, Rome, Italy”). The setup was optimized by considering the specific environment (spaces narrower than the domestic room ones). Particular attention has been devoted to the positioning of the environmental tag on the floor: in order to avoid any fall hazard, the carpets have been removed and the tags have been directly attached on the tiles. The volunteer (Fig. 8.15-b) was not fully aware of all the functionalities of the system, therefore providing a not-biased

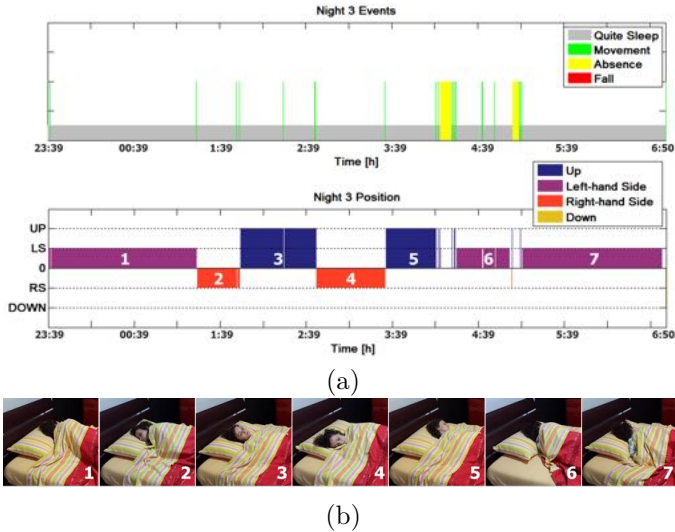


Figure 8.16.: Young volunteer. a) traces from one of the three nights sleep activity and automatic classification of the body postures during the quiet sleep state. b) Snapshots of body postures as recorded by a videocamera corresponding to the NIGHTcare profiles.

behavior during the three nights. Fig. 8.18 shows the NIGHTcare responses over one of the three nights. The patient went to bed around 22:30 and slept approximately until 5:30, with a short absence around 1:00 for going to the toilet. The sleep was peaceful, with only 10 small movements detected over the entire night and a quite constant posture.

It is worth noticing that the elderly user changed position less frequently than the young volunteer, due to the slowness and movement difficulties typical of the advanced age. The sleep appears well reproducible throughout the course of the three nights, as clearly demonstrated by the aggregated data about the body posture and the movements in Fig. 8.19. Each night, the lady went to bed between the 22:15 and the 22:30 and slept until 5:15-5:30 in the morning. She went to the bathroom around 1:00 and took approximately

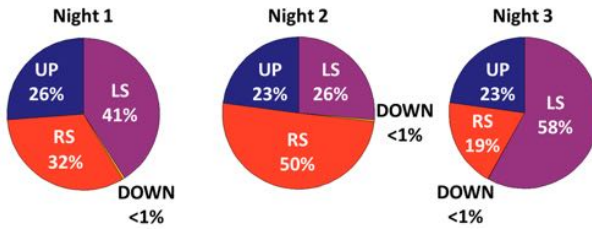


Figure 8.17.: Young volunteer. Overall percentages of time spent in each position by the user during the three monitored nights. The recorded number of body movements during three night were {12, 8, 7} respectively, while the number of absences from the bed were {3, 2, 2}.

5-10 minutes to go back to bed.

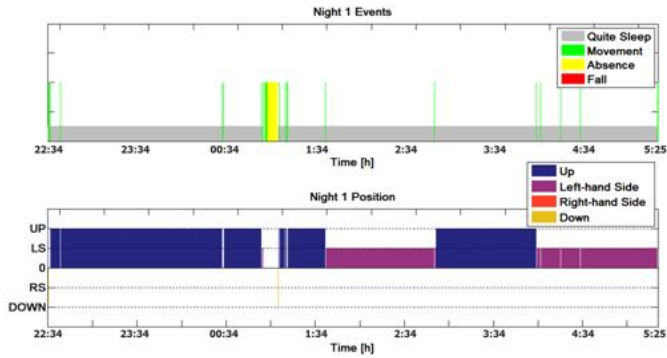


Figure 8.18.: Aged volunteer. NIGHTcare traces from one of the three nights sleep activity and automatic classification of the body postures during the quiet sleep state.

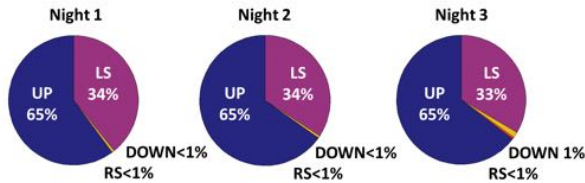


Figure 8.19.: Aged volunteer. Overall percentages of time spent in each position by the user during the three monitored nights. The recorded number of body movements during three night were {8, 6, 5} respectively, while the number of absences from the bed were {1, 1, 3}.

8.6. Conclusions

The results demonstrated that it is possible to remotely monitor the state and the activity of young and elderly people during the night that by processing only electromagnetic signals backscattered from combined wearable and ambient tags. The sleep events (quiet sleep, absence from bed and falls) were recognized with 100% accuracy and the instantaneous posture with an accuracy higher than the 95% (within the 20-volunteers experimental campaign). The applied threshold-based algorithm does not require a starting ad-personam training phase as standard classification techniques thus reducing the complexity and the duration of the installation procedures. The platform is completely compliant with the EM exposure limits and hence it is suitable to be installed in both domestic and hospital environments. An early demonstrator of the system can be found at [131] (Fig. 8.20).

The system is easily scalable since a single reader connected to a set of antennas can monitor, in time division, a multiplicity of users and a network of readers could easily cover a large infrastructure like a nursing home. Real-time access to the data can be given from both fixed (desktop) and mobile devices (tablet, smart-phones) checked by qualified personnel, able to access the server if provided of security credentials. The personnel is therefore able to control the whole nursing home from any location.

Beside the remote observation of patients, the system produces statistical data about the individual sleep behavior that can be useful to make correlation with pharmacologic therapies. It is worth noticing that the system can be further simplified by reducing the number of tags worn by the subject. Without any wearable tag the system is still able to retrieve the status of the sleeper (presence, absence, fall) while early theoretical analysis demonstrated that it is possible to infer the sleeper posture and activity by considering only two wearable tags placed asymmetrically on the chest and on the back and by exploiting the shadowing effects of the human body on the communication link between floor tags and reader.

A natural expansion of the platform can be envisaged by augmenting the same infrastructure with epidermal temperature sensor for fever detection (see chapter 8), humidity sensor tags under the mat-

press to monitor incontinence and other miniaturized tags placed over medicines and tools to enrich the patients' behavioral analysis, as exemplified in the next chapter.



Figure 8.20.: Demonstrator of the NighCare System[131].

Advanced Human-Things Interactions and Multi-parameters monitoring

The chapter describes the multi-level monitoring of complex spaces by using conventional analog tag and custom configurable RFID boards equipped with dedicated sensors. The system provides the real-time detection of a plethora of events ranging from environmental accidents, up to the (un)authorized access to a critical area and the tampering/overloading of equipments.

People's wellness and healthcare assessment in living and medical environments benefit from a continuous and reliable monitoring of critical parameters such as the temperature, the presence/level of humidity, and some other gases. For example, the control of air quality inside the operating theater is useful into avoid the inhalation of anesthetic gases by the personnel or the contamination of the patient under surgery. For example, the control of air quality and temperature inside operating theaters and post-operative recovery room warrants attention, and merits long-term surveillance to protect both surgical patients and workers by preventing bacteria growth.

This chapter presents a complete RFID-SN performing the jointed monitoring of environmental parameters and the humans' interac-

tions with the surroundings at the purpose to detect and event predict the occurrence of anomalous events. The system, which physically implements the hierarchical structure of Fig. 6.13, consists of a multi-antenna reader unit that interrogates a variety of conventional tags and a multi-function RFID sensor nodes.

The *analog tags* (e.g. the conventional RFID tags) are displaced onto moving parts of the *space*, like cabinet windows or mobile equipments, as well as onto the access doors and on the wall of critical areas of the infrastructure to be monitored. The data produced by those tags is the level of the electromagnetic field (in the form of RSSI) they backscatter toward the A_m antenna of the reader during the interrogation. During an initial calibration, the system stores the electromagnetic fingerprint of the environment, e.g. the values of the RSSI produced by the various sensors in stationary conditions as in the case of an anti-theft system. Accordingly, any geometrical change of the environment such as somebody moving inside [132], the people's interaction with doors, cabinets or with any other critical device will produce an *environmental modulation* of the backscattered fields and it will be perceived by the system as a perturbation of the RSSI collected by the reader. Due to the uncertainties related to such measurements [35], these analog RFID tags are preferably used as thresholds sensors since they provide information about those events that are characterized by a strong contrast between normal and abnormal working conditions (e.g. the opening/closing of doors and cabinets and shadowing/scattering caused by human presence). This class of sensors include also the wearable badges [57] used for identifying authorized personnel accessing the targeted areas. The *digital tags* are instead provided with specific internal/external sensors that produce quantitative data about the specific physical parameters under observation (light, humidity, temperature, deformation and others) is directly suitable for a remote interpretation.

The presented study addresses the implementation of the control and coordinations software and the deployment of the whole network in a real environment. The presented architecture was originally developed in the framework of the SCISSOR European Project that is concerned with the security of critical infrastructures (pipelines, power generation, nuclear plants...) against cyber-attacks and phys-

ical threats. For this reason, the potentials of the system will be exemplified through an industrial-oriented application. Nevertheless, the proposed example is not out of the mainstream of the thesis, as the the platform is inherently versatile and tailorable to any specific domestic, residential or clinical settings in terms of physical coverage area (number of rooms), personal and ambient parameters to be monitored and, accordingly, the type of detectable events.

9.1. The Radio-board

The core of the RFID-SN is a fully configurable digital tag, hereafter denoted as *radio-board*, able to integrate different sensors for sampling and transmitting multiple environmental parameters. The *radio-board* is based on a RFID chip [40] that provide a native integrated electronics for sensing beside the pure identification features. It includes an Analog-to-Digital Converter (ADC) capable to control up to two analog external sensors (resistive, capacitive, optical...) and an integrated temperature sensor with programmable dynamic range in the interval $-40/150^{\circ}\text{C}$. The chip can be used in fully passive mode for synchronous reading, or in battery-assisted mode for extended read range (P_{chip} from -5 dBmW down to -15 dBmW) and/or autonomous (asynchronous) logging mode.

To master the wide range of functionalities the IC is provided with, the transponder was engineered to make it operating in several radiation and sensing modalities while making use of a same mother PCB layout. The *radio-board* is hence composed of three parts (Fig. 9.1): i) a radiating meander-line antenna; ii) a spiral impedance transformer iii) additional expansion traces for battery and sensors interconnections. The board is equipped with several tuning elements (trimming points, solderable elements and lumped impedances) properly located onto the conductive traces. By acting on such elements, the performance of the radio-board can be optimized in terms of frequency of operation, impedance matching, radiation gain depending on the target positioning. The board can be used either as a tunable standalone sensor for application onto low permittivity and low-losses materials, or as a basic module to be coupled to an external patch-like booster for application

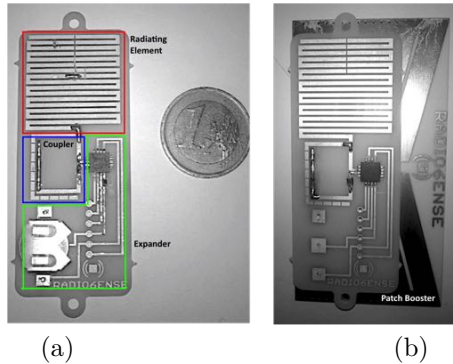


Figure 9.1.: Prototypes of configurable radio-board: a) Stand-alone configuration equipped with a battery; b) Battery-less *radio-board* coupled to a patch-like booster.

over electromagnetic-hostile things, such as lossy materials (concrete walls) or metallic surfaces. The experimented read-ranges of both the configurations were 2 m and 7 m, respectively for the passive and bap mode (@868 MHz, 3.2 W EIRP).

The digital tag works as a multi-channel sensor node, even if the local computation capability is rather modest and restricted to sensor handling. Each tag reproduces at the lowest level the concept of a modularity own to the architecture of the RFID-SN since the logic unit of the board can selectively activate one or more sensors according to the custom-commands that are elaborated by the control software running on the central unit.

9.2. Control & Coordination Software

The RFID-SN is governed by a software module (hereafter denoted as *RadioScan*), written in C# .NET, which implements the remote control over the multi-level architecture of the network in Fig. 6.13. The structure of network is declared by means of an XML file which is associated to *RadioScan*. This file can be modified at run-time for achieving a dynamic control over the system, for example to switch

from asynchronous to synchronous mode and increase the sampling time within a specific zone if an anomalous event was suspected.

The Config file is conceived to implement the tree diagram in Fig. 6.13. *RadioScan* sets the operative configuration of the sensor network by *i*) selecting the zones of the space to be controlled (by switching on and off the corresponding antenna of the reader); *ii*) defining the specific interrogation modalities of the zones in terms of sampling rate, frequency and power emitted by each reader antenna; *iii*) selecting the things of each zone to be monitored and the relative attributes (by enabling/disabling tags and activating the embedded sensors).

Fig. 9.2 shows an example of config file describing a network consisting of four reader antennas sourced at 868 MHz by 30 dBm power according to the sequential rotation {1,2,4,3}. The spatial architecture is defined in the <NetworkConfiguration> section where each antenna of the reader is associated with the list of the tags to be interrogated within the corresponding zone of the space (ZONE 1 "name=" tag_list_A.1). Those *radio-boards* that are equipped with multiple sensors ("type" = Radio-Board) require additional fields for the selection of the on-board sensors and the settings of the corresponding sensor front-end, such as the type of the sensor, the voltage levels defining the dynamic range and the resolution of the sensors and the parameters for data-logging functionalities.

The output of the software are *i*) a Log file containing the current network configuration (active reader antennas and corresponding detected sensors) which is automatically saved at runtime when the software is started and *ii*) a formatted string containing the time stamp and the (multi) sensor data of each tag at the current interrogation cycle. The string is both stored in a local text file and streamed over TCP-IP port for remote processing.

In a possible complete architecture, these outputs could be accessed in real-time by an upper Decision layer (whose description is out of the scope of this thesis) that implements detection algorithms and, if needed, sends back the Control Software some input commands to consequently update the network topology. Provided that each sensing node is reconfigurable via software, the RFID-SN as a whole is definitely provided with the capability of self-configuration, which

is a key requirement for IOT platforms.

```
<InterrogationSettings>
  <add key="FrequencyRegion" value="European" />
  <add key="Frequency(MHz)" value="868" />
  <add key="Power(dBm)" value="31" />
  <add key="ReaderAntennas" value="1243" />
  <add key="Mode" value="RealTime" />
  <add key="SamplingTime(sec)" value="1" />
  <add key="TCP/IP_stream" value="true"/>
</ InterrogationSettings >

<NetworkConfiguration>

<ZONE1 name="tag_list_A.1">
  <tag name="T1" type="analog"></tag>
  <tag name="T2" type="RadioBoard
  Sensor Enabled ( RSSI="true" Temp="true"
                  Ext1="false" Ext2="true" Battery="false")

  Sensor Types (Sensor1="." Sensor2="Light_")

  Sensor Front-End Settings (V1="210" V2="310" ground="false"
                             Rref="8" current="31"....)

  DataLogger Settings (State="Start" Interval="1"
                      Delay="6" Storage="normal"
                      Form="outoflimits"...)</tag>
  <tag name="T3" type="analog"></tag>
</ZONE1>
<ZONE2 name="tag_list_A.2">
  <tag name="T4" type="RadioBoard
  Sensor Enabled ( RSSI="true" Temp="true"
                  Ext1="false" Ext2="true" Battery="false")
</ZONE2>
```

Figure 9.2.: Example of Config File defining the configuration of the network.

9.3. Application to the Physical Security in Electric Plants

The following application example lies out of healthcare scenario. The entire RFID-SN was indeed primarily tested in the context of the EU-funded SCISSORS project (Security in trusted SCADA and Smart Grids, www.scissor-project.com) aimed at developing a solution for integrated monitoring and protection of critical industrial settings possibly exposed to cyber attacks. The project addresses the design of a holistic, multi-layered, security monitoring and mitigation framework, spanning all the issues related to the control *i*) of the environment, *ii*) of the network traffic, *iii*) of the hardware and software system components, *iv*) of the people accessing the infrastructure, and *v*) the independent monitoring of the control process itself. The environmental sensing and monitoring layer of SCISSORS are demanded to the proposed RFID-SN.

A first version of the RFID-SN was deployed and preliminary tested within the Electrical transformer secondary substation of the University of Rome Tor Vergata (Fig. 9.3 a). Similarly to other smart-grid substations, the bunker room is located in the basement of the building and it is a restricted access area. The room contains two working transformers, several control cabinets, a couple of electric generators and many high-power cable bundles.

9.3.1. Events to be detected

The events to be detected were the authorized/un-authorized accesses to the cabin, possible tampering of the machineries, humidity changes, flooding of sensitive areas and power overload of wire harnesses. At this purpose, the radio-boards were equipped with humidity and light sensors and with high-temperature external probes. Analog tags were used as well to detect intrusions and mechanical changes of the room. Each event has been detected through the processing of a single attribute or a combination of them (Tab. 9.1).

Table 9.1.: Events to be detected by the RFID-SN inside the electrical cabin and corresponding attributes to be measured.

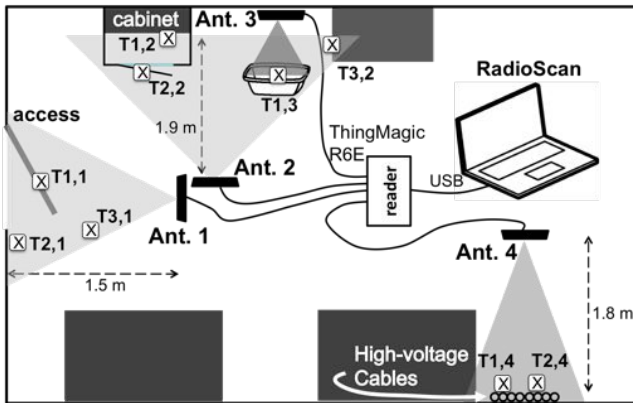
EVENT	ATTRIBUTES
Authorized/un-authorized access	RSSI from tags installed onto the access door; ID code from wearable tags; Light on/off;
Flooding	RSSI from tags placed over the floor; Ambient Humidity;
Harness Overload	Temperature variation of cables and bundles of cables (high and low range);
Manumission of cabinets	RSSI from tags placed onto the cabinet window; Temperature variation inside the cabin;

9.3.2. Network configuration

The configuration of the RFID-SN is sketched in Fig. 9.3 (b). A 1W long range RFID reader (ThingMagic M6E) connected to four antennas (circularly and linearly polarized patches) was used to monitor four different zones ($M=4$) in the cabin: Access (A_1); Cabinets and energy meters (A_2); Flooding sensitive area (A_3); High-power Cable bundles (A_4). The set of RFID tag (Tab.Tab. 9.2) comprised five radio-boards, embedding heterogeneous sensors, and four analog sensor tags [57], hereafter referred to as W-tags. Those latter are platform-tolerant tag which can be used as wearable badge for automatic access identification of operators, as RSSI markers over doors and cabinet windows to detect a possible interaction with a persons and even deployed over the ground and wall for flooding control. The overall number of channels of the network was $C = 10$.



(a)



(b)

Figure 9.3.: a) Electrical transformer secondary substation of the University of Rome “Tor Vergata”. b) Schematic representation of the deployed RFID-SN. The gray triangles highlights the read region (zone) of each antenna.

Measurements were carried out in both rest (stationary) and operative (dynamic) conditions. The critical events listed in Tab. 9.1

Table 9.2.: Network Configuration

ANTENNAS (zones and events)	TAGS	SENSOR CHANNEL
A₁ : Zone 1 (Authorized/un-authorized access)	$T_{1,1}$ - W-tag	$S_{1,1,1}$: RSSI
	$T_{2,1}$ - R-board	$S_{1,2,1}$: RSSI $S_{2,2,1}$: Light (S133-14 p.diode)
	$T_{3,1}$ - W-tag	$S_{1,3,1}$: RSSI
A₂ : Zone 2 (Manumission of cabinets and flooding)	$T_{1,2}$ - R-board	$S_{1,1,2}$: Temp (internal sensor)
	$T_{2,2}$ - W-tag	$S_{2,2,2}$: RSSI
	$T_{3,2}$ - R-board	$S_{1,3,2}$: RH% (HCZ-D5 sensor)
A₃ :Zone 3 (Flooding)	$T_{1,3}$ - W-tag	$S_{1,1,3}$: RSSI
A₄ : Zone 4 (Harness Overload)	$T_{1,4}$ - R-board	$S_{1,1,4}$: Temp (PT1000)
	$T_{2,4}$ - R-board	$S_{1,2,4}$: Temp (internal sensor)

were emulated several times by the help of volunteers.

9.3.3. Flooding and humidity

Flooding is a recurring event in smart grids, especially when the infrastructure comprises several underground cabins. In the case of partial flooding the signals backscattered by the W-tags placed on the critical regions of the floor are strongly perturbed. Eventually, when a tag is sensibly submerged by water it becomes undetectable by the reader due to the abrupt change of the electromagnetic parameters of the surrounding medium which detunes the antenna. In addition to this threshold detection, the Radio-boards with relative humidity sensors can be used to detect abnormal variation of the environmental relative humidity (%RH) which can be related to flooding.

The flooding event was emulated (Fig. 9.4) by filling a plastic basin

with water. A W-tag ($T_{1,3}$) was placed on the bottom of the basin. In normal conditions (absence of water), the tag was detected by the antenna A_3 with a stable level of RSSI ($S_{1,1,3}$). Then, as soon as it was covered by the liquid, it was severely mismatched and became unreachable by the antenna.

The humidity change was instead simulated by placing the Radio-board $T_{3,2}$ equipped with the humidity sensor into a glass bell together with a piece of wet cotton. When closing the glass, the internal relative humidity gradually increased up to saturation. Then, it rapidly came back to the initial ambient condition as soon as the top was removed. An example with some open/close cycles is reported in Fig. 9.5 showing the impedance of the sensor ($S_{1,3,2}$) which is inversely proportional to the humidity level detected by the antenna A_2 .

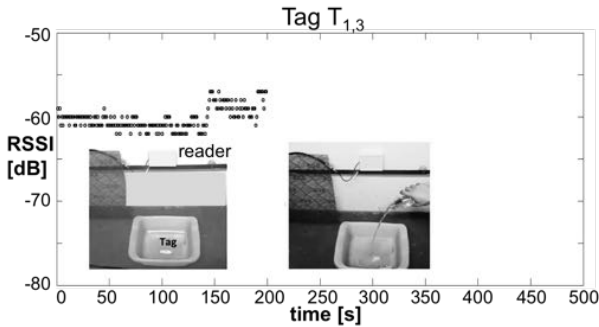


Figure 9.4.: Backscattered power from the analog tag $T_{1,3}$ during the simulation of a flooding event.

9.3.4. Harness overloading

An anomalous working load of the cabin transformer could produce high currents over the distribution cables. Radio-boards including internal temperature sensors and/or connected to external high-temperature probes can be placed over the cable harness to monitor their surface temperature which is related to the currents flowing into the cables themselves. Those sensors can be also used to obtain

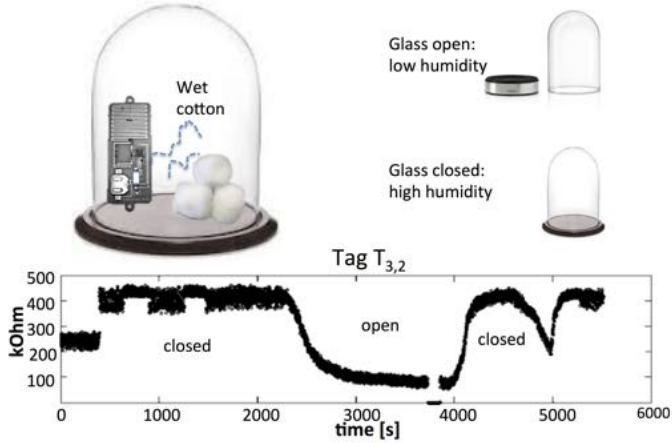


Figure 9.5.: Impedance of the humidity sensor connected to the Radio-Board $T_{3,2}$ measured during cyclic humidity variations induced by opening/closing the glass bell.

indirect information about the aging of the dielectric insulators of the harness.

In the present experiment, some events of power overloading were reproduced by manually warming-up two harness inside the cabin by using a heat-gun. Fig. 9.6 shows the temperatures ($S_{1,1,4}$ and $S_{1,2,4}$) detected by the two Radio-boards ($T_{1,4}$ and $T_{2,4}$) attached over the two considered cables running along the perimeter wall of the cabin, the first one integrating a platinum thermo-resistance (PT1000) whose extremal sensitive part was at direct contact with electric cables and the second one detecting the temperature by its internal sensor .

9.3.5. Cabin Access and Manumission

In normal conditions, the door of the cabin is closed and the internal scenario is completely dark: accordingly, a low-light signal can be collected by the light sensor of a Radio-board $T_{2,1}$ placed

in proximity of the access doors. If somebody opens/tampers the door and gets inside the cabin, the system will detect an increase of the light (coming from outside or emitted by a torch or by any other light source), as well as a distortion of the RF fingerprint of the cabin due to the presence of moving people which perturbs the electromagnetic field produced by the reader antennas. Finally, if the subject is provided with an RFID badge, the passive network is able to verify his identity and his right to access the cabin, for instance in case he is a maintenance personnel.

9.3.5.1. Authorized access

Fig. 9.8 shows a subset of the signals recorded by the sensor network when an authorized technician came into the cabin for ordinary maintenance (screenshots in Fig. 9.7). In the initial reference condition, the light in the room was off ($S_{2,2,1}$ signal of RadioBoard $T_{2,1}$) and the W-tags for the access control ($T_{1,1}$) and cabinet opening ($T_{2,2}$) returned stable RSSI values. No authorized people were detected inside the ambient (null signal from wearable tag $T_{3,1}$). The evident drop in the value of the RSSI collected by sensor $T_{1,1}$ reveals the opening of access door. Immediately after, the person entering the room was automatically recognized by the system and classified as “authorized person” through his badge identification ($S_{1,3,1} \neq 0$). The maintenance technician turned on the light ($S_{2,2,1}$ switches to ON state) and opened the electrical cabinet (sensor on the door cabinet $T_{2,2}$ was no longer read in the open position) to perform ordinary operations, with no modification of the equipment temperature. Finally, the technician approached the exit door and turned-off the light; the system detected again his badge and recorded the exit.

9.3.5.2. Un-Authorized access and attack

In a second experiment, the person entering the room was an intruder without any badge. He in the dark by using a torch, opened the windows of the a cabinet and artificially increased the temperature of an internal equipment to emulate a tampering event (Fig. 9.9). The multi-parameter recording by the RFID-SN is shown

in Fig. 9.10 and could be interpreted, a posteriori, as follows. When the person came inside, the system recognized the door opening through a perturbation of the RSSI from the tag $T_{1,1}$. Since no pre-registered ID code was detected, the person could be classified as an intruder. Then a variation in the light level was revealed by the sensor $T_{2,1}$ for a short period suggesting that the intruder turned on the light just for a few seconds or used a torch. The sensor $T_{2,2}$ detected an interaction with the cabinet and during this time interval the internal temperature of the cabinet abnormally increased (sensor $S_{1,1,2}$ of $T_{1,2}$). This event could be considered as a warning of a potential power overload of some internal circuitry produced by a possible manumission. The sensor $T_{1,1}$ at the main door detected again an interaction when the attacker came out the cabin.

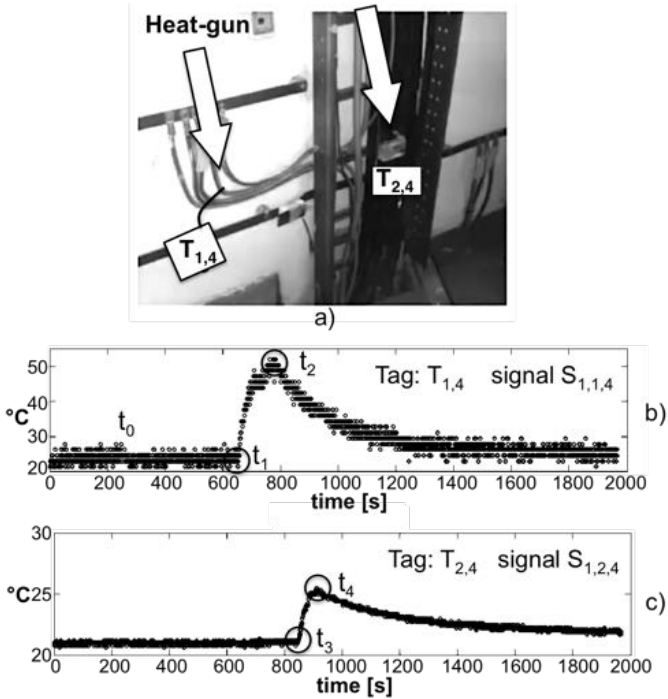


Figure 9.6.: Power overloading of two cables a) equipped with radio-boards $T_{2,4}$ (internal temperature sensor) and $T_{1,4}$ (external PT1000 temperature sensor). b) and c) Temperature recording during an artificial warming by an heat gun in the time intervals $[t_1, t_2]$ and $[t_3, t_4]$ for the two cables, respectively.

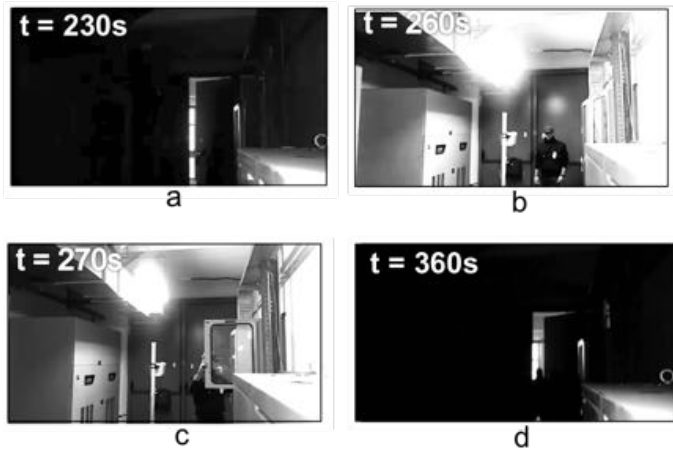


Figure 9.7.: Screenshots from the authorized access to the electric cabin and interaction with an equipment. a) door opening; b) light on and RF badge detection; c) cabinet opening; d) light off, badge recognized, door open and closed

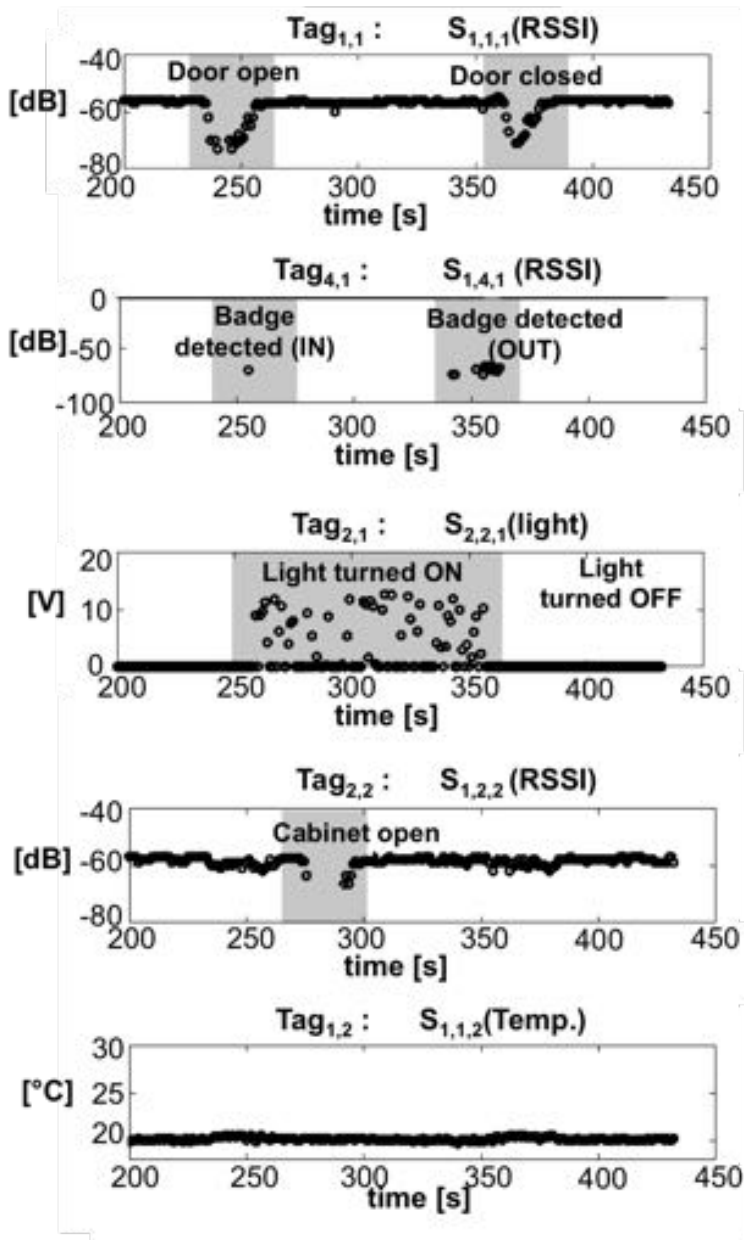


Figure 9.8.: Sub-set of signals collected by the RFID-SN in case of authorized access to the electric cabinet.

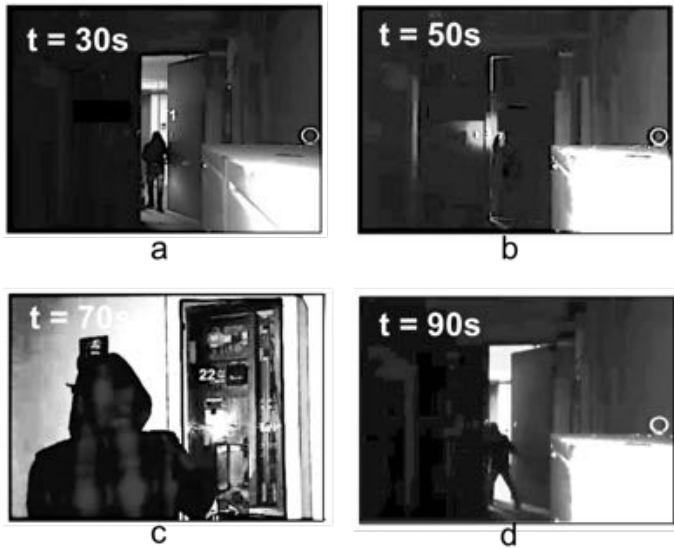


Figure 9.9.: Screenshots from the un-authorized access to the electric cabin with tampering. a) door open; b) torch pointing toward the light sensor; c) cabinet opening and tampering; d) attacker going outside

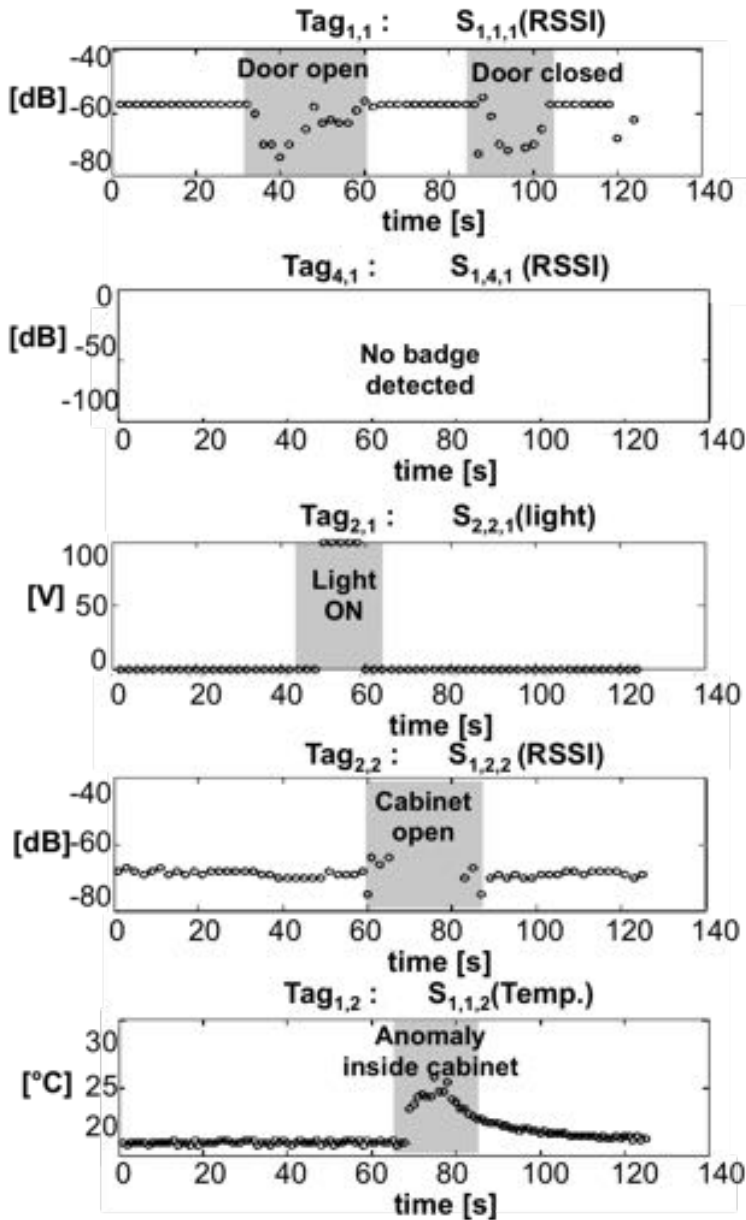


Figure 9.10.: RFID-SN measurements in case of an un-authorized access to the electric cabinet producing a thermal anomaly.

9.4. Conclusions

The proposed platform exploits the combined processing of analog and digital signals to capture the users' interaction with specific nearby objects and the variations of ambient parameters. In the presented experiment the deployment of the network inside the cabin required a try and error effort to identify the best position of the reader antennas so that all the tags were correctly read by the network. This procedure could however be driven by electromagnetic modeling as in [116] which includes the scattering of the nearby environment, and by evolutive optimization algorithms as in [133] for automatic antenna placement.

Despite the first implementation of the system aimed at empowering the traditional supervisory control of industrial processes¹, the same architecture is prone to be straight away adopted for health-care monitoring. By using the same physical rationale, the attributes listed in Tab. 9.1 can be processed in similar combinations to detect health-related significant events. Just to give few examples: the badge detection helps identifying patients and medical personnel entering limited-access zone of the hospital like infective disease wards and, accordingly, to control and the reduce the virus spreading; the monitoring of the subject's interactions with the medicine cabinets permits to transparently verify its compliance with the medical treatment in real-life conditions, while the overall fluctuation of analog signals from wearable and ambient tags gives a rough estimation of its activity rate.

¹A demo video of a realistic testbed running in an operational smart grid in Favignana (Italy) can be found at <https://www.youtube.com/user/Radio6ense>.

10

Conclusions

Driven by the enormous progress in the cutting-edge field of *Epidermal Electronics*, this Thesis has faced the challenging issues related to the remote powering and communication with the emerging class of tattoo-like devices. The main scientific contribution of the work regarded the development of a new typology of bio-integrated UHF RFID sensors suitable for direct placement over the human epidermis. The topic was addressed from an electromagnetics point view both at the hardware and the system level, drawing a possible path towards the fulfillment of IoT Smart Spaces where people empowered by imperceptible sensors, the surrounding environment and their mutual interactions are pervasively monitored.

Starting with a theoretical approach, the physics of the phenomena were investigated in detail to define fundamental limitations and upper bounds in the performance achievable by UHF radiators placed over lossy medium. The relationship between the antenna size, shape and materials and the corresponding radiating/matching properties as well as the strong effects exerted by the intra/inter-subjects variability of tissue compositions were clarified through both numerical and experimental analysis. Particular effort was then given to the selection of thin-epidermal membranes and, above all, to the experimental characterization of their static and even time-variant UHF dielectric properties. The described

method has broad validity and was successfully cross-applied to the RF measurements of heterogenous materials far from epidermal background such as rubber compounds, glasses. Advanced fabrication processes were also explored to look for cost-effective and easily accessible method to deposit conductive traces over thin specialized film. As the lower conductivity of the radiator has been demonstrated not to have a crucial role, low-cost ink-jet printing using sintering-free conductive inks deposited by COTS printers turn out to be an appealing solution, especially for the rapid mass prototyping of epidermal devices.

The gained knowledge led to the design of a miniaturized epidermal RFID sensor suitable to the accurate - clinically significant- measurement of the skin temperature. It is worth noticing that the developed technology has already moved from the level of laboratory demonstrator to a device with proven utility in human clinical studies currently on-going at the Tor Vergata Hospital.

The presented findings can be considered for the electromagnetic community a useful benchmark providing guidelines for the optimal design, fabrication and experimentation of real RFID epidermal transponders.

Overall, the work pushed forward the current boundary of radio-sensor skin technology, that was mostly limited to low-frequency NFC systems, laying the basis for the inception of breathtaking innovations in the healthcare practices of tomorrow. Since UHF epidermal transponders don't require the active users' collaboration, they are ready to become the building block of new-generation distributed assisting systems capable to collect information about the health and wellness of freely moving people crossing through gate-like setup connected to the IoT infrastructure. This represents a decisive step forwards with respect to the state of the art where skin-tight devices are usually considered as single entities not connected to the IoT. This potentiality was clearly demonstrated through the implementation of a RFID-based ecosystem wherein the skin sensors can be integrated with more assessed wearable and environmental tag. Thanks its adaptive and scalable structure the proposed wireless sensing platform can be deployed in any health-related scenarios, including home and community-based settings. The presented examples showed the feasibility of extracting high-

level information (sleep behavior, anomalous events...) through the processing of heterogeneous multi-channel electromagnetic signals coming from the interaction between one or more users and the surroundings environment.

Open issues and Future Research

Despite the significant accomplishments, several issues are still open and intriguing for future research perspectives.

The first aspect concerns how to improve the radiation efficiency of epidermal antennas and, accordingly, the range of the RFID link. In the author's opinion, there is a rather small margin to improve their efficiency/gain without increasing the thickness, but some solutions are still worthy to be explored. A possible way to increase the decoupling of the antenna from the body, and hence its efficiency, could be the use of ultra-thin biocompatible membranes with a huge dielectric constant and low losses, like polymers doped with ceramic powders [134]. This topic opens to fruitful collaboration with material scientists to synthesize novel engineered membranes. The second - more electromagnetic-oriented- option considers the investigation of artificial magnetic surfaces (AMC) as ultra-thin skin-decoupling layer, possibly in combination with the above high-permittivity films. Currently, similar configurations require a surface area bigger than the antenna size and are hence not suitable to a comfortable skin application [135].

Boosting the epidermal radio-sensors with a local power source to reduce the IC sensitivity would likely remain the most efficient method to significantly increase the interrogation distance. Organic polymer-based conductors (PEDOT-PSS, polyaniline...) are promising for the development of eco-friendly and biocompatible non-metallic thin film batteries (thickness $< 100\mu m$) that can be transparently integrated within the antenna element through a one-step multimaterial ink-jet printing process.

Furthermore, to really implement the idea of "lab on skin", the sensing functionalities of the epidermal radio-sensor must be expanded. On-going research is already experimenting nano-based resistive

(e.g. graphene oxide) sensors connected to IC for the multifunctional temperature and perspiration monitoring. These receptors has a great potential to be functionalized with chemical/biological substances for the selective detection of sweat electrolytes, metabolites, pathogenic bacteria. Digital and analog transducing mechanisms could be also combined by depositing the tag on the advanced hydrogel-like substrates sensitive to the fluids exchanges s at the skin interface.

Concerning the system issues, major constrains for the massive adoption of RFID in IoT Healthcare system are posed by the energy supply management of the readers. Real applications would greatly benefit from the large scale production of full RFID nodes with self-sufficient power for both communication and computation and also wireless data connectivity toward the cloud. A very focused effort is then required to implement low-computational detection algorithms that can be locally run at node level for real-time detection and event prediction of anomalous events. Furthermore, in spite of the EPC is a standard protocol, the proprietary software libraries for control the reader and handle the sensor-oriented IC handling are heavily manufacturer-dependent. A general purpose, and possibly open-source development framework would really simplify the design and implementation of high-level applications.

Appendix A: Legacy

The author's work has simulated the development of an original research branch concerning the Finger-Augmented Devices (FAD) [136], i.e. a particular wearable technology aimed at turning the human fingers into enhanced sensing surfaces for advanced human computer interfaces.

Indeed, as stated in the introduction, epidermal sensors can have the twofold role of *sensing the body through the skin* and *sensing the surroundings through the skin*. In the latter case skin-mounted devices are used to replace damaged sensory functions (e.g. tactile, thermal...) and even extend the sensorial capabilities beyond the innate senses.

This appendix presents the proof of concept of a novel RFID-FAD assistive device consisting of a wrist-worn reader and a conformable addendum on the distal phalange integrating a tag with a thermal sensor on the tip. The system is aimed at providing impaired people with a lack of thermal feeling with a feedback about the temperature sensed by the their fingertips.

The following study was supported by a Master Thesis student, Mrs. Veronica De Cecco, who worked under the author's supervision.

Finger-Augmented RFID System to Restore Peripheral Thermal Feeling

Peripheral neuropathy [137] is a pathological condition caused by damages to the nerve pathways responsible for receiving, transmitting, or processing external stimuli. Diabetes, thyroid disorders, rheumatoid arthritis, alcoholism and vitamin B12 deficiency as well as medical treatments (HIV drugs, statins, radio and chemotherapy) are common causes of this transient or permanent disorder, which is usually accompanied by somatosensory impairments, including the loss of pain, touch and/or temperature sensation. Among these disease-related crippling symptoms, dealing with lack of the temperature feeling, especially concerning the heat sensation, seriously impacts on the execution of common tasks which require judging the temperature of everyday things like the dish or bath water. It can even result in severe burns occurring before the subjects' awareness. While medical treatments (antidepressant and anti-seizure) are often merely a palliative, and in any case not tolerable over the long-term in the form of irreversible pathology, there exists a concrete social need to provide impaired subjects with comfortable technological solutions recovering their physical limitations and hence improving the quality of their daily life.

This study investigates the possibility of RFID-based *finger-augmented*

device [136] able to artificially restore the temperature feeling of the fingertips. The wireless system, hereafter denoted as *RadioFingerTip* (Fig. 11.1), comprises an epidermal-like battery-less tag properly shaped around the fingers with temperature sensing capability and a wristband module integrating the interrogating antenna and a miniaturized reader unit. The fingertip tag is illuminated by the reader antenna and, as soon as the user touches an object with its fingertip, the temperature value of the contacted surface is transmitted back to the reader where it becomes available for processing. This apparatus exploits a “hand-free” interaction in a way that compliments the natural affordances of everyday interaction with objects and doesn’t hinder the fine-grained dexterity of the dominant hand, thus greatly improving its social acceptance by the users.



Figure 11.1.: Concept of the RADIOFingerTip system for augmented touch comprising an epidermal UHF RFID sensor tag and a wrist interrogating device like a smartwatch.

The idea of providing the hand with RFID capability has been already considered in recent years. The use of a glove or RFID bracelet readers, mostly working in the HF band, was proposed to detect the tagged tools people interact with and accordingly infer the performed activities [138, 139, 140]. From another side, finger-worn antennas were presented for general purpose BAN applications in the UHF, ISM and UWB band [141, 142, 143, 144]. More recently, even fingernails have been considered as suitable

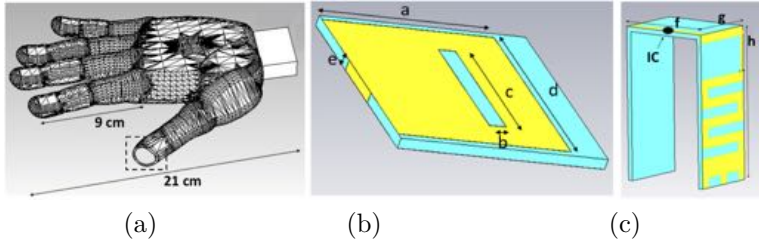


Figure 11.2.: (a) CAD model of the reference hand (b) Layout of the wrist-worn folded patch antenna (c) U-shaped meandered dipole for the fingertip. Sizes (in [mm]): $a=50$, $b=5$, $c=37$, $d=56$, $e=3$, $f=1.9$, $g=45$, $h=14$.

surface for electronic components [145, 146, 147, 148]. However, to the best of author's knowledge, FADs are usually intended to be interrogated by wired, or even wireless, off-the body devices while the case of a whole on-the arm sensing RFID system has not yet been considered so far.

The aim of this early study is to demonstrate whether it is possible to establish a reliable UHF RFID-sensing link through the hand and to quantify the power required to activate the sensor tag.

11.1. Components of *RadioFingerTip* system

The feasibility and the preliminary design of the system (Fig. 11.2) were referred to a realistic hand model that was used for both numerical modeling and rapid prototyping by 3D printing. The reference hand consists of a 3D hollow structure made of a polymer shell ($\epsilon_{ABS} = 1.8$, $\sigma_{ABS} = 10^{-3} S/m$, measured as in chapter 4) filled by a liquid phantom ($\epsilon_{phantom} = 41.2$, $\sigma_{phantom} = 0.95 S/m$, [149]). The wrist antenna was derived from [23]. The layout is a shorted patch provided with a miniaturization slot and a variable short-circuit edge to easily adjust the resonance frequency when the antenna is placed over the hand mockup. The supporting dielectric

is a low-permittivity foam (Forex, $\varepsilon_F = 1.55$, $\sigma_F = 6 \cdot 10^{-4} S/m$) capable of moderate bending around the wrist.

The fingertip tag is a U-shaped meandered line over 0.6 mm biosilicone ($\varepsilon_S = 2.5$, $\sigma_S = 5 \cdot 10^{-3} S/m$, from chapter 4) that can be comfortably wrapped around the index finger. The sensitive part, i.e. the microchip, is placed at the tip of the finger. The edges of the MLA are provided with tuning pinnacles for post-fabrication impedance adjustment with a rate of 5 MHz/pinnacle.

11.2. Prototypes and Measurements

The hand mockup was fabricated by the Zortrax M200 printer using ABS filler with a density of $1.06 kg/dm^3$. The palm and fingers were separately printed and then united by silicone glue. The mockup was filled by a liquid and then sealed through a cover at the wrist level.

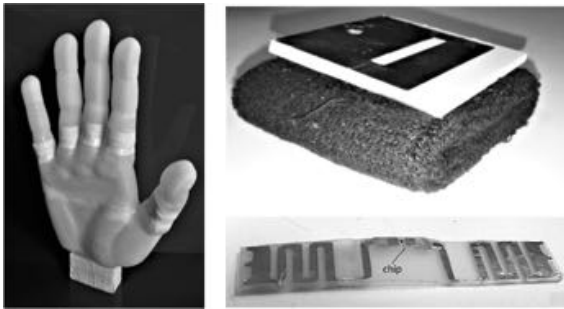


Figure 11.3.: 3D-printed hand mockup and fabricated prototypes of the reader antenna integrated with a sport wristband and of the unfolded fingertip tag

Copper-made prototypes of the antennas were fabricated by two-axis digital plotter (Fig. 11.3). The epidermal tag was glued to the IC NXP G2IL¹ ($Z_{chip} = 25 - j237 \Omega$, $P_{chip} = -18dBm$) terminals

¹It worth specifying that this chip does not allow temperature sensing but the good power sensitivity allowed a useful flexibility during the preliminary experimentation of the RFID link.

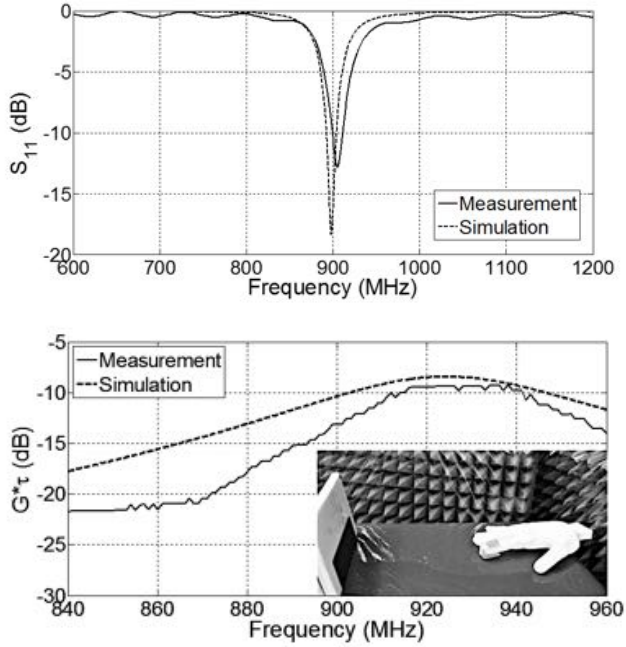


Figure 11.4.: Measurements results for (a) the reflection coefficient of the wrist antenna and (b) the realized gain of the fingertip tag.

and stuck over the U-shaped bio-silicone . The patch antenna was connected to a L-SMA connector and integrated within a sport wristband for better wearability.

First, the two antennas were separately characterized over the mockup in terms of reflection coefficient (reader antenna) and realized gain (fingertip tag). Measurements results shown in Fig.11.4 were in good agreement with the corresponding simulations.

The wrist and the fingertip antennas were then characterized as a whole system. As the on-body communication channel between the antennas takes place in the radiative near field, with the human body producing a strong interactions (scattering and huge

power absorption), the link performance was properly modeled by two-ports network. Port 1 and port 2 corresponds to the reader's antenna and to the tag terminals, respectively,

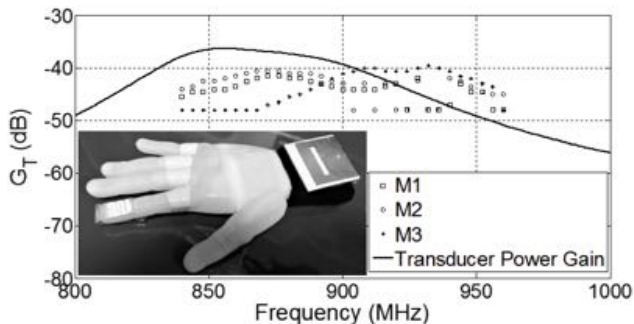


Figure 11.5.: Simulated and measured *transduction power gain* in three measurement sets (M1,.. M3). Inset: full-system measurement set-up.

The communication performance were quantified in terms of the *Transduction Power Gain* (G_T), i.e. the ratio between the power $P_{R \rightarrow T}$ really delivered by the reader to the chip and the available power from the reader generator $P_{av,R}$ [60]:

$$G_T = \frac{P_{R \rightarrow T}}{P_{av,R}} = \frac{4R_{chip}R_G|Z_{21}|^2}{|(Z_{22} + Z_{chip})(Z_{11} + Z_G) - Z_{12}Z_{21}|^2} \quad (11.1)$$

where Z_G is the internal impedance of the reader (50 ohm). This metric accounts for the possible impedance mismatch at the reader-antenna port as well as at the tag-chip interconnection and it can be easily derived from the measurement of the turn-on power P_{to} of the tag ($G_T = P_{chip}/P_{to}$).

The achieved results were in reasonable agreement with simulations around the matched frequency of the wrist antenna. In the most favorable conditions, the maximum transduction gain was $G_T = -40$ dB. In this configuration, by assuming the interrogating antenna

sourced by a power $P_{in}=\{0.5W, 1W\}$, the corresponding maximum deliverable powers to the chip at 900 MHz would be $P_{R-T}=\{-13 \text{ dBmW}, -10 \text{ dBmW}\}$, respectively. These power values are lower than the current sensitivity of microchips with sensing capabilities. However, it is worth noticing that the considered hand model is oversized and the filling liquid is a lossier than the averaged hand tissues, so that the presented analysis provides very conservative (pejorative) results.

11.3. Sensing the temperature of the objects

The proposed system was finally experimented in a realistic application. The fingertip tag was connected to the EM4325 microchip that was thermally characterized in chapter 6. The fingertip and the wrist antennas were worn by a volunteer whose hands was sensibly smaller than the mockup (palm-to index finger distance 160 mm). During the experiment, the volunteer cyclically touched the desk whose surface was at room temperature and a plastic object previously heated up by a hair dryer. The acquisition software displayed in real time the backscattered power and the instantaneous temperature. The dynamic of the experiment is summarized in Fig. 11.6 with some snapshots while a full live demo is available online². The turn-on power required to read the temperature during the various gestures was comprised between $-25 \text{ dBmW} \leq P_{to} \leq -23 \text{ dBmW}$. These values are fully compatible with extremely low-power reader modules.

It is worth mentioning that the hand motion produced some changes of the backscattered field by the fingertip antenna toward the reader due to variable relative position and shadowing between the two antennas. Such a power signature (Fig. 11.6) could be used to detect and recognize particular hand gestures, as recently proposed by the author in [115].

²<https://youtu.be/DGUkYqmt-5Q>

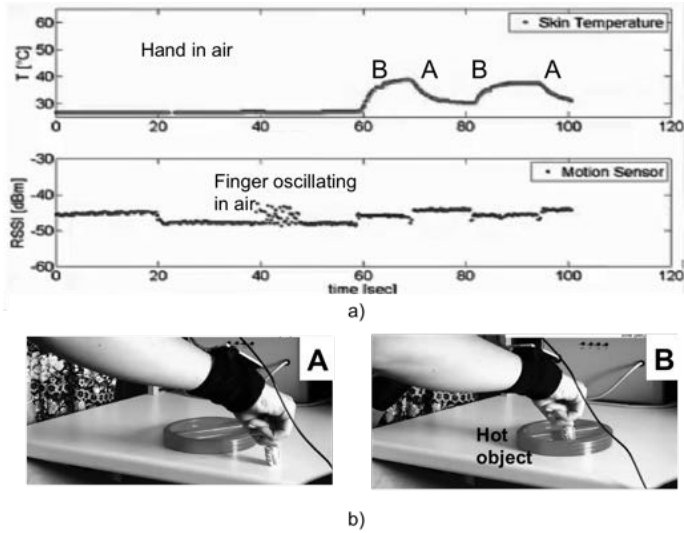


Figure 11.6.: Example of real-time temperature and RSSI measurement by the RADIOFingerTip.

11.4. On-going research

The reported early results are encouraging. In spite of the strong power loss induced by the human body, it is feasible to establish a robust link between an interrogating wrist antenna and a battery-less epidermal finger tag. The required power to activate currently available microchips with sensing capability revealed compatible with state of the art battery-driven readers so that a real integration of all the electronics within a standalone wristband device look feasible. Current research is addressing the response of multiple tags placed on all the five fingertips during the execution of common hand gestures. The multi-finger system is particularly interesting for a multi-parametric sensing, for example to quantify the touch pressure (medical diagnostic, robotic sensor), restore the haptic perception and even measure some not tactile-sensitive parameters of the touched object like the PH.

Appendix B: Other Research

12

RFID-inspired microelectronic systems for Wireless Brain Machine Interfaces

Wireless Brain-Machine interfaces (BMI) are among the ground-breaking applications in the field of body-centric communications for the management and the treatment of severe neurological conditions (spinal cord injury, stroke or multiple sclerosis..)[150, 151]. Typical BMI schemes comprise implant electrodes picking up the neuronal electrical impulses that are transferred to an external unit where the acquired data are decoded into commands for controlling artificial actuators, e.g. prosthetic limbs. To date, one of the main challenges towards clinically viable BMIs is the lack of implantable life-time lasting devices. Indeed, most of the solutions currently adopted in clinical practice require conventional or rechargeable battery, which may cause infection due to replacement surgery or dangerous tissues heating during the charging mode[152]. The implantability poses major constraints on the size and total power supply of these systems. To monitor the electrical activity of the cortical neurons in various locations, high-channel-count recording is needed but the chip area per channel must be small for a compact device. State-of-the-art neural recording microsystems [153] dissipate very low power (less than 10 μ W/channel) thus being suitable to be remotely powered without the need of a local battery.

Short-range RFID backscattering technology based on inductive link is definitely an appealing and safe method for establishing wireless powering of and communicating with miniature battery-free cortical sensors [154, 155]. In such system, an external interrogator transmits a carrier signal from which the implant antenna captures energy to supply the integrated circuit. The data-link is then established through the modulation of the impedance terminating the implant antenna according to the acquired neurosignal. This extremely asymmetric system, where the complexity (and power consumption) is predominant at the interrogator side, enables chronically implantable passive neural sensors resembling RFID tags [151].

Building on the pioneering studies on RFID-inspired neural interfaces [156, 157], this work addresses the design and the optimization radio components of BMI system. First, the feasibility of using flexible electro-textiles in the realization of a comfortable to wear transmitting antennas is explored. For this purpose, both embroidered and commercially available textiles are experimented. Then, the study focuses on the implant side, with particular effort devoted to the miniaturization of the neural antennas which must efficiently couple with the external transmitter to collect sufficient power for microsystem supply.

The presented research activity was carried by the author at the Tampere University of Technology (Finland).

12.1. Modeling of the Transcranial Wireless Link

Short range RFID backscattering technology can be implemented using near-field reactive link. The inductive coupling between mm-sized loop antennas and an external transmitting loop is an effective method to wirelessly transfer energy through short distances and dissipative materials like the human tissues. The wireless link can be modeled as as linear microwave two-port network whose efficiency is described by the *Maximum Operating Power Gain* ($G_{p,max}$) which is the ratio of the power delivered to the implant IC

to the power supplied to the transmit antenna under the hypothesis that the both the ports are simultaneously conjugate matched. The $G_{p,max}$ can be easily expressed in terms of impedance parameters as [60]:

$$G_{p,max} = \frac{|Z_{12}|^2}{S + \sqrt{S^2 - |Z_{12}Z_{21}|^2}} \quad (12.1)$$

$$S = Re(Z_{11})Re(Z_{22}) - Re(Z_{12}Z_{21}) \quad (12.2)$$

where subscript 1 refers to the transmitting antenna port, and subscript 2 refers to the implant antenna port.

When transmitting power towards the human body, the exposure of the tissues to the electromagnetic field must be carefully considered. According to FCC regulations, Specific Absorption Rate (SAR) averaged over a volume containing 1 g of tissue must be at or below 1.6 W/kg. Since skin is the tissue layer nearest to the transmitting antenna, the maximum SAR occurs at the surface of the skin. Due to the relatively weak coupling between the implant and the external antennas, it is hereafter assumed that the load modulation at the implant side produces a negligible effect on the transmit antenna impedance (matching) and on SAR distribution. By numerical modeling the peak spatial average SAR (SAR_{max}) over 1g of tissue, the maximum SAR-compliant transmit power ($P_{t,max}$) can be derived as:

$$P_{t,max} = \frac{1.6 \text{ W/kg} \cdot \tau_{S-ta}}{SAR_{max}} \cdot P_t \quad (12.3)$$

where P_t is the simulation test transmit power and τ_{S-ta} is the power transmission coefficient between the simulation test source and the transmit antenna. The available power to the implant IC with the maximum allowed transmit power is:

$$P_L = G_{p,max} \cdot P_{t,max} \quad (12.4)$$

This power would be delivered to an implant IC which is conjugate-matched with the inductive implant antenna through a capacitive on-chip matching network. The voltage amplitude at the IC is given by :

$$V_{IC} = \sqrt{\frac{2|Z_{IC}|^2}{Re(Z_{IC})} \tau_{ra-IC} P_L} \quad (12.5)$$

where τ_{ra-IC} is power transmission coefficient determined by the antenna and IC input impedances Z_{ra} and Z_{IC} , respectively.

12.2. Electro-Textile Transmit Antennas

The outside-the-body unit that powers and communicates with implant must be lightweight low-profile and flexible such to comfortably conform to the users' head. These requirements can be satisfied by transmitting antennas made of electrically conductive textiles, also known as electro-textiles. Embroidered structures created from conductive thread and conductive fabrics were hence considered for the design of a wearable external transmit loop.

Simulations were performed by using a full-wave electromagnetic solver based on finite element method (ANSYS HFSS v. 15.05). The human head model consisted of 4 layered sphere with an outer diameter of 9.2 cm (2 mm skin, 2 mm fat, 7 mm bone and brain). The transmit antenna was placed 5 mm away from skin, while the implant site was the brain cortex just beneath the skull (see the inset of Fig. 12.1).

The textile conductors were modeled as infinitely thin surface characterized by the sheet resistance (R_S) of $0.4\Omega/\square$ and $1.25\Omega/\square$, respectively for the copper fabric and the embroidered pattern. These values were experimentally estimated through wireless reflectometry technique described in [158]. The substrate material for both wearable antennas was a flexible cotton fabric ($\epsilon_r = 2.2$, $\tan\delta = 0.08$).

The geometry of the wearable transmitting loops were hence optimized to achieve best link power efficiency with a reference 2-

mm³ copper cubic loop with a magnetodielectric core (SM MDF101: $\epsilon_r = 18$, $\mu_r = 17.5$, $\tan\delta_{magn} = 0.15$, $\tan\delta_{diel} = 0.02$ at 300 MHz). Fig. 12.1 shows the the maximum power transfer to the implant for optimal sized wearable transmitters. For both configurations the best coupling occurred around 300 MHz. At this frequency the loops exhibits the same optimized dimensions (30 mm radius and 17 mm width trace), with the peak $G_{p,max}$ of copper fabric approximately 3 dB higher than that of the embroidered pattern.

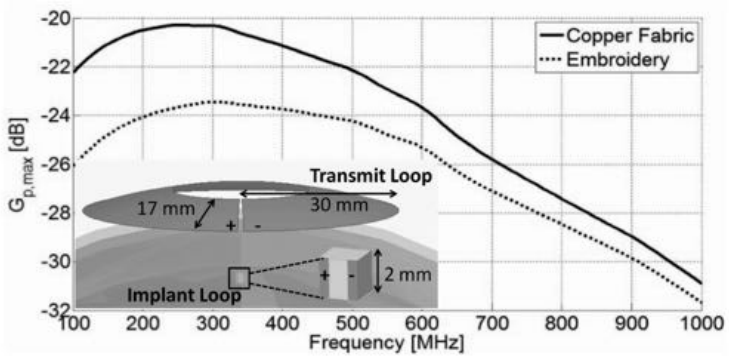


Figure 12.1.: Simulated maximum operating power gain of electro-textile conformal transmit antennas coupled to the SM-MDF101 cored $2 \times 2 \times 2$ mm³ implant antenna.

The electric and magnetic fields at the peak frequency for 100 mW accepted input power are illustrated in Fig. 12.2. The $P_{t,max}$ was estimated by accounting for the highest local SAR value evaluated on the skin surface, which occurs on the skin surface in the close proximity of the transmit antenna port. Simulations predicted 388 μ W of power delivered to the implant IC at 788 mV using the copper fabric transmit antenna, and 415 μ W of power delivered to the implant IC at 552 mV using the embroidered transmit antenna. These values meet the power requirements of the state-of-the-art single-channel neural recording ICs [153].

Tab. 12.1 summarizes the numerical results at 300 MHz.

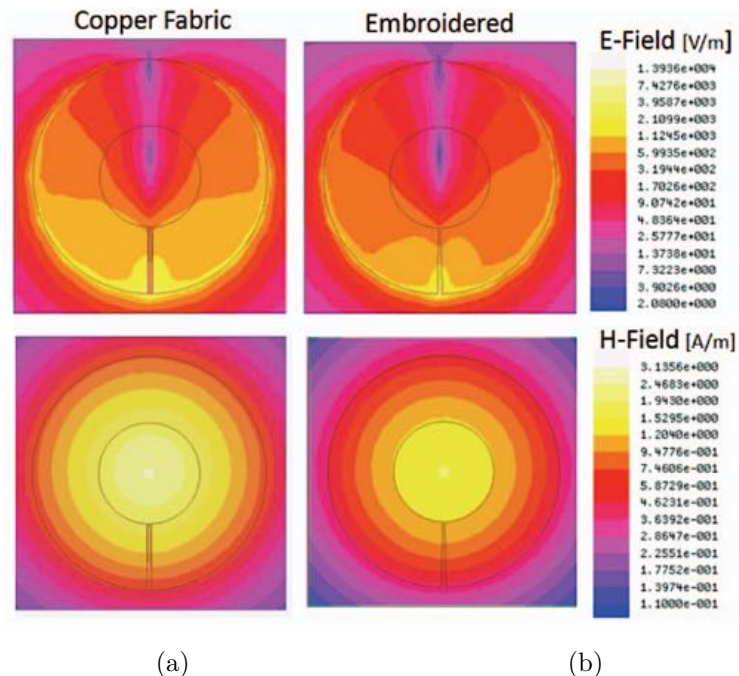


Figure 12.2.: E-field distribution at skin surface and H-field distribution at receiver location for copper fabric (left) and embroidered antennas (right). The accepted power was 100 mW at 300 MHz.

12.2.1. Prototypes and Measurements

The electro-textile antennas were fabricated and experimentally characterized. The conductive fabric was the commercial textile from LessEMF: pure copper taffeta fabric (35% copper). The embroidered antenna was instead sewed by means of the Husqvarna VIKING computer-aided sewing machine using the conductive thread Shieldex 110f34 dtex 2-ply HC. This thread consists of 34 filaments in a yarn; each one composed by two twisted 110 dtex (dtex = g/10000m) raw yarns plated with silver. The embroidered pattern is composed of circular lines of conductive thread sewn along the

Table 12.1.: Simulated results at 300 MHz of electro-textile transmit antennas coupled to the 8 mm³ cubic loop implant.

	$G_{p,max}$ (dB)	$P_{t,max}$ (mW)	V_{IN} (V)	$P_{IC,max}$ (μW)	V_{IC} (mV)
Copper Fabric	-20	45	4.4	388	788
Embroidery	-23	86	6.1	415	552

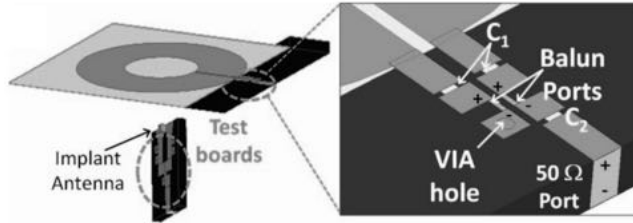
loop. The stitching density along the loop radius was set equal to 1 lines/mm to achieve a sheet resistance of 1.25.

The efficiency of the wireless link was evaluated through two-port measurements with VNA (Agilent PNA E8358A). To get accurate measurements additional circuit board fixtures are needed to match the antennas to the 50 Ω characteristic impedance of VNA ports. A balun is also required to convert the antennas' differential port to a single-ended port, thus ensuring a proper feeding mechanism to the small balanced loops. When adding matching boards to the antennas under test, the presence of lumped (capacitors, inductors, balun) and distributed (transmission line segments and soldering pads) components may affect the link efficiency by decreasing or even increasing the coupling between the two antennas, depending on the matching circuit size. A numerical model was hence implemented to take into account the mismatch and ohmic losses present in the matching circuits, the insertion loss of the balun, and the possible extra coupling mechanism caused by the copper transmission lines. Once this model was validated by the measurement results, the parasitic effects arising from the presence of the test boards can be estimated from the simulation and removed to evaluate the maximum achievable link power efficiency between just the on-body and the implant loop antennas.

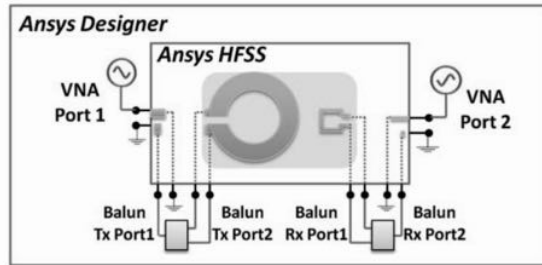
The proposed modeling methodology can be summarized as follows. First, the matching circuit converting impedance of the electro-textile antennas to 50 Ω was designed using circuit design software (Ansys Designer v.8). As the two antennas have nearly similar frequency-dependent input impedances, the same three component circuit can be adopted for both the layouts (Fig. 12.3a). The surface

mounted balun (ATB2012-50011) was included as a 3-port network described by the S-parameters provided by the manufacturer. The matching was obtained by maximizing the transducer power gain ($|S_{21}|^2$) across the matching frequency. Since, the electromagnetic coupling between the transmit and implant antenna is relatively small, based on a reasonable approximation, each antenna was separately conjugate matched to 50Ω without considering the effects of mutual coupling. Then, the whole communication link including the transmit the implant loops and their matching circuits was evaluated by full-wave analysis to assess the effect of test boards on the maximum available power gain. The substrate of the matching board was the 3.175-mm-thick RT/Duroid® 5880 ($\epsilon_r = 2.2$, $\tan\delta = 9e-5$). For the comparison with measured results, the on-body antennas were now assumed as planar and a homogenous parallelepiped-like liquid phantom was used.

The fabricated prototypes connected to their feeding fixtures are illustrated in Fig. 12.4. The matching circuit and the cable connection were coated with Blue-Tack to avoid possible impedance mistuning due to the contact with the liquid. The loops were placed at a fixed distances of 16 ± 1 mm. with the implant immersed 11 ± 1 mm beneath the liquid surface to reproduced the same the distances as in the layered head model. The link power efficiencies between the antennas were derived from the measured S-parameters. In all cases, the peak $G_{p,max}$ is achieved at 305 MHz, near the predicted matched frequency. At this frequency the link power efficiency of the copper fabric transmit loop was 3 dB higher than that of the embroidered prototype, thus confirming the previous numerical results. For comparison, the simulated $G_{p,max}$ curve derived from the S-parameters of the full model of Fig. 12.3.b. Around the matched frequency, simulations are in good agreement with measurements, with small differences (less than 1.4 dB) due to the fabrication uncertainties and components tolerance. The higher discrepancy, which emerges moving away from the matched frequency, can be explained by the increased uncertainty in the VNA measurement due to the mismatch loss at the matching network/antenna interface. Overall, the achieved results clearly demonstrate that we were able to accurately predict the coupling between the two antennas. It is worth noting that the measured peak values of $G_{p,max}$ were



(a)



(b)

Figure 12.3.: Simulation model of the whole communication link. a) Transmit and implant loop with the test boards. A detailed view of matching circuit layout of the wearable transmit antenna is shown on the right. b) Scheme of the full 6-port HFSS model dynamically linked with the components simulated in Designer environment.

significantly higher than those computed by considering only the antennas. This means that the presence of the test boards created an additional unwanted coupling. However, the complete numerical model permits to evaluate and eventually remove the measurement artifacts introduced by the test boards to not overestimate the power deliverable to the neural IC in real applications.

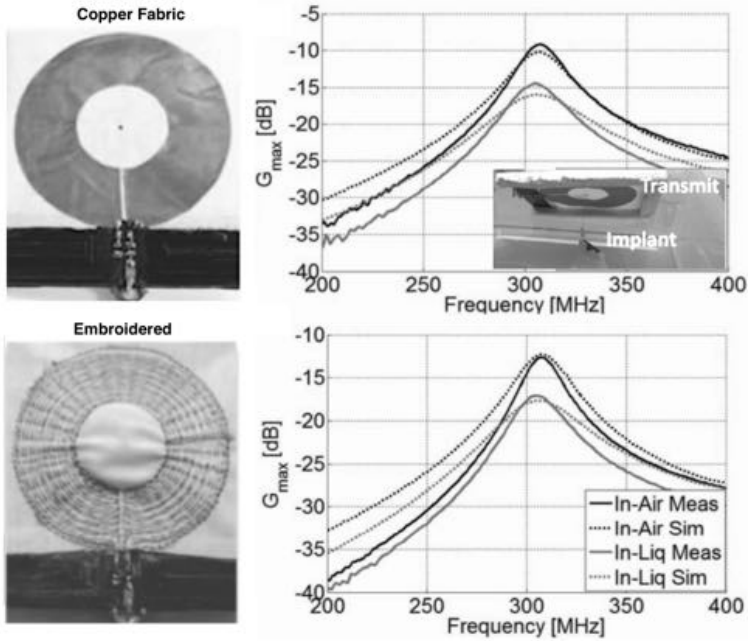


Figure 12.4.: Fabricated antenna prototypes of the copper-fabric (top), and the embroidered (bottom) transmit antennas with the matching boards. On the right side, the $G_{p,max}$ of the wearable antennas coupled to a $2 \times 2 \times 2 \text{ mm}^3$ cubic loop measured in air and in-Liquid. The dashed line refers to the reference simulation results.

12.3. Millimeter size backscattering Neural Tags

Long-term mobile neural recording requires very small neural sensors integrating electrodes, microsystem and an antenna for wireless telemetry. From the clinical point of view, it is desirable that the antenna does not increase the size of the implant significantly from that required by the neural sensor electrodes and the implant IC. This section analyzes the communication performance achievable by mm-size implant antennas.

Simulations consider now a more accurate inhomogeneous human head phantom (Man's Head by HFSS, Fig. 12.5). The implant antenna was positioned in the cerebrospinal (CSF) fluid in correspondence of the primary motor cortex, which is the cortical area that elicits movements of individual body parts. Thus, neural reading and stimulation of this area is the target of BMI for thought-controlled smart prosthetics. For the transmitter antenna instead, a planar loop made of bulk cooper on a rigid substrate as in [157] was placed 5mm away from the skin.

Previous researches on implant loop size showed that 3-D structure provides wider current path and larger coupling area compared to planar loop with the same cross-sectional area [157]. Numerical results reported in Fig. 12.6 confirmed that a 1-mm^3 cubic implant

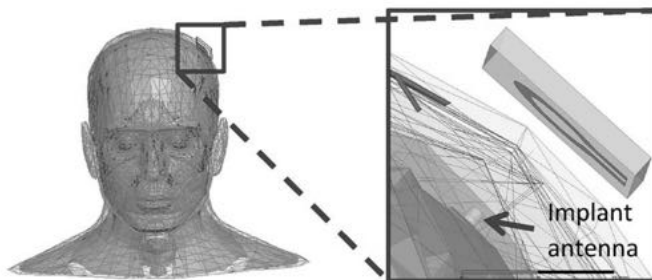


Figure 12.5.: Man's head simulation model and a zoomed image of transmit and implant antennas placed in the model.

achieves higher link power efficiency compared to a planar $2 \times 2 \text{ mm}^2$ implant loop. At higher frequencies, it even performs as strongly as a $3 \times 3 \text{ mm}^2$ implant loop. Consequently, 3-D structure achieves a cross-sectional area reduction of more than 75%. Moreover, cubic structure allows the insertion of magnetic core to further strengthen the magnetic field and thereby the inductive coupling.

As mentioned in the previous section, increasing transmitting loop-to-skin distance decreases SAR in the tissues, but this is at the expense of lower link power efficiency. We investigated this trade-off by simulating $1 \times 1 \times 1 \text{ mm}^3$ copper loop immersed in the CSF fluid in Man's Head Model with the planar solid transmit loop placed at different distances d from the skin. Fig. 12.7 shows the maximum operating power gain ($G_{p,max}$) between the loops in each case along with the power delivered to a conjugate-matched implant IC (P_L) and the corresponding voltage amplitude at its input (V_L) with the maximum SAR compliant transmit power ($P_{t,max}$). The reported parameters were computed from eq. (12.1)-(12.5). The results confirm that increase in d reduces SAR (which allows higher $P_{t,max}$) and $G_{p,max}$. This means that the reduced link power efficiency could be compensated by increasing the transmission power, but considering that in a practical system the transmitter would be a mobile device, this would come at the expense of reduced battery-life. In view of this, $d = 5 \text{ mm}$ appears to be a suitable distance, because compared with distance $d = 7 \text{ mm}$, similar voltage V_L and power P_L are achieved with much higher link efficiency $G_{p,max}$. Thus, the 1-mm^3 copper implant loop supplies 100s of microwatts of power to the implant IC, and generates 150–200 mV of voltage at the IC terminals. According to these results, even though the cubic implant loop is classified as a very small loop antenna, it could power the neural recording IC presented in [153] with up to 92 channels.

12.3.1. Fabrication and Wireless Measurements

Two different very small implant antennas were prototyped and connected to UHF RFID tag IC ((NXP UCODE G2iL, $P_{chip} = -18 \text{ dBm}$) to create a backscattering implantable device. The consid-

ered layouts are a 3D and a planar miniature structures meant for capturing neurosignals over localized or extended cortical area, respectively.

Cubic 1 mm³ Copper Implant Antenna

The 1 mm³ cubic loop was made of 0.05 mm thick copper plate and it was attached to the chip via a small test board, which conjugate matches the input impedance of the implant antenna to the input impedance of the chip. The size of the MC board, containing a parallel capacitor and two series inductors, was kept as small as possible to avoid coupling of the matching circuit (MC) to the reader antenna. The reader loop antenna has a matching circuit for 50 Ω impedance matching at 907 MHz. A surface mount balun (ATB2012-50011) was used to properly convert the differential port of the reader loop antenna to single ended port.

The link performance of the wireless link was quantified through the measurements of *Operating Power Gain*, i.e. the ratio of the power delivered to the implant IC (P_{chip}) to the power delivered to the reader antenna's matching circuit:

$$G_p = \frac{P_{chip}}{P_{to} \cdot G_{t,cable}} \quad (12.6)$$

where P_{to} is the turn-on power of the cubic loop measured by the Voyantic Tagformance RFID measurement system and $G_{t,cable}$ is the transducer power gain of the cable connecting the Tagformance output and the transmitting antenna. The setup for the wireless testing is shown in Fig. 12.8. For the judicious comparison between the simulation and measurement, we implemented the simulation model shown in Fig. 12.8.b, which includes the matching circuits. The lumped components and baluns were modeled in circuit solver Ansys Designer, which was dynamically linked to the electromagnetic fields solver HFSS through ports 1 and 2 sketched in Fig. 12.8.b.

Measurement and simulation results are reported in Fig. 12.9. The measured operating power gain G_p must be considered around 907

MHz, where the reader antenna is matched. Simulations predicted a $G_{p,max}$ of -16 dB between the two ports of the antennas placed at 16 mm distance in air. To evaluate the insertion loss of the reader antenna MC, the $G_{p,max}$ between the implant loop port and the reader MC port (graph ' $s_2, G_{p,max}, in\ air$ ' in Fig. 12.9) was simulated, under the hypothesis of implant loop perfectly matched. At 907 MHz, the $G_{p,max}$ resulted more than 3 dB lower than the that computed between the loop antenna ports due to the insertion loss of the reader antenna MC. On the other hand, the measured operating power gain G_p is approximately 11 dB lower than the simulated link power efficiency between the loop antenna ports. If 3 dB loss is caused by the reader antenna MC, 8 dB remains to be the insertion and matching loss of the implant antenna MC which still requires considerable improvement.

The wireless link efficiency was also measured in the human-head equivalent liquid phantom ($\epsilon_r = 41.5$ and $\sigma = 0.97$ at 900 MHz). The implant antenna was immersed 11 mm beneath the liquid surface and the reader loop 5 mm above, to reproduce the same distances as in the Man's Head Model. Before immersion, the implant test board was coated by the Blu-Tack adhesive to avoid impedance mistuning of the fixture when immersed in the liquid. The measured in-phantom operating power gain G_p was 7 dB lower than the simulated in-phantom maximum operating power gain between the antenna ports (graph ' $s_2, G_{p,max}, in\ phantom$ ' in Fig. 12.9). The detectable mismatch and insertion loss are lower than that of the in-air case, because the resistance of the loop increase when placed in liquid, thus improving the matching and enlarging the frequency bandwidth.

According to the measurement results, at 907 MHz, the reader antenna transmit power from 12.6 is 20.1 mW (-18 dBm - (-34 dB) - 3 dB = 13 dBm). At the same frequency, the maximum allowed transmit power computed using (1) is $P_{t,max} = 50$ mW. As a remarkable results, the IC activates with a transmit power which is 30 mW less than the maximum allowed value, despite the significant insertion and matching loss of the not optimized implant MC.

Ink-Jet Printed Gold Implant Antenna

The larger and extremely low-profile neural tag consists of planar square loop with the outer dimensions of $6.5 \times 6.5 \text{ mm}^2$ and the trace width of 0.75 mm. The antenna shape is suitable for the monolithic integration with an ECoG electrode array to be placed in the inner area. Ink-jet fabrication permits to fabricate a flexible layout that conform to the cerebral cortex. Unlike the low-cost and rapid printing method described in chapter 5, the ink was here deposited by using the highly specialized equipment (FUJIFILM Dimatrix DMP-2800) that permit to precisely control all the settings of the printing system (volume and traveling velocity of the ejected droplet, the gap distance between each droplet, the temperature of the jetted ink and of the substrate..) depending on the properties of the specific ink and substrate. Aiming to have a biocompatible implant, a Au-based nanoparticle (Harima Gold Nanopaste NPG-J) was used, since gold is a well-known stable and inert metal. 16 conductive layers were deposited over a 50 μm thick Kapton (Dupont Type 100 HN Film), which is also a biomaterial. Thermal sintering was done in four cycles at 250 $^\circ\text{C}$ for 1 hour after printing every 4 layers. In simulations the printed pattern was modeled as an infinitely thin material with a sheet resistance of $0.35\Omega/\square$ that was experimentally estimated as in [159].

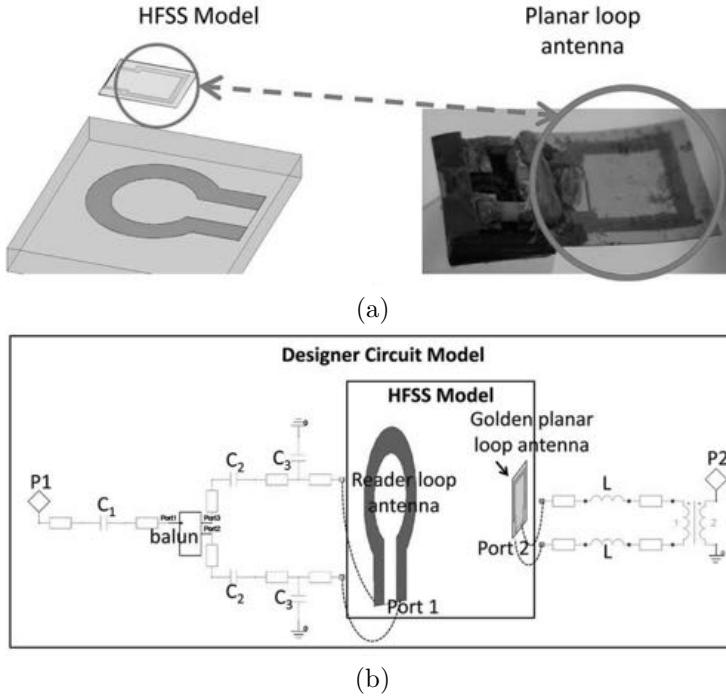


Figure 12.10.: (a) Model and prototype of the planar implant antenna, (b) Simulation model of the entire communication link.

The fabricated loop was then connected to RFID IC chip through a small matching circuit consisting of two series inductors (Fig. 12.10) and tested in air and in liquid phantom, in the same condition as in the previous section. From the comparison of the measured in-air operating power gain G_p (graph 'm, G_p in air' in Fig. 12.11) and the simulated in-air link power efficiency $G_{p,max}$ between the antenna ports (graph 's1, $G_{p,max}$ in air'), a 8 dB mismatch and insertion loss due to antenna test boards is derived at 907 MHz. With 3 dB loss in the reader antenna test board, the implant antenna test board produces 5 dB insertion and matching loss. Again, when immersed in liquid phantom impedance matching in the implant antenna side improves.

According to the in liquid measurement results, the IC turns on with a reader loop transmit power of 4.5 mW (-18 dBm - (-27.5 dB) - 3 dB = 6.5 dBm) that is only 15.5 % of the maximum allowed transmit power. By assuming a perfect impedance matching and a $P_{t,max}$ of 29 mW, 118 μ W could be delivered to the implant.

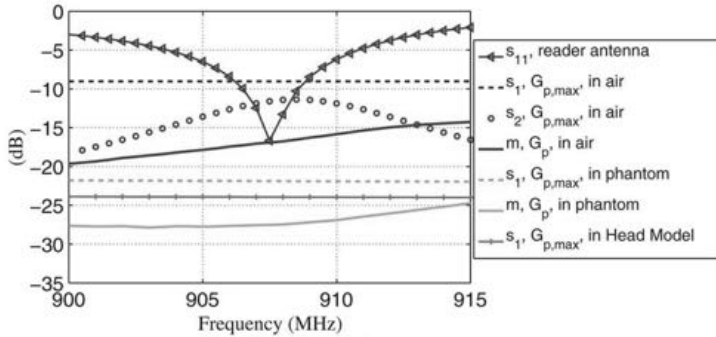
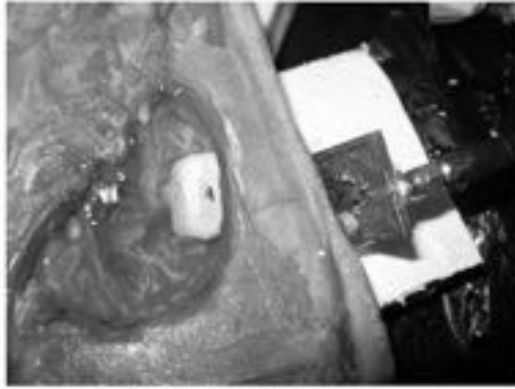


Figure 12.11.: Planar ink-jet printed loop: measurement and simulation results. Legend as in Fig. 11.10.

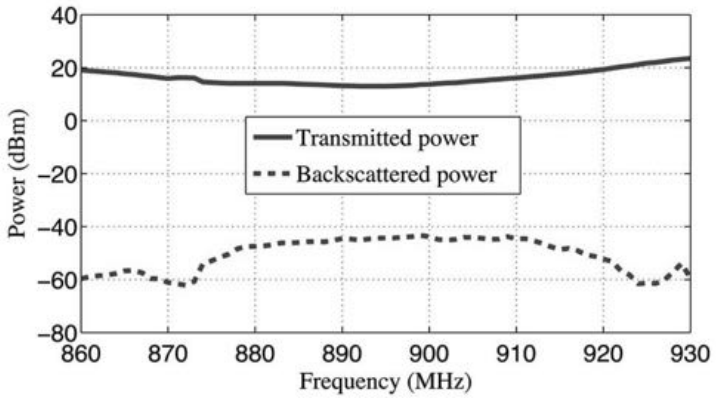
Porcine Measurements

To further assess the applicability of the designed loops in real biological environment, measurements were finally performed inside the head of a post-mortem 5 month old pig. According to the study in [160], the dielectric parameters of the selected pig match with those of an 11-13 years old human. The pig's head was halved and the brain was removed from the skull and refilled by the Satimo's Head Liquid. The cubic 1 mm³ copper cubic loop was immersed in the liquid so that it touched the skull and the reader antenna was placed 5 mm away from the skin (Fig. 12.12.a) in vertical alignment with the implant for maximum magnetic coupling. The approximate thicknesses of the bone, fat and skin layers present in the power path were 20 mm, 5 mm, and 2 mm, respectively. Experiments revealed the feasibility of establishing a wireless link with the mm-size implant, despite of being the tested biological channel was much longer than the corresponding in a human head. Fig.12.12

illustrates the minimum transmit power (P_{to}) that turned on the RFID IC and the corresponding backscattered power signal (P_{BS}) received by the reader unit. According to the measurement results, at 907 MHz the IC turns on with a P_{to} of 14 dBm (27 mW). At this frequency, the power backscattered from the implant was -43 dBm (51 nW), which is still 10-to-20 dB higher than the receiver sensitivity in commercial off-the-shelf RFID readers (specialized equipment could still achieve even better sensitivities).



(a)

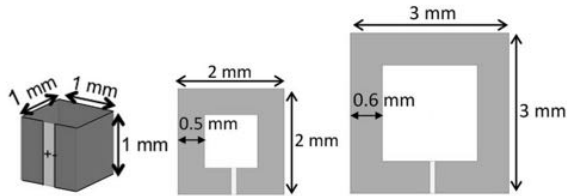


(b)

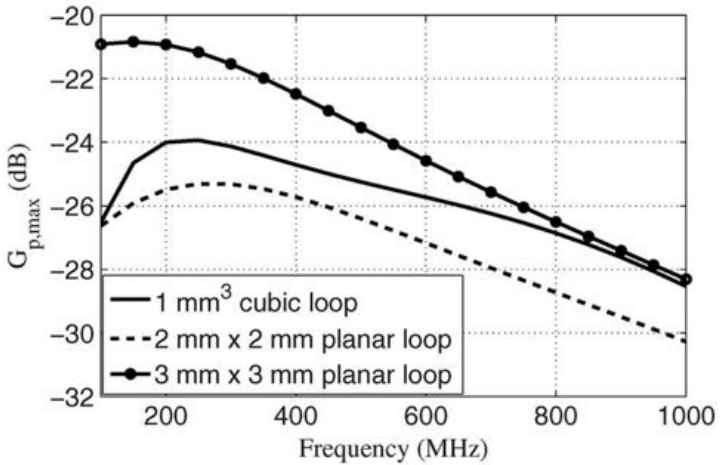
Figure 12.12.: a) Experimental setup for measuring the implant cubic loop in the post-mortem pig's head, b) Measured transmitted and backscattered power at the reader antenna matching circuit port.

12.3.2. Conclusions

Despite the relatively short cm-range communication distance, the required battery-free operation of a cortical implant imposes a major challenge for the wireless power and data telemetry. The presented study experimentally analyzed the feasibility of establishing a wireless link in a real biological environment with implantable microsystems resembling passive radio-transponders. In particular, electro-textile materials were proved to be efficient to create on-body reader antennas being flexible, compact, lightweight and even washable. Antennas patterned from copper fabric outperform embroidered layout by 3 dB. Despite the link power efficiency achieved by wearable transmitters is lower than that achieved by an optimized bulk copper antenna made on solid substrate [157], the power received by a reference implant is still in the same order, meaning that similar powering performance can be achieved at the expense of a bigger size and higher energy consumption. Concerning the implant, two layouts specifically conceived for localized (1 mm^3 cubic loop) and distributed ($6.5 \times 6.5 \text{ mm}^2$) neural recording were demonstrated capable of activating an implanted IC having -18 dBm sensitivity with a significant power margin to not violate the SAR limits.



(a)



(b)

Figure 12.6.: (a) Cubic mm-size and planar implant antennas, (b) Maximum operating power gain (link power efficiency) of the different implant antennas.

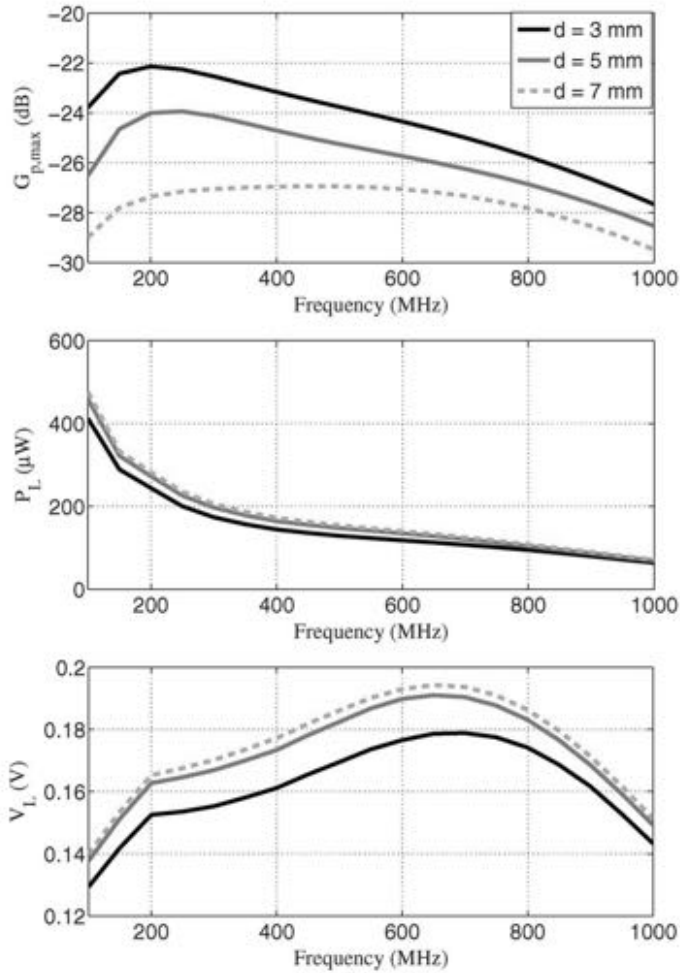
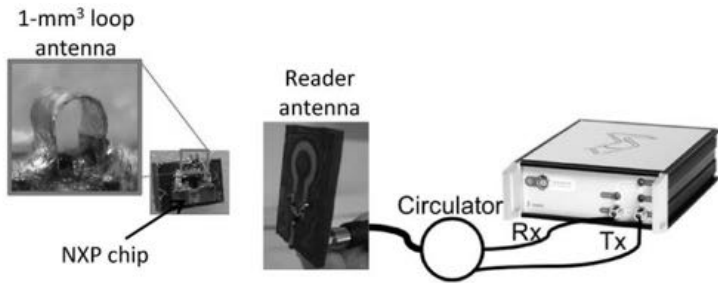
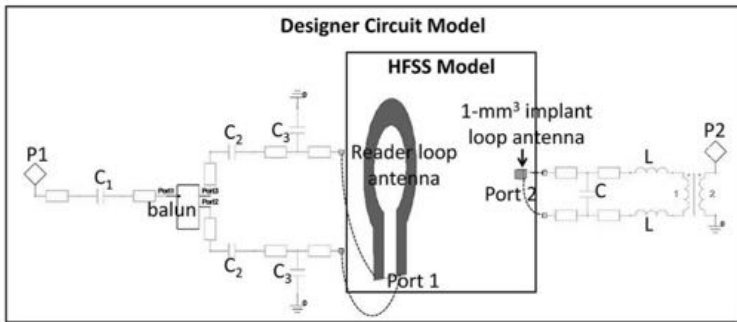


Figure 12.7.: Maximum operating power gain (link power efficiency), power available from the conjugate-matched cubic mm implant loop antenna for the IC and the corresponding voltage at the implant loop terminals for different transmit loop-to-skin distances d .



(a)



(b)

Figure 12.8.: (a) Wireless measurement system, reader and cubic mm implant antenna prototypes; (b) Simulation model of the whole communication link. Reader and implant loop antennas in HFSS model are dynamically linked to the components in Designer environment through Port 1 and Port 2. Components of the matching circuit: $C=8.2$ pF, $L=8.2$ nH, $C1 = 20$ pF, $C2 = 0.5$ pF, $C3 = 1.3$ pF.

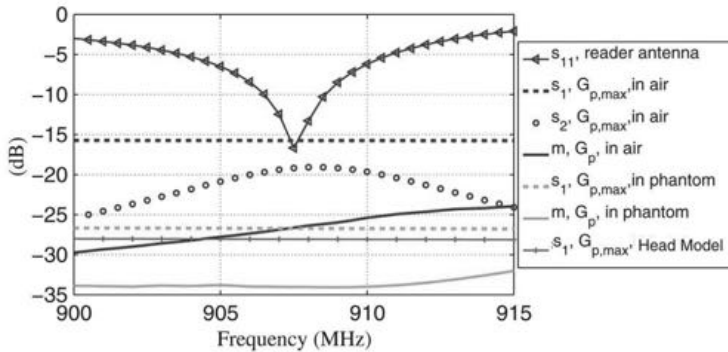


Figure 12.9.: Measurement and simulation results. In legend, subscript 1 refers to the simulated $G_{p,max}$ between the reader and the implant loop ports (Port1 and Port 2), subscript 2 refers to the $G_{p,max}$ between the reader antenna matching circuit port (P1) and implant antenna port (Port 2) ,“s” stands for simulation and “m” for measurement.

Bibliography

- [1] C. V. Forecast, “Cisco visual networking index: Global mobile data traffic forecast update, 2015-2020,” February 2016.
- [2] D.-H. e. a. Kim, “Epidermal electronics,” *Science*, vol. 333, no. 6044, pp. 838–843, 2011.
- [3] R. C. Webb, A. P. Bonifas, A. Behnaz, Y. Zhang, K. J. Yu, H. Cheng, M. Shi, Z. Bian, Z. Liu, Y.-S. Kim *et al.*, “Ultrathin conformal devices for precise and continuous thermal characterization of human skin,” *Nature materials*, vol. 12, no. 10, pp. 938–944, 2013.
- [4] X. Huang, Y. Liu, K. Chen, W.-J. Shin, C.-J. Lu, G.-W. Kong, D. Patnaik, S.-H. Lee, J. F. Cortes, and J. A. Rogers, “Stretchable, wireless sensors and functional substrates for epidermal characterization of sweat,” *small*, vol. 10, no. 15, pp. 3083–3090, 2014.
- [5] J.-W. Jeong, M. K. Kim, H. Cheng, W.-H. Yeo, X. Huang, Y. Liu, Y. Zhang, Y. Huang, and J. A. Rogers, “Capacitive epidermal electronics for electrically safe, long-term electrophysiological measurements,” *Advanced healthcare materials*, vol. 3, no. 5, pp. 642–648, 2014.
- [6] X. Huang, Y. Liu, H. Cheng, W.-J. Shin, J. A. Fan, Z. Liu, C.-J. Lu, G.-W. Kong, K. Chen, D. Patnaik *et al.*, “Materials and designs for wireless epidermal sensors of hydration and strain,” *Advanced Functional Materials*, vol. 24, no. 25, pp. 3846–3854, 2014.
- [7] D. Son, J. Lee, S. Qiao, R. Ghaffari, J. Kim, J. E. Lee, C. Song, S. J. Kim, D. J. Lee, S. W. Jun *et al.*, “Multifunc-

- tional wearable devices for diagnosis and therapy of movement disorders,” *Nature Nanotechnology*, vol. 9, no. 5, pp. 397–404, 2014.
- [8] H. Cheng and V. Vepachedu, “Recent development of transient electronics,” *Theoretical and Applied Mechanics Letters*, vol. 6, no. 1, pp. 21 – 31, 2016. [Online]. Available: <http://www.sciencedirect.com/science/article/pii/S2095034915001105>
- [9] J. Kim, M. Lee, H. J. Shim, R. Ghaffari, H. R. Cho, D. Son, Y. H. Jung, M. Soh, C. Choi, S. Jung *et al.*, “Stretchable silicon nanoribbon electronics for skin prosthesis,” *Nature communications*, vol. 5, 2014.
- [10] J. A. Rogers, R. Ghaffari, and D.-H. Kim, *Stretchable Bioelectronics for Medical Devices and Systems*. Springer, 2016.
- [11] J.-W. Jeong, W.-H. Yeo, A. Akhtar, J. J. Norton, Y.-J. Kwack, S. Li, S.-Y. Jung, Y. Su, W. Lee, J. Xia *et al.*, “Materials and optimized designs for human-machine interfaces via epidermal electronics,” *Advanced Materials*, vol. 25, no. 47, pp. 6839–6846, 2013.
- [12] V. Sridhar and K. Takahata, “A hydrogel-based passive wireless sensor using a flex-circuit inductive transducer,” *Sensors and Actuators A: Physical*, vol. 155, no. 1, pp. 58–65, 2009.
- [13] M. F. Farooqui and A. Shamim, “Low cost inkjet printed smart bandage for wireless monitoring of chronic wounds,” in *2016 IEEE MTT-S International Microwave Symposium (IMS)*, May 2016, pp. 1–4.
- [14] N. Mehmood, A. Hariz, S. Templeton, and N. H. Voelcker, “An improved flexible telemetry system to autonomously monitor sub-bandage pressure and wound moisture,” *Sensors*, vol. 14, no. 11, pp. 21 770–21 790, 2014.
- [15] X. Huang, Y. Liu, G. W. Kong, J. H. Seo, Y. Ma, K.-I. Jang, J. A. Fan, S. Mao, Q. Chen, D. Li *et al.*, “Epidermal radio frequency electronics for wireless power transfer,” *Microsystems & Nanoengineering*, vol. 2, p. 16052, 2016.
- [16] I. Ha, “Technologies and research trends in wireless body area networks for healthcare: a systematic literature review,”

- International Journal of Distributed Sensor Networks*, vol. 2015, p. 4, 2015.
- [17] C. Occhiuzzi, S. Caizzzone, and G. Marrocco, “Passive uhf rfid antennas for sensing applications: Principles, methods, and classifications,” *IEEE Antennas and Propagation Magazine*, vol. 55, no. 6, pp. 14–34, Dec 2013.
- [18] J. Kim, A. Banks, H. Cheng, Z. Xie, S. Xu, K.-I. Jang, J. W. Lee, Z. Liu, P. Gutruf, X. Huang *et al.*, “Epidermal electronics with advanced capabilities in near-field communication,” *small*, vol. 11, no. 8, pp. 906–912, 2015.
- [19] D. P. Rose, M. E. Ratterman, D. K. Griffin, L. Hou, N. Kelley-Loughnane, R. R. Naik, J. A. Hagen, I. Papautsky, and J. C. Heikenfeld, “Adhesive rfid sensor patch for monitoring of sweat electrolytes,” *IEEE Transactions on Biomedical Engineering*, vol. 62, no. 6, pp. 1457–1465, June 2015.
- [20] J. Kim, G. A. Salvatore, H. Araki, A. M. Chiarelli, Z. Xie, A. Banks, X. Sheng, Y. Liu, J. W. Lee, K.-I. Jang *et al.*, “Battery-free, stretchable optoelectronic systems for wireless optical characterization of the skin,” *Science Advances*, vol. 2, no. 8, p. e1600418, 2016.
- [21] M. D. Steinberg, P. Kassal, I. Kereković, and I. M. Steinberg, “A wireless potentiostat for mobile chemical sensing and biosensing,” *Talanta*, vol. 143, pp. 178 – 183, 2015. [Online]. Available: <http://www.sciencedirect.com/science/article/pii/S0039914015003902>
- [22] P. Kassal, J. Kim, R. Kumar, W. R. de Araujo, I. M. Steinberg, M. D. Steinberg, and J. Wang, “Smart bandage with wireless connectivity for uric acid biosensing as an indicator of wound status,” *Electrochemistry Communications*, vol. 56, pp. 6 – 10, 2015. [Online]. Available: <http://www.sciencedirect.com/science/article/pii/S1388248115000946>
- [23] S. Manzari, C. Occhiuzzi, and G. Marrocco, “Feasibility of body-centric systems using passive textile rfid tags,” *Antennas and Propagation Magazine, IEEE*, vol. 54, no. 4, pp. 49–62, Aug 2012.
- [24] T. Kellomaki, “On-body performance of a wearable single-

- layer rfid tag,” *IEEE Antennas and Wireless Propagation Letters*, no. 11, pp. 73–76, 2012.
- [25] C. Occhiuzzi, S. Cippitelli, and G. Marrocco, “Modeling, design and experimentation of wearable rfid sensor tag,” *Antennas and Propagation, IEEE Transactions on*, vol. 58, no. 8, pp. 2490–2498, aug. 2010.
- [26] M.-C. Tsai, C.-W. Chiu, H.-C. Wang, and T.-F. Wu, “Inductively coupled loop antenna design for uhf rfid on-body applications,” *Progress In Electromagnetics Research*, vol. 143, pp. 315–330, 2013.
- [27] D. M. Dobkin, *The RF in RFID: passive UHF RFID in Practice*. Amsterdam: Elsevier, 2007.
- [28] G. Marrocco, “The art of uhf rfid antenna design: impedance-matching and size-reduction techniques,” *Antennas and Propagation Magazine, IEEE*, vol. 50, no. 1, pp. 66–79, feb. 2008.
- [29] P. Nikitin and K. Rao, “Theory and measurement of backscattering from rfid tags,” *Antennas and Propagation Magazine, IEEE*, vol. 48, no. 6, pp. 212–218, dec. 2006.
- [30] C. Occhiuzzi, S. Caizzone, and G. Marrocco, “Passive uhf rfid antennas for sensing applications: Principles, methods, and classifications,” *Antennas and Propagation Magazine, IEEE*, vol. 55, no. 6, pp. 14–34, Dec 2013.
- [31] C. Occhiuzzi, G. Contri, and G. Marrocco, “Design of implanted rfid tags for passive sensing of human body: the stentag,” *Antennas and Propagation, IEEE Transactions on*, vol. to appear, 2012.
- [32] R. Bhattacharyya, C. Floerkemeier, and S. Sarma, “Towards tag antenna based sensing—an rfid displacement sensor,” in *2009 IEEE International Conference on RFID*. IEEE, 2009, pp. 95–102.
- [33] S. Manzari, A. Catini, G. Pomarico, C. Di Natale, and G. Marrocco, “Development of an uhf rfid chemical sensor array for battery-less ambient sensing,” pp. 1–1, 2014.
- [34] S. Caizzone, C. Occhiuzzi, and G. Marrocco, “Multi-chip rfid antenna integrating shape-memory alloys for detection

- of thermal thresholds,” *Antennas and Propagation, IEEE Transactions on*, vol. 59, no. 7, pp. 2488–2494, July 2011.
- [35] C. Occhiuzzi and G. Marrocco, “Precision and accuracy in uhf-rfid power measurements for passive sensing,” *IEEE Sensors Journal*, vol. PP, no. 99, pp. 1–1, 2016.
- [36] G. Marrocco, “Rfid grids: Part i:electromagnetic theory,” *Antennas and Propagation, IEEE Transactions on*, vol. 59, no. 3, pp. 1019–1026, March 2011.
- [37] [Online]. Available: MagnusUHFRFIDTagIC, ApplicationNote, www.rfmicron.com
- [38] [Online]. Available: MagnusUHFRFIDTagIC, www.rfmicron.com.
- [39] [Online]. Available: EM4325, <http://www.emmicroelectronic.com/products/rf-identification-security/epc-and-uhf-ics/em4325>
- [40] [Online]. Available: SL900Achip, <http://ams.com/eng/Products/UHF-RFID/UHF-Interface-and-Sensor-Tag/SL900A>
- [41] (January 2017). [Online]. Available: ANDY100RFIDIC, <http://www.farsens.com/en/products/andy100/>
- [42] [Online]. Available: BlueSparkTechnologies, <http://www.bluesparktechnologies.com/>
- [43] [Online]. Available: FlexibleLithium-ionBatterybyPanasonic, <http://news.panasonic.com/global/press/data/2016/09/en160929-8/en160929-8.html>
- [44] L. W. Mayer and A. L. Scholtz, “Sensitivity and impedance measurements on uhf rfid transponder chips,” in *Proceedings of the second international EURASIP workshop on RFID technology, Budapest*. Citeseer, 2008.
- [45] C. Balanis, *Antenna Theory: analysis and Design*, 2nd ed. New York: Wiley and Son, 1997.
- [46] A. Sommerfeld, “The propagation of waves in wireless telegraphy,” *Ann. der Phys*, vol. 28, pp. 665–736, March 1926.
- [47] M. A. Ziai and J. C. Batchelor, “Temporary on-skin passive uhf rfid transfer tag,” *IEEE Transactions on Antennas and Propagation*, vol. 59, no. 10, pp. 3565–3571, Oct 2011.

-
- [48] S. Milici, S. Amendola, A. Bianco, and G. Marrocco, "Epidermal rfid passive sensor for body temperature measurements," in *RFID Technology and Applications Conference (RFID-TA), 2014 IEEE*. IEEE, 2014, pp. 140–144.
- [49] V. Sanchez-Romaguera, M. A. Ziai, D. Oyeka, S. Barbosa, J. S. R. Wheeler, J. C. Batchelor, E. A. Parker, and S. G. Yeates, "Towards inkjet-printed low cost passive uhf rfid skin mounted tattoo paper tags based on silver nanoparticle inks," *J. Mater. Chem. C*, vol. 1, pp. 6395–6402, 2013. [Online]. Available: <http://dx.doi.org/10.1039/C3TC31302F>
- [50] T. Kellomaki, "On-body performance of a wearable single-layer rfid tag," *Antennas and Wireless Propagation Letters, IEEE*, vol. 11, pp. 73–76, 2012.
- [51] G. Marrocco, "The art of uhf rfid antenna design: impedance-matching and size-reduction techniques," *Antennas and Propagation Magazine, IEEE*, vol. 50, no. 1, pp. 66–79, feb. 2008.
- [52] <http://www.brooks.af.mil/AFRL/HED/hedr/reports/dielectric/home.html>, C.Gabriel, S.Gabriel, *Compilation of the Dielectric Properties of Body Tissues at RF and Microwave Frequencies*, <http://www.brooks.af.mil/AFRL/HED/hedr/reports/dielectric/home.html>.
- [53] G. Marrocco, "Rfid antennas for the uhf remote monitoring of human subjects," *Antennas and Propagation, IEEE Transactions on*, vol. 55, no. 6, pp. 1862–1870, june 2007.
- [54] [Online]. Available: FEKOSuite7.0,EMSoftwareandSystems, 2014,www.feko.info
- [55] A. Abbosh, "Accurate effective permittivity calculation of printed center-fed dipoles and its application to quasi yagi-uda antennas," *IEEE Transactions on Antennas and Propagation*, vol. 61, no. 4, pp. 2297–2300, 2013.
- [56] C. Occhiuzzi, A. Ajovalasit, M. A. Sabatino, C. Dispenza, and G. Marrocco, "Rfid epidermal sensor including hydrogel membranes for wound monitoring and healing," in *2015 IEEE International Conference on RFID (RFID)*, April 2015, pp. 182–188.

- [57] S. Manzari, S. Pettinari, and G. Marrocco, "Miniaturised wearable uhf-rfid tag with tuning capability," *Electronics Letters*, vol. 48, no. 21, pp. 1325–1326, October 2012.
- [58] R. Lodato, V. Lopresto, R. Pinto, and G. Marrocco, "Numerical and experimental characterization of through-the-body uhf-rfid links for passive tags implanted into human limbs," *IEEE Transactions on Antennas and Propagation*, vol. 62, no. 10, pp. 5298–5306, 2014.
- [59] Y. Liu, K. Contractor, and Y. Kang, "Path loss for short range telemetry," in *4th International Workshop on Wearable and Implantable Body Sensor Networks (BSN 2007)*. Springer, 2007, pp. 70–74.
- [60] S. Orfanidis, *Electromagnetic Waves and Antennas*. New Jersey: Rutgers University, August 2010.
- [61] [Online]. Available: NBSIJDiamondJetSilverNanoparticleInk, MitsubishiImaging(MPM),Inc.,<http://diamond-jet.com/silvernanoparticleink-2.aspx>.
- [62] H. Son and C. Pyo, "Design of rfid tag antennas using an inductively coupled feed," *Electronics Letters*, vol. 41, no. 18, p. 1, 2005.
- [63] G. Marrocco, "Gain-optimized self-resonant meander line antennas for rfid applications," *Antennas and Wireless Propagation Letters, IEEE*, vol. 2, no. 1, pp. 302–305, 2003.
- [64] G. Matzeu, L. Florea, and D. Diamond, "Advances in wearable chemical sensor design for monitoring biological fluids," *Sensors and Actuators B: Chemical*, vol. 211, pp. 403–418, 2015.
- [65] I. Waldron, S. N. Makarov, S. Biederman, and R. Ludwig, "Suspended ring resonator for dielectric constant measurement of foams," *IEEE microwave and wireless components letters*, vol. 16, no. 9, pp. 496–498, 2006.
- [66] S. Ebnesaajjad, *Handbook of biopolymers and biodegradable plastics: properties, processing and applications*. William Andrew, 2012.
- [67] K. Y. You, Z. Abbas, K. Khalid, A. Rahman, and M. Zaki, "Improved dielectric model for polyvinyl alcohol-water hydro-

- gel at microwave frequencies.” *American Journal of Applied Sciences*, vol. 7, no. 2, pp. 270–276, 2010.
- [68] [Online]. Available: MySkin,PicSolution.<http://myskin.picsolution.com/en/index.shtml>
- [69] [Online]. Available: NB-TP-3GU100SilverNanoparticleTransparencyFilm, MitsubishiImaging(MPM),<http://diamond-jet.com/silvernanoarticleink-1-1-1-1.aspx>.
- [70] C. Del Gaudio, A. Bianco, M. Folin, S. Baiguera, and M. Grigioni, “Structural characterization and cell response evaluation of electrospun pcl membranes: micrometric versus submicrometric fibers,” *Journal of Biomedical Materials Research Part A*, vol. 89, no. 4, pp. 1028–1039, 2009.
- [71] Z.-M. Huang, Y.-Z. Zhang, M. Kotaki, and S. Ramakrishna, “A review on polymer nanofibers by electrospinning and their applications in nanocomposites,” *Composites science and technology*, vol. 63, no. 15, pp. 2223–2253, 2003.
- [72] S. Manzari and G. Marrocco, “Modeling and applications of a chemical-loaded uhf rfid sensing antenna with tuning capability,” *Antennas and Propagation, IEEE Transactions on*, vol. 62, no. 1, pp. 94–101, Jan 2014.
- [73] S. Yang, Y.-C. Chen, L. Nicolini, P. Pasupathy, J. Sacks, B. Su, R. Yang, D. Sanchez, Y.-F. Chang, P. Wang, D. Schnyer, D. Neikirk, and N. Lu, ““cut-and-paste” manufacture of multiparametric epidermal sensor systems,” *Advanced Materials*, vol. 27, no. 41, pp. 6423–6430, 2015. [Online]. Available: <http://dx.doi.org/10.1002/adma.201502386>
- [74] S. Khan, L. Lorenzelli, and R. S. Dahiya, “Technologies for printing sensors and electronics over large flexible substrates: a review,” *IEEE Sensors Journal*, vol. 15, no. 6, pp. 3164–3185, 2015.
- [75] Z. Yin, Y. Huang, N. Bu, X. Wang, and Y. Xiong, “Inkjet printing for flexible electronics: Materials, processes and equipments,” *Chinese Science Bulletin*, vol. 55, no. 30, pp. 3383–3407, 2010.
- [76] S. Merilampi, T. Laine-Ma, and P. Ruuskanen, “The characterization of electrically conductive silver ink patterns on

- flexible substrates,” *Microelectronics reliability*, vol. 49, no. 7, pp. 782–790, 2009.
- [77] [Online]. Available: ConductiveInkjetInk9101, MethodeElectronics,Inc.,http://www.methode.com/Documents/TechnicalLibrary/MDC_Inks_Conductive_Inkjet_Ink_9101_Data_Sheet.pdf.
- [78] M. Grouchko, A. Kamyshny, C. F. Mihailescu, D. F. Anghel, and S. Magdassi, “Conductive inks with a “built-in” mechanism that enables sintering at room temperature,” *ACS nano*, vol. 5, no. 4, pp. 3354–3359, 2011.
- [79] Y. Kawahara, S. Hodges, B. S. Cook, C. Zhang, and G. D. Abowd, “Instant inkjet circuits: Lab-based inkjet printing to support rapid prototyping of ubicomp devices,” in *Proceedings of the 2013 ACM International Joint Conference on Pervasive and Ubiquitous Computing*, ser. UbiComp ’13. New York, NY, USA: ACM, 2013, pp. 363–372. [Online]. Available: <http://doi.acm.org/10.1145/2493432.2493486>
- [80] Y. Kawahara, S. Hodges, N. W. Gong, S. Olberding, and J. Steimle, “Building functional prototypes using conductive inkjet printing,” *IEEE Pervasive Computing*, vol. 13, no. 3, pp. 30–38, July 2014.
- [81] T. Ta, M. Fukumoto, K. Narumi, S. Shino, Y. Kawahara, and T. Asami, “Interconnection and double layer for flexible electronic circuit with instant inkjet circuits,” in *Proceedings of the 2015 ACM International Joint Conference on Pervasive and Ubiquitous Computing*. ACM, 2015, pp. 181–190.
- [82] A. Mansour, N. Shehata, B. Hamza, and M. Rizk, “Efficient design of flexible and low cost paper-based inkjet-printed antenna,” *International Journal of Antennas and Propagation*, vol. 2015, 2015.
- [83] T. Yoshiki, S. Shino, and K. Kobayashi, “Process for preparing conductive material,” Sep. 6 2011, uS Patent 8,012,676.
- [84] [Online]. Available: ASTM F1896-98, TestMethodforDeterminingtheElectricalResistivityofaPrintedConductive. 2004
- [85] M. Shahpari and D. V. Thiel, “The impact of reduced conductivity on the performance of wire antennas,” *IEEE Trans-*

- actions on Antennas and Propagation*, vol. 63, no. 11, pp. 4686–4692, 2015.
- [86] Y. Matsuda, S. Shibayama, K. Uete, H. Yamaguchi, and T. Niimi, “Electric conductive pattern element fabricated using commercial inkjet printer for paper-based analytical devices,” *Analytical chemistry*, vol. 87, no. 11, pp. 5762–5765, 2015.
- [87] G. Saggio, F. Riillo, L. Sbernini, and L. R. Quitadamo, “Resistive flex sensors: a survey,” *Smart Materials and Structures*, vol. 25, no. 1, p. 013001, 2015.
- [88] S. Amendola, S. Milici, and G. Marrocco, “Performance of epidermal rfid dual-loop tag and on-skin retuning,” *IEEE Transactions on Antennas and Propagation*, vol. 63, no. 8, pp. 3672–3680, Aug 2015.
- [89] M. Lolli, “Apparatus for making an antenna for wire transponders of electrically conductive material,” Mar. 19 2013, uS Patent 8,397,377. [Online]. Available: <http://www.google.tl/patents/US8397377>
- [90] A. Bongrain, L. Rousseau, L. Valbin, N. Madaoui, G. Lisorgues, F. Verjus, and P. Chapon, “A new technology of ultrathin aln piezoelectric sensor for pulse wave measurement,” *Procedia Engineering*, vol. 120, pp. 459–463, 2015.
- [91] P. H. King, J. Scanlan, and A. Sobester, *From Radiosonde To Papersonde: The Use of Conductive Inkjet Printing in the Massive Atmospheric Volume Instrumentation System (MAVIS) Project*. American Institute of Aeronautics and Astronautics, 2016/08/22 2015. [Online]. Available: <http://dx.doi.org/10.2514/6.2015-0985>
- [92] M. Fierheller and R. G. Sibbald, “A clinical investigation into the relationship between increased periwound skin temperature and local wound infection in patients with chronic leg ulcers,” *Advances in skin & wound care*, vol. 23, no. 8, pp. 369–379, 2010.
- [93] D. G. Armstrong, K. Holtz-Neiderer, C. Wendel, M. J. Mohler, H. R. Kimbriel, and L. A. Lavery, “Skin temperature monitoring reduces the risk for diabetic foot ulceration

- in high-risk patients,” *The American journal of medicine*, vol. 120, no. 12, pp. 1042–1046, 2007.
- [94] R. J. Raymann, D. F. Swaab, and E. J. Van Someren, “Skin temperature and sleep-onset latency: changes with age and insomnia,” *Physiology & behavior*, vol. 90, no. 2, pp. 257–266, 2007.
- [95] B. McFarlin, A. Venable, R. Williams, and A. Jackson, “Comparison of techniques for the measurement of skin temperature during exercise in a hot, humid environment,” *Biology of sport*, vol. 32, no. 1, pp. 11–14, 2015.
- [96] [Online]. Available: Mon-a-therm, <http://www.medtronic.com/covidien/products/temperature-management/mon-a-therm-foley-temperature-sensor-400-tm>
- [97] [Online]. Available: NOVATEMP, SkinTemperatureSensors, 400-700series, http://www.novamed-usa.com/skin_temperature_sensors.html
- [98] W. D. van Marken Lichtenbelt, H. A. Daanen, L. Wouters, R. Fronczek, R. J. Raymann, N. M. Severens, and E. J. Van Someren, “Evaluation of wireless determination of skin temperature using ibuttons,” *Physiology & Behavior*, vol. 88, no. 4, pp. 489–497, 2006.
- [99] [Online]. Available: VitalSenseDermalPatch, PhilipsRespironics, <http://www.actigraphy.com/devices/vitalsense/>
- [100] [Online]. Available: TempTraq, <https://www.temptraq.com>
- [101] K.-G. Ng, S.-T. Wong, S.-M. Lim, and Z. Goh, “Evaluation of the cadi thermosensor wireless skin-contact thermometer against ear and axillary temperatures in children,” *Journal of pediatric nursing*, vol. 25, no. 3, pp. 176–186, 2010.
- [102] “Iso gum: “guide to expression of uncertainties in measurements”, iso/iec guide 98-3:2008.”
- [103] A. Psikuta, R. Niedermann, and R. M. Rossi, “Effect of ambient temperature and attachment method on surface temperature measurements,” *International journal of biometeorology*, vol. 58, no. 5, pp. 877–885, 2014.

-
- [104] E. O. Doebelin and D. N. Manik, “Measurement systems: application and design,” 2007.
- [105] F. A. Duck, *Physical properties of tissues: a comprehensive reference book*. Academic press, 2013.
- [106] K. Stephan and A. Laesecke, “The thermal conductivity of fluid air,” *Journal of physical and chemical reference data*, vol. 14, no. 1, pp. 227–234, 1985.
- [107] U. Varshney, “Pervasive healthcare and wireless health monitoring,” *Mobile Networks and Applications*, vol. 12, pp. 113–127, 2007.
- [108] R. Haux, S. Koch, N. Lovell, M. Marschollek, N. Nakashima, K. Wolf *et al.*, “Health-enabling and ambient assistive technologies: Past, present, future,” *IMIA Yearbook*, 2016.
- [109] A. Kulkarni and S. Sathe, “Healthcare applications of the internet of things: A review,” *International Journal of Computer Science and Information Technologies*, vol. 5, no. 5, pp. 6229–32, 2014.
- [110] S. R. Islam, D. Kwak, M. H. Kabir, M. Hossain, and K.-S. Kwak, “The internet of things for health care: a comprehensive survey,” *IEEE Access*, vol. 3, pp. 678–708, 2015.
- [111] Y. Yuehong, Y. Zeng, X. Chen, and Y. Fan, “The internet of things in healthcare: An overview,” *Journal of Industrial Information Integration*, vol. 1, pp. 3–13, 2016.
- [112] E. Di Giampaolo, F. Forni, and G. Marrocco, “Rfid-network planning by particle swarm optimization,” *ACES Journal*, vol. 25, no. 3, pp. 263–272, March 2010.
- [113] D. Zhang, J. Zhou, M. Guo, J. Cao, and T. Li, “Tasa: tag-free activity sensing using rfid tag arrays,” *IEEE Transactions on Parallel and Distributed Systems*, vol. 22, no. 4, pp. 558–570, 2011.
- [114] R. O. Duda, P. E. Hart, and D. G. Stork, *Pattern classification*. John Wiley & Sons, 2012.
- [115] S. Amendola, L. Bianchi, and G. Marrocco, “Movement detection of human body segments: Passive radio-frequency identification and machine-learning technologies.” *IEEE An-*

- tennas and Propagation Magazine*, vol. 57, no. 3, pp. 23–37, 2015.
- [116] G. Marrocco, E. Di Giampaolo, and R. Aliberti, “Estimation of uhf rfid reading regions in real environments,” *Antennas and Propagation Magazine, IEEE*, vol. 51, no. 6, pp. 44–57, dec. 2009.
- [117] Y. Huizer, C. Swaan, K. Leitmeyer, and A. Timen, “Usefulness and applicability of infectious disease control measures in air travel: A review,” *Travel medicine and infectious disease*, vol. 13, no. 1, pp. 19–30, 2015.
- [118] P. O. Fanger, *Thermal comfort : analysis and applications in environmental engineering*. Malabar, Fla.: R.E. Krieger Pub. Co., 1982.
- [119] B. Isaac and S. Burke, “Unexplained fever: A guide to the diagnosis and management of febrile states in medicine, surgery, pediatrics, and subspecialties,” 1991.
- [120] (1999) European council recommendation 1999/519/ec of 12 july 1999 on the limitation of exposure of the general public to electromagnetic fields (0 hz to 300 ghz). [Online]. Available: http://ec.europa.eu/enterprise/electr_equipement/lv/rec519.pdf
- [121] R. J. Raymann, D. F. Swaab, and E. J. Van Someren, “Cutaneous warming promotes sleep onset,” *American Journal of Physiology-Regulatory, Integrative and Comparative Physiology*, vol. 288, no. 6, pp. R1589–R1597, 2005.
- [122] (2015, May). [Online]. Available: https://www.youtube.com/watch?v=thH_wQ55QeE
- [123] (2016, April). [Online]. Available: <https://www.youtube.com/watch?v=wCt1auNCtOQ>
- [124] C. Occhiuzzi and G. Marrocco, “The rfid technology for neurosciences: Feasibility of limbs’ monitoring in sleep diseases,” *Information Technology in Biomedicine, IEEE Transactions on*, vol. 14, no. 1, pp. 37–43, jan. 2010.
- [125] R. L. S. Torres, D. C. Ranasinghe, Q. Shi, and A. P. Sample, “Sensor enabled wearable rfid technology for mitigating the

- risk of falls near beds,” in *RFID (RFID), 2013 IEEE International Conference on*. IEEE, 2013, pp. 191–198.
- [126] E. Hoque, R. F. Dickerson, and J. A. Stankovic, “Monitoring body positions and movements during sleep using wisps,” in *Wireless Health 2010*. ACM, 2010, pp. 44–53.
- [127] D. Ranasinghe, R. S. Torres, K. Hill, and R. Visvanathan, “Low cost and batteryless sensor-enabled radio frequency identification tag based approaches to identify patient bed entry and exit posture transitions,” *Gait & Posture*, vol. 39, no. 1, pp. 118–123, 2014.
- [128] P. Barsocchi, “Position recognition to support bedsores prevention,” *IEEE journal of biomedical and health informatics*, vol. 17, no. 1, pp. 53–59, 2013.
- [129] [Online]. Available: AD-843UHFRFIDinlay,<http://rfid.averydennison.com/products/ad-843/>
- [130] [Online]. Available: CAENR4301P-Ion,<http://www.caenrfid.it/en/CaenProd.jsp?parent=59&idmod=750>
- [131] [Online]. Available: Nightcaredemo,<https://youtu.be/-v13OmL0LL8>
- [132] S. Amendola, R. Lodato, S. Manzari, C. Occhiuzzi, and G. Marrocco, “Rfid technology for iot-based personal health-care in smart spaces,” *Internet of Things Journal, IEEE*, vol. 1, no. 2, pp. 144–152, April 2014.
- [133] F. F. E. Di Giampaolo and G. Marrocco, “Rfid-network planning by particle swarm optimization,” *Aces Journal*, vol. 25, no. 3, pp. 263–272, March 2010.
- [134] C. A. Grabowski, S. P. Fillery, H. Koerner, M. Tchoul, L. Drummy, C. W. Beier, R. L. Brutchey, M. F. Durstock, and R. A. Vaia, “Dielectric performance of high permittivity nanocomposites: impact of polystyrene grafting on batio₃ and tio₂,” *Nanocomposites*, vol. 2, no. 3, pp. 117–124, 2016.
- [135] H. R. Raad, A. I. Abbosh, H. M. Al-Rizzo, and D. G. Rucker, “Flexible and compact amc based antenna for telemedicine applications,” *IEEE Transactions on antennas and propagation*, vol. 61, no. 2, pp. 524–531, 2013.
- [136] R. Shilkrot, J. Huber, J. Steimle, S. Nanayakkara, and

- P. Maes, "Digital digits: A comprehensive survey of finger augmentation devices," *ACM Computing Surveys (CSUR)*, vol. 48, no. 2, p. 30, 2015.
- [137] P. J. Dyck, *Peripheral neuropathy*. Elsevier Inc., 2005.
- [138] E. Berlin, J. Liu, K. Van Laerhoven, and B. Schiele, "Coming to grips with the objects we grasp: detecting interactions with efficient wrist-worn sensors," in *Proceedings of the fourth international conference on Tangible, embedded, and embodied interaction*. ACM, 2010, pp. 57–64.
- [139] J. R. Smith, K. P. Fishkin, B. Jiang, A. Mamishev, M. Philipose, A. D. Rea, S. Roy, and K. Sundara-Rajan, "Rfid-based techniques for human-activity detection," *Communications of the ACM*, vol. 48, no. 9, pp. 39–44, 2005.
- [140] K. P. Fishkin, M. Philipose, and A. Rea, "Hands-on rfid: wireless wearables for detecting use of objects," in *Ninth IEEE International Symposium on Wearable Computers (ISWC'05)*, Oct 2005, pp. 38–41.
- [141] H. Horie and H. Iwasaki, "Wearable finger ring type antenna made of fabric cloth for ban use at uhf and ism bands," in *Microwave Workshop Series on RF and Wireless Technologies for Biomedical and Healthcare Applications (IMWS-BIO), 2013 IEEE MTT-S International*, Dec 2013, pp. 1–3.
- [142] W. Farooq, M. Ur-Rehman, Q. H. Abbassi, X. Yang, and K. Qaraqe, "Design of a finger ring antenna for wireless sensor networks," in *2016 10th European Conference on Antennas and Propagation (EuCAP)*, April 2016, pp. 1–4.
- [143] H. Goto and H. Iwasaki, "A low profile monopole antenna with double finger ring for ban and pan," in *Antenna Technology (iWAT), 2011 International Workshop on*, March 2011, pp. 227–230.
- [144] R. Bainbridge and J. A. Paradiso, "Wireless hand gesture capture through wearable passive tag sensing," in *2011 International Conference on Body Sensor Networks*, May 2011, pp. 200–204.
- [145] E. Tamaki and K. Iwasaki, "Gesturenail: wireless hand gesture ssystem," *International Journal of Computer Science, Engineering and Applications*, vol. 3, no. 5, p. 29, 2013.

-
- [146] H.-L. C. Kao, A. Dementyev, J. A. Paradiso, and C. Schmandt, "Nailo: fingernails as an input surface," in *Proceedings of the 33rd Annual ACM Conference on Human Factors in Computing Systems*. ACM, 2015, pp. 3015–3018.
- [147] E. Tamaki and K. Iwasaki, "A half-implant device on fingernails," in *Proceedings of the extended abstracts of the 32nd annual ACM conference on Human factors in computing systems*. ACM, 2014, pp. 1447–1452.
- [148] K. C. Vega and H. Fuks, *Beauty Technology: Designing Seamless Interfaces for Wearable Computing*. Springer, 2016.
- [149] [Online]. Available: Tissuesimulatingliquids, <https://www.speag.com/products/dasy6/tissue-simulating-liquids/head-tissue-2/>
- [150] J. M. Carmena, "Advances in neuroprosthetic learning and control," *PLoS Biol*, vol. 11, no. 5, p. e1001561, 2013.
- [151] J. M. Rabaey, "Brain-machine interfaces as the new frontier in extreme miniaturization," in *2011 Proceedings of the European Solid-State Device Research Conference (ESSDERC)*. IEEE, 2011, pp. 19–24.
- [152] D. A. Borton, M. Yin, J. Aceros, and A. Nurmikko, "An implantable wireless neural interface for recording cortical circuit dynamics in moving primates," *Journal of neural engineering*, vol. 10, no. 2, p. 026010, 2013.
- [153] R. Muller, S. Gambini, and J. M. Rabaey, "A 0.013, 5, dc-coupled neural signal acquisition ic with 0.5 v supply," *IEEE Journal of Solid-State Circuits*, vol. 47, no. 1, pp. 232–243, 2012.
- [154] Z. Xiao, C. M. Tang, C. M. Dougherty, and R. Bashirullah, "A 20 x00b5;w neural recording tag with supply-current-modulated afe in 0.13 x00b5;m cmos," in *2010 IEEE International Solid-State Circuits Conference - (ISSCC)*, Feb 2010, pp. 122–123.
- [155] H. N. Schwerdt, J. Chae, and F. A. Miranda, "Wireless performance of a fully passive neurorecording microsystem embedded in dispersive human head phantom," in *Proceedings of the 2012 IEEE International Symposium on Antennas and Propagation*. IEEE, 2012, pp. 1–2.

- [156] T. Bjorninen, R. Muller, P. Ledochowitsch, L. Sydanheimo, L. Ukkonen, M. M. Maharbiz, and J. M. Rabaey, "Design of wireless links to implanted brain-machine interface micro-electronic systems," *IEEE Antennas and Wireless Propagation Letters*, vol. 11, pp. 1663–1666, 2012.
- [157] E. Moradi, T. Björninen, L. Sydänheimo, L. Ukkonen, and J. M. Rabaey, "Analysis of wireless powering of mm-size neural recording tags in rfid-inspired wireless brain-machine interface systems," in *RFID (RFID), 2013 IEEE International Conference on*, April 2013, pp. 8–15.
- [158] K. Koski, A. Vena, L. Sydänheimo, L. Ukkonen, and Y. Rahmat-Samii, "Design and implementation of electro-textile ground planes for wearable uhf rfid patch tag antennas," *IEEE Antennas and Wireless Propagation Letters*, vol. 12, pp. 964–967, 2013.
- [159] E. Moradi, S. Amendola, T. Bjorninen, L. Sydanheimo, L. Ukkonen, J. M. Carmena, and J. M. Rabaey, "Wireless testing of ink-jet printed mm-size gold implant antennas for brain-machine interfaces," in *2014 IEEE Antennas and Propagation Society International Symposium (APSURSI)*, 2014.
- [160] A. Peyman, C. Gabriel, E. Grant, G. Vermeeren, and L. Martens, "Variation of the dielectric properties of tissues with age: the effect on the values of sar in children when exposed to walkie-talkie devices," *Physics in medicine and biology*, vol. 54, no. 2, p. 227, 2008.

List of Publications

Journals

1. S. Amendola, A. Palombi, G. Marrocco, “Inkjet Printing of Epidermal RFID Antennas by Self-Sintering Conductive Ink”, in *IEEE Transactions on Microwave Theory and Techniques*, under review.
2. C. Occhiuzzi, S. Amendola, S. Manzari, G. Marrocco, “RFID-based Multilevel Sensing Network for Industrial Internet of Things”, in *IEEE Journal of Radio Frequency Identification*, under review.
3. S. Amendola and G. Marrocco, “Optimal Performance of Epidermal Antennas for UHF Radiofrequency Identification and Sensing”, in *IEEE Transactions on Antennas and Propagation*, Nov. 2016.
4. C. Occhiuzzi, S. Amendola, S. Manzari, S. Caizzzone, G. Marrocco, “Configurable RFID Sensing Antenna Breadboard for Industrial IoT,” in *Electronics Letters*, pp.2, Dec. 2016.
5. S. Amendola, G. Bovesecci, A. Palombi, P. Coppa, G. Marrocco, “Design, Calibration and Experimentation of an Epi-

- dermal RFID sensor for remote Temperature Monitoring”, in *IEEE Sensors Journal*, vol. 16, no. 19, pp. 7250-7257, July 2016.
6. S. Amendola, S. Milici and G. Marrocco, “Performance of Epidermal RFID Dual-loop Tag and On-Skin Retuning,” in *IEEE Transactions on Antennas and Propagation*, vol. 63, no. 8, pp. 3672-3680, Aug. 2015.
 7. S. Amendola, L. Bianchi and G. Marrocco, “Body Movements Classification by Passive Radiofrequency Identification and Machine Learning Technologies”, *IEEE Antennas and Propagation Magazine*, vol. 57, n.3, June 2015.
 8. E. Moradi, S. Amendola, T.Björninen, L.Sydänheimo, J.M. Carmena, J. M. Rabaey, L Ukkonen, “Backscattering Neural Tags for Wireless Brain-Machine Interface Systems”, in *IEEE Transactions on Antennas and Propagation*, vol. 63, no. 2, pp. 719-726, Feb. 2015.
 9. S. Amendola, R. Lodato, S. Manzari, C. Occhiuzzi, G. Marrocco, “RFID Technology for IoT-Based Personal Healthcare in Smart Spaces,” *Internet of Things Journal*, IEEE , vol.1, no.2, pp.144,152, April 2014.
 10. C. Occhiuzzi, C. Vallese, S. Amendola, S. Manzari and G. Marrocco “NIGHT-Care: A Passive RFID System for Remote Monitoring and Control of Overnight Living Environment”, *Procedia Computer Science*, vol. 32, pp. 190-197, 2014.
 11. G. Casati, M. Longhi, D. Latini, F. Carbone, S. Amendola, F. Del Frate, G. Schiavon and G. Marrocco, “The Interrogation Footprint of RFID-UAV: Electromagnetic Modeling and Experimentations”, in *IEEE Journal of Radio Frequency Identification*, under review.

Book Chapters

1. S. Amendola, C. Occhiuzzi, G. Marrocco, “More than Wearable: Epidermal Antennas for Tracking and Sensing”, Chapter in *Electromagnetics of Body-Area Networks: Antennas*,

Propagation, and RF Systems, pp. 319-350, Wiley-IEEE Press, 2016.

2. C. Occhiuzzi, C. Vallese, S. Amendola, S. Manzari, and G. Marrocco, "Ambient Intelligence System for the Remote Monitoring and Control of Sleep Quality" Chapter in *Wearable Electronics Sensors: For Safe and Healthy Living*, pp. 263-282, Springer International Publishing, 2015.
3. S. Amendola, C. Occhiuzzi, S. Manzari, G. Marrocco, "RFID wireless sensor networks for monitoring Industrial and Critical IoT Infrastructures", Chapter to appear in *New Advances in the Internet of Things*, by Springer Editor, 2017.

Conferences

1. C. Miozzi, S. Amendola, A. Bergamini, G. Marrocco, "Reusable Battery-less Wireless Epidermal Temperature Sensor", submitted to *14th International Conference on Wearable and Implantable Body Sensor Networks (BSN2017)*, Eindhoven (Netherlands), May 2017.
2. V. Di Cecco, S. Amendola, P.P. Valentini, and G. Marrocco, "Finger-Augmented RFID System to Restore Peripheral Thermal Feeling", submitted to 2017 IEEE International Conference on RFID, Arizona, USA, May 2017.
3. C. Occhiuzzi, S. Amendola, S. Manzari, S. Caizzzone, G. Marrocco, "RFID Sensing Breadboard for Industrial IoT", accepted to the *International Applied Computational Electromagnetics Society (ACES) Symposium*, Florence, March 2017.
4. S. Amendola, A. Palombi, L. Rousseau, G. Lissorgues, G. Marrocco, "Manufacturing Technologies for UHF RFID Epidermal Antennas", *European Microwave Conference (EuMC), 2016 European*, London, October 2016.
5. C. Occhiuzzi, S. Amendola, S. Manzari, G. Marrocco "Industrial RFID Sensing Networks for Critical Infrastructure Security", *Microwave Conference (EuMC), 2016 European*, London, October 2016.

6. S. Amendola, G. Marrocco, “Epidermal UHF antennas for skin sensing: fundamental limitations and optimal performance”, *XXI RiNEm*, Parma, Sept. 2016.
7. C. Occhiuzzi, S. Amendola, S. Manzari, G. Marrocco, “ Passive RFID Sensor Network for Industrial Internet of Things”, *XXI RiNEm*, Parma, Sept. 2016.
8. S. Amendola, G. Bovesecci, P. Coppa and G. Marrocco, “Thermal characterization of Epidermal RFID sensor for Skin Temperature Measurements”, *Antennas and Propagation (APSURSI), 2016 IEEE International Symposium on*, Puerto Rico, June 26 - July 1, 2016.
9. S. Amendola, G. Marrocco “Epidermal UHF Antennas for Skin Sensing: Fundamental Limitations and Optimal Performance”, *Antennas and Propagation (APSURSI), 2016 IEEE International Symposium on*, Puerto Rico, July 1, 2016.
10. G. Marrocco, S. Amendola e C. Occhiuzzi, “Antennas and Sensors for Epidermal Electronics”, Tutorial, *IEEE 15th Mediterranean Microwave Symposium*, Dec. 2015, Lecce, Italy,
11. S. Amendola, C. Occhiuzzi, A. Ajovalasit, M. A. Sabatino, C. Dispenza, G. Marrocco, “Dielectric Characterization of Biocompatible Hydrogels for Application to Epidermal RFID Devices”, *Microwave Conference (EuMC), 2015 European*, pp. 379-382, Paris, 2015.
12. S. Amendola, S. Milici, C. Occhiuzzi, G. Marrocco, “On-Skin Tunable RFID Loop Tag for Epidermal Applications”, *2015 IEEE International Symposium on Antennas and Propagation & USNC/URSI National Radio Science Meeting*, pp. 202-203, Vancouver, BC, July 2015.
13. S. Amendola, L. Bianchi, and G. Marrocco, “Combined passive Radiofrequency identification and machine learning technique to recognize human motion,” *2014 44th European Microwave Conference*, pp. 1044-1047, Rome (Italy), Oct. 2014,
14. S. Milici, S. Amendola, A. Bianco and G. Marrocco, “Epidermal RFID Passive Sensor for Body Temperature Measurements”, *2014 IEEE RFID Technology and Applications (RFID-TA) Conference*, pp-140-144, Tampere, (Finland), Sept. 2014.

-
15. G. Marrocco, C. Occhiuzzi, C. Vallese, S. Amendola, S. Manzari, “Multi-channel processing of RFID backscattering for monitoring of overnight living”, 2014 URSI General Assembly and Scientific Symposium, Beijing, China, August 2014.
 16. S. Amendola, E. Moradi, K. Koski, T.Björninen, L.Ukkonen, L.Sydänheimo, Y.R.Samii, J.M. Rabaey, “Design and Optimization of mm-size Implantable and Wearable On-Body Antennas for Biomedical Systems”, *Antennas and Propagation (EUCAP), 8th European Conference on*, pp. 520-524, The Hague, Netherlands, April 2014.
 17. E. Moradi, S. Amendola, T. Bjorninen, L. Sydanheimo, L. Ukkonen, J.M. Carmena, J.Mm Rabaey, “Wireless testing of ink-jet printed mm-size gold implant antennas for Brain-Machine Interfaces,” *Antennas and Propagation Society International Symposium (APSURSI), 2014 IEEE*, pp. 963-964, July 2014.

Awards

1. 2015, Women in Wireless Power Transfer Award, from *European Cooperation in Science and Technology (WIPE COST IC1301)*.
2. 2015, Best Student Presentation Award, *2nd European School on RFID Harvesting and Sensing*, Valence.
3. 2014, Honorable Mention, IEEE MTT-S/AP-S 2014 Prize, Chapter of Central-South Italy.

